Springer Theses
Recognizing Outstanding Ph.D. Research

Jonathan Breeze

Temperature and Frequency Dependence of Complex Permittivity in Metal Oxide Dielectrics: Theory, Modelling and Measurement

Springer

Springer Theses

Recognizing Outstanding Ph.D. Research

Aims and Scope

The series "Springer Theses" brings together a selection of the very best Ph.D. theses from around the world and across the physical sciences. Nominated and endorsed by two recognized specialists, each published volume has been selected for its scientific excellence and the high impact of its contents for the pertinent field of research. For greater accessibility to non-specialists, the published versions include an extended introduction, as well as a foreword by the student's supervisor explaining the special relevance of the work for the field. As a whole, the series will provide a valuable resource both for newcomers to the research fields described, and for other scientists seeking detailed background information on special questions. Finally, it provides an accredited documentation of the valuable contributions made by today's younger generation of scientists.

Theses are accepted into the series by invited nomination only and must fulfill all of the following criteria

- They must be written in good English.
- The topic should fall within the confines of Chemistry, Physics, Earth Sciences, Engineering and related interdisciplinary fields such as Materials, Nanoscience, Chemical Engineering, Complex Systems and Biophysics.
- The work reported in the thesis must represent a significant scientific advance.
- If the thesis includes previously published material, permission to reproduce this must be gained from the respective copyright holder.
- They must have been examined and passed during the 12 months prior to nomination.
- Each thesis should include a foreword by the supervisor outlining the significance of its content.
- The theses should have a clearly defined structure including an introduction accessible to scientists not expert in that particular field.

More information about this series at http://www.springer.com/series/8790

Jonathan Breeze

Temperature and Frequency Dependence of Complex Permittivity in Metal Oxide Dielectrics: Theory, Modelling and Measurement

Doctoral Thesis accepted by
London South Bank University, London, UK

Springer

Author
Dr. Jonathan Breeze
Imperial College London
London
UK

Supervisors
Prof. Neil McN. Alford
Imperial College London
London
UK

Prof. Hari Reehal
Imperial College London
London
UK

ISSN 2190-5053 ISSN 2190-5061 (electronic)
Springer Theses
ISBN 978-3-319-44545-8 ISBN 978-3-319-44547-2 (eBook)
DOI 10.1007/978-3-319-44547-2

Library of Congress Control Number: 2016947940

Printed on acid-free paper

This Springer imprint is published by Springer Nature
The registered company is Springer International Publishing AG Switzerland

Supervisor's Foreword

In the past few decades there has been an explosion in satellite and mobile telecommunications technology. It is estimated that there are now more mobile phones than there are people on the planet. Microwave communications for voice, images, data and music are also closely correlated with the gross domestic product of a nation so the importance of the technology cannot be overstated. Microwave dielectrics play a key role in the development of the technology. Dielectric resonators are able to act as tuning forks; when an electromagnetic wave interacts with a dielectric the material resonates. Furthermore the wavelength of the electromagnetic waves can be "compressed" to be much shorter than the free space wavelength, permitting miniaturisation that is proportional to the reciprocal of the material's relative permittivity. The length of time that the resonator can "ring" once it has been struck with the electromagnetic wave is known as the quality factor or 'Q'. The Q is a measure of the material's dielectric loss and it is crucial that the loss be as low as possible. Finally the temperature coefficient of the dielectric constant (sometimes expressed as the temperature coefficient of frequency) is the third important parameter. Here, these three parameters are explored from the viewpoint of both theory and experiment.

Historically, the dielectric loss in particular has proven exceptionally difficult to describe, and the best theories so far have unfortunately been physically correct but practically unsatisfactory as they have been unable to predict the microwave dielectric loss in real materials that contain defects—all materials contain defects.

The thesis explores metal oxide based microwave dielectric ceramics, important materials in radio, microwave and terahertz applications. The performance of devices using these materials are often limited by absorption of electromagnetic energy or dielectric loss, which has been described theoretically as due to anharmonic coupling between lattice vibrations (phonons). Quantum field theory had been applied successfully to develop a theory of loss, yet absolute values of predicted losses were often orders of magnitude different to measurements. Historically, this was due to a lack of accurate data on the lattice dynamical properties of metal oxides and needing to resort to empirical models of

anharmonicity. This thesis shows for the first time that a theory of anharmonic phonon coupling using results from density function perturbation theory can predict from first principles the complex permittivity of metal oxides as a function of temperature and frequency. Here, the temperature and frequency dependence of relative permittivity and loss for MgO were calculated and found to be in excellent agreement with microwave measurements and terahertz spectroscopy. These results provide insight into the mechanisms of dielectric loss in oxides and offer the opportunity of engineering better dielectrics, especially for the rapidly developing terahertz field where losses are important.

The work was supported by the Engineering and Physical Sciences Research Council.

London, UK
June 2016

Prof. Neil McN. Alford

Abstract

This thesis investigates the dielectric properties of metal oxide ceramics at microwave frequencies. Dielectric ceramics are an important class of material for radio frequency, microwave and emergent terahertz technologies. Their key property is the complex permittivity, its real part permits miniaturisation of devices and its imaginary part is responsible for absorption of electromagnetic energy. Absorption limits the practical performance of many microwave devices such as filters, oscillators, passive circuits and antennas. The complex permittivity as a function of temperature for low-loss dielectrics is determined by measuring the resonant frequency of dielectric resonators and using the radial mode-matching technique to extract the dielectric properties.

There have been only a handful of publications on the theory of dielectric loss whose predictions have often been unfortunately unsatisfactory when compared to the measurements of real crystals, sometimes differing by orders of magnitude. The main reason for this is the lack of accurate data for anharmonic coupling coefficients and phonon eigenfrequencies at arbitrary q vectors in the Brillouin zone.

Here, a quantum field theory of losses in dielectrics shall be applied using results from density functional perturbation theory, to predict from first principles the complex permittivity of metal oxides as functions of frequency and temperature.

Acknowledgements

I extend my greatest thanks to my wife Caroline for her love, support and patience and my family who have always believed in me. My children Elinor and Iolo have often missed out on stuff because their dad has been preoccupied or working on his 'big homework'. Massive thanks to my good friend Prof. Neil Alford for his enthusiasm, encouragement, entertainment value and above all his patience. Professor Laurence Dunne has stimulated many off-topic and sometimes heated conversations, thanks for those. I have always been grateful to Prof. Jerzy Krupka for his encouragement, guidance and inspiration. Not to forget dear Prof. Hari Reehal for not giving up on me! I would also like to thank my *germà d'una altra mare*, Xavi and my old colleagues: Rob, Peter, Anna-Karin, Vinnie, Steve, Tom, Tony and Matjaž for their warm camaraderie over the *many* years.

Contents

List of Figures

List of Tables

Chapter 1
Introduction

1.1 The Radio Revolution

On 12 December, 1901 the age of wireless telecommunications began in earnest when Guglielmo Marconi transmitted the first transatlantic radio message from Poldhu in Cornwall, England to St. John's in Newfoundland, Canada. This pioneering form of communication has had a profound impact on many aspects of our way of life. A century later, radio and microwave communications have undergone a transformation that has resulted in them becoming ubiquitous. In recent decades, our use of the radio and microwave frequency bands of the electromagnetic spectrum has increased enormously. From 1 kHz to 100 GHz, the spectrum has been allocated and exploited by applications in radar, metrology, astronomy, telecommunications, radiometry, medicine and security (Fig. 1.1). In the late 1980s, mobile personal telephones became available to the public and satellite television made it possible to watch hundreds of channels broadcast all over the world. Almost everyone in reasonably developed countries now own a mobile telephone and in developing countries, mobile and satellite telecommunications have improved quality of life in areas where land-based networks required infeasibly large financial investment in infrastructure.

Radio and microwave communications have had a dramatic effect on consumer lifestyle especially regarding mobile devices. Each new generation of device brings greater use of frequency bandwidth, faster data rates and higher degrees of miniaturisation. Full integration of video, audio and Internet into compact hand-held terminals such as smartphones, tablets and laptop computers places ever-increasing demands on the electronic components used in their manufacture and has changed the way people work, organise and communicate in a fundamental way. The current 4^{th} generation of mobile broadband communication technology offers data rates up to 100 Mbs^{-1}, directly competing with fast fibre-optic and cable-based Internet provision. The number of satellites launched each year increases steadily as new advanced systems (constellations) with greater capacity, bandwidth and connectivity are developed and launched. Hundreds of satellite television channels, transmitted

J. Breeze, *Temperature and Frequency Dependence of Complex Permittivity in Metal Oxide Dielectrics: Theory, Modelling and Measurement*, Springer Theses, DOI 10.1007/978-3-319-44547-2_1

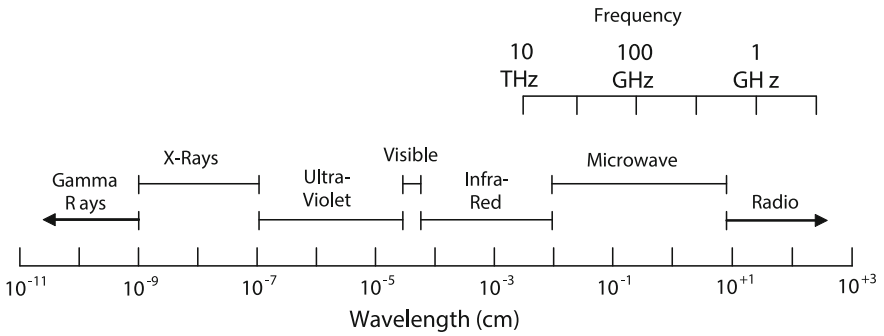

Fig. 1.1 The electromagnetic spectrum

from communications satellites in geostationary orbit can be viewed by a receiver on any continent on the planet, even Antarctica. It has been suggested that the fall of the iron curtain in Eastern Europe was accelerated by the fact that people had access to satellite transmitted television news services. The Iridium satellite system consisting of more than sixty low-earth orbit satellites launched in the late 1990s was one of the first examples of a satellite constellation that offered truly global mobile telecommunications to anyone in possession of a dedicated handset. Since then, people have been able to make telephone calls and access the Internet from the most remote locations on our planet. The fairly recent explosion in Internet and information-based communications demand has further resulted in a huge new frequency band between 20 and 30 GHz being allocated to broadband multimedia satellite communications. Additionally, hand-held devices such as smart-phones and specialised receivers can pinpoint their exact position on the surface of the planet using the Global Positioning System (GPS). This network of satellites, initially developed by the United States military, provides timing signals that allow receivers to accurately triangulate their position. The next generation of navigation via satellite, being developed by the European Space Agency is the Global Navigation Satellite System (GNSS). It marks the beginning of large-scale commercial exploitation of this kind of service allowing a multitude of applications for satellite-guided and tracked transport vehicles that will have a major impact on the logistics of agriculture, transportation and navigation. Satellites and interplanetary probes use orbiting radar systems to map the surface of Earth and other planets in the solar system. Radar has been used by commercial and military aircraft for the past sixty years to navigate and avoid mid-air collisions. Soon, radar use will be much more widespread and utilised on an everyday basis by road vehicles, cyclists and even pedestrians to warn of and prevent imminent collisions. Until recently the terahertz region of the electromagnetic spectrum had been relatively unexploited in comparison to the microwave and optical frequency ranges. New semiconductor devices and technologies have opened up this exciting frequency band with promise of novel applications in medicine, imaging, security and telecommunications. All modern embodiments of radio, microwave and terahertz technologies have one particular thing in common, they exploit dielectric ceramics.

1.2 Metal Oxide Microwave Dielectric Ceramics

The discovery of superconductivity at a record high temperature of 90 K (−180 °C) in a lanthanum cuprate ceramic by Bednorz and Muller in 1981 heralded a flurry of activity in the ceramics processing, experimental physics and theoretical condensed matter physics of metal oxides. This new class of materials, now known as high-temperature superconductors (HTS) are superconducting at temperatures as high as 125 K. Compared with the previous record in low temperature superconductors of 23 K this was an incredible surprise. However, it still remains for a satisfactory theoretical explanation of this effect to be developed after 30 years of intense activity in the field. Nevertheless, there is no doubt that this discovery provided a huge impetus in metal oxide ceramics spanning an enormous range of functional properties such as piezoelectrics, pyroelectrics, ferroelectrics, superconductors, semiconductors, ionic conductors and dielectrics.

Microwave dielectric ceramics are crucially important materials in microwave and radio frequency technology. In planar form they comprise substrates onto which electronic circuits can be printed. In bulk form they are used in resonators, filters, oscillators and antennas. Their main advantage is miniaturisation by virtue of their relative electric permittivity ε_r, allowing reductions in size by a factor of $\sqrt{\varepsilon_r}$. For example, a satellite cavity filter multiplexer manufactured from silver plated Invar alloy and weighing 1.5 Kg can be replaced by dielectric resonators and lightweight alloys for a fraction of the weight and volume as shown in Fig. 1.2. Considering that satellite launch costs are $10,000 per Kg this offers a significant advantage. The properties to consider when utilising dielectrics are

- Relative permittivity ε_r: allows device miniaturisation.
- Loss tangent $\tan\delta$: a measure of how much a material absorbs electromagnetic radiation. Its reciprocal is the dielectric quality factor Q_d.
- Temperature coefficients of permittivity τ_ε and thermal expansion α: dictates how resonant frequencies change with temperature.

Fig. 1.2 Size comparison of conventional and dielectric resonator C-Band output multiplexer filters. Image courtesy of Alcatel Espace

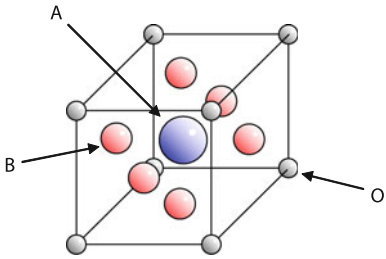

Fig. 1.3 The Perovskite unit cell

Often, the last two properties concerning temperature coefficients are lumped together, forming the temperature coefficient of resonant frequency τ_f. Richtmyer [1] first proposed using unmetallised dielectrics as resonators in 1939, but it was not until the 1960s that the first practical resonators were constructed by O'Bryan [2] and Negas. In 1981, Plourde and Ren [3] noted that of the best available dielectrics at that time, the highest ε_r was ~ 40, the highest dielectric Q was 9,000 (at 4 GHz) and the τ_f were typically in the region of 2-20 ppmK^{-1}. Today, most commercially available dielectrics have ε_r in the range 20–90 and Q values above 100,000 at 1 GHz. Many crystal structures are exhibited by microwave dielectrics, but one of the most common for temperature stable materials is the perovskite structure shown in Fig. 1.3. Perovskites have chemical formula ABO_3 and are named after the mineral $CaTiO_3$.

The first technique used to measure the properties of microwave dielectrics was the Hakki–Coleman technique [4], which involved placing a sample between two conducting plates and measuring the resonant frequency and quality factor of an excited mode using a network analyser. These measurements were then used to calculate the relative permittivity ε_r and loss tangent $\tan\delta$ of the material. Unfortunately, the Hakki–Coleman apparatus suffered from large measurement errors attributable to the structure being open at the sides, permitting electromagnetic energy to escape via radiation. A much improved method utilises a closed cylindrical cavity to house the dielectric. This arrangement is known as a *shielded dielectric resonator* and is one of the most accurate and practical methods of measuring dielectric properties. Accurate modelling of the fields within the dielectric resonators using Maxwell's equations allows the dielectric properties to be measured as functions of temperature and frequency. This will be investigated in Chaps. 2 and 3.

1.3 Review of Dielectric Loss

The focus of this thesis is the experimental characterisation and theoretical prediction of microwave dielectric losses in single-crystal ceramics. The phenomenon of microwave dielectric loss is a process whereby electromagnetic energy stored within a material is converted into vibrational energy. In classical terms, a time varying electric field couples to optically active polarised vibrations within the dielectric. These

polarised lattice vibrations couple to other vibrational modes through *anharmonicity* and irreversibly transfer energy to them. The observable macroscopic effect is an increase in the temperature of the material and decay of the energy stored within dielectric medium.

Maxwell's equations in a general medium (in SI units) are

$$\begin{aligned}\nabla \cdot \mathbf{D} &= \rho,\\ \nabla \cdot \mathbf{B} &= 0,\\ \nabla \times \mathbf{E} &= -\frac{\partial \mathbf{B}}{\partial t},\\ \nabla \times \mathbf{H} &= \mathbf{J} + \frac{\partial \mathbf{D}}{\partial t},\end{aligned}$$

where **D**, **B**, **E**, **H** and **J** are the electric displacement, magnetic field, electric field, magnetic field strength and current density vectors, defined by the constitutive relations

$$\begin{aligned}\mathbf{D} &= \varepsilon \mathbf{E},\\ \mathbf{B} &= \mu \mathbf{H},\\ \mathbf{J} &= \sigma \mathbf{E},\end{aligned}$$

where the quantities ε, μ and σ are the electric permittivity, magnetic permeability and electrical conductivity respectively. In the following treatment, for the sake of simplicity, the following will be assumed:

- The magnetic permeability μ is equal to that of free-space, i.e. $\mu = \mu_0$.
- The electric permittivity ε will be taken to be isotropic, hence $\varepsilon = \varepsilon_0 \varepsilon_r$.
- The current density is zero $\mathbf{J} = 0$ in an ideal insulator.

The relative permittivity ε_r is generally a complex quantity

$$\varepsilon_r = \varepsilon' + i\varepsilon'',$$

where the imaginary part, ε'' accounts for the dissipation of the electric field within the dielectric. The rate of change of energy per unit volume in a body can be calculated from the Poynting vector **S**, also known as the energy flux vector:

$$\mathbf{S} = \mathbf{E} \times \mathbf{H}.$$

By taking its divergence and using the continuity condition we can calculate the rate of change of energy per unit volume [5]:

$$-\nabla \cdot \mathbf{S} = \left(\mathbf{E} \frac{\partial \mathbf{D}}{\partial t} + \mathbf{H} \frac{\partial \mathbf{B}}{\partial t} \right).$$

Since the magnetic field does not do work on charged particles we shall assume that it has no role in dielectric loss, and so

$$-\nabla \cdot \mathbf{S} = \mathbf{E}\frac{\partial \mathbf{D}}{\partial t} = i\omega\varepsilon|\mathbf{E}|^2,$$

where $\mathbf{D} = \varepsilon\mathbf{E}$ and a time dependence of $e^{i\omega t}$ for the electric field $\mathbf{E}$ and displacement $\mathbf{D}$ is assumed. Since the rate of energy loss (power dissipation) $\nabla \cdot \mathbf{S}$, is a real quantity, it must depend on the imaginary part of the complex permittivity,

$$\nabla \cdot \mathbf{S} = \omega\varepsilon''|\mathbf{E}|^2.$$

The energy dissipated per oscillatory cycle of the field, W is therefore

$$W = \frac{2\pi}{\omega}\nabla \cdot \mathbf{S} = 2\pi\varepsilon''|\mathbf{E}|^2.$$

At resonance the electric energy density and magnetic energy density are equal, so the time-averaged stored energy in the dielectric is twice the time-averaged electric energy

$$U = \varepsilon'|\mathbf{E}|^2.$$

The *dielectric* quality factor Q_d[1] is defined as the 2π times the ratio of the time-averaged energy stored in the resonator to the energy dissipated per cycle of the field,

$$Q_d = 2\pi\frac{U}{W} = \frac{\varepsilon'}{\varepsilon''}. \tag{1.3.1}$$

The reciprocal of the dielectric quality factor Q_d is known as the loss factor or tangent delta,

$$\tan\delta = \frac{1}{Q_d} = \frac{\varepsilon''}{\varepsilon'}. \tag{1.3.2}$$

It is the fraction of electrical energy dissipated in a medium per field cycle period. As shown above, by conservation of energy, the power dissipated in the resonator is the negative of the rate of change of stored energy U. The definition of Q allows an equation for the time evolution of U to be written

$$\frac{dU}{dt} = -\frac{\omega_0}{Q}U$$

which has solution

$$U(t) = U_0 e^{-\omega_0 t/Q},$$

where U_0 is the initial energy stored in the resonator and ω_0/Q is the decay constant.

[1] The quality factor Q of a resonator is not the reciprocal of the $\tan\delta$ but depends on other sources of loss such as metallic wall losses and coupling/radiative losses.

The theory of microwave dielectric loss is a subject that has not been studied extensively and the number of relevant publications in the literature reflects that. It is a phenomenon associated with the interaction of vibrational collective excitations that propagate in insulating crystal lattices. These vibrational collective excitations are synonymous with sound waves and exhibit quasi-particle-like behaviour as *phonons*. Phonons can be classified as either acoustic or optical. Acoustic phonons are much like compressive and shear sound waves for long wavelengths and do not couple to macroscopic electric fields. Optical phonons normally occur at higher frequencies, usually in the terahertz to infrared, and behave quite differently at long wavelengths and couple strongly to macroscopic electric fields. Unlike acoustic phonons whose frequencies vanish at long wavelengths, optical phonon frequencies have limiting values. Both types of phonon attenuate via two main types of scattering mechanism: interaction with other phonons (intrinsic) and scattering from defects such as grain boundaries, dislocations and point defects (extrinsic). The intrinsic mechanism is due to *anharmonicity* of the inter-ionic potential and will be the subject of the theoretical part of this thesis.

Early investigations into dielectric loss were conducted at the turn of the 20th century by Debye [6–10] who studied the dipole relaxation of liquids from a classical perspective. This work was built upon later by Fröhlich [11]. Quantum mechanical theories were developed describing anharmonic phonon–phonon absorption processes in the far infrared for alkali halides by Woods and Cochran in 1960, followed by Stolen and Dransfield (1965) and Eldridge and Kembry (1973) [12–14]. A study on microwave absorption was also reported by Silverman in 1961, who investigated losses in cubic strontium titanate [15]. A few years later in 1973, Sham, who had been developing a quantum field theory of second sound in solids, instigated research with Sparks into multi-phonon absorption culminating in 1981 with the popular Sparks–King–Mills model [16–18]. It proposed that phonon transitions occurred across the frequency gap between acoustic and optical phonons at the Brillouin zone boundary. The theory was then improved upon by Subbaswamy and Mills by taking into account the finite lifetime of the thermal phonons involved in the process [19]. Significant work on the anharmonic optical properties of insulators was also published in the 1960 and 1970s by Cowley and Coombs [20, 21].

The most thorough and prominent work on microwave dielectric loss from a theoretical point of view was conducted by Gurevich [22–25]. He developed a rigorous and analytical quantum theory that predicted the temperature and frequency dependence of losses. Gurevich's theory took crystal symmetry into account and incorporated ideas proposed by Herring regarding phonon–phonon collisions between accidentally degenerate low-energy acoustic phonons [26–28]. The validity of Gurevich's theory has been confirmed in measurements of the temperature and frequency dependence of high-quality single crystals of sapphire by Braginsky and Ilchenko [29] and also in polycrystalline analogues of single crystals by Alford et al. [30]. Gurevich's theoretical foundation on dielectric loss was further built upon by Tagantsev

to better describe losses in non-centrosymmetric crystals such as ferroelectrics [31–34]. However, the main drawback of these theories was the lack of accurate data for phonon dispersion and the anharmonicity of crystal lattices. This meant that although frequency and temperature dependencies of loss were correctly described, the absolute magnitude of the predicted loss was sometimes orders of magnitude different to that measured. Astonishing advances in computing power, molecular dynamical simulations and quantum mechanical codes have now enabled predictions of the lattice dynamical properties of insulators. A molecular dynamics study by Deppe in 1992, predicted the frequency response of the transverse optic phonon in Lithium Iodide by taking the autocorrelation of the time-domain dipole moment [35]. Inter-ionic potentials in molecular dynamics were empirically derived by fitting calculated lattice dynamical properties to measured physical properties such as the bulk modulus. The advent of *density functional theory* (DFT) had the greatest impact on the field and for first time it became possible to predict the lattice dynamical properties of materials *ab-initio* from first principles. DFT uses pseudopotentials to approximate the electronic structure of atoms without any empirical requirements at all. Another important milestone in the first-principles study of anharmonic phonon processes was established by Debernardi in 1995 who developed the '$2n + 1$' theorem based upon density functional perturbation theory [36–39]. It enabled the calculation of the anharmonicity of crystal lattices, allowed the lifetime of Raman modes to be calculated with good accuracy and precipitated much further work into the anharmonic properties of semiconductors [40–44]. Most of this work however has concentrated on properties at infrared and optical frequencies. Recently, for the microwave frequency range, Wu and Shtin separately computed the microwave dielectric losses in binary oxides using quantum theories of anharmonic phonon interactions [45, 46]. However, both models used empirically derived inter-ionic potentials. Aupi and Shimada have also applied the Sparks–King–Mills model with estimates of the lattice anharmonicity and thermal phonon lifetimes measured by Raman spectroscopy to Sapphire and Lanthanum Aluminate with some success [47, 48]. However, there is doubt about the validity of using the lifetimes measured by Raman spectroscopy to describe infrared active phonons in these models. Dunne et al. also reported a novel approach to dielectric loss based on the fluctuation-dissipation theory without implicit recourse to phonon–phonon interactions.

To date, there have been no reports of microwave dielectric losses calculated from first principles. This thesis aims to address this omission and also go further by attempting to fully describe the complex permittivity frequency and temperature dependence for a simple microwave dielectric (in this case MgO) using density functional perturbation theory and a general theory of microwave absorption by anharmonic phonons.

1.4 Structure of Thesis

After the introductory chapter the thesis will be loosely structured into three parts of two chapters. Part 1: Chaps. 2 and 3 is on the modelling of dielectric resonators and the measurement of dielectric properties. Part 2: Chaps. 4 and 5 concerns the theory, modelling and prediction of the harmonic properties of the metal oxide dielectrics MgO, $LaAlO_3$, TiO_2 and Al_2O_3. Finally, Part 3: Chaps. 6 and 7 discusses the theory of anharmonic interactions and provides predictions of the complex permittivity of MgO as a function of temperature and frequency.

Chapter 2: Modelling Dielectric Resonators

Maxwell's equations are applied to the problem of modelling a shielded uniaxially anisotropic dielectric resonator using the *radial mode matching* method.

Chapter 3: Measurement of Dielectric Properties

The experimental apparatus for measuring the dielectric properties of samples as functions of temperature from room temperature down to temperatures of 10K.

Chapter 4: Lattice Dynamics and Density Functional Perturbation Theory

The lattice dynamics of insulating crystals are reviewed, followed by a brief treatise on density functional methods. The calculation of phonon modes, dynamical matrices, Born effective charges and LO-TO splitting are discussed.

Chapter 5: Harmonic Properties of Metal Oxide Dielectrics

The harmonic properties of MgO, $LaAlO_3$, TiO_2 and Al_2O_3, such as phonon frequency dispersion relations and relative permittivities are calculated using DFPT and compared to the experimentally measured values.

Chapter 6: Theory of Anharmonic Phonons

The theory of anharmonic crystal lattices is discussed within the framework of lattice dynamics. A quantum field theory of anharmonic phonons is introduced and lowest order anharmonic phonon interactions are investigated and expressions derived for the self-energy of phonons.

Chapter 7: Anharmonic Properties of MgO

Results from DFPT and quantum field theory are used to calculate the self-energy for transverse optic phonons as a function of frequency and temperature. An in-depth investigation into the frequency and temperature dependence of the individual phonon–phonon interactions that contribute to the inverse lifetime is conducted and comparison with experiment is made.

Chapter 8: Summary and Conclusions

A short review of the thesis with conclusions and a summary of future work that could be carried out.

1.5 Publications by the Author

The author has published the following journal papers with some relevance to the topic discussed.

'Room-temperature solid-state maser'
M. Oxborrow, J.D. Breeze and N.McN. Alford, Nature **488**, 353 (2012).

'Better than Bragg: Optimizing the quality factor of resonators with aperiodic dielectric reflectors'
J. Breeze, M. Oxborrow and N.McN. Alford, Applied Physics Letters, **99**, 113515 (2011).

'Intrinsic microwave dielectric loss of lanthanum aluminate'
T. Shimada, K. Ichikawa, T. Minemura, H. Yamauchi, W. Utsumi, Y. Ishii, J. Breeze and N.M. Alford, IEEE Transactions on Ultrasonics, Ferroelectrics and Frequency Control, **57**, 2243 (2010).

'Temperature-stable and high Q-factor TiO_2 Bragg reflector resonator'
J. Breeze, J. Krupka, A. Centeno and N.M. Alford, Applied Physics Letters **94**, 082906 (2009).

'Do grain boundaries affect microwave dielectric loss in oxides?'
J.D. Breeze and J.M. Perkins, D.W. McComb and N.M. Alford, Journal of the American Ceramic Society, **92**, 671 (2009).

'Enhanced quality factors in aperiodic reflector resonators'
J. Breeze, J. Krupka and N.M. Alford, Applied Physics Letters, **91**, 152902 (2007).

'Measurements of permittivity, dielectric loss tangent and resistivity of float-zone silicon at microwave frequencies'
J. Krupka, J. Breeze, A. Centeno, N. Alford, T. Claussen and L. Jensen, IEEE Transactions on Microwave Theory and Techniques, **54**, 3995 (2006).

'Quasi-classical fluctuation-dissipation description of dielectric loss in oxides with implications for quantum information processing'
L.J. Dunne, A.-K. Axelsson, N.M. Alford, J. Breeze, X. Aupi, E.J. Brändas, International Journal of Quantum Chemistry, **106**, 986 (2006).

'Microwave dielectric loss in oxides: Theory and experiment'
X. Aupi, J. Breeze, N. Ljepojevic, L.J. Dunne, N. Malde, A.-K. Axelsson and N.M. Alford, Journal of Applied Physics, **95**, 2639 (2004).

References

1. R.D. Richtmyer, Dielectric Resonators. J. Appl. Phys. **10**, 391 (1939)
2. H.M. O'Bryan, J. Thompson, J.K. Plourde, A new $BaO\text{-}TiO_2$ compound with temperature-stable high permittivity and low microwave loss. J. Am. Ceram. Soc. **57**, 450 (1974)

3. J.K. Plourde et al., $Ba_2Ti_9O_{20}$ as a microwave dielectric resonator. J. Am. Ceram. Soc. **58**, 418 (1975)
4. B.W. Hakki, P.D. Coleman, A dielectric resonator method of measuring inductive capacities in the millimeter range. IEEE Trans. Microwave Theory Tech. **8**, 402 (1960)
5. L.D. Landau, E.M. Lifshitz, L.P. Pitaevskii, *Electrodynamics of Continuous Media*, 2nd edn. (Butterworth-Heinemann, Oxford, 1984)
6. P. Debye, Der Lichtdruck auf Kugeln von Beliebigem Material. Annalen der Physik **335**, 57 (1909)
7. P. Debye, Zur theorie der Spezifischen Wärmen. Annalen der Physik **344**, 789 (1912)
8. P.J.W. Debye, Zur Theorie der Anomalen Dispersion im Gebiete der Langwelligen Elektrischen Strahlung. Berichte Deutschen Physikalischen Gesellschaft **15**, 777 (1913)
9. P. Debye, *Vortrage uber die kinetische Theorie der Materie und der Elektrizität*, vol. 6 (Teubner, Leipzig, 1914)
10. P. Debye, *Polar Molecules* (Dover, Mineola, 1929)
11. H. Fröhlich, *Theory of Dielectrics*, 2nd edn. (Oxford University Press, Oxford, 1958)
12. A.D.B. Woods, W. Cochran, B.N. Brockhouse, Lattice dynamics of alkaline halides crystals. Phys. Rev. **119**, 980 (1960)
13. R. Stolen, K. Dransfeld, Far-infrared lattice absorption in alkali halides crystals. Phys. Rev. **139**, A1295 (1965)
14. J.E. Eldridge, K.A. Kembry, Further measurements and calculations of the far-infrared anharmonic optical properties of KI between 12 and 300 K. Phys. Rev. B **8**, 746 (1973)
15. B.D. Silverman, Microwave absorption in cubic strontium titanate. Phys. Rev. **125**, 1921 (1962)
16. L.J. Sham, Equilibrium approach to second sound in solids. Phys. Rev. **156**, 494 (1967)
17. M. Sparks, L.J. Sham, Theory of multiphonon absorption in insulating crystals. Phys. Rev. B **8**, 3037 (1973)
18. M. Sparks, D.F. King, D.L. Mills, Simple theory of microwave absorption in alkali halides. Phys. Rev. B **26**, 6987 (1982)
19. K.R. Subbaswamy, D.L. Mills, Theory of microwave absorption in wide-band-gap insulators: the role of thermal phonon lifetimes. Phys. Rev. B **33**, 4213 (1986)
20. R.A. Cowley, Lattice dynamics of an anharmonic crystal. Adv. Phys. **12**, 421 (1963)
21. G.J. Coombs, R.A. Cowley, Paraelectric, piezoelectric and pyroelectric crystals: I. Dielectric properties. J. Phys. C: Solid State Phys. **6**, 121 (1973)
22. V.L. Gurevich, Dielectric losses in crystals. Fizika Tverdogo Tela **21**, 3453 (1979)
23. V.L. Gurevich, A.K. Tagantsev, Intrinsic dielectric loss in crystals: low temperatures. Sov. Phys. JETP **64**, 142 (1986)
24. V.L. Gurevich, *Transport in Phonon Systems*, 1st edn. (North-Holland Physics Publishing, Amsterdam, 1986)
25. V.L. Gurevich, A.K. Tagantsev, Intrinsic dielectric loss in crystals. Adv. Phys. **40**, 719 (1991)
26. C. Herring, Effect of time-reversal symmetry on energy bands of crystals. Phys. Rev. **52**, 361 (1937)
27. C. Herring, Accidental degeneracy in energy bands of crystals. Phys. Rev. **52**, 365 (1937)
28. C. Herring, Role of low-energy phonons in thermal conduction. Phys. Rev. **95**, 954 (1954)
29. V.B. Braginsky, V.S. Ilchenko, K.S. Bagdassarov, Experimental observation of fundamental microwave absorption in high-quality dielectric crystals. Phys. Lett. A **120**, 300 (1987)
30. N.M. Alford et al., Dielectric loss of oxide single crystals and polycrystalline analogues from 10 to 320 K. J. Eur. Ceram. Soc. **21**, 2605 (2001)
31. A.K. Tagantsev, Effect of weak electric field on dielectric losses in centrally symmetric ferroelectric materials of displacement type. Zhurnal Eksperimentalnoi i Teoreticheskoi Fiziki **77**, 1993 (1979)
32. A.K. Tagantsev, Dielectric losses in displacive ferroelectrics. Zhurnal Eksperimentalnoi i Teoreticheskoi Fiziki **86**, 2215 (1984)
33. A.K. Tagantsev, Weak ferroelectrics. Ferroelectrics **79**, 57 (1988)
34. A.K. Tagantsev, J. Petzelt, N. Setter, Relation between intrinsic microwave and submillimeter losses and permitivity in dielectrics. Solid State Commun. **87**, 1117 (1993)

35. J. Deppe et al., Molecular-dynamics study of the lattice-vibration contribution to the frequency-dependent dielectric constant of lithium iodide. Phys. Rev. B **45**, 5687 (1992)
36. A. Debernardi, S. Baroni, E. Molarini, Anharmonic phonon lifetimes in semiconductors from density-functional perturbation theory. Phys. Rev. Lett. **75**, 1819 (1995)
37. A. Debernardi, M. Cardona, Isotopic effects on the lattice constant in compound semiconductors by perturbation theory: an ab initio calculation. Phys. Rev. B **54**, 11305 (1996)
38. A. Debernardi, Phonon linewidth in III-V semiconductors from density-functional perturbation theory. Phys. Rev. B **57**, 12847 (1998)
39. A. Debernardi, M. Cardona, First principles calculation of the real part of phonon self energy in compound semiconductors. Phys. B: Condens. Matter **263**, 687 (1999)
40. G. Lang et al., Anharmonic line shift and linewidth of the Raman mode in covalent semiconductors. Phys. Rev. B **59**, 6182 (1999)
41. G. Deinzer, G. Birner, D. Strauch, Ab initio calculation of the linewidth of various modes in germanium and silicon. Phys. Rev. B **67**, 144304 (2003)
42. G. Deinzer et al., Intrinsic lifetimes and anharmonic frequency shifts of long-wavelength optical phonons in polar crystals. Phys. Rev. B **69**, 014304 (2004)
43. H.M. Lawler, E.L. Shirley, Anharmonic effects on infrared spectra of GaAs and GaP: first-principles calculations. Phys. Rev. B **70**, 245209 (2004)
44. E.L. Shirley, H.M. Lawler, Two-phonon infrared spectra of Si and Ge: calculating and assigning features. Phys. Rev. B **76**, 054116 (2007)
45. E.J. Wu, G. Ceder, Computational investigation of dielectric absorption at microwave frequencies in binary oxides. J. Appl. Phys. **89**, 5630 (2001)
46. N.A. Shtin, J.M.L. Romero, E. Prokhorov, Theory of fundamental microwave absorption in sapphire (α-Al_2O_3). J. Appl. Phys. **106**, 104115 (2009)
47. X. Aupi et al., Microwave dielectric loss in oxides: theory and experiment. J. Appl. Phys. **95**, 2639 (2004)
48. T. Shimada et al., Intrinsic microwave dielectric loss of lanthanum aluminate. IEEE Trans. Ultrason., Ferroelectr. Freq. Control **57**, 2243 (2010)

Chapter 2
Modelling Dielectric Resonators

There are many techniques available for characterising the complex permittivity of microwave dielectric ceramics as functions of temperature and frequency. For materials with modest dielectric loss ($\tan\delta > 10^{-3}$) broadband transmission line measurements can yield the complex permittivity with reasonable accuracy over a wide frequency range. However, for very low loss dielectrics ($\tan\delta < 10^{-4}$) such as the ones studied here, a dielectric resonator technique is required. A dielectric resonator consists of a cylindrical dielectric sample mounted upon a low-loss, low-permittivity support such as quartz or polystyrene, housed within a conducting metallic cylindrical cavity. Microwaves are coupled into the resonator via ports, small loops or probe antennas protruding through the walls of the cavity. The coupling strength is set very low to prevent the resonant frequency of the mode from being perturbed. The resonant frequency and quality factor of a suitable resonant mode can then be measured using a network analyser, either in reflection (one-port) or transmission (two-port). To extract the relative permittivity and loss tangent of a dielectric sample from a microwave measurement or to be able to predict the resonant frequency and quality factor of a resonator, it is necessary to accurately model the electromagnetic fields of resonant modes within dielectric resonator structures. This chapter will apply Maxwell's equations to model the resonant modes supported by cylindrical dielectric resonators using the rigorous analytical technique known as radial mode matching.

2.1 Introduction to Microwave Dielectrics

The dielectric properties of interest to engineers and scientists are the relative permittivity, loss tangent and temperature coefficient of permittivity. They are all, strictly speaking, temperature and frequency dependent, although the relative permittivity is fairly constant over microwave frequencies and can therefore be considered constant to all intensive purposes.

J. Breeze, *Temperature and Frequency Dependence of Complex Permittivity in Metal Oxide Dielectrics: Theory, Modelling and Measurement*, Springer Theses, DOI 10.1007/978-3-319-44547-2_2

Relative Permittivity, ε_r

The real part of the complex permittivity ε_r allows device dimensions to be reduced by a factor of $\sqrt{\varepsilon_r}$ and varies greatly in microwave ceramics, from $\varepsilon_r \approx 4$ for quartz (SiO_2) to $\varepsilon_r > 4000$ for ferroelectrics such as $BaTiO_3$. Almost all single crystal microwave dielectrics with non-cubic crystal structure have anisotropic relative permittivities. For example, a biaxial dielectric would have permittivity tensor:

$$\boldsymbol{\varepsilon} = \begin{bmatrix} \varepsilon_x & 0 & 0 \\ 0 & \varepsilon_y & 0 \\ 0 & 0 & \varepsilon_z \end{bmatrix}.$$

For instance, single crystal rutile TiO_2 is uniaxially anisotropic and has permittivities $\varepsilon_{r,\perp} = 86$ and $\varepsilon_{r,\parallel} = 163$, perpendicular and parallel to the crystal c-axis [1]. Most polycrystalline microwave ceramics have isotropic relative permittivity due to the random orientation of their crystallites, although processing conditions such as temperature gradients can sometimes result in slight anisotropy in the relative permittivity.

Loss Tangent, $\tan\delta$

The ratio of the imaginary and real parts of the complex permittivity, $\tan\delta = \varepsilon''/\varepsilon'$, limits the performance of microwave devices due to absorption of microwave electric field energy. The dielectric quality factor Q_d, an often quoted figure of merit is the reciprocal of the loss tangent, $Q_d = 1/\tan\delta$. The loss tangent is sometimes assumed to vary linearly with frequency, leading to the often quoted Qf factor where the dielectric quality factor Q_d is multiplied by the frequency at which it was measured. Typically, higher permittivity dielectrics have higher dielectric losses. Anisotropic dielectrics such as single crystals will also have tensorial loss tangents with identical symmetry to their relative permittivity tensors. For example, rutile TiO_2 has $\tan\delta_\perp = 1.5 \times 10^{-4}$ and $\tan\delta_\parallel = 1.8 \times 10^{-4}$ for loss tangents perpendicular and parallel to the c-axis at 10 GHz and room temperature.

Temperature Coefficient of Permittivity, τ_ε

This property governs how the centre frequency of a filter or resonant frequency of a dielectric resonator varies with temperature. It is given by the fractional change in the relative permittivity as the temperature varies:

$$\tau_\varepsilon = \frac{1}{\varepsilon_r}\frac{\partial\varepsilon_r}{\partial T}.$$

The temperature coefficient of permittivity (sometimes abbreviated as TCε_r) is often not the property quoted by ceramic manufacturers and engineers. Instead the τ_f or temperature coefficient of frequency (TCf) is reported. This is erroneous since the τ_f is also dependent on the thermal expansion coefficients of the ceramic and the metallic shield, the resonator geometry and resonant mode's electric and magnetic field distributions. Temperature coefficients can be tuned in ceramics by careful

Table 2.1 Typical dielectric properties of some polycrystalline microwave dielectric materials at room temperature [2]

Material	ε_r	$\tau_\varepsilon(\text{ppmK}^{-1})$	$Q_d = 1/\tan\delta$	f(GHz)
$Ba(Mg_{1/3}Ta_{2/3})O_3$	24	0	26,000	10
$Ba(Zn_{1/3}Ta_{2/3})O_3$	30	$-6, \ldots, +6$	12,000	6
$(Zr_{0.8}Sn_{0.2})TiO_4$	38	$-6, \ldots, +6$	8,000	7
$0.7CaTiO_3$-$0.3NdAlO_3$	43	0	7,000	6.7
Al_2O_3	10	+120	100,000	10
TiO_2	100	−900	17,000	3

Table 2.2 Typical dielectric properties of the some single crystal microwave dielectric materials at room temperature [2]. The perpendicular ($\perp$) and parallel ($\parallel$) subscripts refer to components with respect to the crystal c-axis

Material	$\varepsilon_\perp$	$\varepsilon_\parallel$	$\tau_{\varepsilon,\perp}(\text{ppmK}^{-1})$	$\tau_{\varepsilon,\parallel}(\text{ppmK}^{-1})$	$Qf_\perp$	$Qf_\parallel$
SiO_2	4.443	4.644	9	28.7	1,400,000	2,100,000
MgF_2	5.48	4.765	210	–	490,000	220,000
$SrLaAlO_4$	16.85	19.8	50	–	628,000	181,000
Al_2O_3	9.935	11.59	85	121	1,170,000	1,890,000
TiO_2	85.7	163.2	−760	−1200	64,600	56,300

attention to processing, doping and solid solution stoichiometry. For anisotropic dielectrics, the τ_ε also has the same symmetry as the relative permittivity and loss tangent tensors. Again, for rutile TiO_2, values are $\tau_{\varepsilon,\perp} = 760$ ppmK^{-1} and $\tau_{\varepsilon,\parallel} = -1200$ ppmK^{-1} at room temperature. Tables 2.1 and 2.2 show dielectric properties for some common polycrystalline and single crystal microwave dielectric materials.

2.2 Measuring Microwave Dielectric Properties

The measurement of the resonant frequency and quality factor of dielectric resonators as functions of temperature and frequency allows the complex permittivity of a dielectric material to be determined. To transform these measurements into values for the relative permittivity ε_r, loss tangent $\tan\delta$ and temperature coefficient of permittivity τ_ε accurate electromagnetic modelling is required. Furthermore, accurate modelling allows for the optimisation of resonator geometries with respect to losses and spurious modes. The simplest type of apparatus which can be used to measure the dielectric properties of microwave ceramics is the Courtney holder. This device consists of a parallel pair of circular plates which sandwich a small cylindrical ceramic sample. The open sides allow probes or antennae to be inserted in order to excite the resonant mode. The technique was first proposed by

Hakki and Coleman [3] and later analysis of errors and temperature effects were reported by Courtney [4]. Providing that the distance between the plates (the height of the sample) is less than half the free-space wavelength then the electric field of the TE_{011} mode should decay evanescently away from the sample along the radial direction and therefore should not radiate significantly. Kobayashi [5, 6] studied a resonator consisting of a dielectric rod short-circuited at both ends by metal plates and found that the finite diameter of the plates meant that microwave energy could escape by radiation. Furthermore, the transverse magnetic modes (TM) were found to be unsuitable for accurate measurement of the permittivity. The absence of a radial cut-off frequency for TM modes means they have low quality factor due to radiation losses. Small air gaps between the resonator and the plates have considerable effect on the resonant frequency and can lead to large uncertainties in the computed relative permittivity. Ohmic losses induced in the metal plates, due to their proximity to the dielectric sample, limit the measurable $\tan\delta$ since they become the dominant loss mechanism when the dielectric sample has low losses. An obvious loss mitigating step is to separate the dielectric sample from the plates and to use a low-permittivity low-loss dielectric such as quartz or PTFE for support if required. Closing the sides of the resonator will also eliminate radiation losses. DelaBalle et al. [7] numerically studied the case of a dielectric puck within a cavity separated from the cavity walls and Hong [8] studied shielded resonators consisting of pucks placed upon a substrate. Zaki et al. [9] reported highly accurate mode matching results for dielectric samples placed upon low-permittivity supports within cylindrical cavities. Later, Krupka [10], Tobar [11] and Kobayashi [12] reported theoretical and experimental findings for anisotropic dielectrics (mostly single crystals) using highly accurate Rayleigh–Ritz and mode matching methods. They later extended these models to include higher order whispering gallery modes (WGM) which allowed components of the complex permittivity tensor both perpendicular and parallel to the cylindrical axis to be measured [1, 13]. The natural evolution of devices for measuring the complex permittivity of low-loss dielectrics has led to *shielded dielectric resonators* being the most widely employed structures today for measuring the properties of microwave dielectric ceramics.

2.3 Modelling Shielded Dielectric Resonators

Most electromagnetic modelling techniques (and all commercially available software packages), whether they are rigorous or not, take as input the geometry of a structure and the electromagnetic properties of the materials that define it. Typically, the output is the frequency response, or in the case of resonators, the resonant modes of the system. This is important from an engineering point of view when designing devices with an intended frequency response using materials with known properties. From a meteorological point of view this is a hindrance since it is often the electrical properties that are sought given a resonator geometry and measured frequency response. This presents what is known as an *inverse problem* that can be tackled in

various ways. For example, the permittivity of a sample could be found by successive iteration, varying the permittivity in the model until the resonant frequency agrees with measurement. Alternatively, generating a lookup table of values for resonant frequency versus permittivity and interpolating between them could provide reasonably accurate estimates of the permittivity given the resonant frequency. However, both these methods are inherently inefficient since they both require many computation steps. It is desirable to be able to directly calculate the permittivity and loss tangent of a material given a resonant frequency and geometrical description. This is accomplished by modifying existing techniques to solve for permittivity instead of resonant frequency. For the finite-difference time-domain (FDTD) method, the eigenmodes are extracted by spectral analysis of the time-domain response and so this technique cannot be modified. Frequency domain methods such as finite differences or finite elements could be used effectively, but both these techniques have high computational cost if very accurate results are required. The quasi-analytical *mode matching* technique is probably the most accurate method of modelling dielectric resonators, whose accuracy is governed by the number of terms in the truncated series expansion of eigenmode basis functions. The advantage of this technique is that it has very low computational overhead and is very amenable to quickly processing large numbers of data points, which is the case for temperature measurements or optimisation algorithms.

The shielded dielectric resonator as shown in Fig. 2.1, is the most common type of dielectric resonator geometry due to its ease of construction, elimination of radiative losses and reduction of ohmic losses in the conducting shield. It is also the most extensively studied due to its practical application in microwave filters and oscillators as resonant elements. The structure consists of a metal cylindrical cavity, constructed from a high electrical conductivity material such as copper or a silver-plated metal such as brass or aluminium. Inside the cavity is a support structure which is commonly a disk, cylinder or substrate of low-permittivity, low-loss dielectric such as quartz or alumina. The purpose of the support structure is to move the dielectric sample away from the conducting shield to reduce ohmic losses. The dielectric resonator itself is usually a ceramic disk or ring placed on top of the support structure.

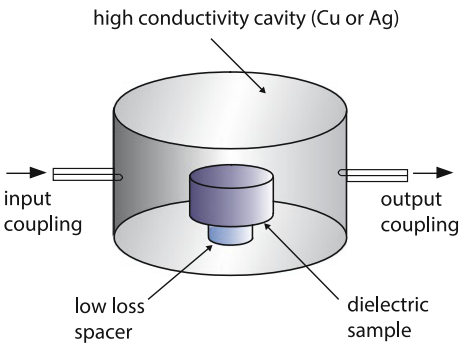

Fig. 2.1 Shielded dielectric resonator

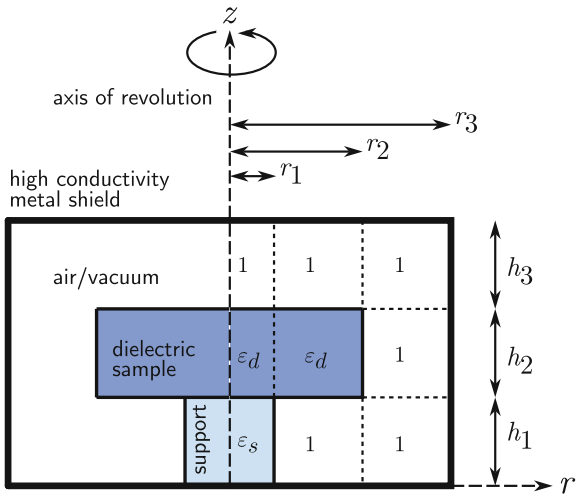

Fig. 2.2 Cross section of dielectric resonator geometry showing how the regions form a 3 × 3 problem space where each piecewise element has an assigned relative permittivity tensor

The structure is symmetrical about the cylindrical axis and so can be considered as a body of revolution with the cross section shown in Fig. 2.2. In the $r - z$ plane, the resonator system can be split up into piecewise regular regions in which the permittivity tensor is homogeneous. The permittivity tensor in each of the nine cells can be represented by a matrix ε_{ijk} where i and j index the layer and radial region of the cell, respectively, and k indexes the component of the permittivity tensor. The electromagnetic fields in each region can be expanded as an infinite series of linear combinations of eigenmodes (basis functions). When the tangential electric and magnetic fields are matched at the interfaces between regions and the boundary conditions on the metallic shield are satisfied, an infinite homogeneous system of linear equations is obtained. The solutions are non-trivial only when the determinant of a characteristic matrix vanishes. Hence, the resonant frequencies or the permittivity can be found by searching for the zeros of the determinant. In practice it is necessary to truncate the series expansion to include a finite number of basis functions. The number of basis functions is increased until an acceptable level of convergence is achieved. For cylindrical symmetric resonators the mode matching method can be approached in two different ways. The axial mode matching method proposed by Zaki [9] first solves a set of eigenvalue problems in the radial direction to obtain eigenvalues which are then used to generate an eigenproblem by matching the fields across layers in the axial direction. Conversely, the radial mode matching method [14] first obtains the eigenvalues for an array of multilayered parallel plate waveguides in the axial direction. Following this step, the fields are matched across region boundaries in the radial direction. Although both radial and axial mode matching techniques have similar accuracy and performance, the radial mode matching technique has an advantage because the first step of the process solves transcendental equations containing only trigonometric functions, whereas the axial technique involves transcendental equations containing Bessel functions.

2.4 Maxwell Equations in Cylindrical Coordinates

To solve the shielded dielectric resonator problem using either the radial or axial mode matching method, one begins with Maxwell's equations in cylindrical coordinates (Fig. 2.3). Maxwell's equations for time harmonic electric **E** and magnetic **H** fields of frequency ω in a linear, homogeneous and source-free medium with anisotropic relative electric permittivity $\tilde{\varepsilon}_r$ and magnetic permeability of free-space, $\mu = \mu_0$ are:

$$\begin{aligned} \nabla \times \mathbf{E} &= -i\omega\mu_0 \mathbf{H}, \\ \nabla \times \mathbf{H} &= +i\omega\varepsilon_0\tilde{\varepsilon}_r \mathbf{E}, \\ \nabla \cdot (\tilde{\varepsilon}_r \mathbf{E}) &= 0, \\ \nabla \cdot \mathbf{H} &= 0. \end{aligned} \tag{2.4.1}$$

The relative permittivity tensor, constrained by the coordinate system to be uniaxial is given by

$$\tilde{\varepsilon}_r = \begin{bmatrix} \varepsilon_t & 0 & 0 \\ 0 & \varepsilon_t & 0 \\ 0 & 0 & \varepsilon_z \end{bmatrix},$$

where ε_t and ε_z are the transverse and longitudinal components with respect to the z-axis. The relative permittivity tensor will be assumed to be purely real, since for useful microwave dielectrics the imaginary part is much smaller than the real part, $\varepsilon'' \ll \varepsilon'$. Equations (2.4.1) can be rearranged in terms of **E** and **H**:

$$\begin{aligned} \mathbf{E} &= -\frac{i}{\omega\varepsilon_0}\tilde{\varepsilon}_r^{-1} \nabla \times \mathbf{H}, \\ \mathbf{H} &= +\frac{i}{\omega\mu_0} \nabla \times \mathbf{E}. \end{aligned} \tag{2.4.2}$$

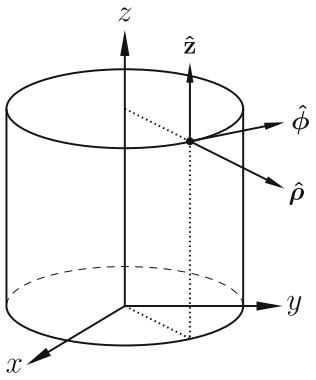

Fig. 2.3 Cylindrical coordinate system

Since the relative permittivity tensor $\tilde{\varepsilon}_r$ is diagonal it is easily inverted and so evaluating the curl operators in cylindrical coordinates provides expressions for the electric and magnetic field components:

$$
\begin{aligned}
E_\rho &= -\frac{i}{\omega\varepsilon_0\varepsilon_t}\left\{\frac{1}{\rho}\frac{\partial H_z}{\partial\phi} - \frac{\partial H_\phi}{\partial z}\right\} \\
E_\phi &= -\frac{i}{\omega\varepsilon_0\varepsilon_t}\left\{\frac{\partial H_\rho}{\partial z} - \frac{\partial H_z}{\partial\rho}\right\} \\
E_z &= -\frac{i}{\omega\varepsilon_0\varepsilon_z\rho}\left\{\frac{\partial}{\partial\rho}\left(\rho H_\phi\right) - \frac{\partial H_\rho}{\partial\phi}\right\} \\
H_\rho &= +\frac{i}{\omega\mu_0}\left\{\frac{1}{\rho}\frac{\partial E_z}{\partial\phi} - \frac{\partial E_\phi}{\partial z}\right\} \\
H_\phi &= +\frac{i}{\omega\mu_0}\left\{\frac{\partial E_\rho}{\partial z} - \frac{\partial E_z}{\partial\rho}\right\} \\
H_z &= +\frac{i}{\omega\rho\mu_0}\left\{\frac{\partial}{\partial\rho}\left(\rho E_\phi\right) - \frac{\partial E_\rho}{\partial\phi}\right\}.
\end{aligned}
\tag{2.4.3}
$$

The equations in ρ and ϕ can be reformulated entirely in terms of the axial field components E_z and H_z by substitution,

$$
\begin{aligned}
\left(\frac{\partial^2}{\partial z^2} + k_0^2\varepsilon_t\right)E_\rho &= \frac{\partial^2 E_z}{\partial\rho\partial z} - \frac{i\omega\mu}{\rho}\frac{\partial H_z}{\partial\phi} \\
\left(\frac{\partial^2}{\partial z^2} + k_0^2\varepsilon_t\right)E_\phi &= \frac{1}{\rho}\frac{\partial^2 E_z}{\partial\phi\partial z} + i\omega\mu\frac{\partial H_z}{\partial\rho} \\
\left(\frac{\partial^2}{\partial z^2} + k_0^2\varepsilon_t\right)H_\rho &= \frac{\partial^2 H_z}{\partial\rho\partial z} + \frac{i\omega\varepsilon_0\varepsilon_t}{\rho}\frac{\partial E_z}{\partial\phi} \\
\left(\frac{\partial^2}{\partial z^2} + k_0^2\varepsilon_t\right)H_\phi &= \frac{1}{\rho}\frac{\partial^2 H_z}{\partial\phi\partial z} - i\omega\varepsilon_0\varepsilon_t\frac{\partial E_z}{\partial\rho},
\end{aligned}
\tag{2.4.4}
$$

where k_0 is the free-space wavenumber. Modes that propagate in the axial z direction can be classified as follows:

- **Transverse electric (TE)**
  These modes have no axial electric field component ($E_z = 0$) and so the electric field is purely transverse (TE). They are designated as h-modes in the literature due to the axial magnetic field component, H_z.
- **Transverse magnetic (TM)**
  These modes have no axial magnetic field component ($H_z = 0$) and so the magnetic field is purely transverse (TM). They are designated as e-modes in the literature due to the axial electric field component, E_z.
- **Hybrid modes (HE/HM)**
  These modes have both electric and magnetic axial field components ($E_z \neq$

0, $H_z \neq 0$). The designation HE (hybrid electric) or HM (hybrid magnetic) depends on which field is dominant in the axial direction.

The next step is to solve Maxwell's equations for the axial field components E_z and H_z. Application of the curl vector operator to both sides of Maxwell's equations (2.4.1) yields

$$\nabla \times \nabla \times \mathbf{E} = -i\omega\mu_0 \nabla \times \mathbf{H} = k_0^2 \tilde{\varepsilon}_r \mathbf{E} \tag{2.4.5}$$

$$\nabla \times \nabla \times \mathbf{H} = +i\omega\varepsilon_0 \nabla \times \tilde{\varepsilon}_r \mathbf{E}. \tag{2.4.6}$$

Applying the double curl vector identity, $\nabla \times \nabla \times \mathbf{A} = \nabla (\nabla \cdot \mathbf{A}) - \nabla^2 \mathbf{A}$, to (2.4.5) gives

$$\nabla^2 \mathbf{E} - \nabla (\nabla \cdot \mathbf{E}) + k_0^2 \tilde{\varepsilon}_r \mathbf{E} = 0. \tag{2.4.7}$$

The divergence of the electric displacement $\mathbf{D}$ is zero, $\nabla \cdot \mathbf{D} = 0$, due to the absence of free charges. For an isotropic dielectric the divergence of the electric field is also zero, because $\nabla \cdot (\varepsilon_r \mathbf{E}) = \varepsilon_r \nabla \cdot \mathbf{E} = 0$. However, for an anisotropic dielectric the divergence of the electric field is not zero since

$$\nabla \cdot (\tilde{\varepsilon}_r \mathbf{E}) = \varepsilon_t \nabla \cdot \mathbf{E} - \varepsilon_t \left(1 - \frac{\varepsilon_z}{\varepsilon_t}\right) \frac{\partial E_z}{\partial z} = 0,$$

resulting in

$$\nabla \cdot \mathbf{E} = \left(1 - \frac{\varepsilon_z}{\varepsilon_t}\right) \frac{\partial E_z}{\partial z}. \tag{2.4.8}$$

Substituting (2.4.8) into (2.4.7) yields

$$\nabla^2 \mathbf{E} - \left(1 - \frac{\varepsilon_z}{\varepsilon_t}\right) \nabla \frac{\partial E_z}{\partial z} + k_0^2 \tilde{\varepsilon}_r \mathbf{E} = 0. \tag{2.4.9}$$

Taking the z component yields the Helmholtz wave equation in E_z:

$$\nabla^2 E_z - \left(1 - \frac{\varepsilon_z}{\varepsilon_t}\right) \frac{\partial^2 E_z}{\partial z^2} + k_0^2 \varepsilon_z E_z = 0. \tag{2.4.10}$$

The Laplacian operator ∇^2, in cylindrical coordinates (see Fig. 2.3) is given by

$$\nabla^2 = \frac{1}{\rho} \frac{\partial}{\partial \rho} \left(\rho \frac{\partial}{\partial \rho}\right) + \frac{1}{\rho^2} \frac{\partial^2}{\partial \phi^2} + \frac{\partial^2}{\partial z^2}. \tag{2.4.11}$$

A solution for E_z of the form

$$E_z(\rho, \phi, z) = R(\rho)\Phi(\phi)Z(z),$$

can be sought by the method of separation of variables. Substituting this in the scalar wave equation (2.4.10) and dividing throughout by $E_z = R(\rho)\Phi(\phi)Z(z)$ produces

$$\frac{1}{\rho R(\rho)}\frac{\partial}{\partial\rho}\left[\rho\frac{\partial R(\rho)}{\partial\rho}\right]+\frac{1}{\rho^2\Phi(\phi)}\frac{\partial^2\Phi(\phi)}{\partial\phi^2}+\frac{1}{Z(z)}\frac{\varepsilon_z}{\varepsilon_t}\frac{\partial^2 Z(z)}{\partial z^2}+k_0^2\varepsilon_z=0. \quad (2.4.12)$$

The third term is independent of both ρ and ϕ and further inspection shows that this term must also be independent of z since the other terms are independent of z and the whole expression sums to zero. The third term must therefore be a coefficient,

$$\frac{1}{Z(z)}\frac{\varepsilon_z}{\varepsilon_t}\frac{\partial^2 Z(z)}{\partial z^2}=-\frac{\varepsilon_z}{\varepsilon_t}\beta^2. \quad (2.4.13)$$

The $-\beta^2$ coefficient is chosen since $Z(z)$ is expected to have an axial variation of the form $e^{i\beta z}$ where β is the propagation constant. Substitution of (2.4.13) into (2.4.12) and multiplying throughout by ρ^2 yields

$$\frac{\rho}{R(\rho)}\frac{\partial}{\partial\rho}\left[\rho\frac{\partial R(\rho)}{\partial\rho}\right]+\frac{1}{\Phi(\phi)}\frac{\partial^2\Phi(\phi)}{\partial\phi^2}+\rho^2\left(k_0^2\varepsilon_z-\frac{\varepsilon_z}{\varepsilon_t}\beta^2\right)=0. \quad (2.4.14)$$

The second term is a function only of ϕ and so the same term independence argument also applies in this case, with m being the azimuthal dependence assuming a variation of the form $e^{im\phi}$, resulting in

$$\frac{1}{\Phi(\phi)}\frac{\partial^2\Phi(\phi)}{\partial\phi^2}=-m^2. \quad (2.4.15)$$

Substitution of (2.4.15) into (2.4.14) and multiplying throughout by $R(\rho)$ gives

$$\rho\frac{\partial}{\partial\rho}\left[\rho\frac{\partial}{\partial\rho}R(\rho)\right]+\left[\lambda^e\rho^2-m^2\right]R(\rho)=0, \quad (2.4.16)$$

where $\lambda^e = k_0^2\varepsilon_z - \frac{\varepsilon_z}{\varepsilon_t}\beta^2$. Notice that (2.4.16) is a partial differential equation in ρ only. We have now separated (2.4.12) into three partial differential equations in $R(\rho)$, $\Phi(\phi)$ and $Z(z)$ (2.4.16), (2.4.15) and (2.4.13). The two equations in z and ϕ are harmonic and therefore have trigonometric solutions. Equation (2.4.16) is a Bessel differential equation of order m and argument $\sqrt{\lambda^e}\rho$. A general solution for $E_z(\rho, \phi, z)$ is therefore given by

$$E_z=\left[A^eJ_m(\xi^e\rho)+B^eY_m(\xi^e\rho)\right]\left[a^e\sin\beta^ez+b^e\cos\beta^ez\right]\left\{\begin{matrix}\cos m\phi\\ \sin m\phi\end{matrix}\right\}, \quad (2.4.17)$$

where $\xi^e = \sqrt{\lambda^e}$ and A^e, B^e, a^e and b^e are coefficients. The e superscript identifies this as an e-mode. J_m and Y_m are Bessel functions of the first and second kinds of

order m [15]. If the Bessel function argument ξ^e is imaginary, then the radial solution will consists of the modified Bessel functions of the first and second kind:

$$I_m(x) = (-i)^m J_m(ix)$$

and

$$K_m(x) = \frac{\pi}{2} i^{m+1} \left[J_m(ix) + iY_m(ix) \right].$$

The radial solution in this case would be

$$R^e(\rho) = A^e I_m(|\xi^e|\rho) + B^e K_m(|\xi^e|\rho).$$

Similarly if the propagation constant is imaginary, the trigonometric functions in the axial eigenfunction are replaced by hyperbolic functions and take the form

$$Z^e(z) = a^e \sinh |\beta^e| z + b^e \cosh |\beta^e| z.$$

Applying the vector identity to the double curl of $\mathbf{H}$, (2.4.6) and noting that the divergence of the magnetic field is zero, $\nabla \cdot \mathbf{H} = 0$, due to the absence of magnetic monopoles, yields:

$$\nabla^2 \mathbf{H} + i\omega\varepsilon_0 \nabla \times \tilde{\varepsilon}_r \mathbf{E} = 0, \tag{2.4.18}$$

and again taking the z component results in the Helmholtz wave equation for H_z:

$$\nabla^2 H_z + k_0^2 \varepsilon_t H_z = 0. \tag{2.4.19}$$

Similar derivation as above for E_z leads to the general solution for H_z:

$$H_z = \left[A^h J_m(\xi^h \rho) + B^h Y_m(\xi^h \rho) \right] \left[a^h \sin \beta^h z + b^h \cos \beta^h z \right] \begin{Bmatrix} \cos m\phi \\ \sin m\phi \end{Bmatrix}, \tag{2.4.20}$$

where $\xi^h = \sqrt{\lambda^h}$ and A^h, B^h, a^h and b^h are coefficients. The separation constant in this case is given by $\lambda^h = k_0^2 \varepsilon_t - (\beta^h)^2$. Remembering that the axial electric and magnetic fields are a superposition of an infinite number of eigenmodes, for any eigenmode p, the radial functions in ρ can be represented by

$$R_p^{e,h}(\rho) = A_p^{e,h} P_p^{e,h}(\rho) + B_p^{e,h} Q_p^{e,h}(\rho), \tag{2.4.21}$$

where

$$P_p^{e,h}(\rho) = \begin{cases} J_m(\xi_p^{e,h}\rho), & \lambda_p^{e,h} > 0 \\ I_m(\xi_p^{e,h}\rho), & \lambda_p^{e,h} < 0 \end{cases} \tag{2.4.22}$$

$$Q_p^{e,h}(\rho) = \begin{cases} Y_m(\xi_p^{e,h}\rho), & \lambda_p^{e,h} > 0 \\ K_m(\xi_p^{e,h}\rho), & \lambda_p^{e,h} < 0 \end{cases} \tag{2.4.23}$$

and $\xi_p^{e,h} = \sqrt{|\lambda_p^{e,h}|}$. The axial eigenfunctions can be represented by

$$Z_p^{e,h}(z) = \begin{cases} a_p^{e,h} \sin \beta_p^{e,h} z + b_p^{e,h} \cos \beta_p^{e,h} z, & (\beta_p^{e,h})^2 > 0 \\ a_p^{e,h} \sinh |\beta_p^{e,h}| z + b_p^{e,h} \cosh |\beta_p^{e,h}| z, & (\beta_p^{e,h})^2 < 0 \end{cases} \tag{2.4.24}$$

and the azimuthal variation by

$$\Phi_m^e(\phi) = \begin{Bmatrix} \cos m\phi \\ \sin m\phi \end{Bmatrix} \tag{2.4.25}$$

and

$$\Phi_m^h(\phi) = \begin{Bmatrix} -\sin m\phi \\ \cos m\phi \end{Bmatrix}. \tag{2.4.26}$$

Note that $\Phi^{e\prime}(\phi) = m\Phi_m^h(\phi)$ and $\Phi^{h\prime}(\phi) = -m\Phi_m^e(\phi)$, where the prime indicates the derivative with respect to ϕ. General solutions can therefore be expressed in the form:

$$E_z = \sum_p R_p^e(\rho) Z_p^e(z) \Phi_m^e(\phi)$$
$$H_z = \sum_p R_p^h(\rho) Z_p^h(z) \Phi_m^h(\phi),$$

where the summation is over an infinite number of eigenmodes p. The transverse field components are obtained from the axial components using Eqs. (2.4.4),

$$\begin{aligned} E_\rho &= \frac{\varepsilon_z}{\varepsilon_t \lambda^e} \frac{\partial^2 E_z}{\partial \rho \partial z} - \frac{i\omega\mu}{\rho\lambda^h} \frac{\partial H_z}{\partial \phi} \\ E_\phi &= \frac{\varepsilon_z}{\varepsilon_t \lambda^e \rho} \frac{\partial^2 E_z}{\partial \phi \partial z} + \frac{i\omega\mu}{\lambda^h} \frac{\partial H_z}{\partial \rho} \\ H_\rho &= \frac{1}{\lambda^h} \frac{\partial^2 H_z}{\partial \rho \partial z} + \frac{i\omega\varepsilon_0\varepsilon_z}{\rho\lambda^e} \frac{\partial E_z}{\partial \phi} \\ H_\phi &= \frac{1}{\rho\lambda^h} \frac{\partial^2 H_z}{\partial \phi \partial z} - \frac{i\omega\varepsilon_0\varepsilon_z}{\lambda^e} \frac{\partial E_z}{\partial \rho} \end{aligned} \tag{2.4.27}$$

yielding a complete set of field components for each eigenmode p. The field components in cylindrical coordinates can then be written as infinite sums over p:

$$
\begin{aligned}
E_\rho &= \frac{\varepsilon_z}{\varepsilon_t}\sum_p R_p^{e\prime}(\rho)Z_p^{e\prime}(z)\Phi_m^e(\phi) + \frac{im\omega\mu}{\rho}\sum_p R_p^h(\rho)Z_p^h(z)\Phi_m^e(\phi)\\
E_\phi &= \frac{m\varepsilon_z}{\rho\varepsilon_t}\sum_p R_p^e(\rho)Z_p^{e\prime}(z)\Phi_m^h(\phi) + i\omega\mu\sum_p R_p^{h\prime}(\rho)Z_p^h(z)\Phi_m^h(\phi)\\
E_z &= \sum_p \lambda_p^e R_p^e(\rho)Z_p^e(z)\Phi_m^e(\phi)\\
H_\rho &= \frac{im\omega\varepsilon_0\varepsilon_z}{\rho}\sum_p R_p^e(\rho)Z_p^e(z)\Phi_m^h(\phi) + \sum_p R_p^{h\prime}(\rho)Z_p^{h\prime}(z)\Phi_m^h(\phi)\\
H_\phi &= -i\omega\varepsilon_0\varepsilon_z\sum_p R_p^{e\prime}(\rho)Z_p^e(z)\Phi_m^e(\phi) - \frac{m}{\rho}\sum_p R_p^h(\rho)Z_p^{h\prime}(z)\Phi_m^e(\phi)\\
H_z &= \sum_p \lambda_p^h R_p^h(\rho)Z_p^h(z)\Phi_m^h(\phi),
\end{aligned}
\tag{2.4.28}
$$

where the factors $\lambda_p^{e,h}$ have been incorporated into E_z and H_z and primed radial and axial functions represent derivatives with respect to ρ or z. This set of equations allows the field components in any region to be conveniently defined as series expansions of basis functions.

2.5 Multilayer Waveguide Eigenvalues

The multilayer waveguide geometry consists of a parallel plate waveguide partially filled with different layers of dielectric. The eigenvalues λ^e and λ^h can be found for any partial radial region by solving the multilayer waveguide problem shown in Fig. 2.4. Since the axial fields are a superposition of TE and TM modes, the eigenvalues can be found for them independently.

The $\sin m\phi$ and $\cos m\phi$ azimuthal terms can be omitted since they are the same for all layers and radial regions for a given m. Hence, the eigenvalues λ_p^e and λ_p^h are independent of the azimuthal index m. This fact can be used for computational efficiency when searching for solutions for different m indices since the eigenvalues only need to be calculated once for all m. The radial functions can also be omitted since they are layer independent for any partial radial region. For TM modes, where $H_z = 0$, the system of equations for an eigenmode in layer i for a particular partial region is

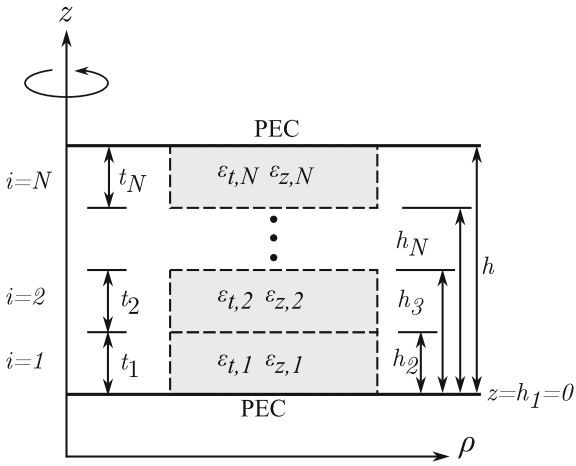

Fig. 2.4 The anisotropic dielectric-loaded parallel plate waveguide. There are N layers of dielectric each with thickness t_i, where $i = 1, 2, \ldots, N$. The multilayer is sandwiched by perfect electric conductors (PEC)

$$
\begin{aligned}
E^e_{\rho,i} &= \frac{\varepsilon_{z,i}}{\varepsilon_{t,i}}\beta^e_i\left[a^e_i\cos\beta^e_i(z-h_i) - b^e_i\sin\beta^e_i(z-h_i)\right]\\
E^e_{\phi,i} &= \frac{\varepsilon_{z,i}}{\varepsilon_{t,i}}\frac{m}{\rho}\beta^e_i\left[a^e_i\cos\beta^e_i(z-h_i) - b^e_i\sin\beta^e_i(z-h_i)\right]\\
E^e_{z,i} &= \lambda^e\left[a^e_i\sin\beta^e_i(z-h_i) + b^e_i\cos\beta^e_i(z-h_i)\right]\\
H^e_{\rho,i} &= \frac{im\omega\varepsilon_0\varepsilon_{z,i}}{\rho}\left[a^e_i\sin\beta^e_i(z-h_i) + b^e_i\cos\beta^e_i(z-h_i)\right]\\
H^e_{\phi,i} &= -i\omega\varepsilon_0\varepsilon_{z,i}\left[a^e_i\sin\beta^e_i(z-h_i) + b^e\cos\beta^e_i(z-h_i)\right]\\
H^e_{z,i} &= 0.
\end{aligned}
\tag{2.5.1}
$$

Similarly, For TE modes, where $E_z = 0$,

$$
\begin{aligned}
E^h_{\rho,i} &= \frac{im\omega\mu}{\rho}\left[a^h_i\sin\beta^h_i(z-h_i) + b^h_i\cos\beta^h_i(z-h_i)\right]\\
E^h_{\phi,i} &= i\omega\mu\left[a^h_i\sin\beta^h_i(z-h_i) + b^h_i\cos\beta^h_i(z-h_i)\right]\\
E^h_{z,i} &= 0\\
H^h_{\rho,i} &= \beta^h_i\left[a^h_i\cos\beta^h_i(z-h_i) - b^h_i\sin\beta^h_i(z-h_i)\right]\\
H^h_{\phi,i} &= -\frac{m}{\rho}\beta^h_i\left[a^h_i\cos\beta^h_i(z-h_i) - b^h_i\sin\beta^h_i(z-h_i)\right]\\
H^h_{z,i} &= \lambda^h\left[a^h_i\sin\beta^h_i(z-h_i) + b^h_i\cos\beta^h_i(z-h_i)\right],
\end{aligned}
$$

where h_i is the height where layer i with thickness t_i begins. The eigenvalues λ^e_p and λ^h_p can be obtained for the multilayer problem by matching the tangential field components at the interfaces between layers and enforcing the boundary conditions on the perfect electric conductors (PEC) at the top and bottom. Matching the tangential

TM and TE fields at the interfaces between layers i and $i+1$ at $z = h_{i+1}$:

$$\begin{aligned} E^e_{\rho,i} &= E^e_{\rho,i+1} \quad E^h_{\rho,i} = E^h_{\rho,i+1} \\ E^e_{\phi,i} &= E^e_{\phi,i+1} \quad E^h_{\phi,i} = E^h_{\phi,i+1} \\ H^e_{\rho,i} &= H^e_{\rho,i+1} \quad H^h_{\rho,i} = H^h_{\rho,i+1} \\ H^e_{\phi,i} &= H^e_{\phi,i+1} \quad H^h_{\phi,i} = H^h_{\phi,i+1}, \end{aligned}$$

results in four equations,

$$\begin{aligned} \frac{\varepsilon_{z,i}}{\varepsilon_{t,i}}\beta^e_i\left(a^e_i\cos\beta^e_i t_i - b^e_i\sin\beta^e_i t_i\right) &= \frac{\varepsilon_{z,i+1}}{\varepsilon_{t,i+1}}\beta^e_{i+1}a^e_{i+1} \\ \varepsilon_{z,i}\left(a^e_i\sin\beta^e_i t_i + b^e\cos\beta^e_i t_i\right) &= \varepsilon_{z,i+1}b^e_{i+1} \\ \left(a^h_i\sin\beta^h_i t_i + b^h_i\cos\beta^h_i t_i\right) &= b^h_{i+1} \\ \beta^h_i\left(a^h_i\cos\beta^h_i t_i - b^h_i\sin\beta^h_i t_i\right) &= \beta^h_{i+1}a^h_{i+1}. \end{aligned}$$

These four equations can be written as a pair of transfer matrix equations relating the coefficients in layer $i+1$ to those in layer i,

$$\begin{bmatrix} a^e_{i+1} \\ b^e_{i+1} \end{bmatrix} = \mathcal{Z}^e_{i,i+1}\begin{bmatrix} a^e_i \\ b^e_i \end{bmatrix},$$
$$\begin{bmatrix} a^h_{i+1} \\ b^h_{i+1} \end{bmatrix} = \mathcal{Z}^h_{i,i+1}\begin{bmatrix} a^h_i \\ b^h_i \end{bmatrix}.$$

The axial transfer matrices $\mathcal{Z}^e_{i,i+1}$ and $\mathcal{Z}^h_{i,i+1}$ are

$$\mathcal{Z}^e_{i,i+1} = \begin{bmatrix} \frac{\varepsilon_{z,i}\varepsilon_{t,i+1}}{\varepsilon_{t,i}\varepsilon_{z,i+1}}\frac{\beta^e_i}{\beta^e_{i+1}}\cos\beta^e_i t_i & -\frac{\varepsilon_{z,i}\varepsilon_{t,i+1}}{\varepsilon_{t,i}\varepsilon_{z,i+1}}\frac{\beta^e_i}{\beta^e_{i+1}}\sin\beta^e_i t_i \\ \frac{\varepsilon_{z,i}}{\varepsilon_{z,i+1}}\sin\beta^e_i t_i & +\frac{\varepsilon_{z,i}}{\varepsilon_{z,i+1}}\cos\beta^e_i t_i \end{bmatrix}$$
$$\mathcal{Z}^h_{i,i+1} = \begin{bmatrix} \frac{\beta^h_i}{\beta^h_{i+1}}\cos\beta^h_i t_i & -\frac{\beta^h_i}{\beta^h_{i+1}}\sin\beta^h_i t_i \\ \sin\beta^h_i t_i & +\cos\beta^h_i t_i \end{bmatrix},$$

where the propagation coefficients $\beta^{(e,h)}_i$ in each layer are calculated from the eigenvalues $\lambda^{(e,h)}$:

$$\beta^e_i = \sqrt{\varepsilon_{t,i}k_0^2 - \frac{\varepsilon_{t,i}}{\varepsilon_{z,i}}\lambda^e}$$
$$\beta^h_i = \sqrt{\varepsilon_{t,i}k_0^2 - \lambda^h}.$$

The PEC boundary condition at the bottom of the multilayer forces the tangential electric field components to be zero,

$$a_1^e = 0$$
$$b_1^h = 0.$$

The coefficients b_1^e and a_1^h can be initially set to unity, then once the eigenvalues have been found, the coefficients a_i^e, b_i^e, a_i^h and b_i^h in all layers are normalised by taking inner products. The coefficients in subsequent layers, $i > 1$, are obtained by applying the transfer matrices to the set of coefficients in the previous layer. Successive multiplication propagates the coefficients for the bottommost layer to the final topmost layer, $i = N$:

$$\begin{bmatrix} a_N^e \\ b_N^e \end{bmatrix} = \prod_{i=1}^{N-1} \mathcal{Z}_{i,i+1}^e \begin{bmatrix} a_1^e \\ b_1^e \end{bmatrix}$$
$$\begin{bmatrix} a_N^h \\ b_N^h \end{bmatrix} = \prod_{i=1}^{N-1} \mathcal{Z}_{i,i+1}^h \begin{bmatrix} a_1^h \\ b_1^h \end{bmatrix}.$$

The eigenvalues are found by searching for solutions which satisfy the boundary conditions on the upper PEC boundary at $z = h$, that the transverse electric field components are zero:

$$E_{\rho,N}^e(h) = 0$$
$$E_{\phi,N}^e(h) = 0$$
$$E_{\rho,N}^h(h) = 0$$
$$E_{\phi,N}^h(h) = 0.$$

These conditions are given by

$$a_N^e \cos \beta_N^e t_N - b_N^e \sin \beta_N^e t_N = 0,$$
$$a_N^h \sin \beta_N^h t_N + b_N^h \cos \beta_N^h t_N = 0. \tag{2.5.2}$$

It can be shown that although there are an infinite number of solutions for the eigenvalues λ_p^e and λ_p^h, there are only a finite number of positive solutions due to the cut-off condition [14]:

$$\lambda_p^{e,h} < k_0^2 \varepsilon_{z,t}^{\max},$$

where the superscript 'max' denotes the highest value of permittivity throughout all the regions in the entire structure. This cut-off condition is used as an upper bound for all eigenvalues. The eigenvalue search is conducted by setting $\lambda^{e,h}$ to a value slightly smaller than $k_0^2 \varepsilon_{z,t}^{\max}$ (setting to exactly this value would mean that $\beta^{e,h}$ would be zero). $\lambda^{e,h}$ is then decreased by small steps until a sign change in Eqs. (2.5.2) is observed. Once a zero has been *bracketed* in this way, the solution can be refined using a root-finding algorithm such as the bisection method [16], Ridders' method [17] or the Brent method [18]. When using the transfer matrix technique, care must be taken to avoid cases where the propagation coefficient $\beta^{e,h}$

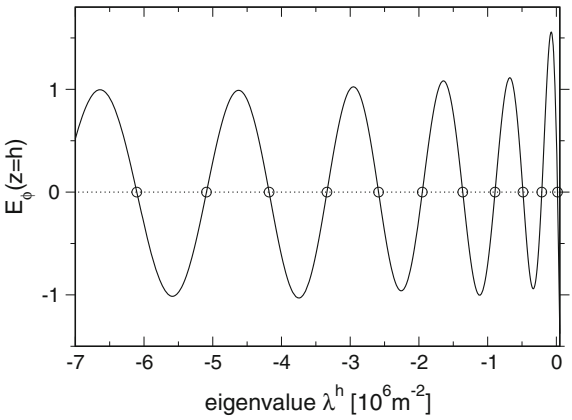

Fig. 2.5 Searching for the *h*-mode (TE) eigenvalues for a 3-layer problem at 10 GHz. The thicknesses of the layers were $t_1 = 4.0$ mm, $t_2 = 5.0$ mm and $t_3 = 6.0$ mm and the transverse permittivities $\varepsilon_{t,1} = 4.3$, $\varepsilon_{t,2} = 10.0$ and $\varepsilon_{t,3} = 1.0$. The circles locate the positions of the eigenvalues

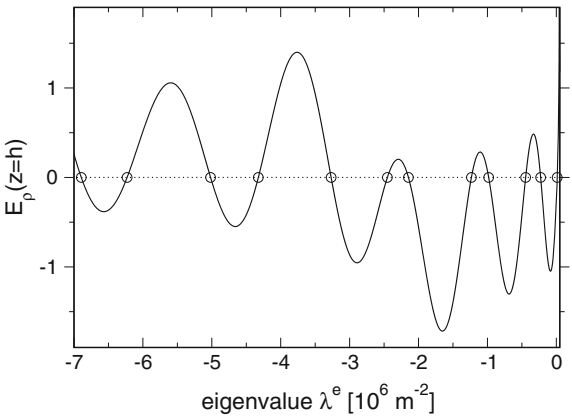

Fig. 2.6 Searching for the *e*-mode (TM) eigenvalues for a 3-layer problem at 10 GHz. The thicknesses of the layers were $t_1 = 4.0$ mm, $t_2 = 5.0$ mm and $t_3 = 6.0$ mm and the transverse permittivities $\varepsilon_{t,1} = 4.3$, $\varepsilon_{t,2} = 10.0$ and $\varepsilon_{t,3} = 1.0$. The circles locate the positions of the eigenvalues

is zero for any layer since this might result in false zeroes. Figures 2.5 and 2.6 show plots of the transverse electric field at the upper PEC for an example three-layer multilayer eigenvalue problem at a frequency of 10 GHz. The first four axial TE and TM eigenmodes are shown in Figs. 2.7 and 2.8. The shaded region shows where the permittivity is highest. Note that E_ϕ is continuous across the dielectric interfaces for the TE case whereas H_ϕ is discontinuous. The derivatives of both are, however, both continuous across the dielectric interfaces.

To be able to use these eigenmodes as basis function for a series expansion of the fields, they are required to be orthogonal and normalised. To investigate this, the previous derivation of the wave equations for the axial fields E_z and H_z, is applied but taking the permittivity tensor to be a function of z. The zero divergence of the displacement, $\nabla \cdot \mathbf{D} = 0$ leads to the following expression for the divergence of the electric field:

$$\nabla \cdot \mathbf{E} = -\frac{1}{\varepsilon_t} \frac{\partial}{\partial z} (\varepsilon_z E_z) + \frac{\partial E_z}{\partial z},$$

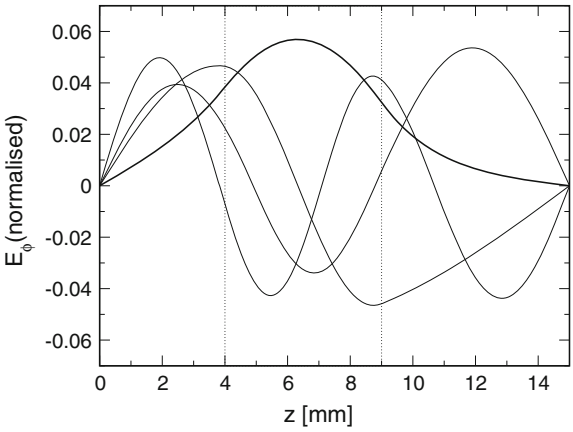

Fig. 2.7 First four axial TE eigenmodes for 3-layer problem at 10 GHz. The thicknesses of the layers were $t_1 = 4.0$ mm, $t_2 = 5.0$ mm and $t_3 = 6.0$ mm and the transverse permittivities $\varepsilon_{t,1} = 4.3$, $\varepsilon_{t,2} = 10.0$ and $\varepsilon_{t,3} = 1.0$

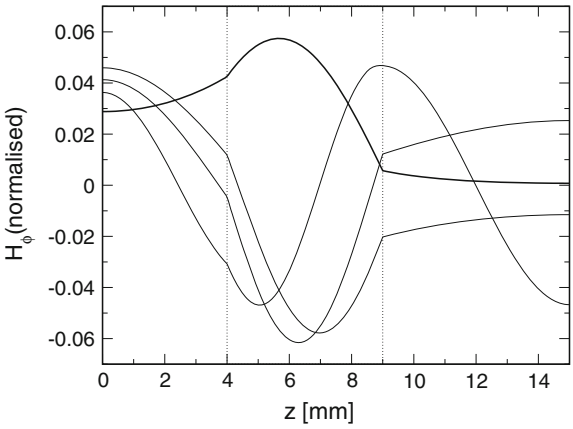

Fig. 2.8 First four axial TM eigenmodes for 3-layer problem at 10 GHz. The thicknesses of the layers were $t_1 = 4.0$ mm, $t_2 = 5.0$ mm and $t_3 = 6.0$ mm and the transverse permittivities $\varepsilon_{t,1} = 4.3$, $\varepsilon_{t,2} = 10.0$ and $\varepsilon_{t,3} = 1.0$

and so the partial differential equation for E_z is modified slightly:

$$\nabla^2 E_z + \frac{\partial}{\partial z}\left[\frac{1}{\varepsilon_t}\frac{\partial}{\partial z}(\varepsilon_z E_z)\right] - \frac{\partial^2 E_z}{\partial z^2} + k_0^2 \tilde{\varepsilon}_r \mathbf{E} = 0.$$

Substituting $E_z = R(\rho)\Phi(\phi)Z(z)$, dividing throughout by E_z and equating the term in z to the same coefficient in Eq. (2.4.13), namely $-\beta^2 \varepsilon_t/\varepsilon_t$, produces a Sturm–Liouville [15] partial differential equation:

$$\frac{\partial}{\partial z}\left\{\frac{1}{\varepsilon_t}\frac{\partial}{\partial z}\left[\varepsilon_z Z(z)\right]\right\} + \left(k_0^2 - \frac{\lambda_e}{\varepsilon_z}\right)\left[\varepsilon_z Z(z)\right] = 0.$$

The weighted inner product of two axial TM eigenmodes spanning the height h of a resonator is then:

$$\int_0^h \varepsilon_z Z_p^e(z) Z_q^e(z) dz = \delta_{pq}$$

where δ_{pq} is the Kronecker delta. The inner product for TE eigenmodes can be found similarly, yet is not weighted:

$$\int_0^h Z_p^h(z) Z_q^h(z) dz = \delta_{pq}.$$

The orthonormality of the axial eigenmodes whilst not entirely crucial for a field expansion to be possible, nevertheless make the matching of field at the radial interfaces easier, since the field series can be *tested* by appropriate eigenmodes resulting in diagonal matrices which are easier to invert.

2.6 The Radial Mode Matching Method

Once a prescribed number of eigenvalues λ_p^{ej} and λ_p^{hj} and their associated eigenmodes have been found for the multilayer parallel waveguide for each radial region j, it is necessary to execute the next step which is matching the transverse fields at the interfaces between radial regions. The equations for the transverse fields E_ϕ, H_ϕ, E_z and H_z, (omitting ϕ dependence) (Eq. 2.4.28) are:

$$\begin{aligned}
E_\phi(\rho, z) &= \frac{m\varepsilon_z}{\rho\varepsilon_t} \sum_p R_p^e(\rho) Z_p^{e\prime}(z) + i\omega\mu \sum_p R_p^{h\prime}(\rho) Z_p^h(z) \\
E_z(\rho, z) &= \sum_p \lambda_p^e R_p^e(\rho) Z_p^e(z) \\
H_\phi(\rho, z) &= -i\omega\varepsilon_0\varepsilon_z \sum_p R_p^{e\prime}(\rho) Z_p^e(z) - \frac{m}{\rho} \sum_p R_p^h(\rho) Z_p^{h\prime}(z) \\
H_z(\rho, z) &= \sum_p \lambda_p^h R_p^h(\rho) Z_p^h(z).
\end{aligned} \tag{2.6.1}$$

Recalling that the radial functions are given by

$$R_p^{e,h}(\rho) = A_p^{e,h} P_p^{e,h}(\rho) + B_p^{e,h} Q_p^{e,h}(\rho), \tag{2.6.2}$$

and matching the tangential fields on the boundaries between regions $j+1$ and j at radius ρ:

$$\begin{aligned}
E_\phi^{j+1}(\rho) &= E_\phi^j(\rho) \\
E_z^{j+1}(\rho) &= E_z^j(\rho) \\
H_\phi^{j+1}(\rho) &= H_\phi^j(\rho) \\
H_z^{j+1}(\rho) &= H_z^j(\rho),
\end{aligned}$$

results in the following set of four equations (where the ρ and z dependence of the radial and axial eigenfunctions is assumed):

$$\begin{aligned}
&\frac{m\varepsilon_z}{\rho\varepsilon_t}\sum_p P^e_{p,j+1}Z^{e\prime}_{p,j+1}A^e_{p,j+1}+\frac{m\varepsilon_z}{\rho\varepsilon_t}\sum_p Q^e_{p,j+1}Z^{e\prime}_{p,j+1}B^e_{p,j+1}\\
&\qquad+i\omega\mu\sum_p P^{h\prime}_{p,j+1}Z^h_{p,j+1}A^h_{p,j+1}+i\omega\mu\sum_p Q^{h\prime}_{p,j+1}Z^h_{p,j+1}B^h_{p,j+1}=\\
&\frac{m\varepsilon_z}{\rho\varepsilon_t}\sum_p P^e_{p,j}Z^{e\prime}_{p,j}A^e_{p,j}+\frac{m\varepsilon_z}{\rho\varepsilon_t}\sum_p Q^e_{p,j}Z^{e\prime}_{p,j}B^e_{p,j}+i\omega\mu\sum_p P^{h\prime}_{p,j}Z^h_{p,j}A^h_{p,j}+i\omega\mu\sum_p Q^{h\prime}_{p,j}Z^h_{p,j}B^h_{p,j}\\
&\qquad\sum_p \lambda^e_{p,j+1}P^e_{p,j+1}Z^e_{p,j+1}A^e_{p,j+1}+\sum_p \lambda^e_{p,j+1}Q^e_{p,j+1}Z^e_{p,j+1}B^e_{p,j+1}=\\
&\qquad\qquad\sum_p \lambda^e_{p,j}P^e_{p,j}Z^e_{p,j}A^e_{p,j}+\sum_p \lambda^e_{p,j}Q^e_{p,j}Z^e_{p,j}B^e_{p,j}\\
&\qquad i\omega\varepsilon_0\varepsilon_z\sum_p P^{e\prime}_{p,j+1}Z^e_{p,j+1}A^e_{p,j+1}+i\omega\varepsilon_0\varepsilon_z\sum_p Q^{e\prime}_{p,j+1}Z^e_{p,j+1}B^e_{p,j+1}\\
&\quad+\frac{m}{\rho}\sum_p P^h_{p,j+1}Z^{h\prime}_{p,j+1}A^h_{p,j+1}+\frac{m}{\rho}\sum_p Q^h_{p,j+1}Z^{h\prime}_{p,j+1}B^h_{p,j+1}=\\
&\qquad i\omega\varepsilon_0\varepsilon_z\sum_p P^{e\prime}_{p,j}Z^e_{p,j}A^e_{p,j}+i\omega\varepsilon_0\varepsilon_z\sum_p Q^{e\prime}_{p,j}Z^e_{p,j}B^e_{p,j}\\
&\qquad\quad+\frac{m}{\rho}\sum_p P^h_{p,j}Z^{h\prime}_{p,j}A^h_{p,j}+\frac{m}{\rho}\sum_p Q^h_{p,j}Z^{h\prime}_{p,j}B^h_{p,j}\\
&\quad\sum_p \lambda^h_{p,j+1}P^h_{p,j+1}Z^h_{p,j+1}A^h_{p,j+1}+\sum_p \lambda^h_{p,j+1}Q^h_{p,j+1}Z^h_{p,j+1}B^h_{p,j+1}=\\
&\qquad\qquad\sum_p \lambda^h_{p,j}P^h_{p,j}Z^h_{p,j}A^h_{p,j}+\sum_p \lambda^h_{p,j}Q^h_{p,j}Z^h_{p,j}B^h_{p,j}\,.
\end{aligned}$$

Multiplying each equation with appropriate axial eigenmodes (labelled q) as testing functions, integrating from $z=0$ to $z=h$ and rearranging produces the following block matrix equation relating the coefficients in region $j+1$ with those in region j,

$$\begin{bmatrix} A^e_{j+1}\\ B^e_{j+1}\\ A^h_{j+1}\\ B^h_{j+1}\end{bmatrix}=\underbrace{\left[\begin{array}{cc|cc} C & D & 0 & 0\\ G & H & I & J\\ \hline O & P & Q & R\\ 0 & 0 & W & X\end{array}\right]^{-1}\left[\begin{array}{cc|cc} E & F & 0 & 0\\ K & L & M & N\\ \hline S & T & U & V\\ 0 & 0 & Y & Z\end{array}\right]}_{\mathcal{R}_{j,j+1}(\rho)}\begin{bmatrix} A^e_j\\ B^e_j\\ A^h_j\\ B^h_j\end{bmatrix}. \tag{2.6.3}$$

Analogous to the axial eigenproblem, this introduces the radial transfer matrix $\mathcal{R}_{j,j+1}(\rho)$ which relates the coefficients A^e_j, B^e_j, A^h_j and B^h_j in region j to those in region $j+1$. The matrices represented by capital letters (with rows p and columns q) are

$$
\begin{aligned}
C &= \lambda^e_{p,j+1} P^e_{p,j+1} \delta_{pq} \\
D &= \lambda^e_{p,j+1} Q^e_{p,j+1} \delta_{pq} \\
E &= \lambda^e_{p,j} P^e_{p,j} \left\langle \varepsilon_z Z^e_{q,j+1}, Z^e_{p,j} \right\rangle \\
F &= \lambda^e_{p,j} Q^e_{p,j} \left\langle \varepsilon_z Z^e_{q,j+1}, Z^e_{p,j} \right\rangle \\
G &= i\omega\varepsilon_0 P^{e\prime}_{p,j+1} \delta_{pq} \\
H &= i\omega\varepsilon_0 Q^{e\prime}_{p,j+1} \delta_{pq} \\
I &= \frac{m}{\rho} P^h_{p,j+1} \left\langle Z^e_{q,j+1}, Z^{h\prime}_{p,j+1} \right\rangle \\
J &= \frac{m}{\rho} Q^h_{p,j+1} \left\langle Z^e_{q,j+1}, Z^{h\prime}_{p,j+1} \right\rangle \\
K &= i\omega\varepsilon_0 P^{e\prime}_{p,j} \left\langle Z^e_{q,j+1}, \varepsilon_z Z^e_{p,j} \right\rangle \\
L &= i\omega\varepsilon_0 Q^{e\prime}_{p,j} \left\langle Z^e_{q,j+1}, \varepsilon_z Z^e_{p,j} \right\rangle \\
M &= \frac{m}{\rho} P^h_{p,j} \left\langle Z^e_{q,j+1}, Z^{h\prime}_{p,j} \right\rangle \\
N &= \frac{m}{\rho} Q^h_{p,j} \left\langle Z^e_{q,j+1}, Z^{h\prime}_{p,j} \right\rangle \\
O &= \frac{m}{\rho} P^e_{p,j+1} \left\langle Z^h_{q,j+1}, \frac{\varepsilon_z}{\varepsilon_t} Z^{e\prime}_{p,j+1} \right\rangle \\
P &= \frac{m}{\rho} Q^e_{p,j+1} \left\langle Z^h_{q,j+1}, \frac{\varepsilon_z}{\varepsilon_t} Z^{e\prime}_{p,j+1} \right\rangle \\
Q &= i\omega\mu P^{h\prime}_{p,j+1} \delta_{pq} \\
R &= i\omega\mu Q^{h\prime}_{p,j+1} \delta_{pq} \\
S &= \frac{m}{\rho} P^e_{p,j} \left\langle Z^e_{q,j+1}, \frac{\varepsilon_z}{\varepsilon_t} Z^{e\prime}_{p,j} \right\rangle \\
T &= \frac{m}{\rho} Q^e_{p,j} \left\langle Z^e_{q,j+1}, \frac{\varepsilon_z}{\varepsilon_t} Z^{e\prime}_{p,j} \right\rangle \\
U &= i\omega\mu P^{h\prime}_{p,j} \left\langle Z^h_{q,j+1}, Z^h_{p,j} \right\rangle \\
V &= i\omega\mu Q^{h\prime}_{p,j} \left\langle Z^h_{q,j+1}, Z^h_{p,j} \right\rangle \\
W &= \lambda^h_{p,j+1} P^h_{p,j+1} \delta_{pq} \\
X &= \lambda^h_{p,j+1} Q^h_{p,j+1} \delta_{pq} \\
Y &= \lambda^h_{p,j} P^h_{p,j} \left\langle Z^h_{q,j+1}, Z^h_{p,j} \right\rangle \\
Z &= \lambda^h_{p,j} Q^h_{p,j} \left\langle Z^h_{q,j+1}, Z^h_{p,j} \right\rangle .
\end{aligned}
$$

where the terms inside angular brackets are coupling integrals between axial eigenfunctions in regions j and $j+1$, for example.

$$\int_0^h Z^h_{p,j}(z) Z^h_{q,j+1}(z) dz = \left\langle Z^h_{q,j+1}, Z^h_{p,j} \right\rangle .$$

If the azimuthal index is zero, $m = 0$, then the transverse TE_0 and TM_0 modes become axisymmetric and decoupled, having only electric or magnetic azimuthal field components. The matrices I, J, M, N, O, P, S and T containing terms in m then become zero and the radial transfer matrix $\mathcal{R}^{m=0}$ assumes a much simpler form:

$$\mathcal{R}^{m=0}_{j,j+1}(\rho) = \left[\begin{array}{cc|cc} C & D & 0 & 0 \\ G & H & 0 & 0 \\ \hline 0 & 0 & Q & R \\ 0 & 0 & W & X \end{array}\right]^{-1} \left[\begin{array}{cc|cc} E & F & 0 & 0 \\ K & L & 0 & 0 \\ \hline 0 & 0 & U & V \\ 0 & 0 & Y & Z \end{array}\right] . \tag{2.6.4}$$

The TE and TM mode coefficients A^h_j, B^h_j and A^e_j, B^e_j are become independent of one another and can be solved independently. The radial transfer matrix $\mathcal{R}^{m=0}_{j,j+1}(\rho)$ then splits into two smaller transfer matrices for the axisymmetric ($m = 0$) TE and TM modes:

$$\mathcal{R}^{e,m=0}_{j,j+1}(\rho) = \begin{bmatrix} C & D \\ G & H \end{bmatrix}^{-1} \begin{bmatrix} E & F \\ K & L \end{bmatrix}, \tag{2.6.5}$$

$$\mathcal{R}^{h,m=0}_{j,j+1}(\rho) = \begin{bmatrix} Q & R \\ W & X \end{bmatrix}^{-1} \begin{bmatrix} U & V \\ Y & Z \end{bmatrix}. \tag{2.6.6}$$

In a similar way to how the axial eigenproblem was solved earlier by cascading transfer matrices, the modal coefficients A^e_j, B^e_j, A^h_j and B^h_j of the outer region $j = N_\rho$, can be calculated by successive application of radial transfer matrices to the coefficients in the innermost region $j = 1$:

$$\begin{bmatrix} A^e_{N_\rho} \\ B^e_{N_\rho} \\ \hline A^h_{N_\rho} \\ B^h_{N_\rho} \end{bmatrix} = \prod_{j=1}^{N\rho-1} \mathcal{R}_{j,j+1}(\rho_{j+1}) \begin{bmatrix} A^e_1 \\ B^e_1 \\ \hline A^h_1 \\ B^h_1 \end{bmatrix} . \tag{2.6.7}$$

Due to singularities at the origin $\rho = 0$ being unphysical, the set of coefficients B^e_1 and B^h_1 of the Bessel functions of the second kind in the first radial partial region can be set to zero. Similarly to the axial eigenproblem, since the eigenmodes are orthonormal, the set of coefficients A^e_1 and A^h_1 can be initially be set to unity and then renormalised once a solution has been found. The modal coefficients A^e_j, B^e_j, A^h_j and B^h_j for the outer region are used to enforce the boundary condition on the outer radial cavity wall ($\rho = a$), namely that the tangential electric field is zero:

$$E_\phi(a) = \frac{m\varepsilon_z}{a\varepsilon_t}\sum_p A_p^e P_p^e(a) Z_p^{e\prime}(z) + i\omega\mu \sum_p A_p^h P_p^{h\prime}(a) Z_p^h(z)$$
$$+ \frac{m\varepsilon_z}{a\varepsilon_t}\sum_p B^e Q_p^e(a) Z_p^{e\prime}(z) + i\omega\mu \sum_p B_p^h Q_p^{h\prime}(a) Z_p^h(z) = 0$$
$$E_z(a) = \sum_p \lambda_p^e A_p^e P_p^e(a) Z_p^e(z) + \sum_p \lambda_p^e B_p^e Q_p^e(a) Z_p^e(z) = 0 \tag{2.6.8}$$

Similar to the previously applied method of using testing functions, multiplying Eq. (2.6.8) by the appropriate testing function $\varepsilon_z Z_q^e(z)$ and integrating from $z = 0$ to $z = h$, results in the following matrix equation for e-modes:

$$\left[\begin{array}{ccc|ccc} P_1^e(a) & & & Q_1^e(a) & & \\ & \ddots & & & \ddots & \\ & & P_N^e(a) & & & Q_N^e(a) \end{array}\right] \left[\begin{array}{c} A_1^e \\ \vdots \\ A_N^e \\ \hline B_1^e \\ \vdots \\ B_N^e \end{array}\right] = 0, \tag{2.6.9}$$

where for each row $i = 1 \ldots N$, corresponds to each eigenmode in the expansion

$$A_i^e P_i^e(a) + B_i^e Q_i^e(a) = 0.$$

Substituting these into Eq. (2.6.8) and simplifying yields

$$E_\phi(a) = \sum_p A_p^h P_p^{h\prime}(a) Z_p^h(z) + \sum_p B_p^h Q_p^{h\prime}(a) Z_p^h(z) = 0, \tag{2.6.10}$$

which upon multiplication by testing functions $Z_q^h(z)$ and integrating from $z = 0$ to $z = h$ yields another matrix equation for the coefficients of h-modes, A^h and B^h:

$$\left[\begin{array}{ccc|ccc} P_1^{h\prime}(a) & & & Q_1^{h\prime}(a) & & \\ & \ddots & & & \ddots & \\ & & P_N^{h\prime}(a) & & & Q_N^{h\prime}(a) \end{array}\right] \left[\begin{array}{c} A_1^h \\ \vdots \\ A_N^h \\ \hline B_1^h \\ \vdots \\ B_N^h \end{array}\right] = 0, \tag{2.6.11}$$

where for each row $i = 1 \ldots N$, corresponds to each eigenmode in the expansion,

$$A_i^h P_i^{h\prime}(a) + B_i^h Q_i^{h\prime}(a) = 0.$$

These two sets of boundary conditions together form a matrix which when multiplied by the transfer matrix $\mathcal{R}_{1,N_\rho}$, relates the coefficients in the last outer radial region N_ρ to those in the first inner radial region:

$$\mathcal{R}_{1,N_\rho} = \prod_{j=1}^{N\rho-1} \mathcal{R}_{j,j+1}(\rho_{j+1}). \tag{2.6.12}$$

Recalling that the B_1^e and B_1^h coefficients in the innermost region are zero, allows a characteristic matrix equation to be formed:

$$\mathcal{T} \begin{bmatrix} A_{N_\rho}^e \\ \hline A_{N_\rho}^h \end{bmatrix} = 0. \tag{2.6.13}$$

Non-trivial solutions occur when the determinants of the characteristic matrix $\mathcal{T}$ are zero. The zeros of the determinant, $\det(\mathcal{T})$ are found in the same way as the eigenvalues for the multilayer waveguide, bracketing followed by Ridders' method. Once a solution is found the radial coefficients A^e, B^e, A^h and B^h are normalised using the orthonormal properties of Bessel functions.

2.7 Calculating Resonator Losses

Once a solution for a particular mode has been found, the losses in the resonator can be calculated by volume integration of the electric and magnetic field energy densities for all regions and surface integration of the tangential magnetic field on conducting surfaces. The *unloaded* quality factor Q for a resonator is the ratio of total stored energy to the power dissipated per oscillatory cycle with period $T = \frac{2\pi}{\omega}$,

$$Q = \frac{\omega U}{W_d + W_c}$$

where U is the total stored energy in the resonator and W_d and W_c are dielectric and conductor losses. The reciprocal of this, which can be thought of as total loss, is the sum of the dielectric and conductor losses:

$$\frac{1}{Q} = \frac{1}{Q_d} + \frac{1}{Q_c} = \frac{W_d}{\omega U} + \frac{W_c}{\omega U}.$$

Representing the total loss as a sum of individual losses from either dielectric or conductive sources allows these parts to be calculated separately and is also informative when designing resonators, allowing the largest contributors to the total loss to be identified and reduced by attention to geometry or material properties.

Dielectric Losses

The total internal electromagnetic energy in an anisotropic dielectric can be found by integrating the modulus of the electric energy density over the volume of the resonator,

$$U = \sum_p U_p = \frac{1}{2} \sum_p \int_{V_p} \varepsilon_p' \mathbf{E} \cdot \mathbf{E}^* \, \mathrm{d}V,$$

where the summation is over all partial regions p comprising the resonator and U_p is the total internal electromagnetic energy in partial region p. The complex electric permittivity tensor for region p is $\boldsymbol{\varepsilon}_p = \boldsymbol{\varepsilon}_p' + i\boldsymbol{\varepsilon}_p''$ or

$$\boldsymbol{\varepsilon}_p = \varepsilon_0 \begin{bmatrix} \varepsilon_{t,p} & 0 & 0 \\ 0 & \varepsilon_{t,p} & 0 \\ 0 & 0 & \varepsilon_{z,p} \end{bmatrix}.$$

Similarly, the dielectric dissipation for a region p is found by integrating the imaginary part of the electric energy density over the volume V_p

$$W_{d,p} = \frac{\omega}{2} \sum_p \int_{V_p} \boldsymbol{\varepsilon}_p'' \mathbf{E} \cdot \mathbf{E}^* \, \mathrm{d}V.$$

The loss tangent, $\tan\delta = \varepsilon''/\varepsilon'$, the ratio of imaginary and real parts of the complex permittivity, allows the dielectric loss for region p to be written

$$\frac{1}{Q_{d,p}} = \frac{W_{d,p}}{\omega U} = \frac{\tan\delta_p U_p}{U} = P_{d,p} \tan\delta_p,$$

which introduces the electric filling factor for a region p, defined

$$P_{d,p} = \frac{U_p}{U}.$$

The electric filling factor $P_{d,p}$ is the fraction of the total electric energy in a resonator residing within region p. Due to the scale invariance of Maxwell's equations, the electric filling factors are also frequency invariant. To calculate the integrals, the expressions developed earlier for the electric fields can be used:

$$E_\rho = \sum_n R_n^{e\prime}(\rho) Z_n^{e\prime}(z) \Phi_m^e(\phi) + \frac{im\omega\mu}{\rho} \sum_n R_n^h(\rho) Z_n^h(z) \Phi_m^e(\phi)$$

$$E_\phi = \frac{m}{\rho} \sum_n R_n^e(\rho) Z_n^{e\prime}(z) \Phi_m^h(\phi) + i\omega\mu \sum_n R_n^{h\prime}(\rho) Z_n^h(z) \Phi_m^h(\phi)$$

$$E_z = \sum_n \lambda_{tm}^e R_n^e(\rho) Z_n^e(z) \Phi_m^e(\phi).$$

Numerical integration using the QUADPACK [19] quadrature algorithm was chosen for speed and efficiency, since the analytic integrals can become cumbersome, especially for higher order Bessel functions. For axisymmetric modes, the electric filling factors can also be calculated using the *incremental rule* [14], which is based on first order perturbation theory, taking the derivative of the resonant frequency f with respect to the permittivity of a region:

$$P_{d,p} = 2\left|\frac{\partial f}{\partial \varepsilon_p}\right|\frac{\varepsilon_p}{f}.$$

Conductor Losses

In resonator structures, conductor losses occur on metallic surfaces that have finite electrical conductivity. The losses for a particular metallic surface (labelled i) within a resonator are calculated by taking the ratio of the conductive dissipation $W_{c,i}$ per field cycle and the total stored energy U,

$$\frac{1}{Q_{c,i}} = \frac{W_{c,i}}{\omega U}.$$

The dissipation $W_{c,i}$ is found by integrating the tangential magnetic field over the conductive surface i

$$W_{c,i} = \frac{1}{2}R_{S_i}\int_{S_i}|\mathbf{H}_t|^2 \mathrm{d}S.$$

The surface resistance R_{S_i} is given by

$$R_{S_i} = (f\mu_0\pi\rho_i)^{\frac{1}{2}},$$

where f is the resonant frequency and ρ_i is the resistivity of the metallic surface. The total stored magnetic energy can be calculated similarly to the previously calculated electric energy. The magnetic energy at resonance

$$U = \frac{1}{2}\mu_0\int_V \mathbf{H}\cdot\mathbf{H}^*\mathrm{d}V,$$

is equal to the electric energy, hence the loss is then:

$$\frac{1}{Q_{c,i}} = \frac{W_{c,i}}{\omega U} = \frac{R_{S_i}\int_{S_i}|\mathbf{H}_t|^2\mathrm{d}S}{\omega\mu_0\int_V \mathbf{H}\cdot\mathbf{H}^*\mathrm{d}V} = \frac{R_{S_i}}{G},$$

which introduces the *geometric factor* G, for a surface i

$$G_i = \omega\mu_0\frac{\int_V \mathbf{H}\cdot\mathbf{H}^*\mathrm{d}V}{\int_{S_i}|\mathbf{H}_t|^2\mathrm{d}S}.$$

The geometric factor G can be computed in a similar way to the incremental rule by perturbing the dimensions of the cavity:

$$G_i = \frac{\omega^2 \mu_0}{2} \left| \frac{\Delta x}{\Delta \omega} \right|$$

where Δx is a change in one of the cavity dimensions, such as diameter or height.

2.8 Example Resonator

A computer programme was written in the C++ programming language, implementing the radial mode matching technique for uniaxially anisotropic dielectric resonators. An example resonator was modelled to test the radial mode matching method and confirm its accuracy and efficiency. The resonator consisted of a $\varepsilon_r = 10$ dielectric puck with diameter 8.0 mm and height 4.0 mm placed upon a single crystal quartz support of $\varepsilon_t = 4.43$, having diameter 4.0 mm and height 4.0 mm within a silver-plated conducting cavity with diameter 20.0 mm and height 12.0 mm. The number of eigenmodes in the field expansion was increased until a convergence of less than 0.001 MHz was achieved. Figure 2.9 shows the resonant frequency convergence as the number of eigenmodes is increased. Above fifteen modes, the convergence is less than 0.01 MHz and the $TE_{01\delta}$ mode resonance had a frequency of 12.0101 GHz.

Electric filling factors for the dielectric puck and support were calculated to be 0.8929 and 0.0075, meaning 89.3 % of the electric energy resided in the puck and 0.75 % in the support. Geometric factors for the conducting cavity side, bottom and top walls were 6337, 7584 and 8171 Ω respectively, yielding an overall geometric factor of 2427 Ω. Modal field patterns for this resonance are shown in Fig. 2.10.

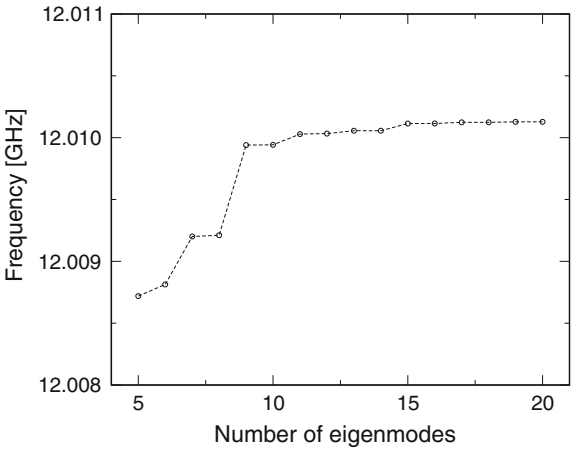

Fig. 2.9 Convergence of $TE_{01\delta}$ mode resonant frequency as a function of number of eigenmodes. Fifteen or more eigenmodes provides convergence of the resonant frequency of less than 0.01 MHz. The resonant frequency is 12.0101 GHz

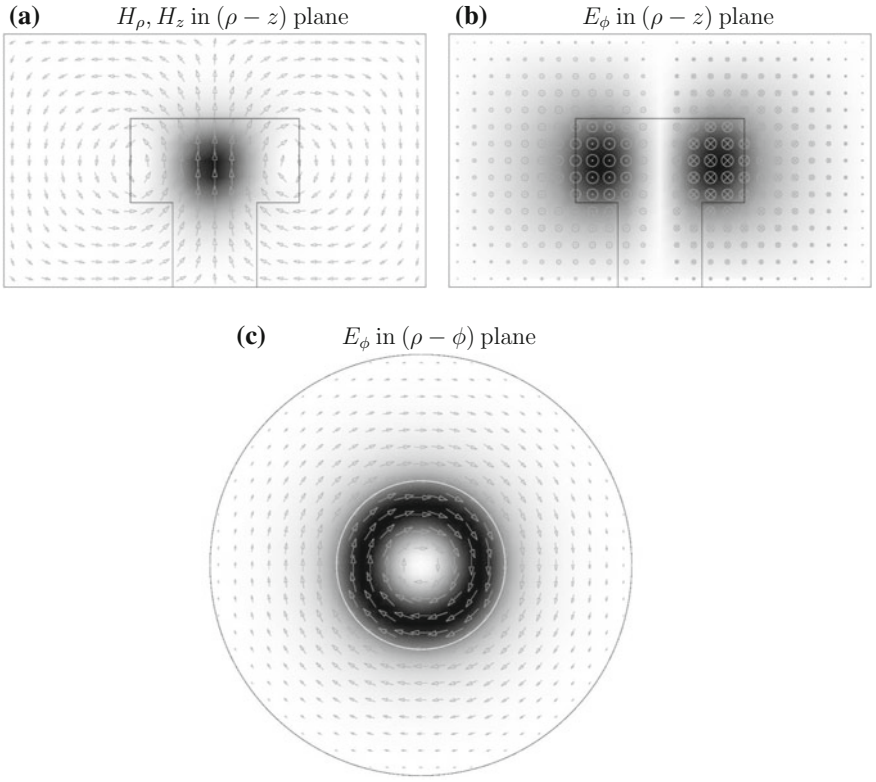

Fig. 2.10 Vector field and magnitude plots of magnetic and electric fields for a $TE_{01\delta}$ mode resonator consisting of a $\varepsilon_r = 10$ dielectric resonator of diameter 8.0 mm and height 4.0 mm placed upon a single crystal quartz support ($\varepsilon_t = 4.43$, diameter 4.0 mm and height 4.0 mm). The conducting cavity has diameter 20.0 mm and height 12.0 mm. Fifteen eigenmodes were used in the expansion of the fields resulting in a solution at 12.0101 GHz with less than 0.01 MHz convergence

2.9 Summary and Conclusions

The various types of resonator for measuring the dielectric properties of microwave ceramics were reviewed. The shielded dielectric resonator was discussed in more detail and then modelled analytically using Maxwell's equations. The radial mode matching method was implemented successfully and then used to model an example dielectric resonator, which demonstrated the efficiency and accuracy of the method.

References

1. M.E. Tobar et al., Anisotropic complex permittivity measurements of mono-crystalline rutile between 10 and 300 K. J. Appl. Phys. **83**, 1604 (1998)
2. N. Alford, M. Sebastian, A.K. Axelsson, Properties of microwave dielectric resonator materials. http://www3.imperial.ac.uk/thinfilms/dielectricproperties
3. B.W. Hakki, P.D. Coleman, A dielectric resonator method of measuring inductive capacities in the millimeter range. IEEE Trans. Microw. Theory Tech. **8**, 402 (1960)
4. W.E. Courtney, Analysis and evaluation of a method of measuring the complex permittivity and permeability of microwave insulators. IEEE Trans. Microw. Theory Tech. **18**, 476 (1970)
5. Y. Kobayashi, S. Tanaka, Resonant modes of a dielectric rod resonator short-circuited at both ends by parallel conducting plates. IEEE Trans. Microw. Theory Tech. **28**, 1077 (1980)
6. Y. Kobayashi, M. Katoh, Microwave measurement of dielectric properties of low-loss materials by the dielectric rod resonator method. IEEE Trans. Microw. Theory Tech. **33**, 586 (1985)
7. J. DelaBalle, P. Guillon, Y. Garault, Local complex permittivity measurement of MIC substrates. Int. J. Electron. Commun. **35**, 80 (1981)
8. U.S. Hong, R.H. Jansen, Numerical analysis of shielded dielectric resonators including substrate, support disc and tuning post. Electron. Lett. **18**, 1000 (1982)
9. K.A. Zaki, C. Chen, New results in dielectric-loaded resonators. IEEE Trans. Microw. Theory Tech. **34**, 815 (1986)
10. J. Krupka, Resonant modes in shielded cylindrical ferrite and single crystal dielectric resonators. IEEE Trans. Microw. Theory Tech. **37**, 691 (1989)
11. M.E. Tobar, A.G. Mann, Resonant frequencies of higher order modes in cylindrical anisotropic dielectric resonators. IEEE Trans. Microw. Theory Tech. **39**, 2077 (1991)
12. Y. Kobayashi, T. Senju, Resonant modes in shielded uniaxial-anisotropic dielectric rod resonators. IEEE Trans. Microw. Theory Tech. **41**, 2198 (1993)
13. J. Krupka et al., Complex permittivity of some ultralow loss dielectric crystals at cryogenic temperatures. Meas. Sci. Technol. **10**, 387 (1999)
14. D. Kajfez, P. Guillon, *Dielectric Resonators*, 1st edn. (Artech House, Inc., Dedham, 1964)
15. M. Abramovitz, I.A. Stegun, *Handbook of Mathematical Functions*, 9th edn. (Dover, New York, 1972)
16. S.D. Conte, C. DeBoor, *Elementary Numerical Analysis: An Algorithmic Approach*, 2nd edn. (McGraw-Hill, New York, 1965)
17. C.J.F. Ridders, Three-point iterations derived from exponential curve fitting. IEEE Trans. Circuits Syst. **26**, 669 (1979)
18. R.P. Brent, *Algorithms for Minimization without Derivatives* (Prentice-Hall, Englewood Cliffs, 1973) (Chap. 4)
19. R. Piessens et al., *QUADPACK, A Subroutine Package for Automatic Integration* (Springer, Berlin, 1983)

Chapter 3
Measurement of Dielectric Properties

This chapter reports on the apparatus used to measure the dielectric properties of microwave dielectrics as a function of temperature, consisting of a shielded dielectric resonator mounted upon the cold head of a cryogenic closed-cycle refrigerator. Resonant frequencies and quality factors of the resonator are measured at discrete temperature intervals using a vector network analyser and computer. The dielectric properties are then extracted using the radial mode matching technique discussed in the previous chapter. Low-temperature values for relative permittivity are compared against theoretical predictions in the subsequent chapters. The loss tangent as a function of temperature provides insight into the prevalence of defects within a sample and also allows for confirmation of theory.

3.1 Dielectric Resonator Measurements

Single-crystal samples of MgO, Al_2O_3, TiO_2 and $LaAlO_3$ in cylindrical form, with approximate diameters $D_d \approx 10\,\text{mm}$ and heights $L_d \approx 5\,\text{mm}$, were obtained from ESCETE Single Crystal Technology BV (Netherlands) and Crystal Systems (USA).

The samples were placed in a silver-plated brass cavity with diameter $D_c = 24.00\,\text{mm}$ and height $L_c = 16.12\,\text{mm}$, to form a shielded dielectric resonator as shown in Fig. 3.1. Samples were supported by a small single-crystal quartz hollow cylindrical support (outer diameter $OD_s = 4.92\,\text{mm}$, inner diameter $ID_s = 1.40\,\text{mm}$, height $L_s = 4.26\,\text{mm}$) and held in place by a PTFE piston and stainless steel spring. Coupling of microwave energy into the dielectric resonator was achieved by small adjustable antennae loops introduced into the sides of the cavity. The orientation of the loops is normal to the cylindrical cavity axis to excite the H_z field component of the TE_{0nm} modes or rotated 90° to excite the TM_{0nm} modes. To extract the relative permittivity and loss tangent of the sample, the three fundamental measurements of a dielectric resonator are the resonant frequency $\omega = 2\pi f_0$, coupling coefficients β_1, β_2 and loaded quality factor Q_L. Measurements of these quantities were performed in

J. Breeze, *Temperature and Frequency Dependence of Complex Permittivity in Metal Oxide Dielectrics: Theory, Modelling and Measurement*, Springer Theses, DOI 10.1007/978-3-319-44547-2_3

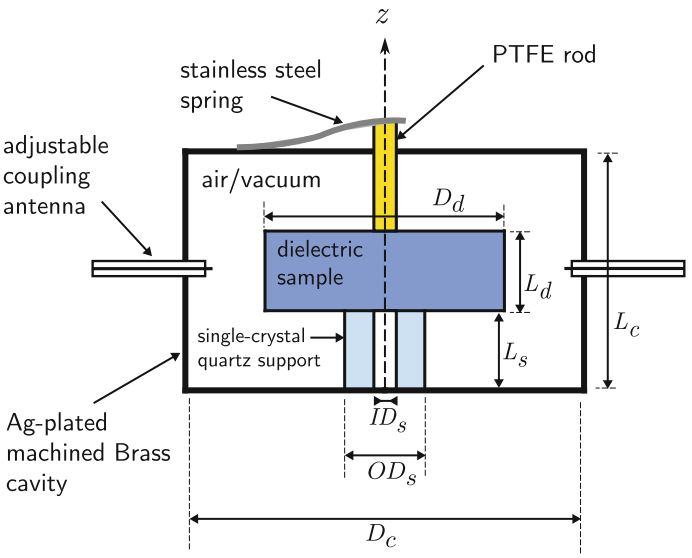

Fig. 3.1 Internal configuration of experimental shielded dielectric resonator. ID_s, OD_s and L_s are respectively the inner diameter, outer diameter and height of the quartz support cylinder. The diameter and height of the dielectric sample are D_d and L_d, and the diameter and height of the cavity are D_c and L_c. The diameter of the PTFE rod is the same as the internal diameter of the quartz spacer ID_s

the frequency domain using an Agilent HP8720C Vector Network Analyser (VNA) with 1-Hz resolution and a frequency range of 50 MHz–40 GHz. Resonances can be probed in either reflection or transmission mode where one or two ports are used to couple the dielectric resonator to transmission lines leading to the VNA. Transmission mode is preferable due to it being an inherently simpler measurement, allowing the coupling to the resonator to be very small. For a two-port device, the transmission and reflection of power is described by scattering or S-parameters.

The relationship between the reflected, transmitted and incident power waves shown in Fig. 3.2 and the S-parameter matrix is given by

$$\begin{pmatrix} b_1 \\ b_2 \end{pmatrix} = \begin{pmatrix} S_{11} & S_{12} \\ S_{21} & S_{22} \end{pmatrix} \begin{pmatrix} a_1 \\ a_2 \end{pmatrix}$$

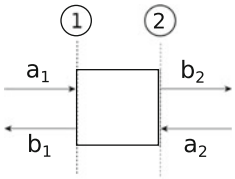

Fig. 3.2 Incident, transmitted and reflected power waves upon and from a two-port device

If the second port is terminated by a load equal to the system impedance Z_0, then the power incident on port two is zero, $a_2 = 0$. If there is power incident upon port one, $a_1 \neq 0$, then the forward scattering parameter S_{21} can be written as the ratio of the outgoing power to the incoming power

$$S_{21} = \frac{b_2}{a_1}.$$

The loaded quality factor Q_L is defined as the ratio of the resonant frequency ω_0 and the bandwidth $\Delta\omega$ at half of the peak power as shown in Fig. 3.3

$$Q_L = \frac{\omega_0}{\Delta\omega}.$$

The unloaded quality factor, Q_0 is then given by

$$Q_0 = (1 + \beta_1 + \beta_2)\, Q_L$$

where β_1 and β_2 are the coupling coefficients of the dielectric resonator to the input and output ports. The coupling coefficients can be calculated from the four S-parameters measured at the resonant frequency $\omega_0 = 2\pi f_0$

$$\beta_1 = \frac{1 - S_{11}}{S_{11} + S_{22}},$$
$$\beta_2 = \frac{1 - S_{22}}{S_{11} + S_{22}},$$
$$S_{21} = S_{12} = \frac{2\sqrt{\beta_1\beta_2}}{1 + \beta_1 + \beta_2}.$$

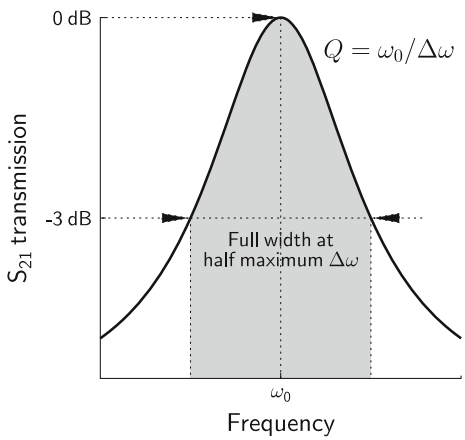

Fig. 3.3 Lorentzian line-shape of a resonance in transmission showing how the quality factor Q_L is defined

If the input and output couplings β_1 β_2 are both equal and weak, then the transmission response should be symmetric and the resonant frequency ω_0 occurs at the peak maximum and the coupling coefficient can be evaluated as

$$\beta = \beta_1 = \beta_2 = \frac{1}{2} \cdot \frac{S_{21}}{1 - S_{21}},$$

which if $S_{21} \ll 1$ then

$$\beta = \frac{1}{2} S_{21}.$$

The unloaded quality factor Q_0 can then be calculated from the measured Q-factor and the coupling coefficient

$$Q_0 = \frac{Q_L}{1 - |S_{21}|}.$$

The transmission at the resonant frequency is known as the *insertion loss*.

3.2 Calculating Dielectric Properties

The relative permittivity ε_r of a dielectric sample is calculated by taking the resonator dimensions, permittivity of support structure and measured resonant frequency as input to the radial mode matching method discussed in the previous chapter. The loss tangent $\tan \delta$ is derived from the unloaded quality factor Q_0, which is the reciprocal of the total loss within the dielectric resonator. The total loss is equal to the sum of losses within the dielectric sample, support and on the conductive surfaces [1]:

$$\frac{1}{Q_0} = P_{e,d} \tan \delta_d + P_{e,s} \tan \delta_s + \frac{R_S}{G},$$

where R_S is the surface resistance of the metallic cavity and G is its geometric factor. The parameters $P_{e,d}$ and $P_{e,s}$ are the electric energy filling factors of the dielectric sample and support structure, respectively, with $\tan \delta_d$ and $\tan \delta_s$ being their associated loss tangents. This relation can be rearranged to provide an expression for the loss tangent within the dielectric sample

$$\tan \delta_d = \frac{1}{P_{e,d}} \left(\frac{1}{Q_0} - P_{e,s} \tan \delta_s - \frac{R_s}{G} \right). \tag{3.2.1}$$

Upon inspection, it can be seen that to calculate $\tan \delta_d$ for a dielectric sample, it is necessary to have previously characterised the surface resistance R_S of the cavity and the loss tangent $\tan \delta_s$ (and relative permittivity) of the support material. These measurements, adjusted for frequency dependence are then combined with the geometric factor G and electric energy filling factors of the dielectric sample and support

using results from the radial mode matching method. To investigate the sensitivity of Eq. 3.2.1 to errors, it is necessary to calculate its partial derivatives with respect to the terms on the right-hand side

$$\begin{aligned}
\frac{\partial(\tan\delta_d)}{\partial P_{e,d}} &= -\frac{1}{P_{e,d}}\tan\delta_d \\
\frac{\partial(\tan\delta_d)}{\partial Q_0} &= -\frac{1}{P_{e,d}Q_0^2} \\
\frac{\partial(\tan\delta_d)}{\partial P_{e,s}} &= -\frac{\tan\delta_s}{P_{e,d}} \\
\frac{\partial(\tan\delta_d)}{\partial(\tan\delta_s)} &= -\frac{P_{e,s}}{P_{e,d}} \\
\frac{\partial(\tan\delta_d)}{\partial R_s} &= -\frac{1}{P_{e,d}G} \\
\frac{\partial(\tan\delta_d)}{\partial G} &= \frac{R_s}{P_{e,d}G^2},
\end{aligned}$$

then apply the chain rule to give an estimate of the error in $\tan\delta_d$

$$\Delta(\tan\delta_d) = -\frac{\Delta P_{e,d}}{P_{e,d}}\tan\delta_d - \frac{\Delta Q_0}{P_{e,d}Q_0^2} - \frac{\Delta P_{e,s}}{P_{e,d}}\tan\delta_s - \frac{P_{e,s}\Delta(\tan\delta_s)}{P_{e,d}} - \frac{\Delta R_s}{P_{e,d}G} + \frac{\Delta G R_s}{P_{e,d}G^2}.$$

Since the electric filling factor of the sample is of the order of unity, $P_{e,d} \approx 1$ and the electric energy filling factor of the support very low, $P_{e,s} \approx 0$, simplification leads to

$$\Delta(\tan\delta_d) \approx -\Delta P_{e,d}\tan\delta_d - \frac{\Delta Q_0}{Q_0^2} - \Delta P_{e,s}\tan\delta_s - \frac{\Delta R_s}{G} + \frac{\Delta G R_s}{G^2}.$$

Terms containing Q_0^2 and G^2 in the denominators can also be neglected since both Q_0 and G should be greater than 10^4 and 10^3 Ω respectively, leading to an estimate of the error

$$\Delta(\tan\delta_d) \approx -\Delta P_{e,d}\tan\delta_d - \Delta P_{e,s}\tan\delta_s - \frac{\Delta R_s}{G}.$$

Assuming relative measurement errors of 10^{-3} and $\tan\delta \approx 10^{-5}$ for both sample and support, a geometric factor G of a few thousand Ω and errors in the electric energy filling factors of the order of 10^{-3}, then an estimate of the error is

$$\Delta(\tan\delta_d) \approx -\Delta P_{e,d}10^{-5} - \Delta P_{e,s}10^{-5} - 10^{-8} \approx 10^{-8}$$

The absolute error in the $\tan \delta_d$ is of the order of 10^{-8} which yields an acceptable relative error of 10^{-3}, demonstrating that the $TE_{01\delta}$ mode is a suitable method for measuring the loss tangent.

3.3 Cryogenic Measurements

The ability to characterise the relative permittivity and loss tangent of microwave dielectrics as a function of temperature and particularly down to cryogenic temperatures is a valuable tool, not only for practical purposes such as designing devices but also to test theoretical predictions and study the effects of extrinsic loss mechanisms such as defects and grain boundaries [2]. The temperature dependence of the intrinsic losses in microwave dielectric single crystals has been the subject of much work by Gurevich and Tagantsev [3–10]. These predictions have been validated for high-

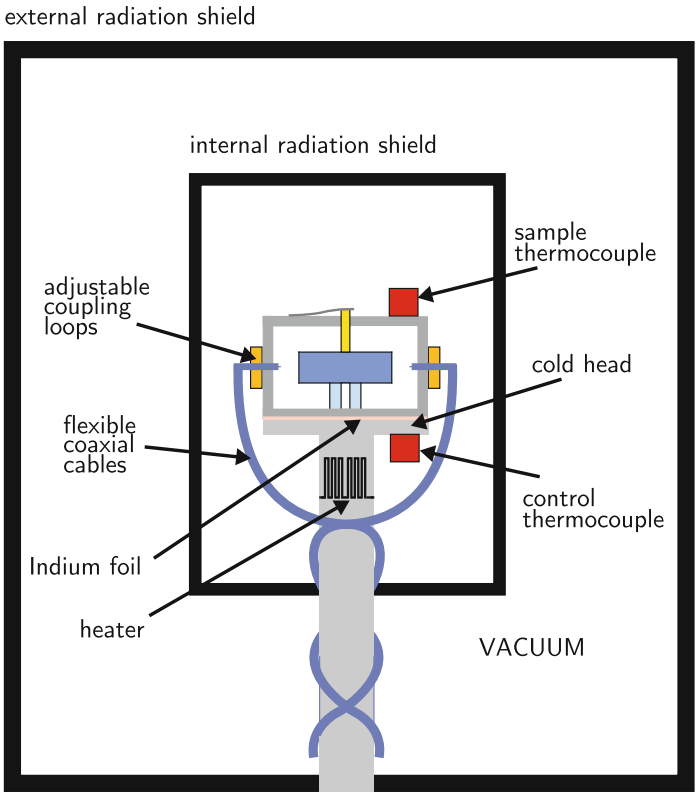

Fig. 3.4 Cryocooler apparatus: The cavity is mounted on the cold head of a Gifford–McMahon closed-cycle cooler. The base temperature of the system in 10 °K

quality single crystals of sapphire by Braginsky [11] and also in their polycrystalline analogues [12].

The apparatus for measuring the properties of dielectric samples as a function of temperature consists of a dielectric resonator mounted on the cold head of a Gifford–McMahon closed-cycle cooler as shown in Figs. 3.4 and 3.5. An indium foil is placed between the base of the resonator and the cold head to ensure good thermal contact. Thermocouples are placed on the cold head and also on the resonator and a thick-film heater is situated just beneath the cold head. Adjustable mechanisms were developed for the coupling loops so that the coupling level could be adjusted to a suitable level. Flexible microwave, thermocouple sensor and heater cables were wrapped around the cold head column and connected to feedthrough bulk heads in the base. The microwave cables terminated in SMA connectors to which a vector network analyzer (VNA) was connected.

The temperature sensor and heater cables were connected to a Lakeshore 330 Temperature Controller. An internal radiation shield was placed around the resonator assembly, followed by an external radiation shield with 'O'-ring gasket to ensure good vacuum. The entire assembly was evacuated using a turbomolecular pump system (Varian Mini-TASK AG81 with FRG-700 Full-Range Gauge). Once a satisfactory

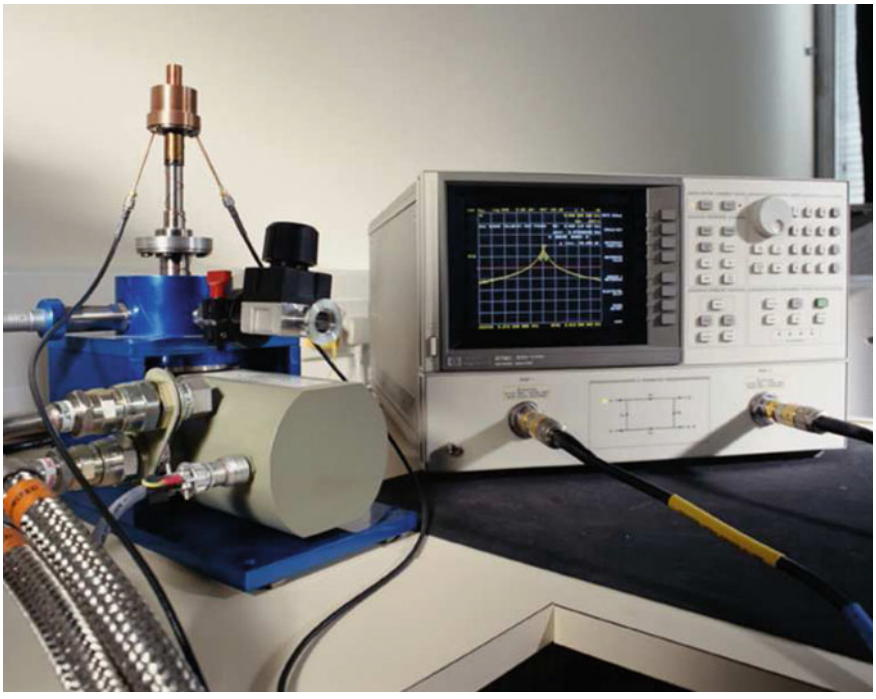

Fig. 3.5 Photograph of cryogenic dielectric resonator apparatus without radiation shields. The transmission frequency trace of a $TE_{01\delta}$ mode can be seen on the VNA monitor

vacuum was achieved ($\sim 10^{-5}$ mBar) and the resonator had outgassed sufficiently (if necessary the cavity can be baked out), the closed-cycle cooler helium compressors were switched on and cooling began by virtue of a Gifford–McMahon closed-cycle engine. As the temperature decreased, the centre frequency of the mode of interest shifted depending on the temperature coefficient of permittivity of the dielectric as well as the thermal expansion coefficients of the components of the dielectric resonator.

The temperature controller and VNA connected via a GPIB interface (General Purpose Interface Bus) to a workstation. A C^{++} computer program was developed to automate the process of tracking modes from room temperature down to 10 K. Once the system achieved a base temperature of 10 K and stabilised, the program instructed the temperature controller to take the system to the first temperature point to be measured, using its built-in PID (proportional-integrator-differentiator) algorithm and the thick-film heater. The program monitored the shift in the centre frequency of the resonance until it stabilised over time and then interrogated the VNA to acquire measurements of the centre frequency, loaded Q-factor and coupling level of the resonance. This process was repeated for small prescribed increments of temperature

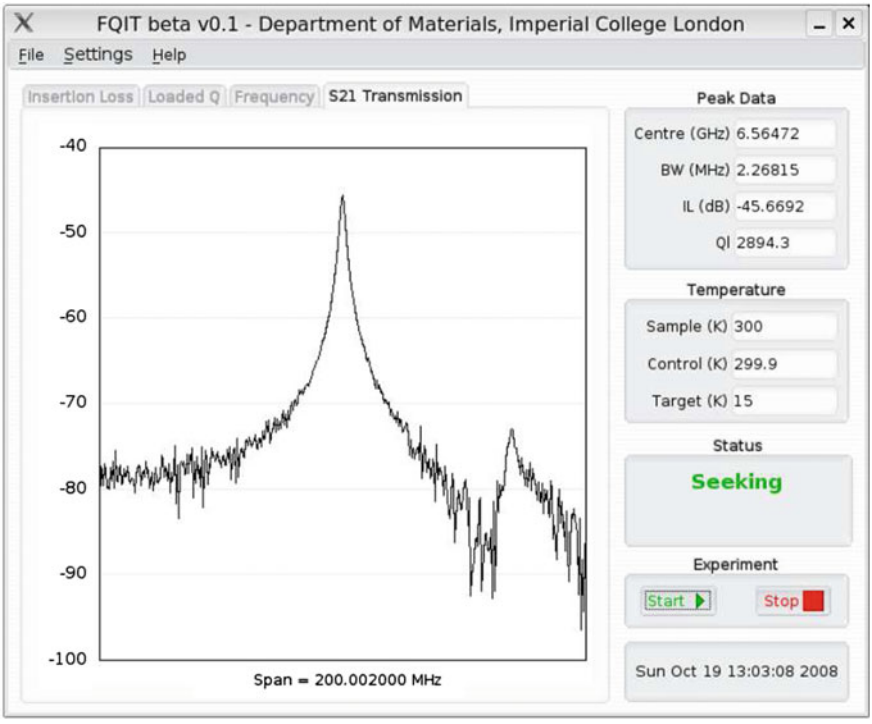

Fig. 3.6 Screenshot of software developed in-house to automatically track and measure the centre frequency and Q-factor of a mode

until the system was again at room temperature. The program repeated the process for decreasing temperature steps saving all data to computer disk. The file containing the centre frequencies, loaded Q-factors and coupling levels was processed by the radial mode matching program to produce the relative permittivity and loss tangent of the sample as a function of temperature. A screenshot of the software is shown in Fig. 3.6. To extract the properties of a dielectric sample from measurements of a dielectric resonator, it is necessary to characterise the temperature dependence of the thermal expansion coefficient and surface resistance of the Ag-plated brass cavity and also the relative permittivity and loss tangent of the single-crystal quartz support.

3.4 Characterisation of Ag-Plated Cavity

The temperature dependence of the coefficient of thermal expansion $\alpha(T)$ and surface resistance $R_s(T)$ of the Ag-plated brass cavity was measured using the TE_{011} mode (empty cavity) over the temperature range 10–300 K. The resonant frequency of this mode is given by

$$f = \frac{c}{2}\left[\left(\frac{2\chi_{01}}{\pi D}\right)^2 + \left(\frac{1}{L}\right)^2\right]^{\frac{1}{2}}, \tag{3.4.1}$$

where c_0 is the speed of light in vacuum, D is the cavity diameter, L is the cavity height and χ_{01} is the first zero of the derivative of the Bessel function of the first kind, J_0'. The cavity in the experimental apparatus had a nominal diameter D of 24.00 mm and a height L of 16.10 mm. The resonant frequency predicted by (3.4.1) was 17.854896 GHz. The TE_{011} mode in the evacuated cavity was measured at room temperature using an Agilent 8720D vector network analyser in transmission mode (S_{21}) with a very small coupling of –58.0 dB. The measured resonant frequency was 17.858433 GHz, which is less 4 MHz from the predicted value. As the temperature varies, the dimensions of the cavity will change according to the linear coefficient of thermal expansion $\alpha(T)$. Since the diameter to length ratio, D/L is invariant with respect to temperature changes since the thermal expansion coefficient of metal is isotropic, it is useful to rearrange (3.4.1) to obtain an expression for the diameter $D(T)$ in terms of the aspect ratio $\eta = D/L$ and the frequency $f(T)$,

$$D(T) = \frac{c_0}{2\pi f(T)}\left(4\chi_{01}^2 + \pi^2\eta^2\right)^{\frac{1}{2}}. \tag{3.4.2}$$

The resonant frequency of the TE_{011} mode was measured over the 10–300 K temperature range, from which the diameter of cavity was calculated from (3.4.2) as shown in Fig. 3.7.

The linear coefficient of thermal expansion at a particular temperature, $\alpha(T)$, was then calculated from the diameter using

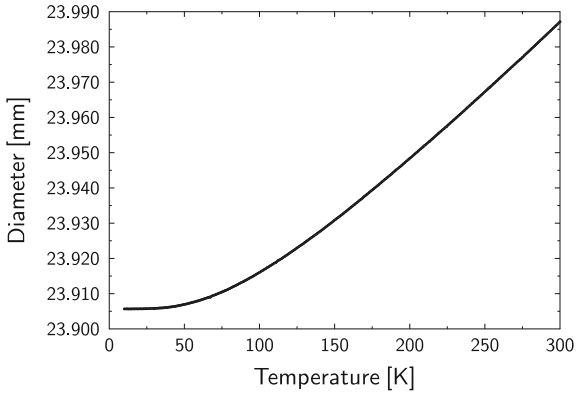

Fig. 3.7 Diameter of Ag-plated brass cavity as a function of temperature over range 10–300 K. The diameter was calculated from the measured resonant frequency of the TE_{011} mode using Eq. 3.4.2

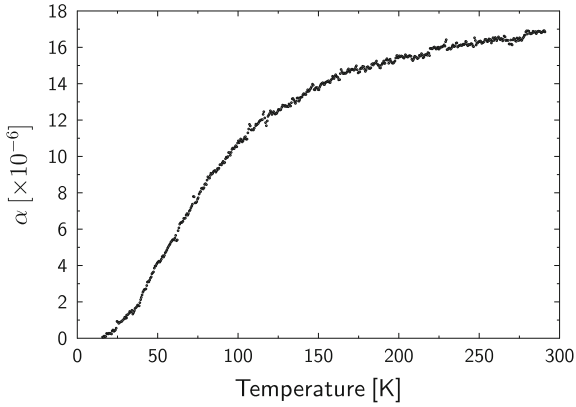

Fig. 3.8 Coefficient of thermal expansion $\alpha(T)$ of 24.00 mm diameter Ag-plated brass cavity

$$\alpha(T) = \frac{1}{D(T)} \frac{\partial D(T)}{\partial T}.$$

Figure 3.8 shows how the linear coefficient of thermal expansion for the cavity varies as a function of temperature in the range 10–300 K. Finally, the surface resistance R_S of the cavity can be characterised by measuring the unloaded Q-factor of the TE_{011} mode as a function of temperature and using the expression

$$Q = \frac{Z_0}{2R_S} \frac{\left(\frac{4\chi_{01}^2}{D^2} + \frac{\pi^2}{L^2}\right)^{3/2}}{\frac{8\chi_{01}^2}{D^3} + \frac{2\pi^2}{L^3}}$$

where Z_0 is the wave impedance of free-space. The surface resistance R_S is related to the conductivity σ by

$$R_S = \left(\frac{\mu_0 \pi f}{\sigma}\right)^{1/2}$$

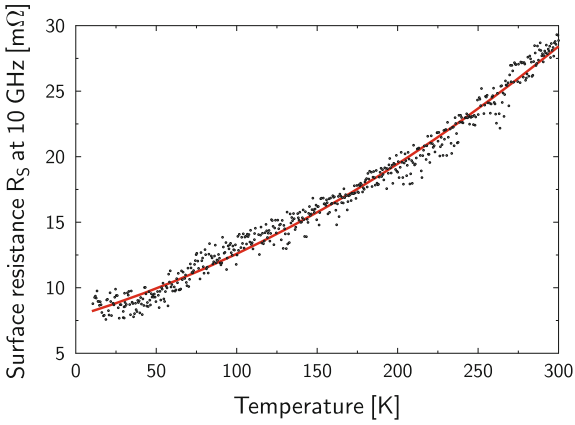

Fig. 3.9 Surface resistance R_S (normalised to 10 GHz) of Ag-plated cavity as a function of temperature. The *thick line* shows a quadratic fit $R_S(T) = 7.8300 + 3.7079 \times 10^{-2}T + 1.0517 \times 10^{-4}T^2(\text{m}\Omega)$ to the measured data

where μ_0 is the permeability of free-space and f is the frequency. Since R_S scales as the square root of the frequency, the change in resonant frequency due to thermal coefficients should be taken into account. For this reason, the surface resistivity is normalised to 10 GHz and shown in Fig. 3.9 where the line shows a quadratic fit for $R_S(T)$.

3.5 Characterisation of Single-Crystal Quartz Support

It now remains to characterise the quartz single crystal used to support the dielectric sample in the cavity. Quartz is a uniaxially anisotropic dielectric with low permittivity and low loss tangent, making it ideal for use as a support material. At room temperature it has anisotropic coefficients of thermal expansion: $7.5 \times 10^{-6}\ K^{-1}$ parallel and $13.7 \times 10^{-6}\ K^{-1}$ perpendicular to the c-axis. The quartz support in this case was a cylinder of c-axis aligned single-crystal quartz with outer diameter 4.92 mm, inner diameter 1.40 mm and height 4.26 mm. The complex permittivity data of quartz were taken from measurements by Krupka [1] at 16.9 and 17.2 GHz. At room temperature, the permittivities parallel and perpendicular to the c-axis, $\varepsilon_\parallel$ and $\varepsilon_\perp$, were 4.644 and 4.443, respectively. The temperature dependencies of $\varepsilon_\parallel$ and $\varepsilon_\perp$ and the loss tangents are shown in Fig. 3.10. The loss tangent perpendicular to the c-axis is fairly constant above 1.0×10^{-5} except in the range 100–150 K where quasi-Debye defect dipole losses are expected to be active [13]. In a TE_{0nm} mode dielectric resonator the electric field only has components in the azimuthal plane, hence the perpendicular component of loss tangent $\tan\delta_\perp$ is the relevant one. The frequency dependence of $\tan\delta_\perp$ has been evaluated up to 35 GHz [14]. Below 16 GHz the loss tangent follows a linear relationship with frequency ($\tan\delta_\perp \sim 2.0 \times 10^{-5}$ at 10 GHz), however above 20 GHz the losses have been observed to saturate at around $\tan\delta_\perp \approx 3.5 \times 10^{-5}$.

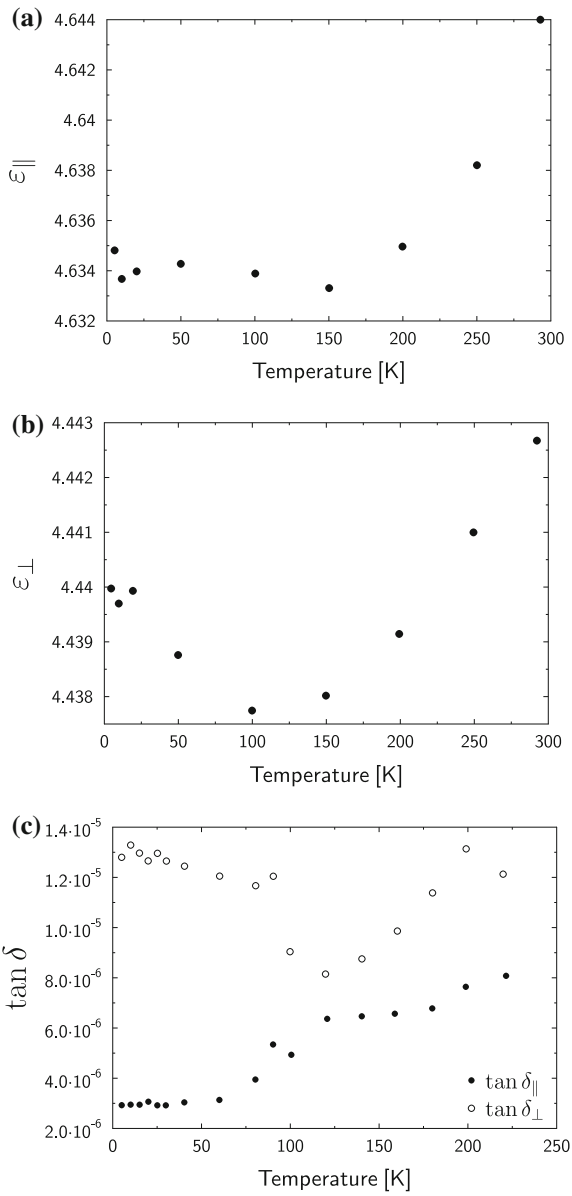

Fig. 3.10 Properties of single-crystal SiO_2 as a function of temperature [1] at 17 GHz. Relative permittivity parallel to the *c*-axis (**a**), perpendicular to the *c*-axis (**b**) and the loss tangent components (**c**)

3.6 Magnesium Oxide — MgO

High-quality magnesium oxide single crystals are popular choices of substrate on which to grow high-temperature superconductor (HTS) and ferroelectric (FE) thin films due to its cubic structure, low microwave loss, isotropic permittivity and low-

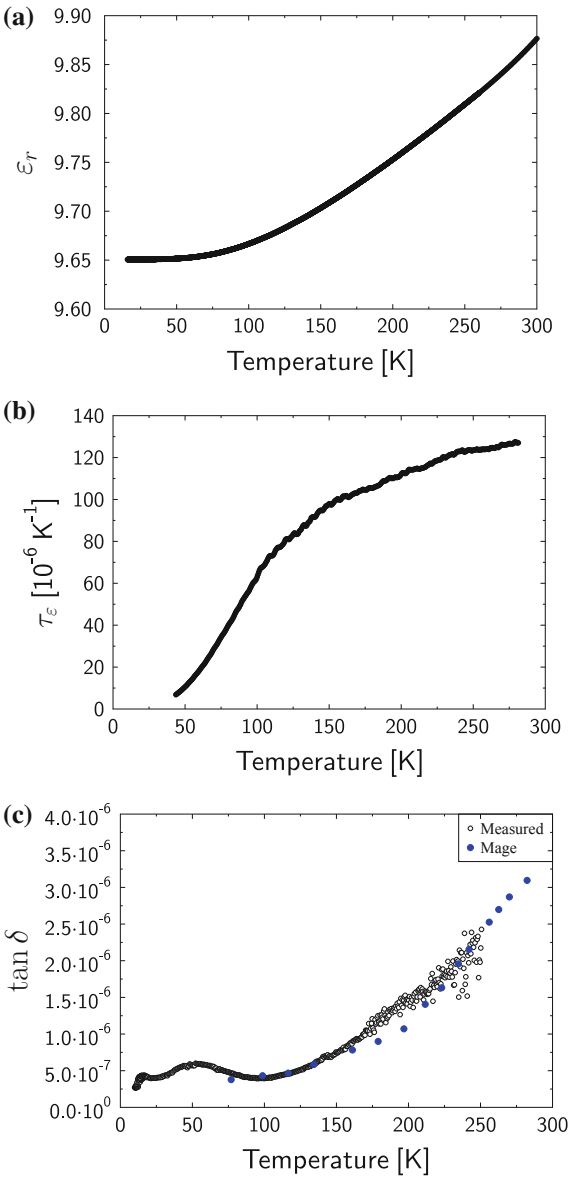

Fig. 3.11 Properties of single-crystal MgO as a function of temperature. **a** Relative permittivity, **b** temperature coefficient of permittivity and **c** loss tangent. Measurement frequency of 10.3 GHz at room temperature

lattice parameter mismatch ($a \approx 4.21$ Å) with a variety of perovskites. Due to the interest in MgO as a substrate, the relative permittivity and loss tangent at microwave frequencies down to cryogenic temperatures have been reported by several authors [15–17].

A single-crystal MgO sample of diameter 10.0 mm and height 4.0 mm was placed within the cavity measurement system. The $TE_{01\delta}$ fundamental mode at room temperature was measured and found to have a resonant frequency of 10.3125 GHz and unloaded Q of 61,515. A relative permittivity ε_r of 9.877 was calculated by solving the characteristic equation provided by the radial mode matching method using 13 modes to ensure a well-converged result. Integration of the electric fields within the dielectric regions yielded dielectric filling factors of $P_d = 0.8702$ and $P_s = 0.0089$ for the sample and support, respectively. The amount of electric energy stored in the support is less than 1 % of that in the dielectric sample. Integration of the magnetic fields over the cavity surface yielded a geometric factor of $G = 2331\ \Omega$. A surface resistance R_S of 30.94 mΩ was calculated from the fit in Fig. 3.9 and appropriately scaled ($f^{1/2}$) to 10.3125 GHz, resulting in a calculated conductor Q-factor of $Q_c = 75,322$. Taking a loss tangent of 2.0×10^{-5} for the quartz spacer and using the equation

$$\tan\delta = \frac{1}{P_d}\left(\frac{1}{Q_0} - P_s \tan\delta_s - \frac{R_s}{G}\right) \tag{3.6.1}$$

resulted in a loss tangent for MgO of $\tan\delta = 3.219 \times 10^{-6}$ at room temperature and 10.3 GHz. The MgO dielectric resonator was then characterised over temperature and processed using the mode matching technique and values for the surface resistance R_S and loss tangent of quartz spacer discussed earlier. The results presented in Fig. 3.11a show that the relative permittivity ε_r decreased monotonically as the temperature was reduced. This is demonstrated by the positive temperature coefficient of permittivity τ_{ε_r} as shown in Fig. 3.11b.

3.7 Lanthanum Aluminate — $LaAlO_3$

Lanthanum Aluminate is another popular choice of substrate for the growth of functional oxide thin films due its high permittivity ($\varepsilon_r \approx 24$), low-loss tangent and suitable crystallographic parameters. Above a temperature of 500 °C, it has the ideal cubic (O_h^1) perovskite structure. Below 500 °C, it has a slightly rhombohedral structure ($D_{3d}^6 \equiv R\bar{3}c$) with a small distortion ($\alpha = 90.1°$). Since the distortion is so small, the low-temperature phase is usually regarded as pseudocubic and isotropic. The measured sample had diameter 10.0 mm and height 4.95 mm. At room temperature the sample was placed in the measurement cavity and produced a $TE_{01\delta}$ mode resonating at a frequency of 6.356 GHz with an unloaded Q-factor of 52,132. The relative permittivity was determined (using mode matching) to be $\varepsilon_r = 24.07$ and the loss tangent $\tan\delta = 1.39 \times 10^{-5}$. The temperature measurements shown in Fig. 3.12

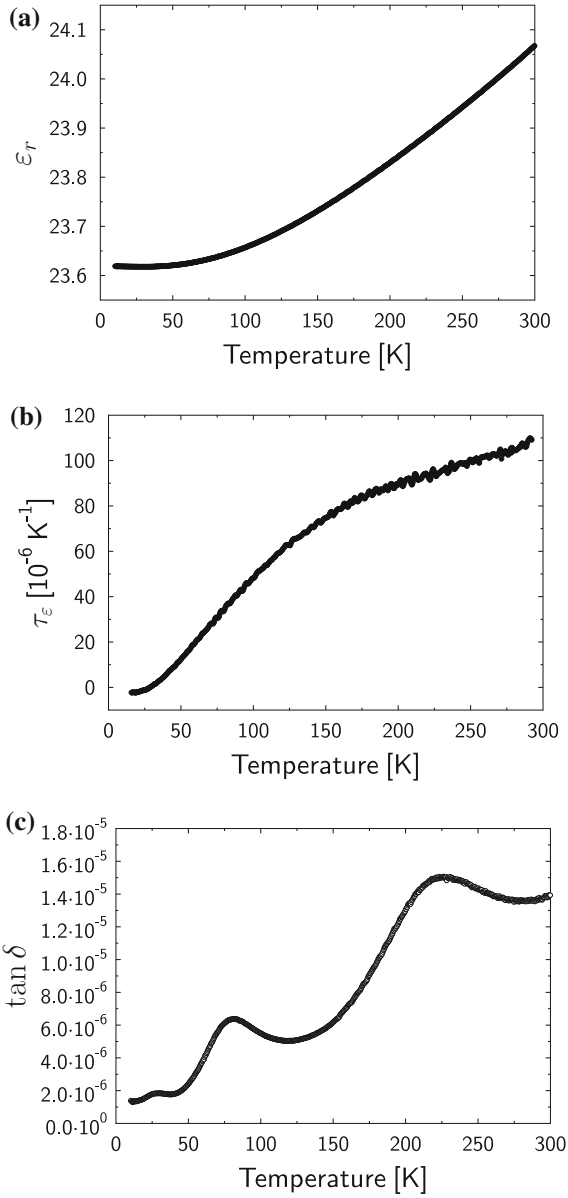

Fig. 3.12 Properties of single-crystal $LaAlO_3$ as a function of temperature. **a** Relative permittivity, **b** temperature coefficient of permittivity and **c** loss tangent. Measurement frequency of 6.4 GHz

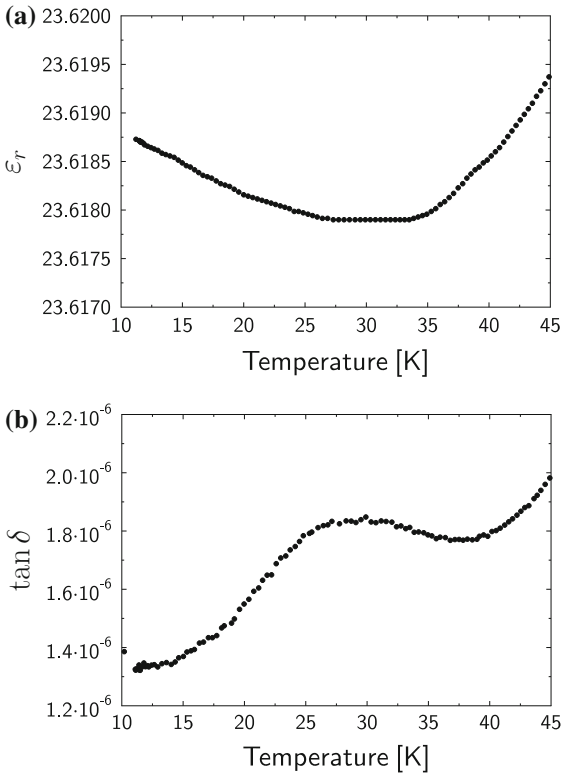

Fig. 3.13 Relative permittivity (**a**) and loss tangent (**b**) of single-crystal $LaAlO_3$ at low temperature. Near 30 K there is a minimum in the permittivity which coincides with an extremum in loss tangent attributable to quasi-Debye dipole relaxation of oxygen defects. The resonant frequency of the $TE_{01\delta}$ mode was 6.2 GHz

show some interesting features. The relative permittivity shows similar behaviour to MgO, monotonically decreasing as the temperature is reduced, with a temperature coefficient of permittivity τ_{ε_r} of similar magnitude. The loss tangent shows a series of prominent humps at temperatures of 30, 80 and 220 K. This has been explained in the literature as a result of quasi-Debye dipole relaxation caused by ions hopping between defect sites under the influence of the microwave field [13, 18]. The defect sites exist due to the twinning behaviour that has been observed for this oxide. Also at around $T \sim 30$ K, the relative permittivity exhibits a minimum where the τ_{ε_r} is zero as shown in Fig. 3.13. This coincides with a small peak in the loss tangent and can be attributed to a very small contribution to the relative permittivity from the dielectric susceptibility of the quasi-Debye dipole relaxation.

3.8 Titanium Dioxide (Rutile) — TiO_2

Single-crystal rutile was the first dielectric material to be used as a dielectric resonator. In 1953 Schlicke [19] investigated the possibility of high permittivity dielectric resonators but it was not until the early 1960s that Okaya [20, 21] first observed microwave resonances in a dielectric resonator of single-crystal rutile TiO_2, and found that they had very poor temperature stability. In 1968, Cohn [22] measured the microwave dielectric properties of polycrystalline rutile using a dielectric resonator and again found the temperature stability to be far too high for practical purposes. Single-crystal rutile at room temperature has highly anisotropic dielectric properties [23]. Perpendicular to the c-axis, the relative permittivity $\varepsilon_\perp = 86$, the loss tangent $\tan\delta_\perp = 1.5 \times 10^{-4}$ and the temperature coefficient of permittivity $\tau_{\varepsilon_\perp} = -760$ ppmK^{-1}. Parallel to the c-axis, the relative permittivity $\varepsilon_\parallel = 163$, the loss tangent $\tan\delta_\parallel = 1.8 \times 10^{-4}$ and the temperature coefficient of permittivity $\tau_{\varepsilon_\parallel} = -1200$ ppmK^{-1}. These loss tangents were normalised to 10 GHz. Recently, Templeton et al. [24] found by careful attention to defect chemistry that losses were due to Ti^{3+} formation and this could be prevented by doping with Al^{3+} ions. The result was polycrystalline rutile with a $\tan\delta$ of 5×10^{-4} at 3 GHz which is comparable to a single crystal. The discovery of titanate-based materials [25, 26] with high relative permittivity ε_r, low loss tangent $\tan\delta$ and near zero (and adjustable) temperature coefficient of permittivity a few years later meant that rutile was generally disregarded as a useful dielectric material until fairly recently. Use of small amounts of rutile which has a highly negative τ_ε to compensate sapphire and alumina resonators which have positive τ_ε in the region of +60 ppmK^{-1} has been reported to provide temperature stability to resonators [27–29] and more recently a high-Q spherical Bragg reflector resonator made entirely from polycrystalline rutile with zero τ_f was reported [30].

Because monocrystalline rutile is highly uniaxially anisotropic with $\varepsilon_\parallel/\varepsilon_\perp \approx 2$, the extraction of the relative permittivity and loss tangents, parallel and perpendicular to the crystallographic axis is slightly more involved than for an isotropic material. The first step is to extract the relative permittivity perpendicular to the c-axis by analysing the transverse $TE_{01\delta}$ mode which only has an azimuthal electric field component, E_ϕ. For a given structure and a measured resonant frequency, the characteristic system of equations resultant from mode matching is first solved for $\varepsilon_{r,\perp}$. For the second step, the relative permittivity parallel to the c-axis is found by measuring the $TM_{01\delta}$ mode and solving the mode matching problem again using the value of $\varepsilon_{r,\perp}$ resultant from the first step. A cylindrical puck of c-axis aligned single-crystal rutile TiO_2, with diameter 9.97 mm and height 4.95 mm was placed in the measurement cavity. The crystal axis of the sample was commensurate with the cavity axis. Coupling loops were oriented horizontally to excite the axial component H_z of the magnetic field for the $TE_{01\delta}$ mode with a coupling level of –50 dB. The room-temperature resonant frequency for this mode was found at 3.4459 GHz with an unloaded Q-factor of 15,450. Subsequent mode matching analysis provided a value for the relative permittivity perpendicular to the c-axis of $\varepsilon_{r,\perp} = 85.62$. The

electric filling factors (azimuthal components) of the rutile sample and the quartz spacer for this mode were calculated to be 0.990 and 6.58×10^{-4}, respectively, and the geometric factor was found to be $G = 1556\ \Omega$. Calculation of the electric filling factors and geometric factor yield the loss tangent $\tan\delta_\perp$ from the unloaded Q-factor measurement and the equation:

$$\tan\delta_\perp = \frac{1}{P_{d,\phi}}\left(\frac{1}{Q_0} - P_{s,\phi}\tan\delta_{s,\perp} - \frac{R_S}{G}\right), \tag{3.8.1}$$

where $P_{d,\phi}$ and $P_{s,\phi}$ are the azimuthal electric energy filling factors for the dielectric and support, respectively, and R_S is the surface resistance scaled to the resonant frequency, $R_S = 15.2\ \text{m}\Omega$. The calculated loss tangent for the perpendicular component was found to be $\tan\delta_\perp = 5.55 \times 10^{-5}$. The second step analyses the $\text{TM}_{01\delta}$ mode, which has both radial E_ρ and axial E_z electric field components and therefore samples both the perpendicular and parallel components of the permittivity tensor. The relative permittivity parallel to the c-axis can then be found from the measured resonant frequency, given the perpendicular permittivity component found from the first step, $\varepsilon_{r,\perp} = 85.62$. It must be noted, that due to the two-step process of determining the parallel relative permittivity component and the singular electric field components of the $\text{TM}_{01\delta}$ mode (which are known to be susceptible to uncertainties in the height of resonator components and air gaps at the sample/spacer interface) this technique is more prone to errors. In addition, because the $\text{TM}_{01\delta}$ mode will have a different resonant frequency to the $\text{TE}_{01\delta}$ mode, the assumption of linear scaling of the loss tangent, $\tan\delta_\perp$, is necessary. Coupling loops were rotated 90° in order to excite the azimuthal magnetic field component of the $\text{TM}_{01\delta}$ mode. The resonant frequency of this mode was found to be 4.2333 GHz from which the relative permittivity parallel to the c-axis, $\varepsilon_{r,\parallel} = 163.2$, was found from mode matching. Electric energy filling factors and geometric factors were then calculated to be $P_{d,\rho} = 0.528$, $P_{d,z} = 0.415$, $P_{s,\rho} = 0.0024$, $P_{s,z} = 0.016$ and $G = 31,753\ \Omega$. The loss tangent perpendicular to the c-axis was linearly scaled to $\tan\delta_\parallel = 6.82 \times 10^{-5}$ and the surface resistance at 4.233 GHz taken to be $R_S = 16.9\ \text{m}\Omega$. The unloaded Q-factor was measured to be 14,620 from which the parallel loss tangent $\tan\delta_\parallel$ is then found from

$$\tan\delta_\parallel = \frac{1}{P_{d,z}}\left(\frac{1}{Q_0} - P_{d,\rho}\tan\delta_\perp - P_{s,\rho}\tan\delta_{s,\perp} - P_{s,z}\tan\delta_{s,\parallel} - \frac{R_s}{G}\right). \tag{3.8.2}$$

The calculated loss tangent for the perpendicular component was found to be $\tan\delta_\perp = 7.64 \times 10^{-5}$. Temperature measurements of the TiO_2 single crystal are shown in Fig. 3.14. The high anisotropy of the relative permittivity can clearly be observed. Unlike MgO and $LaAlO_3$, both the perpendicular $\varepsilon_{r,\perp}$ and parallel $\varepsilon_{r,\parallel}$ components of the permittivity *increase* as the temperature is reduced. This is due to rutile being an *incipient ferroelectric*, exhibiting Curie–Weiss behaviour with a slightly negative Curie temperature. The temperature coefficients of permittivity for both components are an order of magnitude higher than MgO or $LaAlO_3$ and are also anisotropic. The

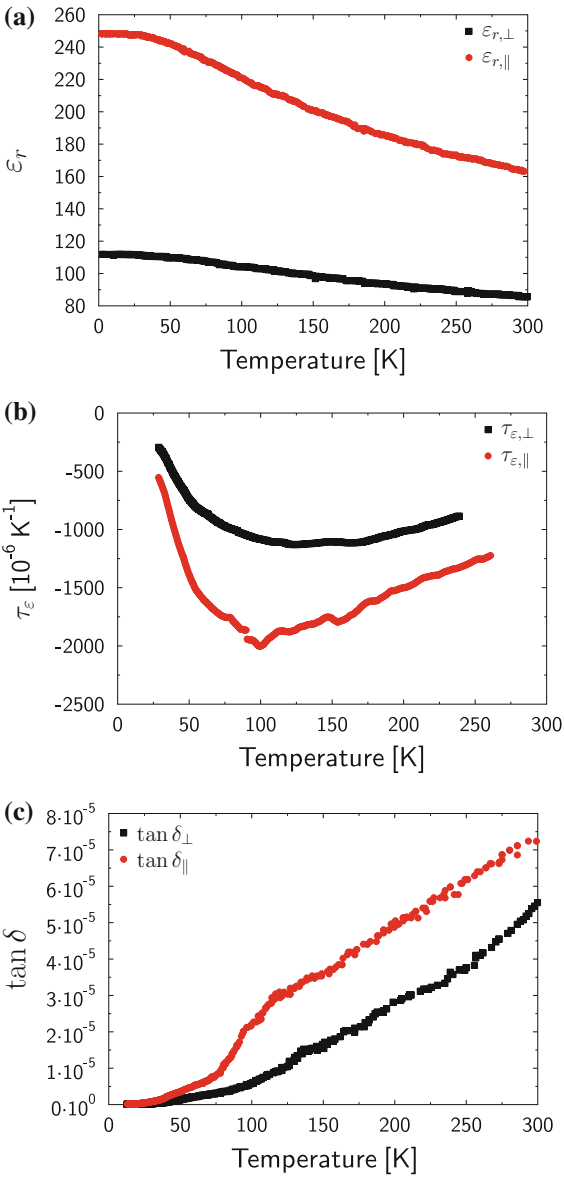

Fig. 3.14 Properties of single-crystal TiO_2 as a function of temperature. **a** Relative permittivity, **b** temperature coefficient of permittivity and **c** loss tangent. The measurement frequency of the $TE_{01\delta}$ mode at room temperature was 3.447 GHz

loss tangent, $\tan\delta_\parallel$ exhibits a pronounced hump around 100 K. This can be attributed to oxygen defects and has been reported widely in the literature [12, 24].

3.9 Aluminium Oxide (Sapphire) — Al_2O_3

Single-crystal aluminium oxide (sapphire) is an interesting microwave dielectric material and has been extensively studied due to it having the lowest loss of any material at room temperature, especially at cryogenic temperatures ($\tan\delta < 10^{-8}$ at 4K) and its superior mechanical properties. Braginsky et al. [11] reported on the temperature dependence of the loss tangent of high-quality single-crystal sapphire. In the temperature range 50–200 K, they found $\tan\delta \sim \omega^{1.7}T^{4.8}$ at 9 and 36 GHz, which confirmed the ωT^5 and $\omega^2 T^4$ temperature dependence of the loss tangent predicted by Gurevich's phonon transport theory for rhombohedral and hexagonal crystals, respectively. Although sapphire's crystal lattice belongs to the rhombohedral D_{3d} symmetry class, its long-wavelength acoustic phonons have hexagonal symmetry [5]. Below 50 K, Braginsky found that the $\tan\delta$ had only a very weak temperature dependence, $\tan\delta \sim \omega T^0$ and was greatly affected by the level of crystal imperfection, correlating with the crystal growth rate. More accurate low-temperature measurements of sapphire using whispering gallery mode resonators were later reported by Krupka and Tobar [1, 16, 27, 28] demonstrating incredibly low losses ($\tan\delta < 10^{-9}$) at helium temperatures (4.2 K). Sapphire grown by different techniques such as the Heat Exchange Method (HEMEX from Crystal Systems) and Czochralski method (Union Carbide) also exhibit different levels of paramagnetic impurity ions (Cr^{3+}, Fe^{3+}) at the part per billion level which can also affect the loss tangent at helium temperatures due to paramagnetic resonances at 11.45 GHz (Cr^{3+}) and 12.05 GHz (Fe^{3+}).

Due to the excellent electromagnetic and mechanical properties of sapphire, it has found many applications in microwave-based technologies. It has found application as a substrate for HTS films in single-crystal form and more widely for microwave integrated circuits in its polycrystalline form (alumina). In bulk form it is employed as the basis for dielectric resonators with very high Q-factors (>100,000 at room temperature) which are used in very low phase-noise microwave oscillators and secondary frequency standards. It was recently found by Bourgeois et al. [31] that trace amounts of Fe^{3+} impurities in high-quality HEMEX sapphire on the level of a few parts per billion allowed for a solid-state maser to be realised operating at helium temperature (4.2 K). Judicious design of a whispering gallery mode (WGM) resonator allowed above-threshold maser oscillation by pumping a high-Q mode coincident in frequency with the electron spin resonance energy levels of the Fe^{3+} spin population. More recently, a room-temperature solid-state maser was demonstrated for the first time by Oxborrow and Breeze [32] which consisted of a cylinder of single-crystal sapphire housing an organic paramagnetic crystal of pentacene-doped p-terphenyl. Above-threshold maser oscillation was achieved by optically pumping the paramagnetic medium into a long-lived spin triplet state whose population inverted energy-level transition coincided with the resonant frequency of the resonator at 1.45 GHz. A dramatic enhancement in the Q-factor of resonators was proposed by Maggiore [33] and Flory et al. [34, 35] who employed monocrystalline sapphire quarter-wave Bragg reflectors to confine the TE_{011} mode. The low-loss tangent allowed resonators

to be produced with Q-factors almost an order of magnitude higher than an optimised $TE_{01\delta}$ or WGM resonator at the same frequency. Breeze [36] then went on to show that the Q-factor of Bragg reflectors were limited by the periodicity and that further enhancements could be made by departing from periodicity. This was demonstrated experimentally for a cylindrical *aperiodic* Bragg resonator, built from plates and rings of sapphire. The aperiodic reflector resonator had $Q = 600,000$ at 30 GHz and room temperature [37], a threefold improvement compared with a conventional Bragg reflector, and is currently the highest Q-factor in a room temperature resonator reported in the literature. Alford et al. [38, 39] found that careful attention to processing conditions and light doping with Ti^{4+} allowed polycrystalline alumina to be produced with very low microwave loss, approaching that of a single crystal. They measured a record $\tan\delta$ of 7.5×10^{-6} at 9 GHz (8.3×10^{-6} normalised to 10 GHz) for this material. The temperature coefficient of permittivity of such an alumina puck was reduced to zero by depositing a thick film of titania (TiO_2) on its surface [29].

A cylindrical puck of c-axis aligned sapphire (Crystal Systems HEMEX) with diameter 9.98 mm and height 4.92 mm was measured. Coupling loops were oriented horizontally to excite the H_z magnetic field component of the $TE_{01\delta}$ mode. The resonance was found at a frequency of 9.9520 GHz with an unloaded Q-factor of 65,200 at a coupling level of –48 dB. The relative permittivity perpendicular to the sapphire axis was calculated using the mode matching technique and found to be $\varepsilon_{r,\perp} = 9.395$. Electric filling factors (azimuthal components) of the sample and the quartz spacer were calculated to be 0.886 and 6.79×10^{-3}, respectively, and the geometric factor of the cavity was found to be $G = 2366\ \Omega$. The perpendicular component of the loss tangent tensor, $\tan\delta_\perp$ was calculated from the measured Q-factor and calculated parameters using the equation

$$\tan\delta_\perp = \frac{1}{P_{d,\phi}}\left(\frac{1}{Q_0} - P_{s,\phi}\tan\delta_{s,\perp} - \frac{R_S}{G}\right) \tag{3.9.1}$$

and found to be $\tan\delta_\perp = 5.35 \times 10^{-6}$. Coupling loops were then rotated 90° in order to excite the azimuthal magnetic field component of the $TM_{01\delta}$ mode. The resonant frequency of this mode was found to be 13.824 GHz from which the relative permittivity parallel to the c-axis was found by mode matching to be $\varepsilon_{r,\parallel} = 11.592$. The electric energy filling factors and geometric factors were then calculated to be $P_{d,\rho} = 0.300$, $P_{d,z} = 0.453$, $P_{s,\rho} = 0.0069$, $P_{s,z} = 0.0056$ and $G = 1557\ \Omega$. The loss tangent perpendicular to the c-axis was linearly scaled to $\tan\delta_\parallel = 7.40 \times 10^{-6}$ and the surface resistance at 13.824 GHz taken to be $R_S = 30.6\ \text{m}\Omega$. The unloaded Q-factor was measured to be 43,540 from which the parallel loss tangent $\tan\delta_\parallel$ is then found from

$$\tan\delta_\parallel = \frac{1}{P_{d,z}}\left(\frac{1}{Q_0} - P_{d,\rho}\tan\delta_\perp - P_{s,\rho}\tan\delta_{s,\perp} - P_{s,z}\tan\delta_{s,\parallel} - \frac{R_s}{G}\right). \tag{3.9.2}$$

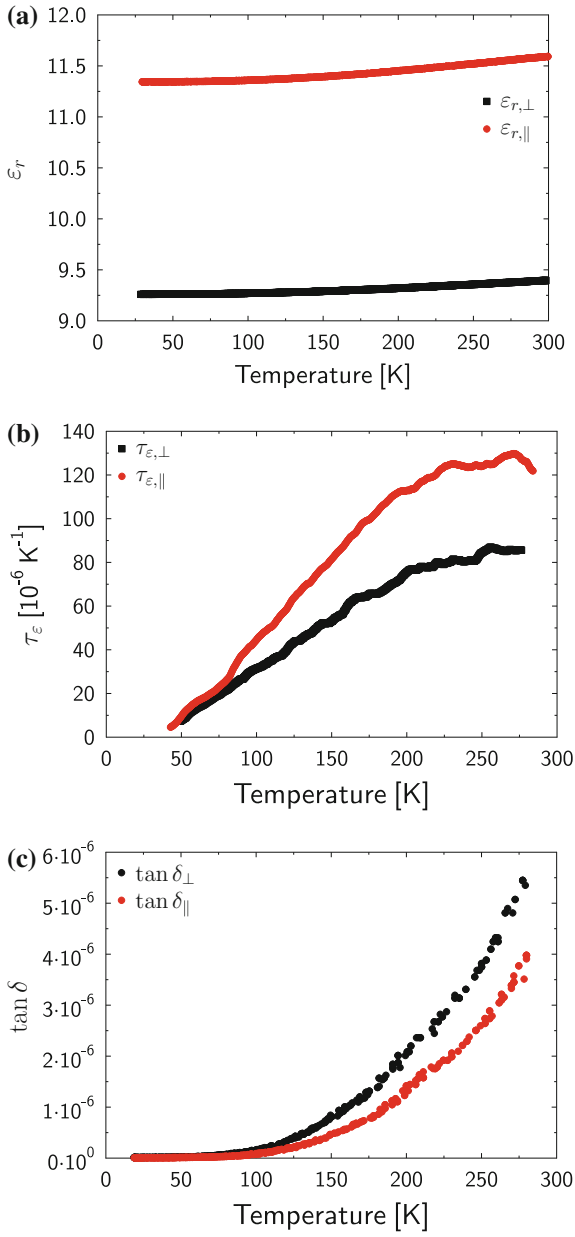

Fig. 3.15 Properties of single-crystal Al_2O_3 (sapphire) as a function of temperature. **a** Relative permittivity, **b** temperature coefficient of permittivity and **c** loss tangent

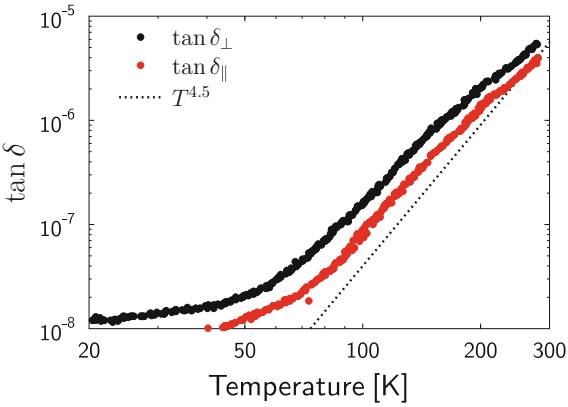

Fig. 3.16 Loss tangent of Al_2O_3 (log scale) as a function of temperature showing $T^{4.5}$ dependence

The calculated loss tangent for the perpendicular component was found to be $\tan\delta_\perp = 3.91 \times 10^{-6}$. Temperature measurements are shown in Fig. 3.15. The anisotropy in the complex permittivity tensor is evident, with both relative permittivity components decreasing as temperature is reduced with positive temperature coefficients of a similar magnitude to MgO and $LaAlO_3$. The loss tangents are also anisotropic and show a steep $T^{4.5}$ temperature dependence as shown for logarithmic scale in Fig. 3.16, in agreement with Braginsky and confirming the predictions of Gurevich and Tagantsev.

3.10 Summary and Conclusions

The apparatus and procedure for measuring the relative permittivity and loss tangent of microwave dielectric samples as functions of temperature were discussed and used to measure the properties of MgO, $LaAlO_3$, TiO_2 and Al_2O_3 from room temperature to around 10 K. The historical background of the single-crystal MgO, $LaAlO_3$, TiO_2 and Al_2O_3 were introduced and their properties as a function of temperature were presented.

References

1. J. Krupka et al., Complex permittivity of some ultralow loss dielectric crystals at cryogenic temperatures. Meas. Sci. Technol. **10**, 387 (1999)
2. J. Breeze et al., Do Grain Boundaries Affect Microwave Dielectric Loss in Oxides? J. Am. Ceram. Soc. **92**, 671 (2009)
3. V.L. Gurevich, Dielectric losses in crystals. Fizika Tverdogo Tela **21**, 3453 (1979)
4. V.L. Gurevich, A.K. Tagantsev, Intrinsic dielectric loss in crystals: low temperatures. Sov. Phys. JETP **64**, 142 (1986)

5. Gurevich, V.L.: *Transport in Phonon Systems*, 1st ed. (North-Holland Physics Publishing, 1986)
6. V.L. Gurevich, A.K. Tagantsev, Intrinsic dielectric loss in crystals. Adv. Phys. **40**, 719 (1991)
7. A.K. Tagantsev, Effect of weak electric field on dielectric losses in centrally symmetric ferroelectric materials of displacement type. Zhurnal Eksperimentalnoi i Teoreticheskoi Fiziki **77**, 1993 (1979)
8. A.K. Tagantsev, Dielectric losses in displacive ferroelectrics. Zhurnal Eksperimentalnoi i Teoreticheskoi Fiziki **86**, 2215 (1984)
9. A.K. Tagantsev, Weak ferroelectrics. Ferroelectrics **79**, 57 (1988)
10. A.K. Tagantsev, J. Petzelt, N. Setter, Relation between intrinsic microwave and submillimeter losses and permitivity in dielectrics. Solid State Commun. **87**, 1117 (1993)
11. V.B. Braginsky, V.S. Ilchenko, K.S. Bagdassarov, Experimental observation of fundamental microwave absorption in high-quality dielectric crystals. Phys. Lett. A **120**, 300 (1987)
12. N.M. Alford et al., Dielectric loss of oxide single crystals and polycrystalline analogues from 10 to 320 K. J. Eur. Ceram. Soc. **21**, 2605 (2001)
13. C. Zuccaro et al., Microwave absorption in single crystals of lanthanum aluminate. J. Appl. Phys. **82**, 5695 (1997)
14. T. Zychowicz, J. Krupka, M. Tobar, Whispering gallery modes in hollow spherical dielectric resonators. J. Eur. Ceram. Soc. **26**, 2193 (2006)
15. J. Mazierska et al., Precise microwave characterization of MgO substrates for HTS circuits with superconducting post dielectric resonator. Supercond. Sci. Technol. **18**, 18 (2005)
16. J. Krupka et al., Dielectric properties of single crystals of Al_2O_3, $LaAlO_3$, $NdGaO_3$, $SrTiO_3$ and MgO at cryogenic temperatures. IEEE Trans. Microw. Theory Tech. **42**, 1886 (1994)
17. J.C. Mage et al., Microwave propertied of MgO single crystals computed from the IR, and measured with a resonator technique. Int. J. Infrared Millim. Waves **15**, 1189 (1994)
18. T. Shimada et al., Intrinsic microwave dielectric loss of lanthanum aluminate. IEEE Trans. Ultrason. Ferroelectr. Frequency Control **57**, 2243 (2010)
19. H.M. Schicke, Quasi-Degenerated modes in high-ϵ dielectric cavities. J. Appl. Phys. **24**, 187 (1953)
20. A. Okaya, The Rutile microwave resonator. Proc. IRE **48**, 1921 (1960)
21. A. Okaya, L.F. Barash, The Rutile microwave resonator. Proc. IRE **50**, 2081 (1962)
22. S.B. Cohn, Microwave bandpass filters containing high Q dielectric resonators. IEEE Trans. Microw. Theory Tech. **16**, 218 (1968)
23. M.E. Tobar et al., Anisotropic complex permittivity measurements of mono-crystalline rutile between 10 and 300 K. J. Appl. Phys. **83**, 1604 (1998)
24. A. Templeton et al., Microwave dielectric loss of titanium oxide. J. Am. Ceram. Soc. **83**, 95 (2000)
25. D.J. Masse et al., A new low-loss high-k temperature-compensated dielectric for microwave applications. Proc. IEEE **59**, 1628 (1971)
26. J.K. Plourde et al., $Ba_2Ti_9O_{20}$ as a microwave dielectric resonator. J. Am. Ceram. Soc. **58**, 418 (1975)
27. M.E. Tobar et al., High-Q sapphire-rutile frequency-temperature compensated microwave dielectric resonators. IEEE Trans. Ultrason. Ferroelectr. Frequency Control **45**, 830 (1998)
28. M.E. Tobar et al., High-Q factor frequency-temperature compensated sapphire Bragg distributed resonator. Electr. Lett. **39**, 293 (2003)
29. J. Breeze et al., Layered Al_2O_3-TiO_2 composite dielectric resonators. Electr. Lett. **36**, 883 (2000)
30. J. Breeze et al., Temperature-stable and high Q-factor TiO_2 Bragg reflector resonator. Appl. Phys. Lett. **94**, 082906 (2009)
31. P.Y. Bourgeois et al., Maser oscillation in a whispering-gallery-mode microwave resonator. Appl. Phys. Lett. **87**, 224104 (2005)
32. M. Oxborrow, J.D. Breeze, N.M. Alford, Room-temperature solid-state maser. Nature **488**, 353 (2012)
33. C.J. Maggiore et al., Low-loss microwave cavity using layered dielectric materials. Appl. Phys. Lett. **64**, 1451 (1994)

34. C.A. Flory, R.C. Taber, High performance distributed Bragg reflector microwave resonator. IEEE Trans. Ultrason. Ferroelectr. Frequency Control **44**, 486 (1997)
35. C.A. Flory, H.L. Ko, Microwave oscillators incorporating high performance distributed Bragg reflector microwave resonators. IEEE Trans. Ultrason. Ferroelectr. Frequency Control **45**, 824 (1998)
36. J. Breeze, J. Krupka, N.M. Alford, Enhanced quality factors in aperiodic reflector resonator. Appl. Phys. Lett. **91**, 152902 (2007)
37. J. Breeze, M. Oxborrow, N.M. Alford, Better than Bragg: Optimizing the quality factor of resonators with aperiodic dielectric reflectors. Appl. Phys. Lett. **99**, 113515 (2011)
38. N.M. Alford, S.J. Penn, Sintered alumina with low dielectric loss. J. Appl. Phys. **80**, 5895 (1996)
39. J.D. Breeze, X. Aupi, N.M. Alford, Ultralow loss polycrystalline alumina. Appl. Phys. Lett. **81**, 5021 (2002)

Chapter 4
Lattice Dynamics and Density Functional Perturbation Theory

The focus of this thesis now shifts towards the physics that describes the properties of microwave dielectrics and the means of computationally predicting them. Lattice dynamics describes the vibrational collective excitations in solids known as *phonons* and is a cornerstone of solid-state physics. Infrared, Raman and neutron-diffraction spectra, specific heat capacity, thermal expansion, heat conduction and electron–phonon interaction-related phenomena such as resistivity of metals and superconductivity are a few examples of where lattice dynamics has been applied with great success. The theory of lattice dynamics dates back to the 30 s and the treatise by Born and Huang [1], which is still regarded today as a reference textbook in the field. Early formulations established the general properties of dynamical matrices without much consideration for the electronic properties that determine them. In the 1970s, a systematic study of these connections was performed by De Cicco and Johnson [2] and Pick, Cohen, and Martin [3]. The establishment of the relationship between the electronic and the lattice-dynamical properties allowed linear response theorems to be formulated which made it possible to calculate the lattice-dynamical properties of materials from first-principles using their electronic structure and without using empirical data. Many *ab-initio* calculations based on the linear response theory of lattice vibrations have been made possible over the past couple of decades due the development of density functional theory (DFT) by Hohenberg and Kohn [4] and Kohn and Sham [5] and its linear response embodiment of density functional perturbation theory (DFPT) [6]. These developments allowed the computationally challenging multi-body problem of interacting electrons to be formulated instead in terms of the electron density. Whereas classical methods rely on fitting potentials to experimentally measured parameters, DFT uses pseudopotentials based on solutions to Schrödinger's equation. Thanks to these theoretical and algorithmic advances, it is now possible to obtain accurate phonon dispersion relations on fine grids of wave-vectors spanning an entire Brillouin zone, which compare favourably with neutron-diffraction data and from which several physical properties of the system such as heat capacities and thermal expansion can be calculated. Furthermore, the ability of DFT to accurately describe anharmonic phenomena such as thermal

J. Breeze, *Temperature and Frequency Dependence of Complex Permittivity in Metal Oxide Dielectrics: Theory, Modelling and Measurement*, Springer Theses, DOI 10.1007/978-3-319-44547-2_4

expansion, optical phonon linewidth broadening and structural phase transitions has added to its appeal as a valuable tool in the study of anharmonic processes.

4.1 Lattice Dynamics

Here we follow the basic theory of lattice dynamics developed by Born and Huang [1]. Consider a crystal consisting of N unit cells with n atoms per unit cell. The position of the κ^{th} atom in the l^{th} unit cell can be written as

$$\mathbf{R}^l_\kappa = \mathbf{R}^l + \boldsymbol{\tau}_\kappa, \quad \kappa = 1, 2, \ldots, n$$

where the lattice vector $\mathbf{R}^l$ can be written in terms of the unit cell basis vectors $\{\mathbf{a}_1, \mathbf{a}_2, \mathbf{a}_3\}$;

$$\mathbf{R}^l = l_1\mathbf{a}_1 + l_2\mathbf{a}_2 + l_3\mathbf{a}_3, \quad l = \{l_1, l_2, l_3\}.$$

The position vector of the κ^{th} atom in the unit cell is then

$$\boldsymbol{\tau}_\kappa = x_1^\kappa\mathbf{a}_1 + x_2^\kappa\mathbf{a}_2 + x_3^\kappa\mathbf{a}_3 \quad 0 \le x_i^\kappa \le 1, \quad i = 1, 2, 3.$$

If the atoms are permitted to vibrate about their equilibrium positions their position vectors become modulated

$$\mathbf{R}^l \to \mathbf{R}^l + \mathbf{u}_\kappa(\mathbf{R}^l),$$

by the displacement vector $\mathbf{u}_\kappa(\mathbf{R}^l)$ of atom κ in unit cell l. The ionic coordinate of any atom i can then be expressed as

$$\mathbf{R}_i = \mathbf{R}^{l_i}_{\kappa_i} + \mathbf{u}^{l_i}_{\kappa_i}$$

where l_i and κ_i label the unit cell and species for atom i. In the harmonic approximation, the total energy is expanded as a Taylor series about the equilibrium positions up to second order in the atomic displacements

$$\mathcal{E} = \mathcal{E}_0 + \frac{1}{2}\sum_{\substack{\alpha_1\alpha_2\\ \kappa_1\kappa_2\\ \mathbf{R}_1\mathbf{R}_2}} \Phi^{\kappa_1\kappa_2}_{\alpha_1\alpha_2}(\mathbf{R}_1\mathbf{R}_2)u^{\kappa_1}_{\alpha_1}(\mathbf{R}_1)u^{\kappa_2}_{\alpha_2}(\mathbf{R}_2) + \mathcal{O}(u^3) + \ldots.$$

where $\Phi^{\kappa_1\kappa_2}_{\alpha_1\alpha_2}(\mathbf{R}_1\mathbf{R}_2)$, the second-order derivative of the total energy

$$\Phi^{\kappa_1\kappa_2}_{\alpha_1\alpha_2}(\mathbf{R}_1\mathbf{R}_2) = \frac{\partial^2\mathcal{E}}{\partial u^{\kappa_1}_{\alpha_1}(\mathbf{R}_1)\partial u^{\kappa_2}_{\alpha_2}(\mathbf{R}_2),}$$

is related to the *interatomic force constants* (IFC) and the dynamical matrix which will be discussed later.

4.2 Hamiltonian of a System of Ions and Electrons

The Hamiltonian of a system of interacting ions and electrons can be written as the sum of kinetic energies and the potential energy of their interactions

$$H = T_{\text{ion}}(\dot{\mathbf{R}}) + T_{\text{el}}(\dot{\mathbf{r}}) + V_{\text{ion-ion}}(\mathbf{R}) + V_{\text{el-el}}(\mathbf{r}) + V_{\text{el-ion}}(\mathbf{r}, \mathbf{R}). \tag{4.2.1}$$

Here, $\mathbf{R}$ denotes the set of ionic coordinates $\mathbf{R}_I$ and $\mathbf{r}$ the set of electronic coordinates and spins $\{\mathbf{r}_i, \boldsymbol{\sigma}_i\}$. Labels on ions and electrons will be upper and lower-case to avoid confusion. The kinetic energy terms are

$$T_{\text{ion}}(\dot{\mathbf{R}}) = \frac{1}{2}\sum_I M_I(\dot{\mathbf{R}}_I)^2$$
$$T_{\text{el}}(\dot{\mathbf{r}}) = \frac{1}{2}\sum_i m_i(\dot{\mathbf{r}}_i)^2,$$

and the interactions between them

$$V_{\text{ion-ion}}(\mathbf{R}) = \frac{e^2}{2}\sum_{I\neq J}\frac{Z_I Z_J}{|\mathbf{R}_I - \mathbf{R}_J|}$$
$$V_{\text{el-el}}(\mathbf{r}) = \frac{e^2}{2}\sum_{i\neq j}\frac{1}{|\mathbf{r}_i - \mathbf{r}_j|}$$
$$V_{\text{el-ion}}(\mathbf{r}, \mathbf{R}) = -\frac{e^2}{2}\sum_{i,I}\frac{Z_I}{|\mathbf{r}_i - \mathbf{R}_I|}.$$

4.3 The Born–Oppenheimer Approximation

The Born–Oppenheimer adiabatic approximation [7] allows the electronic and ionic degrees of freedom to be effectively decoupled. This is due to the large mass difference between electrons and ions resulting in separate dynamics occurring on vastly different timescales. Electrons can follow the nuclear motion at much smaller timescales so that the positions of the nuclei can be considered fixed or clamped. The interaction of the electrons with the nuclei can then be considered to be via an external potential. Ionic motion and hence lattice-dynamical properties of a system is then determined by the eigenvalues $\mathcal{E}$ and eigenfunctions Φ of the Schrödinger equation

$$\left(-\sum_i \frac{\hbar^2}{2M_i}\frac{\partial^2}{\partial \mathbf{R}_i^2} + E(\mathbf{R})\right)\Phi(\mathbf{R}) = \mathcal{E}\Phi(\mathbf{R}), \tag{4.3.1}$$

where $\mathbf{R}_i$ is the position of the i^{th} nucleus, M_i its mass and $\mathbf{R} = \{\mathbf{R}_i\}$ is the set of all nuclear positions. $E(\mathbf{R})$ is the clamped-ion energy, also referred to as the *Born–Oppenheimer energy surface*, which is the ground-state energy of a system of interacting electrons moving within a field of essentially fixed nuclei with coordinates $\mathbf{R}$. The Hamiltonian for such a system of electrons is

$$H(\mathbf{R}) = -\frac{\hbar^2}{2m}\sum_i \frac{\partial^2}{\partial \mathbf{r}_i^2} + \frac{e^2}{2}\sum_{i\neq j}\frac{1}{|\mathbf{r}_i - \mathbf{r}_j|} - \sum_{iI}\frac{Z_I e^2}{|\mathbf{r}_i - \mathbf{R}_I|} + E_N(\mathbf{R}) \quad (4.3.2)$$

where Z_I is the charge on the I^{th} nucleus, $-e$ is the electron charge and $E_N(\mathbf{R})$ is the nuclear electrostatic energy

$$E_N(\mathbf{R}) = \frac{e^2}{2}\sum_{I\neq J}\frac{Z_I Z_J}{|\mathbf{R}_I - \mathbf{R}_J|}.$$

4.4 Hellmann–Feynman Theorem

The equilibrium geometry for the positions of the nuclei will occur when the forces acting upon them vanish. The forces are the partial derivative of the clamped-ion Born–Oppenheimer energy surface term with respect to the positions of the nuclei

$$\mathbf{F}_I = -\frac{\partial E(\mathbf{R})}{\partial \mathbf{R}_I} = 0.$$

The Hellmann–Feynman theorem allows one to calculate derivatives of the Born–Oppenheimer energy surface with respect to any perturbation. The theory states that the derivative of the eigenvalue of a Hamiltonian H_λ which depends on a parameter λ is the expectation value of the derivative of the Hamiltonian

$$\frac{\partial \mathcal{E}_\lambda}{\partial \lambda} = \left\langle \Psi_\lambda \left| \frac{\partial H_\lambda}{\partial \lambda} \right| \Psi_\lambda \right\rangle, \quad (4.4.1)$$

where Ψ_λ is the eigenfunction of H_λ corresponding to the eigenvalue $\mathcal{E}_\lambda$

$$H_\lambda \Psi_\lambda = \mathcal{E}_\lambda \Psi_\lambda. \quad (4.4.2)$$

The force acting on the I^{th} nucleus in the electronic ground state is therefore

$$\mathbf{F}_I = -\frac{\partial E(\mathbf{R})}{\partial \mathbf{R}_I} = -\left\langle \Psi(\mathbf{R}) \left| \frac{\partial H(\mathbf{R})}{\partial \mathbf{R}_I} \right| \Psi(\mathbf{R}) \right\rangle, \quad (4.4.3)$$

where $\Psi(\mathbf{R}) \equiv \Psi(\mathbf{r}, \mathbf{R})$ is the electronic ground-state wave function corresponding to nuclear configuration $\mathbf{R}$ in the Born–Oppenheimer Hamiltonian $H(\mathbf{R})$ (4.3.2). The electron–ion interaction $V_{\text{el-ion}}(\mathbf{r})$ couples the ionic and electronic degrees of freedom through the electronic charge density and can be regarded as an external potential seen by the electrons in the ground state. The ions are regarded as being stationary with respect to the motion of the electrons. In this case the Hellmann–Feynman theory gives

$$\mathbf{F}_I = -\int n_{\mathbf{R}}(\mathbf{r}) \frac{\partial V_{\text{el-ion}}(\mathbf{r})}{\partial \mathbf{R}_I} d\mathbf{r} - \frac{\partial E_N(\mathbf{R})}{\partial \mathbf{R}_I}. \tag{4.4.4}$$

where $n_{\mathbf{R}}(\mathbf{r})$ is the ground-state electron charge density for nuclear arrangement $\mathbf{R}$,

$$n_{\mathbf{R}}(\mathbf{r}) = N \int |\Psi_{\mathbf{R}}(\mathbf{r}, \mathbf{r}_2, \ldots, \mathbf{r}_N)|^2 \, \mathrm{d}\mathbf{r}_2 \mathrm{d}\mathbf{r}_3 \cdots \mathrm{d}\mathbf{r}_N$$

and

$$V_{\text{el-ion}}(\mathbf{r}) = \sum_{iI} \frac{Z_I e^2}{|\mathbf{r}_i - \mathbf{R}_I|}$$

is the electron–ion interaction potential. Differentiating the force on the nuclei again with respect to the nuclear coordinates yields

$$\begin{aligned} \frac{\partial^2 E(\mathbf{R})}{\partial \mathbf{R}_i \partial \mathbf{R}_j} &= -\frac{\partial \mathbf{F}_i}{\partial \mathbf{R}_j} \\ &= \int \frac{\partial n_{\mathbf{R}}(\mathbf{r})}{\partial \mathbf{R}_i} \frac{\partial V_{\text{el-ion}}(\mathbf{r})}{\partial \mathbf{R}_j} d\mathbf{r} + \int n_{\mathbf{R}}(\mathbf{r}) \frac{\partial^2 V_{\text{el-ion}}(\mathbf{r})}{\partial \mathbf{R}_i \partial \mathbf{R}_j} d\mathbf{r} + \frac{\partial^2 E_N(\mathbf{R})}{\partial \mathbf{R}_I \partial \mathbf{R}_J}. \end{aligned} \tag{4.4.5}$$

The second-order derivative of the total energy therefore requires calculation of the ground-state electron charge density $n_{\mathbf{R}}(\mathbf{r})$ and its first derivative with respect to the ionic arrangements $\partial n_{\mathbf{R}}(\mathbf{r})/\partial \mathbf{R}_i$. This was reported by De Cicco and Johnson [2] and Pick, Cohen, and Martin [3]. The terms on the left of (4.4.5) form a matrix called the *interatomic force constants* (IFC) from which the phonon dispersion relations can be derived

$$C_{IJ}^{\alpha\beta} \equiv \frac{\partial^2 E(\mathbf{R})}{\partial \mathbf{R}_I^\alpha \partial \mathbf{R}_J^\beta} = -\frac{\partial \mathbf{F}_I^\alpha}{\partial \mathbf{R}_J^\beta},$$

where α and β label Cartesian coordinates. In the harmonic approximation, the Hamiltonian describing the ionic motion is equivalent to that of a system of independent harmonic oscillators or *normal modes*, with frequencies ω and displacement patterns u_I^α for the I^{th} atom, determined by the secular equation

$$\sum_{J\beta} \left(C_{IJ}^{\alpha\beta} - M_I \omega^2 \delta_{IJ} \delta_{\alpha\beta} \right) u_J^\beta = 0.$$

4.5 Hohenberg–Kohn Theorem

In 1964 Hohenberg and Kohn [4] showed that any property of the ground state of a non-degenerate system of interacting electrons is determined only by its electron density $n(\mathbf{r})$, defined by

$$n(\mathbf{r}) = \sum_i \psi_i^*(\mathbf{r})\psi_i(\mathbf{r}).$$

Furthermore, their theorem states that two different external potentials acting on the electrons cannot be associated with the same ground-state of electronic charge density. This important concept of *invertibility* establishes one-to-one mapping between an external potential and associated ground-state electron density and gives rise to another important concept in DFT, that of the *universal functional*. A functional $F[n(\mathbf{r})]$ of the electron charge density exists such that the functional

$$E[n] = F[n] + \int n(\mathbf{r})V_{\text{ext}}(\mathbf{r})\mathrm{d}\mathbf{r}$$

is minimized by the ground-state of the electron charge density subject to external potential $V_{\text{ext}}(\mathbf{r})$ and constrained by the condition that the total number of electrons is fixed

$$N = \int n(\mathbf{r})d\mathbf{r}.$$

This theorem is the foundation on which density functional theory is built. It replaces the quantum-mechanical problem of finding the ground-state of a system of N electrons with $3N$ degrees of freedom, with a simpler problem, that of minimizing a function of three variables, the components of the position vector $\mathbf{r}$. The question of the form of the functional $F[n]$ is an interesting one since its form is in general unknown.

4.6 Kohn–Sham Orbitals

Kohn and Sham used the fact that $F[n]$ defines the physical properties of a system regardless of the electron–electron interaction. In the case of no electron–electron interactions, $F[n]$ defines the ground-state kinetic energy of a system of non-interacting electrons as a functional of the ground-state charge density distribution $T_0[n]$ [5]. The generally unknown functional $F[n]$ can take the form

$$F[n] = T_0[n] + \frac{e^2}{2}\int \frac{n(\mathbf{r})n(\mathbf{r}')}{|\mathbf{r}-\mathbf{r}'|}d\mathbf{r}d\mathbf{r}' + E_{\text{xc}}[n] \tag{4.6.1}$$

which introduces the *exchange-correlation energy* $E_{\rm xc}[n]$, which allows the problem of a system of interacting electrons to be mapped onto a system of non-interacting electrons subject to an effective potential called the *self-consistent field* (SCF). A set of self-consistent Schrödinger equations known as the Kohn–Sham equations can be created for single electrons,

$$\left[-\frac{\hbar^2}{2m}\nabla^2 + V_{\rm scf}(\mathbf{r})\right]\psi_i(\mathbf{r}) = \epsilon_i\psi_i(\mathbf{r}) \tag{4.6.2}$$

under the influence of a self-consistent potential given by

$$V_{\rm scf}(\mathbf{r}) = V_{\text{el-ion}}(\mathbf{r}) + e^2\int\frac{n(\mathbf{r}')}{|\mathbf{r}-\mathbf{r}'|}d\mathbf{r}' + v_{\rm xc}(\mathbf{r}) \tag{4.6.3}$$

where

$$v_{\rm xc}(\mathbf{r}) = \frac{\delta E_{\rm xc}[n]}{\delta n(\mathbf{r})}$$

is the *exchange-correlation potential*. The ground-state energy and non-interacting kinetic energy are then expressed in terms of the *auxiliary Kohn-Sham orbitals*, $\psi_n(\mathbf{r})$

$$\begin{aligned} n(\mathbf{r}) &= 2\sum_{n=1}^{N/2}|\psi_n(\mathbf{r})|^2 \\ T_0[n] &= -2\frac{\hbar^2}{2m}\sum_{n=1}^{N/2}\int\psi_n^*(\mathbf{r})\frac{\partial^2\psi_n(\mathbf{r})}{\partial\mathbf{r}^2}. \end{aligned} \tag{4.6.4}$$

4.7 The Local Density Approximation

The exchange-correlation energy $E_{\rm xc}[n]$ is most commonly approximated using the *Local Density Approximation* (LDA), in which the exchange and correlation energy per particle is taken to be equal to that of a uniform homogeneous electron gas with the density of the local density $n(\mathbf{r})$,

$$E_{\rm xc}[n] = \int\epsilon_{\rm xc}(n)n(\mathbf{r})d\mathbf{r}$$

where $\epsilon_{\rm xc}(n)$ is the exchange-correlation energy for a particle within an electron gas with density $n = n(\mathbf{r})$. The exchange-correlation potential is given by

$$v_{\rm xc}(\mathbf{r}) = \epsilon_{\rm xc}(n) + n\frac{d\epsilon_{\rm xc}(n)}{dn}.$$

where $n = n(\mathbf{r})$. Values of $\epsilon_{\rm xc}(n)$ were calculated by Ceperley and Alder [8] using Monte Carlo simulations of a homogeneous electron gas and were later parametrized by Perdew and Zunger [9] into simple analytical form. The LDA is exact in the limit of high charge density or for a charge density distribution which varies very slowly in space. The LDA has been immensely successful, much more than expected given its crude approximation, at accurately describing the structural and vibrational properties of metals, semiconductors and insulators. However, it has some drawbacks: an overestimation of cohesive and molecular binding energies, an inability to describe strongly correlated systems such as transition-metal oxides and an underestimation of the valence-conduction band-gap energy.

4.8 Linear Response DFT

As was mentioned earlier, the second-order derivatives of the total energy with respect to displacement of the nuclei can be obtained from the linear response of the electronic charge density distribution to displacement of the positions of nuclei. The following procedure is referred to as *density functional perturbation theory* (DFPT) [10–12]. If we take λ to be the set of parameters $\{\lambda_i\}$ where $\lambda_i \equiv \mathbf{R}_I$, the positions of the nuclei in the case of lattice dynamics, then the first and second derivatives of the ground-state energy, by virtue of the Hellmann–Feynman theorem are

$$\frac{\partial E}{\partial \lambda_i} = \int \frac{\partial V_\lambda(\mathbf{r})}{\partial \lambda_i} n_\lambda(\mathbf{r}) \mathrm{d}\mathbf{r},$$
$$\frac{\partial^2 E}{\partial \lambda_i \partial \lambda_j} = \int \frac{\partial^2 V_\lambda(\mathbf{r})}{\partial \lambda_i \partial \lambda_j} n_\lambda(\mathbf{r}) \mathrm{d}\mathbf{r} + \int \frac{\partial V_\lambda(\mathbf{r})}{\partial \lambda_i} \frac{\partial n_\lambda(\mathbf{r})}{\partial \lambda_j} \mathrm{d}\mathbf{r}.$$

The electron energy response, $\partial n_\lambda(\mathbf{r})/\partial \lambda_i$, can be evaluated by linearising the one-electron Kohn–Sham auxiliary Schrödinger equation and ground-state charge density with respect to wave function, density and potential variations. Linearising the charge density (4.6.4) with respect to a perturbation λ_i leads to

$$\frac{\partial n(\mathbf{r})}{\partial \lambda} = 4\ \mathrm{Re} \sum_{n=1}^{N/2} \psi_n^*(\mathbf{r}) \frac{\partial \psi_n(\mathbf{r})}{\partial \lambda}. \tag{4.8.1}$$

The variation of the Kohn–Sham orbitals (4.6.2) can be derived using standard first-order perturbation theory [13]

$$(H_{\rm scf} - \epsilon_n) \left| \frac{\partial \psi_n}{\partial \lambda} \right\rangle = - \left(\frac{\partial V_{\rm scf}}{\partial \lambda} - \frac{\partial \epsilon_n}{\partial \lambda} \right) |\psi_n\rangle \tag{4.8.2}$$

where H_{scf} is the unperturbed Kohn–Sham Hamiltonian

$$H_{\text{scf}} = -\frac{\hbar^2}{2m}\frac{\partial^2}{\partial \mathbf{r}^2} + V_{\text{scf}}(\mathbf{r}), \tag{4.8.3}$$

$\partial V_{\text{scf}}/\partial\lambda$ is the first-order correction to the self-consistent potential

$$\frac{\partial V_{\text{scf}}}{\partial\lambda} = \frac{\partial V_{\text{el-ion}}(\mathbf{r})}{\partial\lambda} + e^2\int\frac{1}{|\mathbf{r}-\mathbf{r}'|}\frac{\partial n(\mathbf{r}')}{\partial\lambda}\mathrm{d}\mathbf{r}' + \left.\frac{\mathrm{d}v_{xc}(n)}{\mathrm{d}n}\right|_{n=n(\mathbf{r})}\frac{\partial n(\mathbf{r})}{\partial\lambda} \tag{4.8.4}$$

and $\partial\epsilon_n/\partial\lambda$ is the first-order variation in the Kohn–Sham eigenvalue ϵ_n

$$\frac{\partial\epsilon_n}{\partial\lambda} = \left\langle\psi_n\left|\frac{\partial V_{\text{scf}}}{\partial\lambda}\right|\psi_n\right\rangle.$$

Equation 4.8.2 is often referred to as a Sternheimer equation and can be solved self-consistently using (4.8.1–4.8.4) in a similar way to the Kohn–Sham eigenvalue equation, with (4.6.2) being replaced by the Sternheimer equation (4.8.2) for the perturbed system. Since the variation of the self-consistent potential, $\partial V_{\text{scf}}/\partial\lambda$ is a linear functional of $\partial n(\mathrm{r})/\partial\lambda$, which itself depends linearly on all $\partial\psi/\partial\lambda$, the whole self-consistent calculation can be generalized to a linear problem, where the N equations for (4.8.2) are linearly coupled to each other. The set of all $\Delta\psi$ is then the solution of a linear problem with dimension $NM/2 \times NM/2$, where M is the size of the basis set used to describe each ψ_n. Such a large system can be solved directly by iterative methods.

The first-order correction to a given eigenfunction of the Schrödinger equation is usually given by

$$\frac{\partial\psi_n(\mathbf{r})}{\partial\lambda} = \sum_{m\neq n}\psi_m(\mathbf{r})\frac{1}{\epsilon_n-\epsilon_m}\left\langle\psi_m\left|\frac{\partial V_{\text{scf}}}{\partial\lambda}\right|\psi_n\right\rangle$$

where the sum extends over all states in the system, occupied or not, except the state n. The electron charge density linear response can be derived from (4.8.1)

$$\frac{\partial n(\mathbf{r})}{\partial\lambda} = 4\sum_{n=1}^{N/2}\sum_{m\neq n}\psi_n^*(\mathbf{r})\psi_m(\mathbf{r})\frac{1}{\epsilon_n-\epsilon_m}\left\langle\psi_m\left|\frac{\partial V_{\text{scf}}}{\partial\lambda}\right|\psi_n\right\rangle. \tag{4.8.5}$$

Since the terms containing products of occupied states cancel each other, the electron density can be considered not to respond to a perturbation which acts only on the occupied state manifold or to the component of any perturbation which couples occupied states to each other. Evaluation of $\partial\psi_n(\mathbf{r})/\partial\lambda$ would require knowing the full spectrum of Kohn–Sham states and summations over conduction bands. But the derivatives $\partial\psi_n(\mathbf{r})\partial\lambda$ in the linearised Kohn–Sham Hamiltonian (4.8.2) are

orthogonal to all states of the occupied manifold. Alternatively, insertion of (4.8.1) into (4.8.4) and then into the linearised Kohn–Sham Hamiltonian (4.8.2) yields

$$(H_{\text{scf}} - \epsilon_n)\frac{\partial\psi_n(\mathbf{r})}{\partial\lambda} + \sum_{m=1}^{N/2}\left(K_{nm}\frac{\partial\psi_m}{\partial\lambda}\right)(\mathbf{r}) = -\frac{\partial V_{\text{el-ion}}(\mathbf{r})}{\partial\lambda}\psi_n(\mathbf{r}) \tag{4.8.6}$$

where the nonlocal operator K_{nm} is defined

$$\left(K_{nm}\frac{\partial\psi_m}{\partial\lambda}\right)(\mathbf{r}) = 4\int \psi_n(\mathbf{r})\left(\frac{e^2}{|\mathbf{r}-\mathbf{r}'|} + \frac{\delta v_{\text{sc}}(\mathbf{r})}{\delta n(\mathbf{r}')}\right)\psi_m^*(\mathbf{r}')\frac{\partial\psi_m}{\partial\lambda}(\mathbf{r}')\mathrm{d}\mathbf{r}' \tag{4.8.7}$$

This large linear system can be solved with iterative methods yielding a solution that is equivalent to the self-consistent solution of the smaller linear system of the linearised Kohn–Sham Hamiltonian (4.8.2). This approach forms the basis of DFPT, in which for example, the interatomic force constant matrices (IFCs) are calculated at the minima of suitable functionals.

4.9 Phonon Modes in Crystals

In a crystalline solid, the position of the I^{th} atom is

$$\mathbf{R}_I = \mathbf{R}_l + \boldsymbol{\tau}_\kappa = l_1\mathbf{a}_1 + l_2\mathbf{a}_2 + l_3\mathbf{a}_3 + \boldsymbol{\tau}_\kappa$$

where $\mathbf{R}_l$ is the position of the l^{th} unit cell and $\boldsymbol{\tau}_\kappa$ is the equilibrium position of the κ^{th} atom in the unit cell. The unit cell can be written as the sum of three primitive translation vectors $\mathbf{a}_1$, $\mathbf{a}_2$ and $\mathbf{a}_3$ with integer coefficients $l \equiv \{l_1, l_2, l_3\}$. The electronic states can be classified by their wave-vector $\mathbf{k}$ and band index ν

$$\psi_n(\mathbf{r}) \equiv \psi_{\nu,\mathbf{k}}(\mathbf{r})$$
$$\psi_{\nu,\mathbf{k}}(\mathbf{r}+\mathbf{R}_l) = e^{i\mathbf{k}\cdot\mathbf{R}_l}\psi_{\nu,\mathbf{k}}(\mathbf{r})$$

Normal modes (phonons) can also be classified by a wave-vector $\mathbf{q}$ and mode index j. Phonon frequencies $\omega(\mathbf{q})$ and displacement patterns $U_\kappa^\alpha(\mathbf{q})$ are determined by the secular equation

$$\sum_{\alpha_2,\kappa_2}\left(\widetilde{C}_{\kappa_1\kappa_2}^{\alpha_1\alpha_2}(\mathbf{q}) - M_{\kappa_1}\omega^2(\mathbf{q})\delta_{\alpha_1\alpha_2}\delta_{\kappa_1\kappa_2}\right)U_{\kappa_2}^{\alpha_2}(\mathbf{q}) = 0$$

The *dynamical matrix* $\widetilde{C}_{\kappa_1\kappa_2}^{\alpha_1\alpha_2}(\mathbf{q})$ is the Fourier transform of the real-space interatomic force constants (IFCs)

$$\widetilde{C}^{\alpha_1\alpha_2}_{\kappa_1\kappa_2}(\mathbf{q}) = \sum_l e^{-i\mathbf{q}\cdot\mathbf{R}_l} C^{\alpha_1\alpha_2}_{\kappa_1\kappa_2}(\mathbf{R}_l)$$

where the latter were defined as

$$C^{\alpha_1\alpha_2}_{\kappa_1\kappa_2}(\mathbf{R}_l - \mathbf{R}_m) = \frac{\partial^2 E}{\partial u^{\alpha_1}_{\kappa_1}(l)\partial u^{\alpha_2}_{\kappa_2}(m)}$$

and $\mathbf{u}_\kappa(l)$ is the displacement from the equilibrium position for atom κ in the l^{th} unit cell

$$\mathbf{u}_\kappa(l) = \mathbf{R}_I - \mathbf{R}_l - \boldsymbol{\tau}_\kappa.$$

Due to translational invariance the IFCs depend on l and m only through the difference $\mathbf{R}_l - \mathbf{R}_m$. The derivatives of the total energy with respect to atomic displacements are evaluated at the equilibrium positions, $\mathbf{u}_\kappa(l)$ for all atoms. The dynamical matrix can be written as the second derivative of the energy with respect to lattice distortions with wave-vector $\mathbf{q}$

$$\widetilde{C}^{\alpha_1\alpha_2}_{\kappa_1\kappa_2}(\mathbf{q}) = \frac{1}{N}\frac{\partial^2 E}{\partial u^{\alpha_1}_{\kappa_1}(\mathbf{q})^* \partial u^{\alpha_2}_{\kappa_2}(\mathbf{q})}$$

where N is the number of unit cells in the crystal and $\mathbf{u}_\kappa(\mathbf{q})$ is the amplitude of the lattice distortion

$$\mathbf{u}_\kappa(l) = \mathbf{u}_\kappa(\mathbf{q}) e^{i\mathbf{q}\cdot\mathbf{R}_l}$$

In the *frozen-phonon* method, the calculation of the dynamical matrix at arbitrary $\mathbf{q}$-points in the Brillouin zone requires the use of multiple unit cells or super-cells so that a wave-vector $\mathbf{q}$ is one of the reciprocal-lattice vectors. This limits the practicability of the method since the computational cost increases as the cube of the number of atoms.

The dynamical matrix can be split into electronic and ionic contributions

$$\widetilde{C}^{\alpha_1\alpha_2}_{\kappa_1\kappa_2}(\mathbf{q}) = {}^{\text{el}}\widetilde{C}^{\alpha_1\alpha_2}_{\kappa_1\kappa_2}(\mathbf{q}) + {}^{\text{ion}}\widetilde{C}^{\alpha_1\alpha_2}_{\kappa_1\kappa_2}(\mathbf{q})$$

The electronic contribution is

$$\begin{aligned} {}^{\text{el}}\widetilde{C}^{\alpha_1\alpha_2}_{\kappa_1\kappa_2}(\mathbf{q}) = \frac{1}{N}\Bigg[& \int \left(\frac{\partial n(\mathbf{r})}{\partial u^{\alpha_1}_{\kappa_1}(\mathbf{q})}\right)^* \frac{\partial V_{\text{el-ion}}(\mathbf{r})}{\partial u^{\alpha_2}_{\kappa_2}(\mathbf{q})} \mathrm{d}\mathbf{r} \\ & + \delta_{\kappa_1\kappa_2} \int n(\mathbf{r}) \frac{\partial^2 V_{\text{el-ion}}(\mathbf{r})}{\partial u^{\alpha_1}_{\kappa_1}(\mathbf{q}=0)^* \partial u^{\alpha_2}_{\kappa_2}(\mathbf{q}=0)} \mathrm{d}\mathbf{r} \Bigg]. \end{aligned} \tag{4.9.1}$$

The ionic contribution is the second derivative of the ionic electrostatic energy

$${}^{\text{ion}}\widetilde{C}^{\alpha_1\alpha_2}_{\kappa_1\kappa_2}(\mathbf{q}) = \frac{\partial^2 E_N(\mathbf{R})}{\partial \mathbf{R}_I \partial \mathbf{R}_J}$$

and does not depend on the electronic configuration. The first term in (4.9.1) depends on the linear response of the charge density to a lattice distortion and a perturbing potential characterized by a wave-vector $\mathbf{q}$

$$\frac{\partial V_{\text{el-ion}}(\mathbf{r})}{\partial \mathbf{u}_\kappa(\mathbf{q})} = -\sum_l \frac{\partial v_\kappa(\mathbf{r}-\mathbf{R}_l-\boldsymbol{\tau}_\kappa)}{\partial \mathbf{r}} e^{i\mathbf{q}\cdot\mathbf{R}_l}.$$

The advantage of DFPT is that the response to a monochromatic perturbation is also monochromatic with the same wave-vector $\mathbf{q}$ due to the linearity of the DFPT equations with respect to a perturbing potential. Thus, the dynamical matrices can be calculated for any arbitrary $\mathbf{q}$-vector without needing to use super-cells. Real-space IFCs can be obtained by Fourier transforming the dynamical matrices, calculated on a uniform grid of q-points in the Brillouin zone. Once the IFCs have been calculated, the dynamical matrices can be calculated at any $\mathbf{q}$-point by inverse Fourier transforms. This technique of *Fourier interpolation* will be used extensively in subsequent chapters to calculate the phonon eigenfrequencies on very fine grids of $\mathbf{q}$-points.

4.10 Long-Wavelength Phonons and Electric Fields

Phonons in the long-wavelength limit ($\mathbf{q} \to 0$) are associated with macroscopic polarization and electric fields due to long-range Coulomb forces. The observed splitting of the longitudinal optic (LO) and transverse optic (TO) phonons at the zone-centre ($\mathbf{q} = 0$) in polar insulators is a classic example of this. Many properties of an infinite periodic solid are ill-defined in the long-wavelength limit such as the response of the electron density to a macroscopic electric field, since an electrostatic potential describing an electric field $V_{\text{R}} = e\mathbf{E}\cdot\mathbf{r}$ is incompatible with periodic boundary conditions. Recently, the *modern theory of electric polarization* [14, 15] has revolutionized the field, however a more traditional approach using perturbation theory is still valid because the problems of macroscopic electric fields are absent in the linear regime and so the polarization response to an electric field or a lattice distortion is still well defined.

In the long-wavelength limit the energy as a function of atomic displacements and macroscopic electric field $\mathbf{E}$ is [16]

$$\mathcal{E}(\{\mathbf{u}\},\mathbf{E}) = \frac{1}{2}\sum_{\kappa_1\kappa_2}\sum_{\alpha_1\alpha_2}\mathbf{u}_{\kappa_1}\cdot{}^{\text{an}}\widetilde{C}_{\kappa_1\kappa_2}\cdot\mathbf{u}_{\kappa_2} - \frac{\Omega}{2}\mathbf{E}\cdot\boldsymbol{\varepsilon}_\infty\cdot\mathbf{E} - e\sum_{\kappa_1}\mathbf{u}_{\kappa_1}\cdot\mathbf{Z}^*_{\kappa_1}\cdot\mathbf{E} \quad (4.10.1)$$

where Ω is the volume of the unit cell, $\boldsymbol{\varepsilon}_\infty$ is the electronic dielectric tensor, $\boldsymbol{Z}^*_\kappa$ is the *Born effective charge* tensor for atom κ and ${}^{\text{an}}\widetilde{\mathbf{C}}$ is the dynamical matrix at $q = 0$ for vanishing electric field. The polarization induced by a longitudinal phonon in the long-wavelength limit produces a macroscopic electric field which applied a force on the ions and changes the phonon frequency. This is the cause of LO-TO splitting

in polar materials. The expression for the total energy including an electric field, (4.10.1) can be minimized to produce another expression that only depends on the atomic displacements and defines a dynamical matrix with an additional non-analytic contribution

$$\widetilde{C}^{\alpha_1\alpha_2}_{\kappa_1\kappa_2}(\mathbf{q}) = {}^{\text{an}}\widetilde{C}^{\alpha_1\alpha_2}_{\kappa_1\kappa_2}(\mathbf{q}) + {}^{\text{na}}\widetilde{C}^{\alpha_1\alpha_2}_{\kappa_1\kappa_2}(\mathbf{q})$$

where

$${}^{\text{na}}\widetilde{C}^{\alpha_1\alpha_2}_{\kappa_1\kappa_2}(\mathbf{q}) = \frac{e^2}{\Omega}\frac{(\mathbf{q}\cdot\mathbf{Z}^*_{\kappa_1})_{\alpha_1}(\mathbf{q}\cdot\mathbf{Z}^*_{\kappa_2})_{\alpha_2}}{\mathbf{q}\cdot\boldsymbol{\varepsilon}_\infty\cdot\mathbf{q}}.$$

The non-analytic part of the dynamical matrix exhibits non-analytic behaviour in the limit $\mathbf{q}\to 0$, resulting in IFCs with a long-range interatomic dependence due to dipole–dipole interactions. Due to this non-analytic behaviour, the Fourier interpolation method is modified by subtracting a function of $\mathbf{q}$ with the same $\mathbf{q}\to 0$ limit as the non-analytic part from the dynamical matrices in q-space. This removes the long-range dependence from the IFCs and makes them more suitable for Fourier transformation, restoring the previously subtracted non-analytical term to the real-space IFCs.

The microscopic description of the Born effective charges $\boldsymbol{Z}^*$ and $\boldsymbol{\varepsilon}_\infty$ are provided from (4.10.1). The electric induction is

$$\mathbf{D} = -\frac{1}{\Omega}\frac{\partial\mathcal{E}}{\partial\mathbf{E}} = \frac{e}{\Omega}\sum_\kappa \mathbf{Z}^*_\kappa\cdot\mathbf{u}_\kappa + \boldsymbol{\varepsilon}_\infty\mathbf{E}.$$

The macroscopic polarization $\mathbf{P}$, defined by $\mathbf{D}=\mathbf{E}+4\pi\mathbf{P}$ leads to a description for the Born effective charge at zero electric field

$$Z^{*,\alpha\beta}_\kappa = \frac{\Omega}{e}\left.\frac{\partial P_\alpha}{\partial u^\beta_\kappa(\mathbf{q}=0)}\right|_{\mathbf{E}=0}.$$

The electronic dielectric tensor $\boldsymbol{\varepsilon}_\infty$ can be derived by taking the derivative of the polarization with respect to the electric field an equilibrium ionic geometry

$$\varepsilon^{\alpha\beta}_\infty = \delta_{\alpha\beta} + \left.\frac{\partial P_\alpha}{\partial E_\beta}\right|_{\mathbf{u}_\kappa(\mathbf{q}=0)=0}.$$

Using DFPT, $\mathbf{Z}^*$ and $\boldsymbol{\varepsilon}_\infty$ can be calculated without too much difficulty, for example

$$\frac{\partial P_\alpha}{\partial u^\beta_\kappa(\mathbf{q}=0)} = -\frac{e}{N\Omega}\int r\frac{\partial n(\mathbf{r})}{\partial u_\kappa(\mathbf{q}=0)}\mathrm{d}\mathbf{r} + \frac{e}{\Omega}Z_\kappa\delta_{\alpha\beta}.$$

Unfortunately this expression is ill-defined for an infinite crystal with periodic boundary conditions because $\mathbf{r}$ is not lattice periodic. However, the response of the electron charge density to a perturbation is only dependent on off-diagonal matrix elements,

as touched upon earlier in the discussion about the self-cancellation of occupied Kohn–Sham states. These matrix elements are well defined even for macroscopic electric fields, which can be seen if they are written in terms of the commutator between the unperturbed Hamiltonian, a lattice-periodic operator, and $\mathbf{r}$ which is not

$$\langle \psi_m \, |\mathbf{r}| \, \psi_n \rangle = \frac{\langle \psi_m \, |[H_{\mathrm{scf}}, \mathbf{r}]| \, \psi_n \rangle}{\epsilon_m - \epsilon_n}$$

The quantity $\left|\bar{\psi}_n^{\alpha}\right\rangle = r_\alpha \, |\psi_n\rangle$ can be introduced, resulting in

$$(H_{\mathrm{scf}} - \epsilon_n) \left|\bar{\psi}_n^{\alpha}\right\rangle = P_c[H_{\mathrm{scf}}, r_\alpha] \, |\psi_n\rangle$$

where

$$P_c = 1 - \sum_{n=1}^{N/2} |\psi_n\rangle \, \langle \psi_n|$$

is the projector onto the manifold of occupied states. The commutator is related to the momentum operator

$$[H_{\mathrm{scf}}, \mathbf{r}] = -\frac{\hbar^2}{m} \frac{\partial}{\partial \mathbf{r}},$$

if the self-consistent potential is local. The final result for the effective charges is now

$$Z_{\kappa}^{*\alpha\beta} = Z_\kappa + \frac{4}{N} \sum_{n=1}^{N/2} \left\langle \bar{\psi}_n^{\alpha} \left| \frac{\partial \psi_n}{\partial u_\beta(\mathbf{q} = 0)} \right. \right\rangle.$$

Calculation of ε_∞ considers the response of an insulating crystal to an electric field $\mathbf{E}$ described by the non-lattice-periodic potential $V(\mathbf{r}) = e\mathbf{E} \cdot \mathbf{r}$. The same method as the effective charges can be applied, by replacing all occurrences of $\mathbf{r} \, |\psi_n\rangle$ with $\left|\bar{\psi}_n^{\alpha}\right\rangle$. The simplest way of calculating ε_∞ is to keep the electric field $\mathbf{E}$ fixed and to iterate on the potential

$$\frac{\partial V_{\mathrm{scf}}(\mathbf{r})}{\partial \mathbf{E}} = \frac{\partial V(\mathbf{r})}{\partial \mathbf{E}} + \int \left(\frac{e^2}{|\mathbf{r} - \mathbf{r}'|} + \frac{\delta v_{\mathrm{xc}}(\mathbf{r})}{\delta n(\mathbf{r}')} \right) \frac{\partial n(\mathbf{r}')}{\partial \mathbf{E}} \mathrm{d}\mathbf{r}'.$$

Finally, one obtains

$$\varepsilon_{\infty}^{\alpha\beta} = \delta_{\alpha\beta} - \frac{4e}{N\Omega} \sum_{n=1}^{N/2} \left\langle \bar{\psi}_n^{\alpha} \left| \frac{\partial \psi_n}{\partial E_\beta} \right. \right\rangle.$$

Effective charges can also be calculated from the response to an electric field, since they are proportional to the force acting on an ion under an applied electric field. Alternative approaches to the calculation of effective charges and dielectric tensors that do not use perturbation theory have recently been developed in the *modern*

theory of polarization. Effective charges are calculated by taking finite differences of the macroscopic polarization with respect to atomic displacements. Macroscopic polarization is expressed in terms of a topological quantity known as *Berry's phase* [14, 15]. The dielectric tensor can also be calculated using this method by performing finite electric field calculations. The linear response DFPT method and Berry's phase approach yield similar results with the same level of accuracy.

4.11 Implementation

The original and most prevalent implementations of DFT and DFPT are based on the plane-wave pseudopotential (PW-PP) method [17]. Plane-waves have many features that make them attractive: simplicity, orthonormality and the availability of the fast Fourier transform (FFT) algorithm to quickly transform between reciprocal space and real space. An important feature is the absence of Pulay forces [18] that localized basis-set implementations suffer from if their basis set is incomplete. Forces calculated from the Hellmann–Feynman expressions in the PW-PP method do not require any correction. Plane-waves are used with pseudopotentials, a fictitious ion–electric interaction potential which only acts on valence band electrons and mimics the interaction with core electrons. Norm-conserving pseudopotentials (Hamann, Schlüter, Chiang) [19] are uniquely determined by the properties of an isolated atom, whilst the requirement of norm conservation ensures that the pseudopotentials are transferable. That is, the ability of the pseudopotentials to describe a system that is independent of the local chemical environment of the atoms. The pseudopotential approximation assumes that the energy functional is linear with respect to the partitioning of charge into the core and valence states, which works well for most systems. However, in some cases such as alkali atoms, a non-linear core correction [20] can be applied and has proven to be very successful. For computations, the angular momentum part of a pseudopotential can be recast into a *separable* Kleinman and Bylander form [21], consisting of a sum over a few projectors. Norm-conserving pseudopotentials incorporate angular momentum and are thus nonlocal operators, so special care must be taken to ensure that atomic valence band wave functions are sufficiently smooth in the atomic core so that they can be used effectively in a plane-wave basis. The nonlocal term

$$V_{\text{el-ion}}^{\text{NL}}(\mathbf{r}, \mathbf{r}') = \sum_{\kappa,l} \sum_{n,m} D_{nm} \beta_n^*(\mathbf{r} - \mathbf{R}_l - \tau_\kappa) \beta_m(\mathbf{r}' - \mathbf{R}_l - \tau_\kappa).$$

requires some straightforward modifications to the DFT/DPFT equations. Further modifications are necessary for non-linear core corrections and *ultrasoft* pseudopotentials. Together, the use of plane-waves, separable pseudopotentials, FFT algorithms and iterative diagonalization or minimization techniques allows for efficient and quick solution of the Kohn–Sham equations for systems up to a few hundred

atoms. The technical implementations of solving the Kohn–Sham equations in the PW-PP method have been described extensively in the literature by Picket [17], Payne et al. [22] and Giannozzi [23] amongst others.

4.12 The Lydanne-Sachs-Teller Relation

In polar materials the long-range Coulomb forces produce macroscopic electric fields in the long-wavelength limit that affect longitudinal optic (LO) modes. Born and Huang [1] developed a phenomenological model describing how zone-centre optical phonons couple with macroscopic electric fields. The most general expression of the energy as a function of optical phonon coordinates and electric field is

$$\mathcal{E}(\mathbf{u}, \mathbf{E}) = \frac{1}{2} M \omega_0^2 u^2 - \frac{\Omega}{2} \varepsilon_\infty E^2 - eZ^* \mathbf{u} \cdot \mathbf{E}$$

where $\mathbf{u}$ is the atomic displacement, $\mathbf{E}$ is the electric field, M is the reduced mass, Ω is the unit cell volume, ε_∞ is the electronic permittivity and Z^* is the Born effective charge of the ions, which describes the coupling between the displacements and the electric field.

The conjugates to the displacement $\mathbf{u}$ and electric field $\mathbf{E}$ are the force acting on the ions, $\mathbf{F}$ and the electric induction $\mathbf{D}$:

$$\mathbf{F} = -\frac{\partial \mathcal{E}}{\partial \mathbf{u}} = -M\omega_0^2 \mathbf{u} + eZ^* \mathbf{E}$$
$$\mathbf{D} = -\frac{1}{\Omega} \frac{\partial \mathcal{E}}{\partial \mathbf{E}} = \frac{e}{\Omega} Z^* \mathbf{u} + \varepsilon_\infty \mathbf{E}.$$

For a medium with no free charges and a static electric field, Maxwell's equations yield $\nabla \cdot \boldsymbol{D} = 0$ and $\nabla \times \boldsymbol{D} = 0$, and since atomic displacement have a spatial dependence $e^{i\mathbf{q}\cdot\mathbf{r}}$ become

$$i\mathbf{q} \cdot \boldsymbol{D} = 0,$$
$$i\mathbf{q} \times \boldsymbol{D} = 0.$$

Transverse optic (TO) modes have atomic displacements perpendicular to the wave-vector $\mathbf{q}$, so that $i\mathbf{q} \cdot \mathbf{u}_\mathrm{T} = 0$ and $\mathbf{E} = 0$. The force on the atoms for the TO mode is therefore $\mathbf{F} = -M\omega_0^2 \mathbf{u}$ and so the transverse optic phonon frequency is $\omega_\mathrm{TO} = \omega_0$. Longitudinal optic (LO) modes have atomic displacements parallel to the wave-vector $\mathbf{q}$, so that $i\mathbf{q} \times \mathbf{u}_\mathrm{L} = 0$ and the electric field is

$$\mathbf{E} = -\frac{e}{\Omega \varepsilon_\infty} Z^* \mathbf{u}.$$

The force on the atoms for the LO mode is therefore

$$\mathbf{F} = -M\left(\omega_0^2 + \frac{e^2 Z^{*2}}{\Omega \varepsilon_\infty M}\right)\mathbf{u},$$

with the atoms vibrating with frequency ω_{LO}

$$\omega_{\mathrm{LO}} = \sqrt{\omega_0^2 + \frac{e^2 Z^{*2}}{\Omega \varepsilon_\infty M}}.$$

The LO phonons clearly have a higher frequency than the TO phonons due to the macroscopic electric field and since the static permittivity ε_0 can be expressed as [1]

$$\varepsilon_0 = \varepsilon_\infty + \frac{e^2 Z^{*2}}{\Omega M \omega_{\mathrm{TO}}^2},$$

leads to a very simple relationship between the static and electronic permittivity and the frequencies of the transverse and longitudinal optic phonons

$$\frac{\varepsilon_0}{\varepsilon_\infty} = \frac{\omega_{\mathrm{LO}}^2}{\omega_{\mathrm{TO}}^2}.$$

This is known as the *Lyddane–Sachs–Teller* relation [24] and is exact for isotropic cubic and tetrahedral systems. It can be generalized to any crystal symmetry [25] with numerous optic modes as a function of field frequency

$$\frac{\varepsilon(\omega)}{\varepsilon_\infty} = \frac{\prod_k^{LO}(\omega_k^2 - \omega^2)}{\prod_j^{TO}(\omega_j^2 - \omega^2)},$$

where ω_k are the longitudinal optic (LO) modes and ω_j are the transverse optic modes.

4.13 Summary and Conclusions

This chapter has reviewed the basic theory of density functional perturbation theory with regards to calculating dynamical matrices and phonon frequencies in the harmonic approximation and taking long-wavelength macroscopic electric fields into account. Furnished with values for the Born effective charges $\mathbf{Z}_\kappa^*$ and dielectric tensors $\boldsymbol{\varepsilon}_\infty$, the frequencies of the long-wavelength zone-centre optic phonons can be calculated, thus enabling the static low-frequency relative permittivity to be evaluated using the Lyddane–Sachs–Teller relation. Being able to also calculate the dynamical

matrices, phonon eigenmodes and eigenfrequencies at any arbitrary **q**-point in the Brillouin zone provides valuable information for a theory of dielectric loss on where transitions between phonon branches can occur.

References

1. M. Born, K. Huang, *Dynamical Theory of Crystal Lattices*, 1st ed. (Oxford University Press, Oxford, 1954)
2. P.D. De Cicco, F.A. Johnson, The quantum theory of lattice dynamics IV. Proc. R. Soc. Lond. A. **310**, 111 (1969)
3. R. Pick, M.H. Cohen, R.M. Martin, Microscopic theory of force constants in the adiabatic approximation. Phys. Rev. B **1**, 910 (1970)
4. P. Hohenberg, W. Kohn, Inhomogeneous electron gas. Phys. Rev. **136**, B864 (1964)
5. W. Kohn, L.J. Sham, Self-consistent equations including exchange and correlation effects. Phys. Rev. **140**, A1133 (1965)
6. S. Baroni, R. Resta, Ab initio calculation of the macroscopic dielectric constant in silicon. Phys. Rev. B **33**, 7017 (1986)
7. M. Born, J.R. Oppenheimer, Zur Quantentheorie der Molekeln. Annelen der Physik **389**, 457 (1927)
8. D.M. Ceperley, B.J. Alder, Exchange-correlation potential and energy for density-functional calculation. Phys. Rev. Lett. **45**, 567 (1980)
9. J.P. Perdew, A. Zunger, Self-interaction correction to density-functional approximations for many-electron systems. Phys. Rev. B **23**, 5048 (1981)
10. S. Baroni, P. Giannozzi, A. Testa, Green's-function approach to linear response in solids. Phys. Rev. Lett. **58**, 1861 (1987)
11. X. Gonze, Adiabatic density-functional perturbation theory. Phys. Rev. A **52**, 1096 (1995)
12. X. Gonze, Perturbation expansion of variational principles at arbitrary order. Phys. Rev. A **52**, 1086 (1995)
13. D. Bohm, *Quantum Theory* (Prentice Hall, New Jersey, 1951)
14. D. Vanderbilt, R.D. King-Smith, Electric polarization as a bulk quantity and its relation to surface charge. Phys. Rev. B **48**, 4442 (1993)
15. R. Resta, Macroscopic polarization in crystalline dielectrics: the geometrical phase approach. Rev. Mod. Phys. **66**, 899 (1994)
16. S. Baroni et al., Phonons and related crystal properties from density-functional perturbation theory. Rev. Mod. Phys. **73**, 515 (2001)
17. W.E. Pickett, Pseudopotential methods in condensed matter applications. Comput. Phys. Rep. **9**, 115 (1989)
18. P. Pulay, Ab initio calculation of force constants and equilibrium geometries in polyatomic molecules: I. Theory. Mol. Phys. **17**, 197 (1969)
19. D. Hamann, M. Schlüter, C. Chiang, Norm-conserving pseudopotentials. Phys. Rev. Lett. **43**, 1494 (1979)
20. S.G. Louie, S. Froyen, M.L. Cohen, Nonlinear ionic pseudopotentials in spin-density-functional calculations. Phys. Rev. B **26**, 1738 (1982)
21. L. Kleinman, D.M. Bylander, Efficacious form for model pseudopotentials. Phys. Rev. Lett. **48**, 1425 (1982)
22. M.C. Payne et al., Iterative minimization techniques for ab initio total-energy calculations: molecular dynamics and conjugate gradients. Rev. Mod. Phys. **64**, 1045 (1992)
23. P. Giannozzi, in *Computational Approaches to Novel Condensed Matter Systems: Applications to Classical and Quantum Systems*, ed. by D. Neilson, M. Das (Plenum, 1995), p. 67
24. R.H. Lyddane, R.G. Sachs, E. Teller, On the polar vibrations of alkali halides. Phys. Rev. **59**, 673 (1941)
25. H. Böttger, *Principles of the Theory of Lattice Dynamics* (Physik-Verlag, 1983)

Chapter 5
Harmonic Properties of Metal Oxide Dielectrics

The advent of quantum mechanical codes implementing density functional theory within the local density approximation for periodic systems has made it possible to predict their properties *ab-initio*, without the use of empirical data. This chapter will use these invaluable tools to calculate some of the properties of microwave dielectric ceramics. Calculation of the complex permittivity of a material at microwave frequencies requires knowledge of harmonic properties such as phonon eigenfrequencies, Born effective charges and electronic permittivity. This chapter will report detailed modelling of the crystal structure and harmonic lattice dynamical properties of MgO, $LaAlO_3$, TiO_2 and Al_2O_3 using density functional perturbation theory (DFPT). For each material the convergence of the ground-state energy with respect to plane-wave cut-off energy and electronic k-point sampling will be investigated. The equilibrium crystal structure and lattice parameters will then be found by minimization of the total energy with respect to lattice parameter and the ionic positions. Phonon dispersion relations and the response to electric fields will be used to calculate the low-frequency permittivity of each material and then compared to low-temperature experimental data. The calculations were performed using freely available quantum mechanical codes within the QUANTUM ESPRESSO suite of packages [1].

5.1 Magnesium Oxide — MgO

Magnesium oxide (MgO) commonly occurs in the earth's mantle and is therefore a well-studied material, both experimentally and theoretically, where most work has focused upon its high-pressure properties. It is stabled-up to pressures of 500 GPa whereupon it undergoes a phase transition from the rock salt structure to the CsCl structure. The face-centred cubic (FCC) rock-salt crystal structure and its primitive unit cell are shown in Fig. 5.1. It has space group $Fm\bar{3}m$ (225) and point group O_h (Pm3m). The primitive unit cell contains a single MgO formula (two atoms) with lattice vectors

J. Breeze, *Temperature and Frequency Dependence of Complex Permittivity in Metal Oxide Dielectrics: Theory, Modelling and Measurement*, Springer Theses, DOI 10.1007/978-3-319-44547-2_5

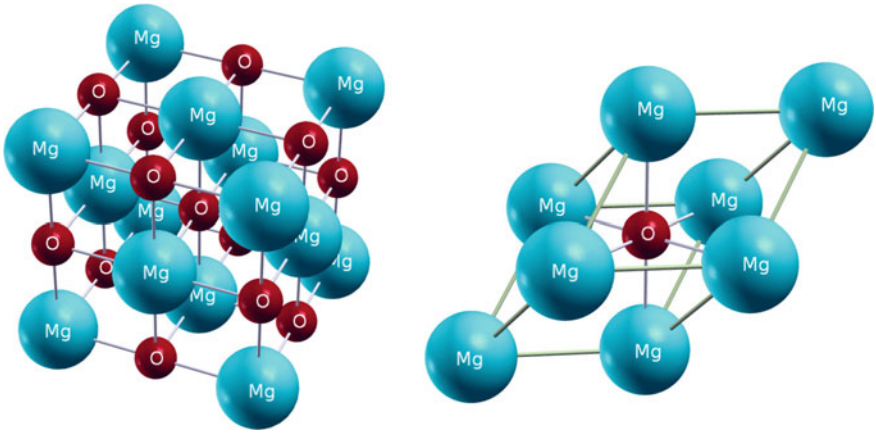

Fig. 5.1 Crystal structure (*left*) and primitive unit cell (*right*) of MgO

Table 5.1 Naturally occurring isotopes of Magnesium and Oxygen

Isotope	Abundance [%]	Atomic weight [amu]
^{12}Mg	78.990	23.985
^{13}Mg	10.000	24.986
^{14}Mg	11.010	25.983
^{8}O	99.756	15.9949
^{9}O	0.039	16.9991
^{10}O	0.205	17.9992

$$\mathbf{a}_1 = \tfrac{1}{2}a_0 \begin{pmatrix} 0 \\ 1 \\ 1 \end{pmatrix}, \quad \mathbf{a}_2 = \tfrac{1}{2}a_0 \begin{pmatrix} 1 \\ 0 \\ 1 \end{pmatrix}, \quad \mathbf{a}_3 = \tfrac{1}{2}a_0 \begin{pmatrix} 1 \\ 1 \\ 0 \end{pmatrix}.$$

The basis vectors $\boldsymbol{\tau}_i$ of the Mg and O atoms, labelled by $i = 1$ and $i = 2$, respectively, are $\boldsymbol{\tau}_1 = (0, 0, 0)$ and $\boldsymbol{\tau}_2 = (\frac{1}{2}, \frac{1}{2}, \frac{1}{2})$. Due to its simplicity and practical use, MgO is a natural choice for the application of a general theory of dielectric loss since the computational time for plane-wave DFPT calculations scale cubically with the number of atoms per unit cell. Both magnesium and oxygen atoms are isotopic occurring in nature with the abundances as shown in Table 5.1. The mean atomic masses of Mg and O are 24.3051 and 15.9994 amu, with variances of 0.437 and 0.009 amu. Whilst the isotopic variance of O is small, that of Mg is appreciable.

Electronic Structure

The pseudopotentials for Mg and O used the Perdew–Zunger exchange-correlation functional [2] within the local density approximation (LDA) (Table 5.2). They were constructed using the norm-conserving Martins–Troullier method [3] with a nonlinear core correction added to the Mg pseudopotential. The plane-wave cut-off energy

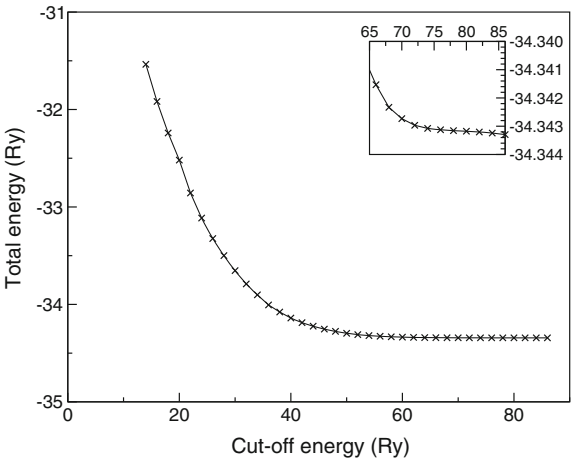

Fig. 5.2 Energy convergence as a function of plane-wave cut-off energy E_c for MgO. Convergence of the total energy occurs for $E_c > 75$ Ry

Table 5.2 Pseudopotentials for Mg and O. The coordinate of maximum for wave functions, cut-off radius r_c and reference configurations

	$r_{\max}$ (a.u.)	r_c (a.u.)	Reference configuration
Magnesium			
$l = 0$	2.52	3.40	$3s^2$
$l = 1$	3.10	3.00	$3s^{1.25}3p^{0.25}$
Oxygen			
$l = 0$	0.87	1.60	$2s^2 2p^4$
$l = 1$	0.81	1.60	$3s^2 2p^4$

E_c
determines the number of plane waves per unit volume and the convergence of the total energy for MgO with respect to the cut-off energy E_c was determined in a straightforward manner by plotting the total energy as a function of E_c. The total energy as shown in Fig. 5.2 is seen to converge as E_c is increased.

The convergence criterion was a change in total energy per unit increase in cut-off energy E_c of less than 10^{-3} Ry. This occurred for a plane-wave cut-off energy, E_c of 75 Ry. An electronic k-space sampling of $8 \times 8 \times 8$ was found to give no discernible improvement over a k-space sampling of $4 \times 4 \times 4$ which was selected for further calculations.

Equilibrium Structure

The equilibrium lattice parameter a_0 for MgO was determined by minimising the total energy with respect to a_0. For a fixed electron cut-off energy E_c of 75 Ry, the plane-wave basis set depends on the volume but the real-space resolution remains the same for arbitrary lattice parameters, causing discontinuities in the total energy.

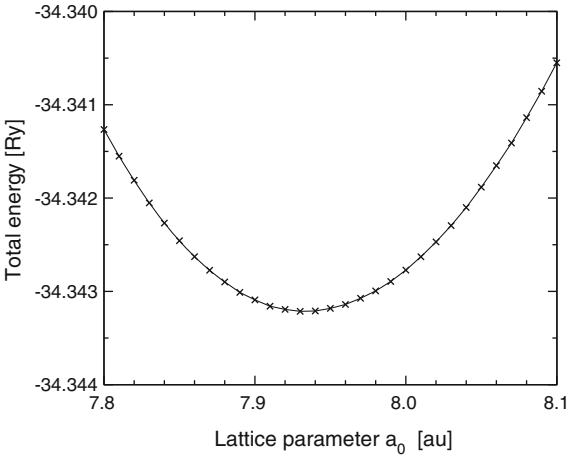

Fig. 5.3 Total energy as a function of lattice parameter a_0 for MgO. Plane-wave cut-off energy $E_c = 75$ Ry. A fit to Murnaghan's equation of state yields a minimum total energy for $a_0 = 7.934$ au (4.197 Å)

Table 5.3 Equilibrium lattice parameter a_0 and bulk modulus B_0 of MgO for plane-wave cut-off energy 75 Ry derived from fit to Muraghan's equation of state

	a_0 [au]	B_0 [Mbar]	B_0'
Theory [4]	7.87	1.62	4.2
Experiment [5]	7.97	1.64	
THIS WORK	7.934	1.694	4.21

The equilibrium lattice parameter a_0 was found by calculating the ground-state total energy for various values of a_0 (see Fig. 5.3) and subsequent fitting to Murnaghan's equation of state

$$P = \frac{B_0}{B_0'}\left[\left(\frac{\Omega_0}{\Omega}\right)^{B_0'} - 1\right]$$

where P is the pressure, B_0 is the bulk modulus, B_0' its derivative with respect to P and Ω is the unit cell volume. The results of the fit are shown in Table 5.3 where the fitted lattice parameter $a_0 = 7.934$ au is underestimated by 0.45 % compared to experiment, which is quite low for the discrepancy expected for the Local Density Approximation.

Lattice Dynamics and Phonons

The Brillouin zone for the reciprocal space of phonons in MgO is a body-centred truncated octahedron as shown in Fig. 5.4. Some of the special high-symmetry points are labelled $\Gamma = (0, 0, 0)$, $X = (0, 1, 0)$, $K = (\frac{3}{4}, \frac{3}{4}, 0)$ and $L = (\frac{1}{2}, \frac{1}{2}, \frac{1}{2})$. By virtue of the Hellman–Feynman theorem, first-order perturbation of the electronic wave functions yields the dynamical matrices which can be diagonalized to yield the phonon eigenfrequencies and eigenvectors. To calculate the eigenfrequencies and eigenvectors at arbitrary **q**-points within the Brillouin zone a Fourier interpolation technique is

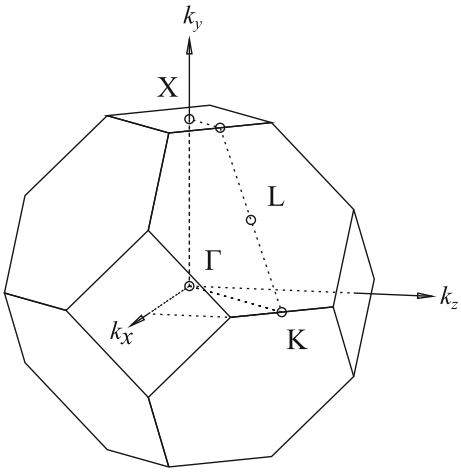

Fig. 5.4 Brillouin zone for a face-centred cubic crystal such as MgO

Table 5.4 8 special **q**-points from Monkhorst–Pack set for $4 \times 4 \times 4$ grid

	q_x	q_y	q_z	Weight
1	0	0	0	1
2	$-\frac{1}{4}$	$-\frac{1}{4}$	$\frac{1}{4}$	8
3	$-\frac{1}{2}$	$-\frac{1}{2}$	$\frac{1}{2}$	4
4	0	0	$\frac{1}{2}$	6
5	$-\frac{1}{4}$	$-\frac{1}{4}$	$\frac{3}{4}$	24
6	$-\frac{1}{2}$	$-\frac{1}{2}$	1	12
7	0	0	1	3
8	$-\frac{1}{2}$	0	1	6

employed. The dynamical matrices are calculated for the eight special **q**-points shown in Table 5.4, corresponding to the Monkhorst–Pack set [6] for the irreducible wedge of a $4 \times 4 \times 4$ grid. Three-dimensional complex Fourier transformation of the dynamical matrices results in the *interatomic force constant* (IFC) matrix. To calculate the dynamical matrices for an arbitrary **q**-point, an inverse three-dimensional complex Fourier transform of the interatomic force constant matrix is performed, the diagonalization of which (taking LO-TO splitting into account as $\mathbf{q} \to 0$) yields the phonon eigenfrequencies and eigenvectors. Calculated eigenfrequencies for phonons at **q**-points of high symmetry within the Brillouin zone presented in Table 5.5 appear to be in good agreement with experiment [5]. Modes are labelled by the high-symmetry point in the Brillouin zone (Γ, X, L) with subscripts denoting the type and polarization of the mode: transverse optic (TO), longitudinal optic (LO), transverse acoustic (TA) and longitudinal acoustic (LA). The frequency gap between the X_{LA} and X_{TO}

Table 5.5 Phonon frequencies (THz) at high-symmetry points Γ, X and L for MgO

	Theory [4] (THz)	Expt. [5] (THz)	THIS WORK (THz)
Γ_{TO}	11.72	12.23	12.31
Γ_{LO}	21.25	21.52	21.06
X_{TA}	8.62	8.96	8.63
X_{LA}	12.59	12.65	12.93
X_{TO}	13.37	13.29	13.70
X_{LO}	16.55	16.61	16.46
L_{TA}	8.20	8.64	8.55
L_{LA}	16.40		16.42
L_{TO}	10.71	11.05	10.83
L_{LO}	17.07		16.94

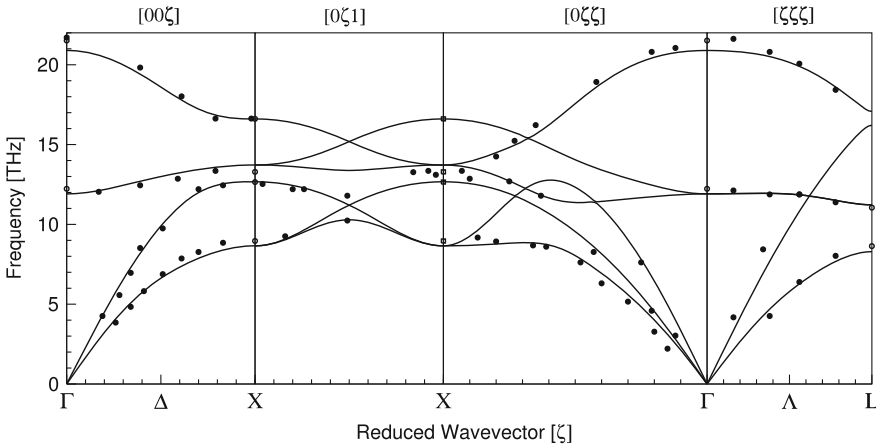

Fig. 5.5 Phonon dispersion curves for MgO. Filled circles are neutron diffraction data [5]

phonons of 0.77 THz (26 cm^{-1}) at the edge of the Brillouin zone is known to be due to the difference in effective mass of the sublattices. The frequency gap is relevant to the type of dielectric loss theory, such as the one proposed by Sparks, King and Mills [7] and others [8], involving the annihilation of a LA phonon and the creation of a TO phonon through the absorption of a microwave photon.

Phonon dispersion curves were generated using dynamical matrix Fourier interpolation along the $\Gamma - \Delta - X - X - \Gamma - L$ path across the Brillouin zone and as Fig. 5.5 shows, they are in very good agreement with neutron diffraction data [5]. Sound velocities in the crystal directions [001], [011] and [111] were calculated for small $\mathbf{q}$-vectors by taking the limit, $v = \frac{\partial \omega}{\partial \mathbf{q}}$ as $\mathbf{q} \rightarrow 0$. Results and comparison with other reported values are shown in Table 5.6.

Table 5.6 Sound velocities (10^5 ms^{-1}) for MgO along high-symmetry directions. v_L and v_T denote longitudinal and transverse velocities respectively. Experimental values are calculated from experimentally determined elastic constants and theoretical values are at a temperature of 0 °K

	[100]		[110]		[111]	
	v_L	v_T	v_L	v_T	v_L	v_T
Expt. Bogardus [9] (25 °C)	9.10	6.60	9.91	5.30	9.91	5.30
Expt. [5]	8.99	6.58	9.80	5.30	10.06	5.76
Theory [4]	9.22	6.47	9.81	5.52	10.01	5.85
THIS WORK	9.46	6.22	9.85	5.59	9.98	5.80

Phonon Density of States

The phonon density of states (DOS) $\rho(\omega)$ is defined such that there are $\rho(\omega)d\omega$ modes in the frequency range between ω and $\omega + d\omega$

$$\rho(\omega) = \sum_{j}^{3N} \int F(\mathbf{q}j)\delta\left(\omega - \omega_{\mathbf{q}j}\right) d\mathbf{q}$$

where $F(\mathbf{q}j)$ is a weighting function which is set to unity for this case. It is normalized so that its integral over the frequency domain is equal to the number of degrees of freedom

$$\int_0^\infty \rho(\omega)d\omega = 3N,$$

where N is the number of atoms in the unit cell and $3N$ is therefore the number of normal modes in the crystal. The phonon DOS provides information on regions in the frequency domain where the density of phonon modes is highest and is inversely proportional to the group velocity for a particular mode.

Figure 5.6 shows the phonon density of states for MgO. It was calculated using Blöchl's improved tetrahedron method of Brillouin zone integration [10] upon a $48 \times 48 \times 48$ grid covering the Brillouin zone (110,592 $\mathbf{q}$-points with weighting factor $F(\mathbf{q}j) = 1$). Near 8.6 THz there is a peak corresponding to zone-boundary transverse acoustic (TA) phonons at the L, X and K-points. From 10.8 to 13.7 THz there is a band where the density of states for transverse optic (TO) modes is high, followed by a lower band from 16.4 to 21.1 THz occupied by longitudinal optic (LO) modes. Setting the weighting factor to $F(\mathbf{q}j) = |e_\kappa(\mathbf{q}j)|^2$, where $e_\kappa(\mathbf{q}j)$ is the eigenvector for atom κ on phonon branch j with momentum $\mathbf{q}$, allows the phonon DOS to be projected onto individual phonon branches as shown in Fig. 5.7.

This demonstrates the degree of overlap in the DOS of different phonon branches, TA-TA and LA-TO for instance and also reveals the frequencies at which the critical points (where the DOS is discontinuous) exist.

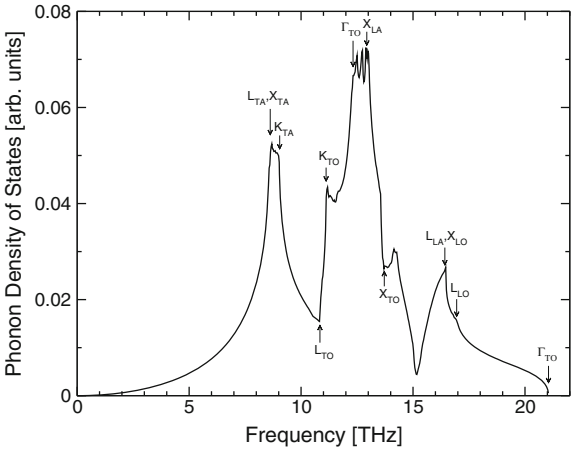

Fig. 5.6 Phonon density of states $\rho(\omega)$ for MgO, calculated over a $48 \times 48 \times 48$ **q**-point grid covering the Brillouin zone using Bröchl's improved tetrahedron method [10]

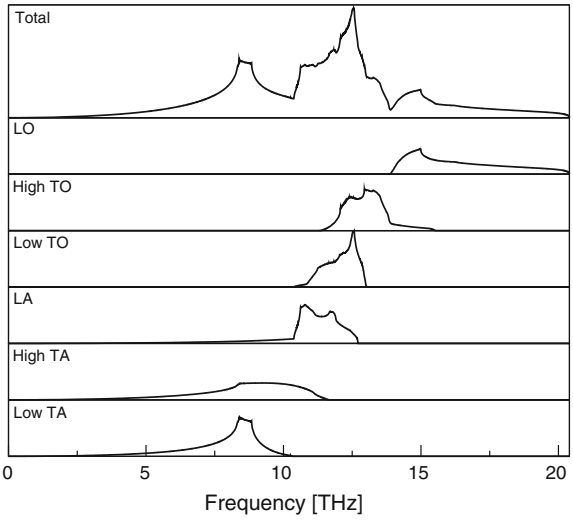

Fig. 5.7 Phonon density of states $\rho(\omega)$ of MgO for different polarization branches, calculated over a $48 \times 48 \times 48$ **q**-point grid covering the Brillouin zone using Bröchl's improved tetrahedron method [10]

The Born effective charges for Mg and O are $Z^*_{\mathrm{Mg}} = 1.922$ and $Z^*_{\mathrm{O}} = -2.027$ which shows that the bonding in MgO is highly ionic with very little dynamical charge transfer. The high frequency permittivity calculated by DFPT is $\varepsilon_\infty = 3.30$ which is slightly higher than the experimentally determined value of 2.93. The Lyddane–Sachs–Teller (LTS) relation [11] allows the low-frequency electric relative permittivity ε_0 to be calculated for MgO from the optical phonon frequencies

$$\varepsilon_0 = \varepsilon_\infty \frac{\omega^2_{\mathrm{LO}}}{\omega^2_{\mathrm{TO}}}, \tag{5.1.1}$$

where the longitudinal and transverse optical eigenfrequencies at the Γ point ($\mathbf{q} = 0$) have the values calculated in Table 5.5: $\omega_{\mathrm{LO}} = 21.06$ THz and $\omega_{\mathrm{TO}} = 12.3$ THz. The LTS relation yields a value for the static permittivity (at absolute zero temperature) of $\varepsilon_0 = 9.674$ which compares very favourably with the low-temperature measurement of $\varepsilon_0 = 9.651$ at a temperature of 15 K reported in Chap. 3.

5.2 Lanthanum Aluminate — $LaAlO_3$

Lanthanum aluminate is a popular choice of substrate for the growth of functional oxide thin-films due its high permittivity ($\varepsilon_r \sim 24$), low loss-tangent and suitable crystallographic parameters for the growth of perovskite oxides. Above a temperature of 500 °C, it has the ideal cubic (O_h^1) perovskite structure as shown in Fig. 5.8. Below 500 °C, it has a slightly rhombohedral structure ($D_{3d}^6 \equiv R\bar{3}c$), with a small distortion ($\alpha = 90.1°$). Since the distortion is so small, the low-temperature phase is usually regarded as pseudocubic and isotropic. However, the distortion does lead to twinning defects and accompanying oxygen vacancies in single crystals [12]. The cubic perovskite structure will be considered here.

Structure

The primitive unit cell contains five atoms: one lanthanum, one aluminium and three oxygens with position vectors $\boldsymbol{\tau}_{\mathrm{Al}} = \left(\frac{1}{2}, \frac{1}{2}, \frac{1}{2}\right)$, $\boldsymbol{\tau}_{\mathrm{La}} = (0, 0, 0)$, $\boldsymbol{\tau}_{\mathrm{O_1}} = \left(0, \frac{1}{2}, \frac{1}{2}\right)$, $\boldsymbol{\tau}_{\mathrm{O_2}} = \left(\frac{1}{2}, \frac{1}{2}, 0\right)$ and $\boldsymbol{\tau}_{\mathrm{O_3}} = \left(\frac{1}{2}, 0, \frac{1}{2}\right)$.

Ultrasoft Vanderbilt pseudopotentials were used in this study using the Perdew–Zunger exchange-correlation energy functional within the local density approximation (LDA). A plane-wave cut-off energy of $E_c = 40$ Ry was found to provide

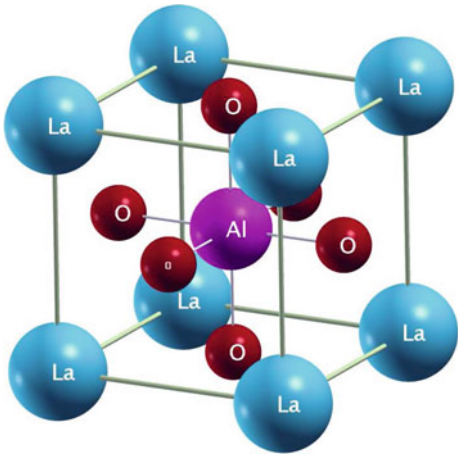

Fig. 5.8 Unit cell of lanthanum aluminate ($LaAlO_3$). It has a pseudocubic perovskite structure with a slight rhombohedral distortion ($\alpha = 90.1°$)

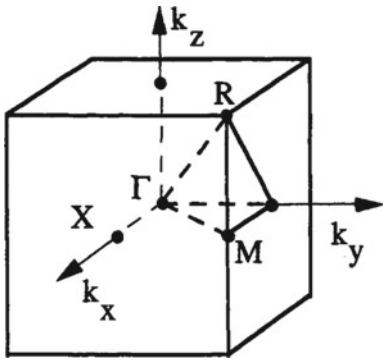

Fig. 5.9 Brillouin zone for simple cubic crystal such as $LaAlO_3$

adequate convergence of the total self-consistent energy. The ground-state lattice parameter a_0 was found by fitting Murnaghan's equation to be $a_0 = 7.090$ a.u.

Lattice Dynamical Properties

The Brillouin zone for the simple cubic phase of $LaAlO_3$ is shown in Fig. 5.9. Phonons at the special points Γ, X and M and along the path $\Gamma - X - M - \Gamma$ were calculated by diagonalizing the dynamical matrices and taking TO-LO splitting into account (see Table 5.7). They were found to be in good agreement with neutron diffraction data [13]. Phonon dispersion curves were calculated using Fourier interpolation of the interatomic force constants and are shown in Fig. 5.10 with experimental data determined from neutron diffraction [13]. $LaAlO_3$ has four degenerate optical phonon

Table 5.7 Phonon frequencies (cm^{-1}) at high-symmetry points Γ, X and M for $LaAlO_3$. Experimental values were from neutron diffraction data [13]

	Expt. [13] [cm^{-1}]	THIS WORK [cm^{-1}]
Γ_{TO}	186.0	184.3
Γ_{LO}		277.0
Γ_{silent}		309.8
Γ_{TO}		421.7
Γ_{LO}		587.3
Γ_{TO}		641.0
Γ_{LO}		707.6
M_{LA}	101.8	106.9
M_{TA}	139.3	140.5
M_{LO}	210.2	170.6
M_{TO}		322.3
X_{TA}	110.4	111.0
X_{LA}	209.2	212.1
X_{TO}	250.5	258.4
X_{LO}		351.3

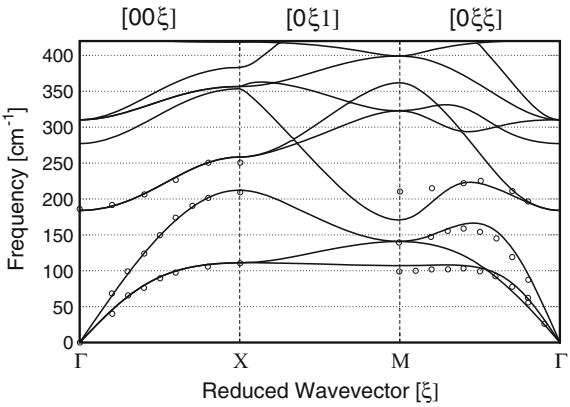

Fig. 5.10 Phonon dispersion diagram for Lanthanum Aluminate ($LaAlO_3$). Solid lines are from DFTP calculations and filled circles are neutron diffraction data [13]

modes, three of which are infrared active and contribute to the low-frequency relative permittivity. At the Γ point, the TO/LO frequencies of the modes are 184/277, 421/589 and 638/712 cm^{-1}. The low-frequency (static) relative permittivity can be readily calculated using the generalised Lyddane–Sachs–Teller relation

$$\varepsilon_r = \varepsilon_\infty \frac{\prod_k^{\mathrm{LO}} \omega_k^2}{\prod_j^{\mathrm{TO}} \omega_j^2}, \tag{5.2.1}$$

where the electronic permittivity was calculated to be $\varepsilon_\infty = 4.48$. The relative permittivity was calculated to be $\varepsilon_r = 24.12$, which compares favourably with the experimental value of $\varepsilon = 23.62$ measured using the dielectric resonator technique at a temperature of 10 K.

5.3 Titanium Dioxide (Rutile) — TiO_2

In its Rutile phase, titanium dioxide is an interesting material due to it having very high permittivity and a very high degree of anisotropy. It is often called paraelectric or an *incipient ferroelectric* due to the temperature dependence of its high relative permittivity. The Γ-point optical modes largely responsible for its high permittivity soften (reduce in frequency) considerably as the temperature is decreased but do not become imaginary, which signal a ferroelectric phase transition. The frequencies of the zone-centre optical phonons are highly sensitive to unit cell volume and pressure and would indeed become unstable (leading to ferroelectricity) if the lattice parameters were changed by a small amount [14].

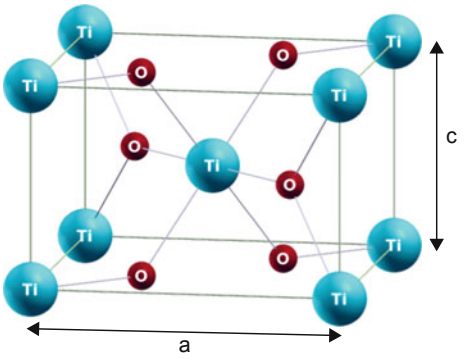

Fig. 5.11 Unit cell of Rutile TiO_2

Structure

Rutile has a tetragonal unit cell with D_{14}^{4h} symmetry and lattice parameters a and c. It contains six atoms (2 Ti, 4 O) as shown in Fig. 5.11. Ti atoms are situated at position vectors $\boldsymbol{\tau}_{\mathrm{Ti}_1} = (0, 0, 0)$ and $\boldsymbol{\tau}_{\mathrm{Ti}_2} = \left(\frac{1}{2}, \frac{1}{2}, \frac{1}{2}\right)$ and O atoms at $\boldsymbol{\tau}_{\mathrm{O}_1} = (u, u, 0)$, $\boldsymbol{\tau}_{\mathrm{O}_2} = (1-u, 1-u, 0)$, $\boldsymbol{\tau}_{\mathrm{O}_3} = \left(\frac{1}{2}-u, \frac{1}{2}+u, \frac{1}{2}\right)$ and $\boldsymbol{\tau}_{\mathrm{O}_4} = \left(\frac{1}{2}+u, \frac{1}{2}-u, \frac{1}{2}\right)$ where $u \approx 0.305$ is an internal coordinate. In this study, both ultrasoft Vanderbilt and norm-conserving pseudopotentials were used with Ceperley–Alder exchange-correlation energy functional within the local density approximation (LDA). Generalised gradient approximations were not used since they are known to predict phonon mode eigenfrequencies which are too soft and in some cases imaginary, leading to structural instability [14]. A plane-wave cut-off energy of 40 Ry was found to provide sufficient convergence of the ground-state energy. Electronic k-points were calculated on a (4, 4, 6) Monkhorst–Pack set shifted by (1, 1, 1) corresponding to nine points in the irreducible wedge of the Brillouin-zone. The lattice parameters a, c, unit cell volume v_0 and internal coordinate u were found by minimising the ground-state energy using the Broyden–Fletcher–Goldfarb–Shanno (BFGS) method of nonlinear optimization [15]. The results shown in Table 5.8 are in excellent agreement with experimentally determined data.

Born Effective Charges, Electronic Permittivity and Phonons

The dynamical matrices and phonon eigenmode frequencies and displacements were calculated at the Brillouin zone centre ($\mathbf{q} = 0$) and 23 other special $\mathbf{q}$-points ($4 \times 4 \times 6$ Monkhorst–Pack set) using the Hellman–Feynmann approach of density functional perturbation theory (DFPT). The Born effective charges and electronic permittivity were used to generated the LO-TO mode splitting when the mode frequencies were calculated from the dynamical matrices. Table 5.9 shows the calculated Born effective charges for titanium and oxygen to be in excellent agreement with the theoretical results of Lee et al. [18]. The Born effective charges are in some cases much higher than the nominal charges of Ti and O ions of $+4$ and -2 respectively, as high as $+7.581$ for Ti ions and -3.800 for O ions in the z direction. This is known to be caused by dynamical charge transfer due to atomic displacement where changes in

Table 5.8 Structural parameters of Rutile. Lattice constants a and c in Å and unit cell volume v_0 in $Å^3$

	a	c	v_0	c/a	u
This Work	4.585	2.935	61.69	0.640	0.305
Experiment					
Abrahams and Bernstein [16]	4.594	2.959	62.43	0.644	0.305
Burdett et al. [17]	4.587	2.954	62.15	0.644	0.305
Theory					
Lee et al. [18]	4.536	2.915	59.98	0.643	0.304
Ramamoorthy et al. [19]	4.567	2.932	61.16	0.642	0.305
Glassford et al. [20–22]	4.653	2.965	64.84	0.637	0.305
Allan and Teter [23]	4.584	2.961	62.22	0.646	0.304
Montanari and Harrison [14]	4.545	2.919	60.30	0.642	0.304

Table 5.9 Born effective charges for Ti and O in Rutile. Note that $Z^*_{yy,\tau} = Z^*_{xx,\tau}$ and $Z^*_{yx,\tau} = Z^*_{xy,\tau}$

	$Z^*_{xx,\mathrm{Ti}}$	$Z^*_{xy,\mathrm{Ti}}$	$Z^*_{zz,\mathrm{Ti}}$	$Z^*_{xx,\mathrm{O}}$	$Z^*_{xy,\mathrm{O}}$	$Z^*_{zz,\mathrm{O}}$
Theory [18]	6.338	0.995	7.541	−3.169	−1.809	−3.771
THIS WORK	6.332	0.994	7.581	−3.187	−1.802	−3.800

Table 5.10 Electronic dielectric permittivity along the a and c directions. Discrepancies between DFT and experiment [24] are due to the well-known underestimation of the core-valence band gap when using the LDA. The LDA band gap is approximately 1.9 eV whilst the experimentally observed band gap is 3.0 eV

	$\varepsilon_{\infty,a}$	$\varepsilon_{\infty,c}$
Experiment [24]	6.843	8.426
Theory [18]	7.535	8.665
- scissor corrected	6.366	7.290
THIS WORK	7.510	8.682

covalent hybridized bonds cause electrons to transfer between oppositely charged ions. The electronic permittivities along the a and c crystal axes were calculated using DFPT and Table 5.10 shows, they are in agreement with the theoretical predictions of Lee et al. [18] but differ from experimentally determined values [24]. Discrepancies between DFPT and experiment can be explained as due to the well-known underestimation of the core-valence band gap when using the local density approximation (LDA). The LDA predicted a band gap of 1.9 eV whilst the experimentally observed

Table 5.11 Phonon frequencies for Rutile at the Γ point in cm^{-1}. Experimental data are taken at room temperature and 5 K for values within parenthesis

Mode		Activity	Theory [18]	Neutrons	IR/Raman	THIS WORK
B_{1u}	Γ_1^+	Silent	116.7	113	-	106.3
B_{1g}	Γ_2^+	Raman	125.2	142	143 (143)	132.0
A_{2u} (TO)	Γ_3^-	Infrared	176.1	173 (142)	167 (144)	140.4
E_u (TO)	Γ_5^-	Infrared	164.8	189	183	163.9
E_u (LO)	Γ_5^-	Infrared	351.5	375	373	355.4
E_u (TO)	Γ_5^-	Infrared	391.3	-	388	388.7
B_{1u}	Γ_2^-	Silent	407.5	406	-	397.5
A_{2g}	Γ_3^+	Silent	415.5	-	-	420.4
E_u (LO)	Γ_5^-	Infrared	441.7	429	458	444.7
E_g	Γ_5^+	Raman	471.5	445	447 (455)	467.2
E_u (TO)	Γ_5^-	Infrared	492.8	494	500	493.9
A_{1g}	Γ_1^+	Raman	622.5	610	612 (611)	615.9
A_{2u} (LO)	Γ_3^-	Infrared	769.3	-	812	765.0
E_u (LO)	Γ_5^-	Infrared	808.4	842	807	801.5
B_{2g}	Γ_4^+	Raman	828.0	825	827	823.8

Lee et al. [18] use LDA and Perdew–Zunger parametrization of Ceperley–Alder data. Montanari [14] also use the LDA and PZ exchange-correlation functional. Neutron diffraction, Infrared and Raman data are taken at room temperature unless displayed within parenthesis which are at 5 K

band gap is 3.0 eV. A scissor correction was applied by Lee et al. bringing the $\varepsilon_{\infty,a}$ value in line with that of experiment, but making the discrepancy in $\varepsilon_{\infty,c}$ greater. The frequencies of the optical phonons at the Brillouin zone centre ($\mathbf{q} = 0$) were calculated and are presented in Table 5.11 showing excellent agreement with experimental data (neutron diffraction, IR and Raman spectroscopy) and theoretical predictions in the literature. The atomic displacement patterns for these optical phonons are shown in Figs. 5.12 and 5.13. The modes can be classified as silent (having no dipole moment), infrared and Raman active. The Rutile phase of TiO_2 has fifteen optical phonon modes, eight of which are infrared active with symmetry representations A_{2u} and E_u. The A_{2u} mode and the three doubly degenerate E_u modes exhibit LO-TO splitting and can be classified into modes with atomic motion along the c-axis or within the ab-plane, respectively. From symmetry considerations and taking into account the LO-TO splitting, the mode that contributes to the static permittivity along the c-axis is the A_{2u} mode with TO/LO frequency 140.4/765.0 cm^{-1} and within the ab-plane, the E_u mode with TO/LO frequencies 163.9/355.3, 388.7/444.7 and 493.9/801.5 cm^{-1}. The low-frequency relative permittivity, calculated using the generalised Lyddane–Sachs–Teller relation for the ab-plane and c-axis, using the above LO-TO mode frequencies and the electronic permittivity tensor calculated earlier yields $\varepsilon_\perp = 110.9$ (ab-plane) and $\varepsilon_\parallel = 250.2$ (c-axis). Values measured using the dielectric resonator technique were $\varepsilon_\perp = 112.6$ and $\varepsilon_\parallel = 250.5$ at a temperature of 15.9 K. This analysis shows that the very high permittivity in the c-axis is solely due to the giant LO-TO splitting of the A_{2u} mode. The permittivity in the ab-plane is also

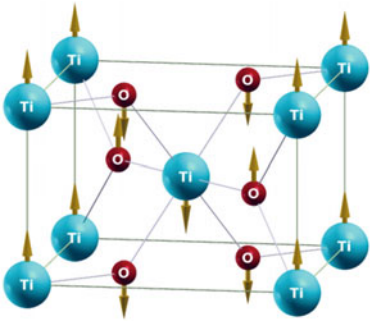

(a) B_{1u} – silent mode at 106.3 cm^{-1}.

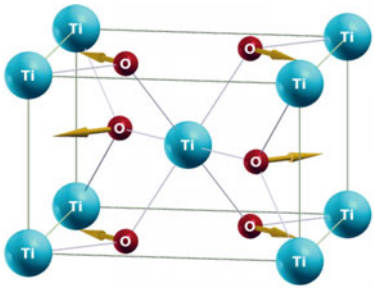

(b) B_{1g} – Raman mode at 132.0 cm^{-1}.

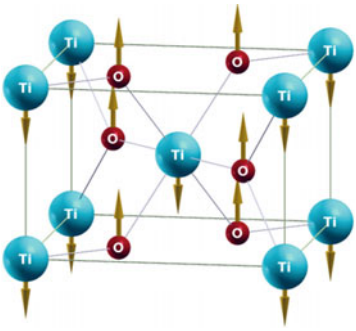

(c) A_{2u} – infrared mode at 140.4 cm^{-1} (TO) and 765.0 cm^{-1}(LO).

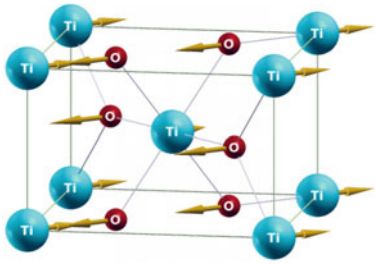

(d) E_u – Infrared mode at 163.9 cm^{-1} (TO) and 355.4 cm^{-1} (LO).

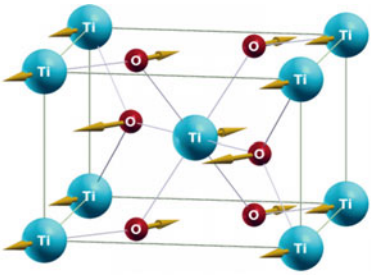

(e) E_u - Infrared mode at 388.7 cm^{-1} (TO) and 444.7 cm^{-1} (LO).

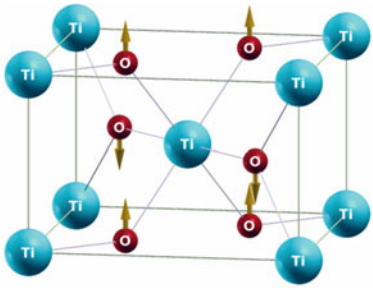

(f) B_{1u} – Silent mode at 397.5 cm^{-1}.

Fig. 5.12 Atomic displacement patterns for lowest eight optical phonon modes at Γ-point in TiO_2. Infrared modes E_u are doubly degenerate and undergo LO-TO frequency splitting

high, with contributions from all three E_u modes albeit with smaller LO-TO splitting than the A_{2u} mode, with the greatest from the lowest frequency E_u mode. Figure 5.14 shows the atomic displacement patterns of the two modes A_{2u} (140.4 cm^{-1}) and E_u

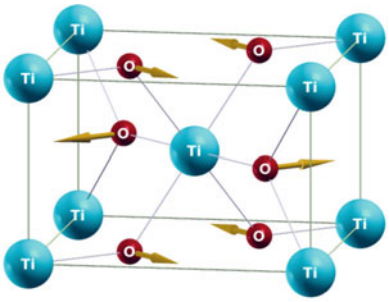

(a) A_{2g} – Silent mode at 420.4 cm^{-1}

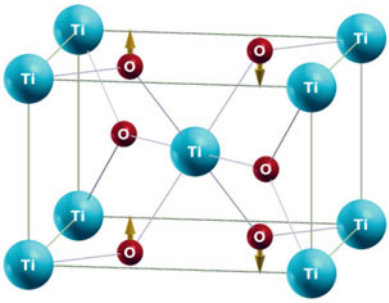

(b) E_g – Raman mode at 467.2 cm^{-1}

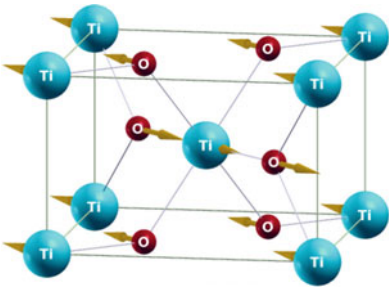

(c) E_u – Infrared mode at 493.9 cm^{-1} (TO) and 801.5 cm^{-1} (LO)

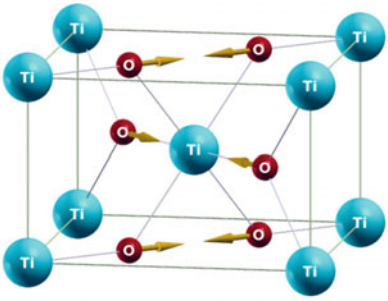

(d) A_{1g} – Raman mode at 615.9 cm^{-1}

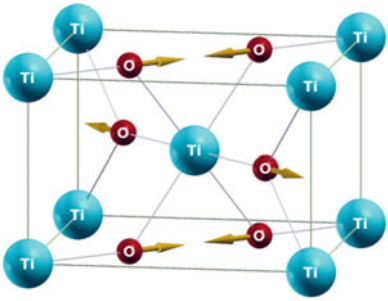

(e) B_{2g} – Raman mode at 823.8 cm^{-1}

Fig. 5.13 Atomic displacement patterns for highest seven optical phonon modes at Γ-point in TiO_2. Modes E_u and E_g are doubly degenerate

(163.9 cm^{-1}), which are responsible for the high static dielectric constant in TiO_2 along the c-axis and within the ab-plane.

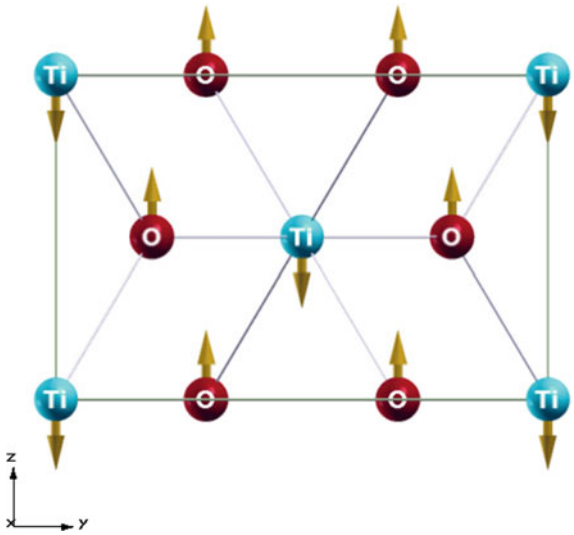

(a) A_{2u} mode

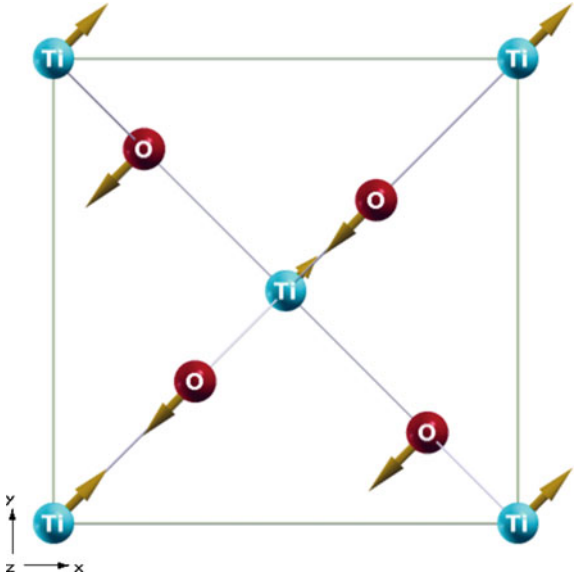

(b) E_u mode

Fig. 5.14 Modes responsible for large dielectric response at low frequencies in TiO_2 where the Ti and O sublattices are displaced in along the c–axis for A_{2u} modes or the ab-plane for E_u modes

Phonon Dispersion Relations

Dynamical matrices were calculated at nine **q**-points corresponding to the Monkhorst–Pack set for a shifted $4 \times 4 \times 6$ mesh. Fourier interpolation of the interatomic force constant matrices, taking LO-TO splitting into account allowed the phonon dispersion relations to be calculated along high-symmetry directions in the Brillouin zone as shown in Fig. 5.15.

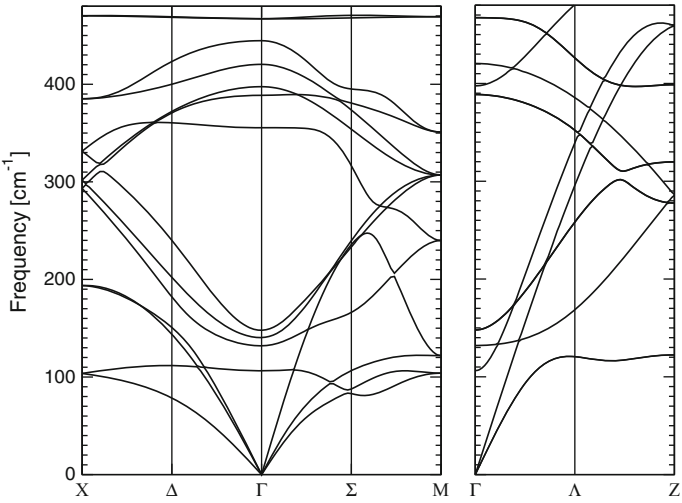

Fig. 5.15 Phonon dispersion for Rutile

5.4 Aluminium Oxide (Sapphire) — α-Al_2O_3

Aluminium oxide in its corundum form, also known as sapphire, is a material with several attractive properties. It is an excellent insulator with high-thermal conductivity and very low dielectric losses. At cryogenic temperatures and microwave frequencies, sapphire dielectric resonators exhibit the lowest dielectric loss of any material [25–28]. A wide electronic band gap means it is transparent from the far infrared up to the deep ultraviolet. Coupled with its outstanding mechanical strength and hardness, this makes it an ideal material for high performance dielectric resonators, substrates and optical windows.

Structure

Sapphire (α-Al_2O_3) crystallizes in the trigonal system with point group $\bar{3}$m (D_{3d}). It has a rhombohedral unit cell with space group R$\bar{3}$c and contains two formula units with ten atoms (four Al and six O) as displayed in Fig. 5.16. The positions of atoms in units of lattice parameter a are shown in Table 5.12, where x and z are internal structural parameters. Norm-conserving pseudopotentials were used with the Ceperley and Alder exchange-correlation energy functional within the local density approximation (LDA). A plane-wave cut-off energy of 80 Ry and electronic k-point sampling from a (4,4,4) Monkhorst–Pack mesh shifted by (1,1,1) provided sufficient convergence of the total energy. The lattice parameter a and internal coordinates x and z were found by minimising the ground-state energy using the Broyden–Fletcher–Goldfarb–Shanno (BFGS) method of nonlinear optimization. The optimized values (Table 5.13) were found to be in excellent agreement with experimental [29] and theoretical [30, 31] data reported in the literature.

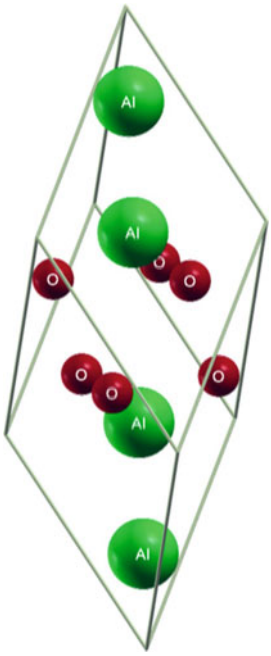

Fig. 5.16 Rhombohedral unit cell of Sapphire Al_2O_3

Table 5.12 Positions of atoms in Sapphire in units of the lattice constant a, where x and z are internal coordinates

Atom			
Al	x	x	x
Al	$-x$	$-x$	$-x$
Al	$\frac{1}{2}-x$	$\frac{1}{2}-x$	$\frac{1}{2}-x$
Al	$x-\frac{1}{2}$	$x-\frac{1}{2}$	$x-\frac{1}{2}$
O	z	$-z+\frac{1}{2}$	$\frac{1}{4}$
O	$\frac{1}{4}$	z	$-z+\frac{1}{2}$
O	$-z+\frac{1}{2}$	$\frac{1}{4}$	z
O	$-z$	$z-\frac{1}{2}$	$-\frac{1}{4}$
O	$-\frac{1}{4}$	$-z$	$z-\frac{1}{2}$
O	$z-\frac{1}{2}$	$-\frac{1}{4}$	$-z$

Lattice Dynamics

A Γ-point ($\mathbf{q} = 0$) phonon calculation produced Born effective charges (see Table 5.14) and electronic permittivity (Table 5.15) inagreement with experiment

Table 5.13 Structural parameters of Sapphire. Lattice constant a in Å and angle α in degrees. x and z are internal coordinates

	a	α	x	z
Experiment				
Lee and Lagerlof [29]	5.128	55.28	0.352	0.556
Theory				
Wolverton and Hass [30]	5.161	55.27	0.352	0.556
Łodziana and Parliński [31]	5.153	55.279	0.353	0.556
This work	5.1533	55.286	0.352	0.556

Table 5.14 Born effective charges for Al and O in sapphire. Note that $Z^*_{yy,\tau} = Z^*_{xx,\tau}$ and $Z^*_{yx,\tau} = Z^*_{xy,\tau}$

	$Z^*_{xx,\mathrm{Al}}$	$Z^*_{xy,\mathrm{Al}}$	$Z^*_{zz,\mathrm{Al}}$	$Z^*_{xx,\mathrm{O}}$	$Z^*_{xy,\mathrm{O}}$	$Z^*_{zz,\mathrm{O}}$
Theory [32]	2.905	0.000	2.870	−1.919	−0.246	−1.920
THIS WORK	2.953	0.027	2.923	−1.921	−0.218	−1.950

Table 5.15 Electronic dielectric permittivity tensor for Al_2O_3 along principle axes

	$\varepsilon^\infty_{x,y}$	ε^∞_z
Theory [32]	3.2	3.1
Expt. [33]	3.2	3.1
THIS WORK	3.204	3.107

and theory. The Born effective charges were close to the nominal charge for the Al^{3+} and O^{-2} ions implying that the bonds in α-Al_2O_3 are strongly ionic. The dynamical matrix at Γ ($\mathbf{q} = 0$) was diagonalised, taking LO-TO splitting into account. The eigenfrequencies of the phonon modes in sapphire at the Γ point are presented in Table 5.16. Sapphire supports twenty-seven optical phonon modes, of which twelve are infrared active. There are four degenerate modes with designation E_u, that have atomic displacement patterns in the xy-plane. The TO/LO frequencies of these modes are 381.3/383.6, 438.3/478.7, 566.0/625.8 and 635.1/894.3 cm^{-1}. These modes are responsible for the transverse permittivity. There are then two modes with designation A_{2u}, whose atomic displacement patterns are in the z-direction and have TO/LO frequencies 392.3/502.3 and 581.7/868.2 cm^{-1}. Application of the Lyddane–Sachs–Teller relation once again reveals the predicted static relative permittivity at absolute zero in directions parallel and perpendicular to the crystal c-axis

$$\varepsilon_\parallel = 11.321$$

Table 5.16 Phonon frequencies for sapphire at the Γ point in cm^{-1}. Theory values are from Heid et al. [32] and experimental values are from Ref. [13] therein [33]

Mode	Activity	Theory	Expt.	THIS WORK
E_u (TO)	Infrared	381.6	386.9	381.3
E_u (LO)	Infrared	383.6	386.9	383.6
A_{2u} (TO)	Infrared	390.9	400.3	392.3
E_u (TO)	Infrared	435.4	443.6	438.3
E_u (LO)	Infrared	480.7	480.3	478.7
A_{2u} (LO)	Infrared	499.7	513.7	502.3
E_u (TO)	Infrared	565.4	570.4	566.0
A_{2u} (TO)	Infrared	571.7	583.7	581.7
E_u (LO)	Infrared	625.1	627.1	625.8
E_u (TO)	Infrared	628.1	637.1	635.1
A_{2u} (LO)	Infrared	860.2	870.6	868.2
E_u (LO)	Infrared	887.3	900.6	894.3
E_g	Raman	379.6	376.9	375.6
A_{1g}	Raman	411.6	416.9	416.3
E_g	Raman	429.0	433.6	428.6
E_g	Raman	442.6	450.3	445.6
E_g	Raman	567.7	577.1	574.0
A_{1g}	Raman	636.1	647.1	637.8
E_g	Raman	746.5	750.5	748.2
A_{2g}	Silent	301.5		302.2
A_{2g}	Silent	536.4		533.0
A_{1u}	Silent	594.4		596.4
A_{1u}	Silent	687.8		692.5
A_{2g}	Silent	747.5		744.8

and

$$\varepsilon_\perp = 9.363.$$

The permittivity of sapphire measured in Chap. 3 was $\varepsilon_\parallel = 11.344$ and $\varepsilon_\perp = 9.260$ at 29 K, once again being in excellent agreement.

5.5 Summary and Conclusions

The low-frequency relative permittivities of MgO, $LaAlO_3$, TiO_2 and Al_2O_3 have been calculated *ab-initio* using density functional perturbation theory (DFPT) and appear to be in excellent agreement with experimental data (see Table 5.17). This may be judicious in some cases, since the electronic permittivity is often slightly

Table 5.17 Summary of predicted permittivities at 0 °K compared to low-temperature experimental values

Material		Theory	Expt.
MgO	ε_r	9.674	9.651
$LaAlO_3$	ε_r	24.12	23.62
TiO_2	$\varepsilon_{r,\perp}$	110.9	112.6
	$\varepsilon_{r,\parallel}$	250.2	250.5
Al_2O_3	$\varepsilon_{r,\perp}$	9.363	9.260
	$\varepsilon_{r,\parallel}$	11.321	11.344

overestimated in some cases, yet compensated by an underestimate of the LO-TO splitting of the optical phonons. Although the calculated harmonic properties are for a temperature of absolute zero and the measurement are at approximately 15 °K, the results are very promising and the dispersion data for phonon eigenmodes (frequency and eigenvectors) will allow for more complex temperature-dependent calculations to be performed such as thermal expansion and anharmonic phonon–phonon interactions.

References

1. P. Giannozzi et al., QUANTUM ESPRESSO: a modular and open-source software project for quantum simulations of materials. J. Phys. Condens. Matter **21**, 395502 (2009)
2. J.P. Perdew, A. Zunger, Self-interaction correction to density-functional approximations for many-electron systems. Phys. Rev. B **23**, 5048 (1981)
3. N. Troullier, J.L. Martins, Efficient pseudopotentials for plane-wave calculations. Phys. Rev. B **43**, 1993 (1991)
4. O. Schütt et al., Ab initio lattice dynamics and charge fluctuations in alkaline-earth oxides. Phys. Rev. B **50**, 3746 (1994)
5. M.J.L. Sangster, G. Peckham, D.H. Saunderson, Lattice dynamics of magnesium oxide. J. Phys. C **3**, 1026 (1970)
6. H.J. Monkhorst, J.D. Pack, Special points for Brillouin-zone integrations. Phys. Rev. B **13**, 5188 (1976)
7. M. Sparks, D.F. King, D.L. Mills, Simple theory of microwave absorption in alkali halides. Phys. Rev. B **26**, 6987 (1982)
8. E.J. Wu, G. Ceder, Computational investigation of dielectric absorption at microwave frequencies in binary oxides. J. Appl. Phys. **89**, 5630 (2001)
9. E.H. Bogardus, Third-order elastic constants of Ge, MgO, and fused SiO_2. J. Appl. Phys. **36**, 2504 (1965)
10. P.E. Blöchl, O. Jepsen, O.K. Andersen, Improved tetrahedron method for Brillouin-zone integrations. Phys. Rev. B **49**, 16223 (1994)
11. R.H. Lyddane, R.G. Sachs, E. Teller, On the polar vibrations of alkali halides. Phys. Rev. **59**, 673 (1941)
12. C. Zuccaro et al., Microwave absorption in single crystals of lanthanum aluminate. J. Appl. Phys. **82**, 5695 (1997)
13. T. Shimada et al., Intrinsic microwave dielectric loss of lanthanum aluminate. IEEE Trans. Ultrason. Ferroelectr. Freq. Control **57**, 2243 (2010)

14. B. Montanari, N.M. Harrison, Lattice dynamics of TiO_2 rutile: influence of gradient corrections in density functional calculations. Chem. Phys. Lett. **364**, 528 (2002)
15. R. Fletcher, *Practical Methods of Optimization* (Wiley, New York, 2013)
16. S.C. Abrahams, J.L. Bernstein, Rutile: normal probability plot analysis and accurate measurement of crystal structure. J. Chem. Phys. **55**, 3206 (1971)
17. J.K. Burdett et al., Structural-electronic relationships in inorganic solids: powder neutron diffraction studies of the rutile and anatase polymorphs of titanium dioxide at 15 and 295 K. J. Am. Chem. Soc. **109**, 3639 (1987)
18. C. Lee, P. Ghosez, X. Gonze, Lattice dynamics and dielectric properties of incipient ferroelectric TiO_2 rutile. Phys. Rev. B **50**, 13379 (1994)
19. M. Ramamoorthy, R.D. King-Smith, D. Vanderbilt, First-principles calculations of the energetics of stoichiometric TiO_2 surfaces. Phys. Rev. B **49**, 7709 (1994)
20. K.M. Glassford et al., Electronic and structural properties of TiO_2 in the rutile structure. Solid State Commun. **76**, 635 (1990)
21. K.M. Glassford, J.R. Chelikowsky, Optical properties of titanium dioxide in the rutile structure. Phys. Rev. B **45**, 3874 (1992)
22. K.M. Glassford, J.R. Chelikowsky, Structural and electronic properties of titanium dioxide. Phys. Rev. B **46**, 1284 (1992)
23. D.C. Allan, M.P. Teter, Local density approximation total energy calculations for silica and titania structure and defects. J. Am. Ceram. Soc. **73**, 3247 (1990)
24. J.G. Traylor et al., Lattice dynamics of rutile. Phys. Rev. B **3**, 3457 (1971)
25. J. Krupka et al., Dielectric properties of single crystals of Al_2O_3, $LaAlO_3$, $NdGaO_3$, $SrTiO_3$ and MgO at cryogenic temperatures. IEEE Trans. Microw. Theory Tech. **42**, 1886 (1994)
26. J. Krupka et al., Complex permittivity of some ultralow loss dielectric crystals at cryogenic temperatures. Meas. Sci. Technol. **10**, 387 (1999)
27. M.E. Tobar et al., High-Q sapphire-rutile frequency-temperature compensated microwave dielectric resonators. IEEE Trans. Ultrason. Ferroelectr. Freq. Control **45**, 830 (1998)
28. M.E. Tobar et al., High-Q factor frequency-temperature compensated sapphire Bragg distributed resonator. Electron. Lett. **39**, 293 (2003)
29. W.E. Lee, K.P.D. Lagerlof, Structural and electron diffraction data for sapphire (α-Al_2O_3). J. Electron Microsc. Tech. **2**, 247 (1985)
30. C. Wolverton, K.C. Hass, Phase stability and structure of spinel-based transition aluminas. Phys. Rev. B **63**, 024102 (2000)
31. Z. Łodziana, K. Parliński, Dynamical stability of the α and θ phases of alumina. Phys. Rev. B **67**, 174106 (2003)
32. R. Heid, D. Strauch, K.-P. Bohnen, Ab initio lattice dynamics of sapphire. Phys. Rev. B **61**, 8625 (2000)
33. A.S. Barker Jr., Infrared lattice vibrations and dielectric dispersion in corundum. Phys. Rev. **132**, 1474 (1963)

Chapter 6
Theory of Anharmonic Phonons

The harmonic approximation truncates the expansion of the total energy in powers of atomic displacements to second-order and so the collective excitations of the lattice known as phonons are independent and non-interacting. The frequencies of harmonic phonons are well-defined and as a result have infinite lifetimes, they never decay and propagate freely through perfect infinite crystals without impingement or attenuation. Since intrinsic dielectric absorption is known to be a phenomenon associated with interacting phonons, the harmonic approximation will clearly be unable to describe it and that the inclusion of higher order anharmonic terms in the energy expansion will be required. Anharmonic phonons couple and exchange energy with each other, allowing non-equilibrium phonon populations and their associated relaxation phenomena to exist. In going from a harmonic description to an anharmonic one, the real-valued eigenfrequency of the harmonic mode is perturbed and suffers a complex frequency shift shown as the *self-energy*. This manifests as a real frequency shift and a broadening in the linewidth of the phonon which is measurable using neutron diffraction spectroscopy.

Dielectric loss is a result of absorption of electromagnetic energy by transverse optical phonons and is therefore an anharmonic process. In this chapter, the theoretical framework of anharmonic lattice vibrations within crystals will be developed followed by a quantum field approach to describe the anharmonic processes which contribute to the phonon self-energy. The quantum field theory of phonons is well established, having been developed in the 1960s by Cowley [1], Alekseev [2], Kadanoff and Baym [3] amongst others. They used the interaction representation to derive temperature-dependent Green functions for phonon propagators and the evolution operator to expand the Green functions into infinite series of terms corresponding to various phonon interactions. These terms can be interpreted using Feynman diagrams and indeed this powerful approach can be used to classify and group diagrams so that the self energy of the phonons can be calculated. This quantum field framework can be readily applied to the problem of calculating the complex

J. Breeze, *Temperature and Frequency Dependence of Complex Permittivity in Metal Oxide Dielectrics: Theory, Modelling and Measurement*, Springer Theses, DOI 10.1007/978-3-319-44547-2_6

permittivity in microwave dielectrics as functions of temperature and frequency for field frequencies far below the transverse optical phonon modes.

6.1 Beyond the Harmonic Approximation

Consider a crystal consisting of N unit cells each containing n atoms per unit cell, where the atoms are in their equilibrium position. The position of the κ^{th} atom in the l^{th} unit cell can be written as

$$\mathbf{R}_l^{\kappa} = \mathbf{R}_l + \boldsymbol{\tau}^{\kappa},$$

where the lattice vector $\mathbf{R}^l$ is the position vector of the l^{th} unit cell and $\boldsymbol{\tau}_\kappa$ the position vector of atom κ with respect to the origin of the unit cell. If the atoms are permitted to vibrate about their equilibrium positions by a displacement vector $\mathbf{u}^{\kappa}(\mathbf{R})$, then the kinetic energy of the lattice is

$$T = \frac{1}{2}\sum_{\kappa\alpha\mathbf{R}} M_\kappa \dot{u}_\alpha^{\kappa}(\mathbf{R})$$

where α is a Cartesian component and M_κ is the mass of atom κ. The equations of motion for atom κ in unit cell $\mathbf{R}_l$ can be set up:

$$M_\kappa \ddot{u}_\alpha^{\kappa}(\mathbf{R}_l) = -\frac{\partial \mathcal{E}}{\partial u_\alpha^{\kappa}(\mathbf{R}_l)},$$

where Φ is the lattice potential energy. The lattice potential energy can then be expanded into a Taylor series in powers of the displacement vectors $\mathbf{u}^{\kappa}(\mathbf{R}_l)$ for the κ^{th} atom within the l^{th} unit cell, about their equilibrium positions

$$\begin{aligned}
\Phi = \Phi_0 &+ \sum_{\kappa\alpha\mathbf{R}} \Phi_\alpha^{\kappa}(\mathbf{R}) u_\alpha^{\kappa}(\mathbf{R}) \\
&+ \frac{1}{2}\sum_{\substack{\kappa_1\alpha_1\mathbf{R}_1 \\ \kappa_2\alpha_2\mathbf{R}_2}} \Phi_{\alpha_1\alpha_2}^{\kappa_1\kappa_2}(\mathbf{R}_1\mathbf{R}_2) u_{\alpha_1}^{\kappa_1}(\mathbf{R}_1) u_{\alpha_2}^{\kappa_2}(\mathbf{R}_2) \\
&+ \frac{1}{3!}\sum_{\substack{\kappa_1\alpha_1\mathbf{R}_1 \\ \kappa_2\alpha_2\mathbf{R}_2 \\ \kappa_3\alpha_3\mathbf{R}_3}} \Phi_{\alpha_1\alpha_2\alpha_3}^{\kappa_1\kappa_2\kappa_3}(\mathbf{R}_1\mathbf{R}_2\mathbf{R}_3) u_{\alpha_1}^{\kappa_1}(\mathbf{R}_1) u_{\alpha_2}^{\kappa_2}(\mathbf{R}_2) u_{\alpha_3}^{\kappa_3}(\mathbf{R}_3) \\
&+ \frac{1}{4!}\sum_{\substack{\kappa_1\alpha_1\mathbf{R}_1 \\ \kappa_2\alpha_2\mathbf{R}_2 \\ \kappa_3\alpha_3\mathbf{R}_3 \\ \kappa_4\alpha_4\mathbf{R}_4}} \Phi_{\alpha_1\alpha_2\alpha_3\alpha_4}^{\kappa_1\kappa_2\kappa_3\kappa_4}(\mathbf{R}_1\mathbf{R}_2\mathbf{R}_3\mathbf{R}_4) u_{\alpha_1}^{\kappa_1}(\mathbf{R}_1) u_{\alpha_2}^{\kappa_2}(\mathbf{R}_2) u_{\alpha_3}^{\kappa_3}(\mathbf{R}_3) u_{\alpha_4}^{\kappa_4}(\mathbf{R}_4) \\
&+ \cdots
\end{aligned}$$

$$+\frac{1}{n!}\sum_{\substack{\kappa_1\alpha_1\mathbf{R}_1\\ \vdots\\ \kappa_n\alpha_n\mathbf{R}_n}}\Phi^{\kappa_1\ldots\kappa_n}_{\alpha_1\ldots\alpha_n}(\mathbf{R}_1\ldots\mathbf{R}_n)u^{\kappa_1}_{\alpha_1}(\mathbf{R}_1)\ldots u^{\kappa_n}_{\alpha_n}(\mathbf{R}_n)$$
$$+\cdots \tag{6.1.1}$$

where

$$\Phi^{\kappa_1\ldots\kappa_n}_{\alpha_1\ldots\alpha_n}(\mathbf{R}_1\ldots\mathbf{R}_n)=\frac{\partial^n\mathcal{E}}{\partial u^{\kappa_1}_{\alpha_1}(\mathbf{R}_1)\ldots\partial u^{\kappa_n}_{\alpha_n}(\mathbf{R}_n)}.$$

The first term Φ_0 is the equilibrium value of the lattice potential energy, the second term vanishes since the atoms are in equilibrium and have no forces acting upon them and the third term is the harmonic lattice potential energy. In the harmonic approximation, the series expansion is truncated at this point so as not to include the higher order terms. The harmonic equations of motion then read

$$M_\kappa\ddot{u}^\kappa_\alpha(\mathbf{R})=-\sum_{\kappa'\mathbf{R}'}\frac{\partial^2\mathcal{E}}{\partial u^\kappa_\alpha(\mathbf{R})\partial u^{\kappa'}_{\alpha'}(\mathbf{R}')}u^{\kappa'}_{\alpha'}(\mathbf{R}').$$

If we safely assume the displacement vectors $\mathbf{u}$ to have a time dependency of the form $e^{-i\omega t}$, the time derivatives in the equations of motion can be evaluated

$$M_\kappa\omega^2u^\kappa_\alpha(\mathbf{R})=\sum_{\kappa'\mathbf{R}'}\Phi^{\kappa\kappa'}_{\alpha\alpha'}(\mathbf{R},\mathbf{R}')u^{\kappa'}_{\alpha'}(\mathbf{R}').$$

This eigenvalue problem can be diagonalized to yield the phonon frequencies, atomic displacement patterns and dynamical matrices.

6.2 Anharmonic Hamiltonian

The Hamiltonian for a system that includes anharmonicity is [4, 5]:

$$H=H_0+H_A$$

where H_0 is the harmonic part of the Hamiltonian and H_A are the additional anharmonic terms from the expansion of the energy above second

$$H_A=\sum_{n\geq3}\frac{1}{n!}\sum_{\substack{\kappa_1\ldots\kappa_n\\ \alpha_1\ldots\alpha_n\\ \mathbf{R}_1\ldots\mathbf{R}_n}}\Phi^{\kappa_1\ldots\kappa_n}_{\alpha_1\ldots\alpha_n}(\mathbf{R}_1,\ldots,\mathbf{R}_n)u^{\kappa_1}_{\alpha_1}(\mathbf{R}_1)\ldots u^{\kappa_n}_{\alpha_n}(\mathbf{R}_n).$$

The atomic displacement can be written in terms of the *phonon field operator* $A(\lambda) = a(\lambda) + a^{\dagger}(\lambda)$

$$u_{\alpha}^{\kappa}(\mathbf{R}) = \sum_{\lambda} \left(\frac{\hbar}{2NM_{\kappa}\omega_{\lambda}} \right)^{\frac{1}{2}} \varepsilon_{\alpha}^{\kappa}(\lambda) e^{i\mathbf{q}\cdot\mathbf{R}} A(\lambda), \tag{6.2.1}$$

where $\lambda \equiv \{\mathbf{q}, j\}$ labels the phonon $\mathbf{q}$-point branch j, and $a(\lambda)$ and $a^{\dagger}(\lambda)$ are the phonon annihilation and creation operators, respectively. Substitution into the Hamiltonian for the n^{th} anharmonic term yields:

$$\begin{aligned} H_A^{(n)} &= \frac{1}{n!} \sum_{\substack{\kappa_1 \ldots \kappa_n \\ \alpha_1 \ldots \alpha_n \\ \mathbf{R}_1 \ldots \mathbf{R}_n}} \Phi_{\alpha_1 \ldots \alpha_n}^{\kappa_1 \ldots \kappa_n}(\mathbf{R}_1, \ldots, \mathbf{R}_n) u_{\alpha_1}^{\kappa_1}(\mathbf{R}_1) \ldots u_{\alpha_n}^{\kappa_n}(\mathbf{R}_n) \\ &= \frac{1}{n!} \left(\frac{\hbar}{2N} \right)^{n/2} \sum_{\lambda_1 \ldots \lambda_n} \sum_{\substack{\kappa_1 \ldots \kappa_n \\ \alpha_1 \ldots \alpha_n \\ \mathbf{R}_1 \ldots \mathbf{R}_n}} \frac{\varepsilon_{\alpha_1}^{\kappa_1}(\lambda_1) \ldots \varepsilon_{\alpha_n}^{\kappa_n}(\lambda_n)}{\left(M_{\kappa_1}\omega_{\lambda_1} \ldots M_{\kappa_n}\omega_{\lambda_n} \right)^{1/2}} \Phi_{\alpha_1 \ldots \alpha_n}^{\kappa_1 \ldots \kappa_n}(\mathbf{R}_1 \ldots \mathbf{R}_n) \\ &\times e^{i(\mathbf{q}_1 \cdot \mathbf{R}_1 + \cdots + \mathbf{q}_n \cdot \mathbf{R}_n)} A(\lambda_1) \ldots A(\lambda_n). \end{aligned}$$

The anharmonic Hamiltonian H_A can in fact be expanded as a power series in any chosen coordinate [6]. For example, H_A expanded in powers of the Fourier components of the ionic displacements in reciprocal space;

$$H_A = \sum_{n \geq 3} \frac{1}{n!} \sum_{\substack{\kappa_1 \ldots \kappa_n \\ \alpha_1 \ldots \alpha_n \\ \mathbf{q}_1 \ldots \mathbf{q}_n}} \Psi_{\alpha_1 \ldots \alpha_n}^{\kappa_1 \ldots \kappa_n}(\mathbf{q}_1, \ldots, \mathbf{q}_n) u_{\alpha_1}^{\kappa_1}(\mathbf{q}_1) \ldots u_{\alpha_n}^{\kappa_n}(\mathbf{q}_n)$$

where the α-component of the Fourier-transformed displacement vector of atom κ of wavevector $\mathbf{q}$ is

$$u_{\alpha}^{\kappa}(\mathbf{q}) = \frac{1}{\sqrt{N}} \sum_{\mathbf{R}} e^{-i\mathbf{q}\cdot\mathbf{R}} u_{\alpha}^{\kappa}(\mathbf{R})$$

and similarly, the Fourier-transformed interatomic force constant matrix:

$$\Psi_{\alpha_1 \ldots \alpha_n}^{\kappa_1 \ldots \kappa_n}(\mathbf{q}_1, \ldots, \mathbf{q}_n) = \frac{\partial^n \mathcal{E}}{\partial u_{\alpha_1}^{\kappa_1}(\mathbf{q}_1) \ldots \partial u_{\alpha_n}^{\kappa_n}(\mathbf{q}_n)}$$

is given by

$$\Psi_{\alpha_1 \ldots \alpha_n}^{\kappa_1 \ldots \kappa_n}(\mathbf{q}_1, \ldots, \mathbf{q}_n) = \frac{1}{N} \sum_{\mathbf{R}_1 \ldots \mathbf{R}_n} \Phi_{\alpha_1 \ldots \alpha_n}^{\kappa_1 \ldots \kappa_n}(\mathbf{R}_1, \ldots, \mathbf{R}_n) e^{i(\mathbf{q}_1 \cdot \mathbf{R}_1 + \cdots + \mathbf{q}_n \cdot \mathbf{R}_n)}.$$

H_A can also be expanded in powers of phonon field operators $A(\lambda)$, which yields

$$H_A = \sum_{\lambda_1 \ldots \lambda_n} V_n(\lambda_1, \ldots, \lambda_n) A(\lambda_1) \ldots A(\lambda_n)$$

where a phonon field operator is the sum of an annihilation and creator operator, given by

$$A(\lambda) = A(\mathbf{q}j) = a(\mathbf{q}j) + a^{\dagger}(-\mathbf{q}j)$$

and

$$V_n(\lambda_1, \ldots, \lambda_n) = \frac{1}{n!} \frac{\partial^n \mathcal{E}}{\partial A(\lambda_1) \ldots \partial A(\lambda_n)}$$

is the n^{th} derivative of the total energy with respect to the phonon field operators also known as the *anharmonic phonon coupling tensor*. Inspection of the terms in the Taylor expansion of the energy in powers of phonon field operators $A(\lambda)$ and atomic displacements $\mathbf{u}_{\alpha}^{\kappa}(\mathbf{R})$ in terms of $A(\lambda)$ (6.2.1):

$$\begin{aligned}
\sum_{\lambda_1 \ldots \lambda_n} V_n(\lambda_1, \ldots, \lambda_n) A(\lambda_1) \ldots A(\lambda_n) &= \frac{1}{n!} \sum_{\substack{\kappa_1 \ldots \kappa_n \\ \alpha_1 \ldots \alpha_n \\ \mathbf{R}_1 \ldots \mathbf{R}_n}} \Phi_{\alpha_1 \ldots \alpha_n}^{\kappa_1 \ldots \kappa_n}(\mathbf{R}_1, \ldots, \mathbf{R}_n) u_{\alpha_1}^{\kappa_1}(\mathbf{R}_1) \ldots u_{\alpha_n}^{\kappa_n}(\mathbf{R}_n) \\
&= \left(\frac{\hbar}{2N}\right)^{\frac{n}{2}} \sum_{\substack{\kappa_1 \ldots \kappa_n \\ \alpha_1 \ldots \alpha_n \\ \mathbf{R}_1 \ldots \mathbf{R}_n}} \Phi_{\alpha_1 \ldots \alpha_n}^{\kappa_1 \ldots \kappa_n}(\mathbf{R}_1, \ldots, \mathbf{R}_n) e^{i(\mathbf{q}_1 \cdot \mathbf{R}_1 + \cdots + \mathbf{q}_n \cdot \mathbf{R}_n)} \\
&\quad \times \sum_{\lambda_1 \cdots \lambda_n} \frac{\varepsilon_{\alpha_1}^{\kappa_1}(\lambda_1)}{\sqrt{M_{\kappa_1} \omega_{\lambda_1}}} \cdots \frac{\varepsilon_{\alpha_n}^{\kappa_n}(\lambda_n)}{\sqrt{M_{\kappa_n} \omega_{\lambda_n}}} A(\lambda_1) \ldots A(\lambda_n),
\end{aligned}$$

yields a general expression for $V_n(\lambda_1, \ldots, \lambda_n)$:

$$\begin{aligned}
V_n(\lambda_1, \ldots, \lambda_n) &= \frac{1}{n!} \left(\frac{\hbar}{2N}\right)^{\frac{n}{2}} \frac{1}{\sqrt{\omega_{\lambda_1} \ldots \omega_{\lambda_n}}} \sum_{\substack{\kappa_1 \ldots \kappa_n \\ \alpha_1 \ldots \alpha_n \\ \mathbf{R}_1 \ldots \mathbf{R}_n}} \Phi_{\alpha_1 \ldots \alpha_n}^{\kappa_1 \ldots \kappa_n}(\mathbf{R}_1, \ldots, \mathbf{R}_n) \\
&\quad \times e^{i(\mathbf{q}_1 \cdot \mathbf{R}_1 + \cdots + \mathbf{q}_n \cdot \mathbf{R}_n)} \frac{\varepsilon_{\alpha_1}^{\kappa_1}(\lambda_1)}{\sqrt{M_{\kappa_1}}} \ldots \frac{\varepsilon_{\alpha_n}^{\kappa_n}(\lambda_n)}{\sqrt{M_{\kappa_n}}}. \qquad (6.2.2)
\end{aligned}$$

If we write

$$\widetilde{\Psi}_{\alpha_1 \ldots \alpha_n}^{\kappa_1 \ldots \kappa_n}(\mathbf{q}_1, \ldots, \mathbf{q}_n) = \sum_{\mathbf{R}_1 \ldots \mathbf{R}_n} \frac{\Phi_{\alpha_1 \ldots \alpha_n}^{\kappa_1 \ldots \kappa_n}(\mathbf{R}_1, \ldots, \mathbf{R}_n) e^{i(\mathbf{q}_1 \cdot \mathbf{R}_1 + \cdots + \mathbf{q}_n \cdot \mathbf{R}_n)}}{\sqrt{M_{\kappa_1} \ldots M_{\kappa_n}}} \qquad (6.2.3)$$

then

$$V_n(\lambda_1,\ldots,\lambda_n)=\left(\frac{\hbar}{2N}\right)^{\frac{n}{2}}\frac{1}{\sqrt{\omega_{\lambda_1}\ldots\omega_{\lambda_n}}}\sum_{\substack{\kappa_1\ldots\kappa_n\\ \alpha_1\ldots\alpha_n}}\widetilde{\Psi}^{\kappa_1\ldots\kappa_n}_{\alpha_1\ldots\alpha_n}(\mathbf{q}_1,\ldots,\mathbf{q}_n)\varepsilon^{\kappa_1}_{\alpha_1}(\lambda_1)\ldots\varepsilon^{\kappa_n}_{\alpha_n}(\lambda_n), \tag{6.2.4}$$

and $\widetilde{\Psi}^{\kappa_1\ldots\kappa_n}_{\alpha_1\ldots\alpha_n}(\mathbf{q}_1,\ldots,\mathbf{q}_n)$ is recognisable as a n^{th} order dynamical tensor:

$$\widetilde{\Psi}^{\kappa_1\ldots\kappa_n}_{\alpha_1\ldots\alpha_n}(\mathbf{q}_1,\ldots,\mathbf{q}_n)=\frac{1}{\sqrt{M_{\kappa_1}\ldots M_{\kappa_n}}}\frac{\partial^n\mathcal{E}}{\partial u^{\kappa_1}_{\alpha_1}(\mathbf{q}_1)\ldots\partial u^{\kappa_n}_{\alpha_n}(\mathbf{q}_n)}.$$

Taking the derivative with respect to atomic displacement with wavevector $\mathbf{q}$ of the harmonic dynamical matrix given by:

$$\widetilde{\Psi}^{\kappa_1\kappa_2}_{\alpha_1\alpha_2}(\mathbf{q}_1,\mathbf{q}_2)=\frac{1}{\sqrt{M_{\kappa_1}M_{\kappa_2}}}\frac{\partial^2\mathcal{E}}{\partial u^{\kappa_1}_{\alpha_1}(\mathbf{q}_1)\partial u^{\kappa_2}_{\alpha_2}(\mathbf{q}_2)}$$

and dividing by the square root of the atomic mass, leads to an expression for the third-order dynamical tensor

$$\widetilde{\Psi}^{\kappa_1\kappa_2\kappa_3}_{\alpha_1\alpha_2\alpha_3}(\mathbf{q}_1,\mathbf{q}_2,\mathbf{q}_3)=\frac{1}{\sqrt{M_{\kappa_1}M_{\kappa_2}M_{\kappa_3}}}\frac{\partial^3\mathcal{E}}{\partial u^{\kappa_1}_{\alpha_1}(\mathbf{q}_1)\partial u^{\kappa_2}_{\alpha_2}(\mathbf{q}_2)\partial u^{\kappa_3}_{\alpha_3}(\mathbf{q}_3)}.$$

Hence, higher order dynamical tensors are derivatives of the harmonic dynamical matrix with respect to atomic displacements with wavevector $\mathbf{q}$ in the Brillouin zone

$$\widetilde{\Psi}^{\kappa_1\kappa_2\kappa_3}_{\alpha_1\alpha_2\alpha_3}(\mathbf{q}_1,\mathbf{q}_2,\mathbf{q}_3)=\frac{1}{\sqrt{M_{\kappa_3}}}\frac{\partial}{\partial u^{\kappa_3}_{\alpha_3}(\mathbf{q}_3)}\widetilde{\Psi}^{\kappa_1\kappa_2}_{\alpha_1\alpha_2}(\mathbf{q}_1,\mathbf{q}_2),$$

where

$$u^{\kappa}_{\alpha}(\mathbf{q})=\sum_j\left(\frac{\hbar}{2NM_\kappa\omega_\lambda}\right)^{\frac{1}{2}}\varepsilon^{\kappa}_{\alpha}(\lambda)A(\lambda)$$

$$A(\lambda)=\sum_{\kappa\alpha}\left(\frac{2NM_\kappa\omega_\lambda}{\hbar}\right)^{\frac{1}{2}}\varepsilon^{\kappa}_{\alpha}(\lambda)^*u^{\kappa}_{\alpha}(\mathbf{q}),$$

and $\varepsilon^{\kappa}_{\alpha}(\lambda)$ is the displacement pattern for mode $\lambda\equiv\{\mathbf{q},j\}$, where $\mathbf{q}$ is wavevector and j is the phonon branch index. For the third-order anharmonic coupling tensor, we now have

$$V_3(\lambda_1,\lambda_2,\lambda_3)=\left(\frac{\hbar}{8N^3\omega_{\lambda_1}\omega_{\lambda_2}\omega_{\lambda_3}}\right)^{\frac{1}{2}}\sum_{\substack{\kappa_1\kappa_2\kappa_3\\ \alpha_1\alpha_2\alpha_3}}\frac{\partial\Psi^{\kappa_1\kappa_2}_{\alpha_1\alpha_2}(\mathbf{q}_1,\mathbf{q}_2)}{\partial u^{\kappa_3}_{\alpha_3}(\mathbf{q}_3)}\frac{\varepsilon^{\kappa_1}_{\alpha_1}(\lambda_1)}{\sqrt{M_{\kappa_1}}}\frac{\varepsilon^{\kappa_2}_{\alpha_2}(\lambda_2)}{\sqrt{M_{\kappa_2}}}\frac{\varepsilon^{\kappa_3}_{\alpha_3}(\lambda_3)}{\sqrt{M_{\kappa_3}}},$$

and similarly for the fourth-order anharmonic coupling tensor

$$V_4(\lambda_1,\lambda_2,\lambda_3,\lambda_4) = \left(\frac{\hbar^2}{16N^4\omega_{\lambda_1}\omega_{\lambda_2}\omega_{\lambda_3}\omega_{\lambda_4}}\right)^{\frac{1}{2}} \sum_{\substack{\kappa_1\kappa_2\kappa_3\kappa_4\\ \alpha_1\alpha_2\alpha_3\alpha_4}} \frac{\partial^2\Psi^{\kappa_1\kappa_2}_{\alpha_1\alpha_2}(\mathbf{q}_1,\mathbf{q}_2)}{\partial u^{\kappa_3}_{\alpha_3}(\mathbf{q}_3)u^{\kappa_4}_{\alpha_4}(\mathbf{q}_4)} \times \frac{\varepsilon^{\kappa_1}_{\alpha_1}(\lambda_1)}{\sqrt{M_{\kappa_1}}}\frac{\varepsilon^{\kappa_2}_{\alpha_2}(\lambda_2)}{\sqrt{M_{\kappa_2}}}\frac{\varepsilon^{\kappa_3}_{\alpha_3}(\lambda_3)}{\sqrt{M_{\kappa_3}}}\cdot\frac{\varepsilon^{\kappa_4}_{\alpha_4}(\lambda_4)}{\sqrt{M_{\kappa_4}}}\cdot$$

6.3 Quantum Field Theory of Anharmonic Phonons

Much of the quantum field theory of phonons was developed in the 1960s with seminal works by Cowley [1], Thouless [7], Alekseev [2], Kadanoff and Baym [3] and later by Wallis, Maradudin and Fein [5]. This powerful technique permitted the self-energy of phonons to be calculated rigorously and led to theoretical predictions for the imaginary part of the relative permittivity at frequencies below the transverse optic phonon. In Dirac notation, the one-phonon Green function for an eigenstate $|i\rangle$ is defined

$$G(\mathbf{q}j,\mathbf{q}'j';t) = \langle i|\mathcal{T}[A(\mathbf{q}j;t)A^\dagger(\mathbf{q}'j';0)]|i\rangle,$$

where $A(\mathbf{q}j;t)$ is the time-dependent normal-mode field operator for a phonon with wavevector $\boldsymbol{q}$ on branch j in the Heisenberg representation,

$$A(\mathbf{q}j;t) = e^{iHt/\hbar}A(\mathbf{q}j;0)e^{-iHt/\hbar}$$

and $\mathcal{T}$is the Dyson chronological operator, which orders operators with earlier times to the right:

$$\mathcal{T}O_1(t_1)O_2(t_2) = \begin{cases} O_1(t_1)O_2(t_2) & (t_1 > t_2),\\ O_2(t_2)O_1(t_1) & (t_2 > t_1). \end{cases}$$

The one-phonon Green function G is zero unless $\mathbf{q}-\mathbf{q}' = \boldsymbol{Q}$, where $\mathbf{Q}$ is a reciprocal lattice vector. In what follows, $\mathbf{Q} = 0$ and $\mathbf{q} = \mathbf{q}'$, unless otherwise stated. We now take the thermal average of the Green function:

$$\begin{aligned} G(\mathbf{q}jj';t) &= \frac{1}{Z}\sum_i e^{-\beta H}\langle i|\mathcal{T}[A(\mathbf{q}j;t)A^\dagger(\mathbf{q}j';0)]|i\rangle\\ &= \frac{1}{Z}\sum_i \langle i|e^{-\beta H}\mathcal{T}[A(\mathbf{q}j;t)A^\dagger(\mathbf{q}j';0)]|i\rangle\\ &= \langle\mathcal{T}[A(\mathbf{q}j;t)A^\dagger(\mathbf{q}j';0)]\rangle \end{aligned}$$

where the partition function Z, in the absence of a chemical potential is defined as

$$\begin{aligned} Z &= \sum_i \langle i|e^{-\beta H}|i\rangle \\ &= \mathrm{Tr}\left\{e^{-\beta H}\right\} \end{aligned}$$

and $\beta = 1/k_B T$. Introducing the Matsubara imaginary time change of variable $\tau = it$, the Green functions cease to be time-dependent and become dependent on the 'temperature' τ.

$$G(\boldsymbol{q}\, jj'; \tau) = \begin{cases} Z^{-1}\mathrm{Tr}\left\{e^{-(\beta-\tau/\hbar)H} A(\mathbf{q}j) e^{-\tau H/\hbar} A^\dagger(\mathbf{q}j')\right\}, & \tau > 0 \\ Z^{-1}\mathrm{Tr}\left\{e^{-\beta H} A^\dagger(\mathbf{q}j') e^{\tau H/\hbar} A(\mathbf{q}j) e^{-\tau H/\hbar}\right\}. & \tau < 0 \end{cases}$$

The trace is defined for a general operator A, as

$$\mathrm{Tr}\{A\} = \sum_i \langle i|A|i\rangle$$

where the states i span the complete set of orthonormal functions. The trace has some very interesting and important properties [8, 9]. The completeness relation states that

$$\sum_f |f\rangle\langle f| = 1$$

and it can be shown that it has the same value whichever complete set is chosen to perform the summation. This is easily shown as follows:

$$\sum_i \langle i|A|i\rangle = \sum_{if} \langle i|f\rangle\langle f|A|i\rangle = \sum_{if} \langle f|A|i\rangle\langle i|f\rangle = \sum_f \langle f|A|f\rangle.$$

If the operator A is taken as the product of a number of operators $A_1, A_2, \ldots, A_N$, the cyclic property of the trace follows from the completeness relation:

$$\mathrm{Tr}\{A_1 \ldots A_{N-1} A_N\} = \mathrm{Tr}\{A_N A_1 \ldots A_{N-1}\}.$$

If we suppose that the imaginary time τ lies in the range $-\beta\hbar < \tau < 0$, then it follows that $\tau + \beta\hbar > 0$ and using the cyclic property of the trace:

$$\begin{aligned} G(\mathbf{q}jj'; \tau + \beta\hbar) &= Z^{-1}\mathrm{Tr}\{e^{\tau H/\hbar} A(\mathbf{q}j) e^{-\tau H/\hbar} e^{-\beta H} A^\dagger(\mathbf{q}j')\} \\ &= Z^{-1}\mathrm{Tr}\{e^{-\beta H} A^\dagger(\mathbf{q}j') e^{\tau H/\hbar} A(\mathbf{q}j) e^{-\tau H/\hbar}\} \\ &= G(\mathbf{q}jj'; \tau). \end{aligned} \tag{6.3.1}$$

This remarkable feature demonstrates the $\beta\hbar$ periodicity of the Matsubara imaginary time, suggesting that the Green function can be expanded into a discrete Fourier series

$$G(\mathbf{q}jj';\tau) = \sum_{n=-\infty}^{\infty} G(\mathbf{q}jj';i\omega_n)e^{i\omega_n\tau}$$

where $\omega_n = 2\pi n/\beta\hbar$, provided that $-\beta\hbar < \tau < 0$. The Fourier coefficients

$$\begin{aligned} G(\mathbf{q}jj';i\omega_n) &= \frac{1}{\beta\hbar}\int_0^{\beta\hbar} G(\mathbf{q}jj';\tau)e^{-i\omega_n\tau}\,\mathrm{d}\tau \\ &= \frac{1}{\beta\hbar}\int_0^{\beta\hbar} \langle \mathcal{T}[A(\mathbf{q}j;\tau)A^{\dagger}(\mathbf{q}j';0)]\rangle e^{-i\omega_n\tau}\,\mathrm{d}\tau \end{aligned}$$

are only defined at the infinite set of points $i\omega_n$, but are connected to the retarded Green function by analytical continuation of the imaginary axis into the upper complex frequency half-plane by the relation:

$$G^R(\mathbf{q}jj';\omega) = -\beta \lim_{\gamma\to 0^+} G(\mathbf{q}jj';\omega + i\gamma).$$

A spectral representation of the Green function, $\rho(\boldsymbol{q}jj',\omega)$ can be formulated by introducing the spectral density function

$$G(\boldsymbol{q}jj';i\omega_n) = \frac{1}{\beta\hbar}\int_{-\infty}^{\infty} \frac{\rho(\boldsymbol{q}jj';\omega)}{\omega + i\omega_n} d\omega.$$

In the harmonic approximation the bare Green function propagator can be shown to be

$$G_0(\mathbf{q}j;\tau) = \frac{e^{-\tau\omega(\mathbf{q}j)}}{1 - e^{-\hbar\beta\omega(\mathbf{q}j)}} + \frac{e^{\tau\omega(\mathbf{q}j)}}{1 - e^{\hbar\beta\omega(\mathbf{q}j)}}$$

where $j = j'$ and its transform:

$$\begin{aligned} G_0(\mathbf{q}j;i\omega_n) &= \frac{1}{\hbar\beta}\left[\frac{1}{\omega(\mathbf{q}j) + i\omega_n} + \frac{1}{\omega(\mathbf{q}j) - i\omega_n}\right] \\ &= \frac{\delta_{jj'}}{\hbar\beta}\frac{2\omega(\mathbf{q}j)}{\omega(\mathbf{q}j)^2 + \omega_n^2}. \end{aligned}$$

The spectral density function for the harmonic case is

$$\rho_0(\mathbf{q}j;\omega) = \delta(\omega - \omega(\mathbf{q}j)) - \delta(\omega + \omega(\mathbf{q}j))$$

which consists of two delta functions at the poles $i\omega_n = \pm\omega(\mathbf{q}j)$ where $\omega(\mathbf{q}j)$ are the phonon frequencies. Phonon–phonon interactions alter the form of the Green function

by shifting the poles off the imaginary axis by an amount corresponding to the complex self-energy $\Sigma = \Delta + i\Gamma$. The delta functions then broaden into Lorentzian functions with spectral densities of the form:

$$\rho(\mathbf{q}j;w) = \frac{2\Gamma(\mathbf{q}j)}{\left[\omega - \Omega(\mathbf{q}j)\right]^2 + \Gamma(\mathbf{q}j)^2} - \frac{2\Gamma(\mathbf{q}j)}{\left[\omega + \Omega(\mathbf{q}j)\right]^2 + \Gamma(\mathbf{q}j)^2}.$$

6.4 The Evolution Operator

Introducing the perturbation development or evolution operator $S(\tau_1, \tau_2)$:

$$S(\tau_1,\tau_2) = 1 + \sum_{n=1}^{\infty} \frac{(-1)^n}{n!} \int_{\tau_1}^{\tau_2} \mathrm{d}\tau_1 \int_{\tau_1}^{\tau_2} \mathrm{d}\tau_2 \ldots \int_{\tau_1}^{\tau_2} \mathrm{d}\tau_n \, \mathcal{T}\{H_A(\tau_1)\ldots H_A(\tau_n)\},$$

which operates on a harmonic system using the anharmonic Hamiltonian as a perturbation, generates many correlation functions of phonon field operators. Applying the evolution operator

$$S(\beta\hbar;0) = 1 + \sum_{n=1}^{\infty} \frac{(-1)^n}{n!} \int_{0}^{\beta} \mathrm{d}\tau_1 \int_{0}^{\beta} \mathrm{d}\tau_2 \ldots \int_{0}^{\beta} \mathrm{d}\tau_n \, \mathcal{T}\{H_A(\tau_1)\ldots H_A(\tau_n)\},$$

to the Green function:

$$G(\mathbf{q}jj';\tau) = \langle S(\beta\hbar;0)\rangle_0^{-1} \langle \mathcal{T}[A(\mathbf{q}j;\tau)A^{\dagger}(\mathbf{q}j')S(\beta\hbar;0)]\rangle_0 \tag{6.4.1}$$

where the thermal average is that of the harmonic system, results in a series expansion for the Green function of the form:

$$G(\mathbf{q}jj';\tau) = G^{(0)}(\mathbf{q}jj';\tau) + G^{(1)}(\mathbf{q}jj';\tau) + \cdots + G^{(n)}(\mathbf{q}jj';\tau) + \cdots$$

where the terms follow the order of the expansion in n and the first term is the harmonic phonon propagator G_0. Higher order terms involve pairs of phonon field operators which can be visualised using Feynman diagrams and classified into *connected* diagrams, those with a pair of external phonons entering and leaving the diagram and *disconnected* diagrams, those that do not. The disconnected diagrams are cancelled exactly by terms in the denominator of the Green function expansion and hence do not contribute to the self-energy. Of the connected diagrams, if it is possible to separate the external phonon lines by severing a single internal line, then the diagram is said to be *reducible* and can be broken into a series of *irreducible* diagrams. An elegant way of generating the Feynman diagrams up to a prescribed order using a double-time Green function approach was proposed by Della Valle [10] and the results up to and including fourth-order are shown in Figs. 6.1 and 6.2 for frequency-independent and frequency-dependent cases. This approach lends

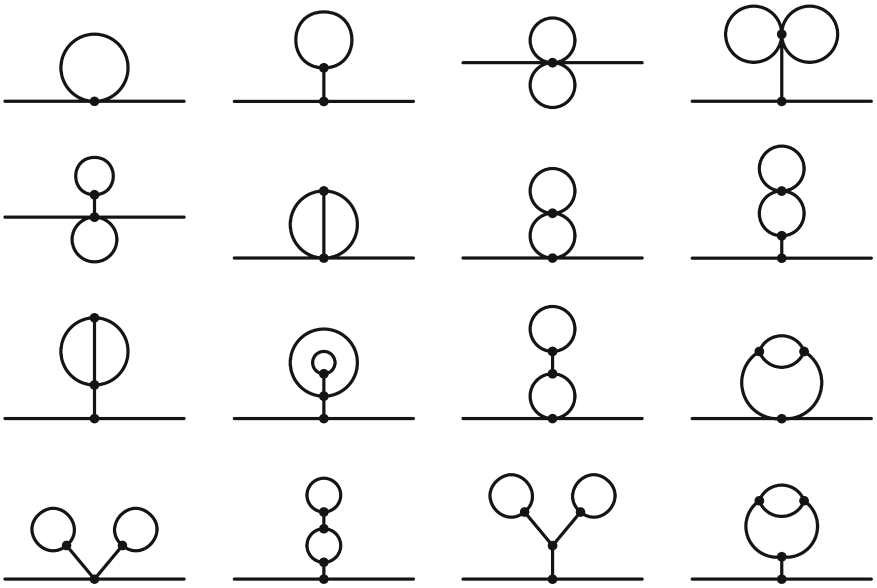

Fig. 6.1 Frequency-independent reducible Feynman diagrams up to fourth order. In order of expansion from *top-left* to *bottom-right* calculated using Della Valle's double-time Green function method [10]

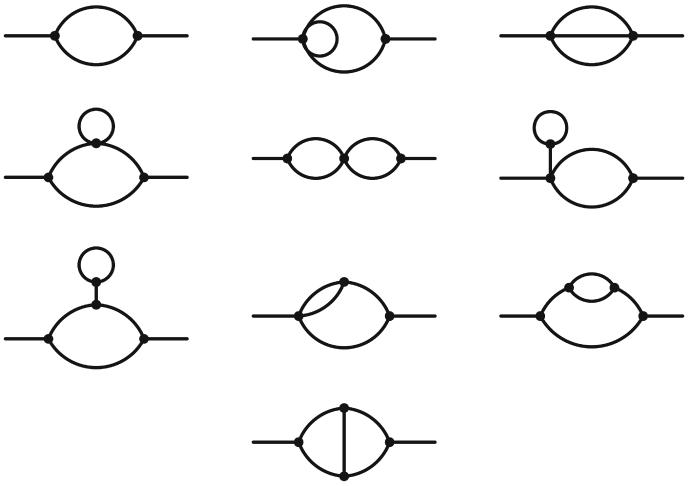

Fig. 6.2 Frequency-dependent reducible Feynman diagrams up to fourth-order. In order of expansion from *top-left* to *bottom-right* calculated using Della Valle's double-time Green function method [10]

itself well to an algorithmic or computational method of automatically generating all reducible diagrams up to a prescribed order.

6.5 Graphical Representation of Green Functions

To graphically represent the series for the Green function, $G(\mathbf{q}jj';\tau)$ a vertex exists for each time τ and anharmonic coupling coefficient V_m $(m = 3, 4, \ldots)$ from the anharmonic Hamiltonian. Lines are drawn between the vertices from τ_i to τ_j and associated with a phonon Green function $G_0(\mathbf{q}jj';\tau_i - \tau_j)$. Every line is labelled by a wavevector $\mathbf{q}$ and branch j. Momentum $\mathbf{q}$ and energy ω must be conserved at each vertex. The following method can be used to derive expressions for the self-energy of connected Feynman diagrams containing independent phonons with Green functions of the form $G_0(\mathbf{q}jj';i\omega_n)$ and n vertices.

1. Draw all topologically distinct and different connected diagrams containing n vertices.
2. Associate momenta $\mathbf{q}_i$, frequencies ω_n^i and branch j_i with each line such that external lines are labelled by $\mathbf{q}$, ω_n, j and crystal momentum and energy is conserved at every vertex.
3. Start with a $(-1/\beta\hbar)$ pre-factor.
4. Multiply by $(-\beta)^n$.
5. Multiply by the number of ways of pairing the phonon modes in the diagram, which comes from the symmetry of the vertex V_m in $(\mathbf{q}j\omega)$ and is essentially a combinatorial factor $(a) \times (b) \times (c)$ where
   (a) The number of topologically equivalent diagrams for a fixed arrangement of vertices.
   (b) The number of different labellings $\boldsymbol{q}_i$, j_i at each vertex for each pairing scheme.
   (c) The number of ways of permuting the m-phonon vertices.
6. Multiply by the appropriate anharmonic coupling coefficients V_m for each vertex.
7. For each internal line labelled λ_i, multiply by the phonon propagator $G_0(\mathbf{q}_i j_i; i\omega_n^i)$.
8. Sum over all momenta and branches $\lambda_i \equiv \{\mathbf{q}_i, j_i\}$ and frequencies ω_n^i.

6.6 Evaluating Matsubara Sums

The sums over n can be evaluated using contour integration [1, 3]. For instance, for the contour integral

$$\int_C f(i\omega)\bar{n}(i\omega)d(i\omega) \tag{6.6.1}$$

the contour C is taken around all singularities of the functions $f(i\omega)$ and $\bar{n}(i\omega)$ in the complex plane. If the function $f(i\omega)$ is well behaved and vanishes at infinity then the integral is equal to zero. The summation can then be evaluated in terms of the residues at the p poles of $f(i\omega)$ and n poles of $\bar{n}(i\omega)$;

$$0 = \sum_n R\left[\bar{n}(i\omega_n)\right] f(i\omega_n) + \sum_p R\left[f(i\omega_p)\right]\bar{n}(i\omega_p) \tag{6.6.2}$$

The function $\bar{n}(\omega)$ is the Bose–Einstein phonon population function:

$$\bar{n}(\omega) = \frac{1}{\exp(\beta\hbar\omega) - 1}, \tag{6.6.3}$$

which in the case of an imaginary frequency is

$$\bar{n}(i\omega) = \frac{1}{\exp(i\beta\hbar\omega) - 1}. \tag{6.6.4}$$

This function has singularities at

$$\omega_n = \frac{2\pi n}{\beta\hbar} \tag{6.6.5}$$

where $n \in Z$. The residues at these points are identical and equal to $(-i/\beta\hbar)$. We can therefore simplify

$$\sum_n f(i\omega_n) = \frac{\beta\hbar}{i}\sum_p R\left[f(i\omega_p)\right]\bar{n}(i\omega_p) \tag{6.6.6}$$

where the sum on the right is over the p poles of $f(i\omega)$.

6.7 The Self Energy, Σ

The sum of all irreducible connected diagrams (ones that cannot be split into two diagrams by severing a single propagator line) as shown in Fig 6.3 is known as the *self-energy*, Σ. It is obviously impossible to calculate the diagram series to infinite order and indeed it is also very difficult to calculate the diagrams above a few orders and so it is necessary to truncate the expansion at a point that is computationally convenient. We will now calculate some of the lowest order diagrams using the diagrammatic method and the Matsubara sum technique.

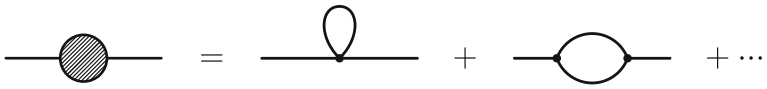

Fig. 6.3 Self-energy summation of irreducible diagrams. The *shaded circle* on the *left* represents the sum of all irreducible diagrams to infinite order

6.7.1 Loop Interaction

The lowest order anharmonic interaction is the 'loop' process shown in Fig. 6.4 and consists of a single fourth-order vertex connecting an internal phonon λ_1 with external phonons λ and λ'. An expression for the self-energy Σ_{loop} can be derived by using the rules for interpreting diagrams. There are twelve ways of pairing the phonon propagators with the single fourth-order vertex and one internal phonon propagator labelled λ_1, so the self-energy Σ_{loop} is given by

$$\Sigma_{loop} = \frac{12}{\hbar} \sum_{\lambda_1} \sum_{n_1} V_4(\lambda, -\lambda', \lambda_1, -\lambda_1) G_0(\lambda_1; i\omega_{n_1}), \tag{6.7.1}$$

where the bare Green function propagator is given by

$$G_0(\lambda; i\omega_n) = \frac{1}{\beta\hbar} \left\{ \frac{1}{\omega(\lambda) + i\omega_n} + \frac{1}{\omega(\lambda) - i\omega_n} \right\}.$$

To evaluate this using Matsubara sums, first note that $f(i\omega_{n_1}) = G_0(\lambda_1; i\omega_{n_1})$ has two poles at $i\omega_{n_1} = \pm\omega_1$ with residues $R[f(i\omega_{n_1})] = \pm i/\beta\hbar$, where $\omega_i \equiv \omega(\lambda_i)$ for brevity. This leads to

$$\begin{aligned} \sum_{n_1} G_0(\lambda_1; i\omega_{n_1}) &= \frac{\beta\hbar}{i} \sum_{p} R[f(i\omega_p)] \bar{n}(i\omega_p) \\ &= \frac{1}{\exp(\beta\hbar\omega_1) - 1} - \frac{1}{\exp(-\beta\hbar\omega_1) - 1} \\ &= \frac{2}{\exp(\beta\hbar\omega_1) - 1} + 1 \\ &= 2\bar{n}(\omega_1) + 1 \end{aligned}$$

where $\bar{n}(\omega_1)$ is the Bose–Einstein phonon population. Substituting the Matsubara sum into Eq. 6.7.1 results in a final expression for Σ_{loop}, the loop diagram self-energy:

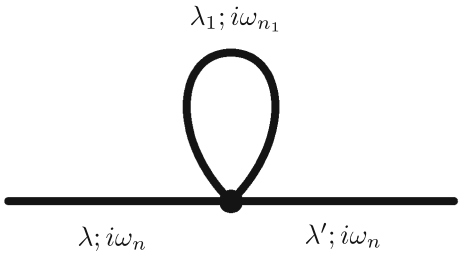

Fig. 6.4 Feynman diagram of 'Loop' interaction

$$\Sigma_{loop} = \frac{12}{\hbar} \sum_{\lambda_1} V_4(\lambda, -\lambda', \lambda_1, -\lambda_1) \left[2\bar{n}(\omega_1) + 1\right]. \tag{6.7.2}$$

Note that this self-energy is *frequency-independent* because the frequency of the $\lambda \equiv \lambda'$ phonon modes does not enter the expression. This manifests as the self-energy being a purely real shift in the frequency of the phonon, $\Sigma_{\text{loop}} = \Delta_{\text{loop}}$. The fourth-order vertex is given by

$$\begin{aligned} V_4(\lambda, -\lambda', \lambda_1, -\lambda_1) = {} & V_4(\mathbf{q}j_1, -\mathbf{q}j_2, \mathbf{0}j, \mathbf{0}j) \\ & \times \left(\frac{\hbar^2}{16N^4 \omega_{\mathbf{q}j_1} \omega_{-\mathbf{q}j_2} \omega_{\mathbf{0}j} \omega_{\mathbf{0}j}} \right)^{\frac{1}{2}} \sum_{\substack{\kappa_1\kappa_2\kappa_3\kappa_4 \\ \alpha_1\alpha_2\alpha_3\alpha_4}} \frac{\partial^2}{\partial u^{\kappa_3}_{\alpha_3}(\mathbf{0}) u^{\kappa_4}_{\alpha_4}(\mathbf{0})} \Psi^{\kappa_1\kappa_2}_{\alpha_1\alpha_2}(\mathbf{q}, -\mathbf{q}) \\ & \times \frac{\varepsilon^{\kappa_1}_{\alpha_1}(\mathbf{q}j_1)}{\sqrt{M_{\kappa_1}}} \frac{\varepsilon^{\kappa_2}_{\alpha_2}(-\mathbf{q}j_2)}{\sqrt{M_{\kappa_2}}} \frac{\varepsilon^{\kappa_3}_{\alpha_3}(\mathbf{0}j)}{\sqrt{M_{\kappa_3}}} \cdot \frac{\varepsilon^{\kappa_4}_{\alpha_4}(\mathbf{0}j)}{\sqrt{M_{\kappa_4}}}. \end{aligned} \tag{6.7.3}$$

where momentum and energy is conserved.

6.7.2 Bubble Interaction

The next anharmonic phonon interaction is the 'bubble' process shown in Fig. 6.5, which consists of two third-order anharmonic vertices which couple the external phonons to two internal phonons λ_1 and λ_2. To derive the self-energy Σ_{bubble}, again the rules can be followed, first noting that there are two vertices and eighteen ways of pairing the phonons, so the pre-factor is $(-18\beta/\hbar)$. The self-energy Σ_{bubble} can then be written:

$$\Sigma_{\text{bubble}} = -\frac{18\beta}{\hbar} \sum_{\lambda_1,\lambda_2} \sum_{n_1} V_3(\lambda, -\lambda_1, -\lambda_2) V_3(-\lambda', \lambda_1, \lambda_2) G_0(\lambda_1; i\omega_{n_1}) G_0(\lambda_2; i\omega_n - i\omega_{n_1}). \tag{6.7.4}$$

To evaluate the Matsubara sum, the poles and residues of

$$f(i\omega_n) = G_0(\lambda_1; i\omega_{n_1}) G_0(\lambda_2; i\omega_n - i\omega_{n_1})$$

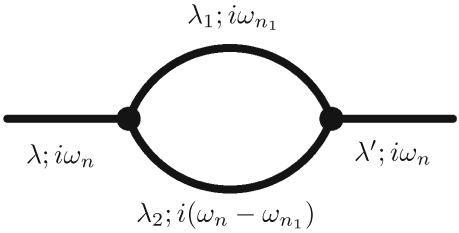

Fig. 6.5 Feynman diagram of 'bubble' interaction

must be found where the bare phonon propagator is given by

$$G_0(\lambda; i\omega_n) = \frac{1}{\beta\hbar}\left\{\frac{1}{\omega(\lambda) + i\omega_n} + \frac{1}{\omega(\lambda) - i\omega_n}\right\}.$$

In the following treatment, $\omega(\lambda_i)$ will be abbreviated by ω_i. Substituting the bare phonon propagator yields:

$$f(i\omega_n) = \frac{1}{(\beta\hbar)^2}\left\{\frac{1}{\omega_1 + i\omega_{n_1}} + \frac{1}{\omega_1 - i\omega_{n_1}}\right\}\left\{\frac{1}{\omega_2 + i(\omega_n - \omega_{n_1})} + \frac{1}{\omega_2 - i(\omega_n - \omega_{n_1})}\right\}. \tag{6.7.5}$$

The poles of $f(i\omega_n)$ occur for $i\omega_{n_1} = \pm\omega_1$ and $i\omega_n - i\omega_{n_1} = \pm\omega_2$. For the pole at $i\omega_{n_1} = +\omega_1$, the residue is

$$\frac{+i}{(\beta\hbar)^2}\left\{\frac{1}{\omega_2 + i\omega_n - \omega_1} + \frac{1}{\omega_2 - i\omega_n + \omega_1}\right\}.$$

For the pole at $i\omega_{n_1} = -\omega_1$, the residue is

$$\frac{-i}{(\beta\hbar)^2}\left\{\frac{1}{\omega_2 + i\omega_n + \omega_1} + \frac{1}{\omega_2 - i\omega_n - \omega_1}\right\}.$$

For the pole at $i\omega_{n_1} = +\omega_2 + i\omega_n$, the residue is

$$\frac{+i}{(\beta\hbar)^2}\left\{\frac{1}{\omega_1 + \omega_2 + i\omega_n} + \frac{1}{\omega_1 - \omega_2 - i\omega_n}\right\}.$$

and finally for the pole at $i\omega_{n_1} = -\omega_2 + i\omega_n$, the residue is

$$\frac{-i}{(\beta\hbar)^2}\left\{\frac{1}{\omega_1 - \omega_2 + i\omega_n} + \frac{1}{\omega_1 + \omega_2 - i\omega_n}\right\}.$$

Using the identity $-\bar{n}(-\omega) = \bar{n}(\omega) + 1$ and the fact that $\bar{n}(\omega + i\omega_n) = \bar{n}(\omega)$ due to $\omega_n = 2\pi n/\beta\hbar$, then after some algebra the summation over $\bar{n}(\omega_1)$ is found to be equal to

$$\frac{1}{\beta\hbar}\left\{\frac{\bar{n}(\omega_2) - \bar{n}(\omega_1)}{\omega_1 - \omega_2 - i\omega_n} + \frac{\bar{n}(\omega_1) + \bar{n}(\omega_2) + 1}{\omega_1 + \omega_2 - i\omega_n} + \frac{\bar{n}(\omega_1) + \bar{n}(\omega_2) + 1}{\omega_1 + \omega_2 + i\omega_n} + \frac{\bar{n}(\omega_1) - \bar{n}(\omega_1)}{\omega_1 - \omega_2 + i\omega_n}\right\}.$$

The self-energy for the bubble diagram, Σ_{bubble} is then

$$\Sigma_{\text{bubble}} = -\frac{18}{\hbar^2}\sum_{\lambda_1,\lambda_2} V_3(\lambda, -\lambda_1, -\lambda_2) V_3(-\lambda', \lambda_1, \lambda_2)$$

$$\times \left\{ [\bar{n}(\omega_2) - \bar{n}(\omega_1)] \left(\frac{1}{\omega_1 - \omega_2 - i\omega_n} + \frac{1}{\omega_1 - \omega_2 + i\omega_n} \right) \right.$$
$$\left. + [\bar{n}(\omega_1) + \bar{n}(\omega_2) + 1] \left(\frac{1}{\omega_1 + \omega_2 - i\omega_n} + \frac{1}{\omega_1 + \omega_2 + i\omega_n} \right) \right\}. \tag{6.7.6}$$

This expression is *frequency-dependent* due to the presence of terms containing $i\omega_n$. To obtain the real (phonon) frequency dependence of the self-energy we perform an analytic continuation of the point $i\omega_n$ from the imaginary axis and into the complex upper-plane by performing the change of variable:

$$i\omega_n \to \Omega + i\eta. \tag{6.7.7}$$

The denominators in the expression for Σ_{bubble} become;

$$\frac{1}{\omega + i\omega_n} \to \frac{1}{\omega + \Omega + i\eta} \tag{6.7.8}$$

The imaginary part η is an infinitesimal quantity introduced so that a Fourier transform remains consistent despite the singularity at $\omega = -\Omega$. Applying Sokhotskii's formula [11] in the limit $\eta \to 0$, yields:

$$\lim_{\eta \to 0^+} \left(\frac{1}{\omega + \Omega \pm i\eta} \right) = \wp \left(\frac{1}{\omega + \Omega} \right) \mp i\pi\delta(\omega + \Omega) \tag{6.7.9}$$

where $\wp$ indicates the Cauchy principal part of the expression inside the brackets. The self-energy is now a complex quantity given by $\Sigma = \Delta + i\Gamma$ where Δ and Γ are given by

$$\Delta_{\text{bubble}}(\Omega) = \frac{18}{\hbar^2} \sum_{\lambda_1, \lambda_2} V_3(\lambda, -\lambda_1, -\lambda_2) V_3(-\lambda', \lambda_1, \lambda_2)$$
$$\times \left\{ [\bar{n}(\omega_2) - \bar{n}(\omega_1)] \left[\wp \left(\frac{1}{\omega_1 - \omega_2 - \Omega} \right) + \wp \left(\frac{1}{\omega_1 - \omega_2 + \Omega} \right) \right] \right.$$
$$\left. + [\bar{n}(\omega_1) + \bar{n}(\omega_2) + 1] \left[\wp \left(\frac{1}{\omega_1 + \omega_2 - \Omega} \right) + \wp \left(\frac{1}{\omega_1 + \omega_2 + \Omega} \right) \right] \right\}$$

and

$$\Gamma_{\text{bubble}}(\Omega) = \frac{18}{\hbar^2} \sum_{\lambda_1, \lambda_2} V_3(\lambda, -\lambda_1, -\lambda_2) V_3(-\lambda', \lambda_1, \lambda_2)$$
$$\times \{ [\bar{n}(\omega_2) - \bar{n}(\omega_1)] [\delta(\omega_1 - \omega_2 - \Omega) + \delta(\omega_1 - \omega_2 + \Omega)]$$
$$+ [\bar{n}(\omega_1) + \bar{n}(\omega_2) + 1] [\delta(\omega_1 + \omega_2 - \Omega) + \delta(\omega_1 + \omega_2 + \Omega)] \}.$$

The real part, Δ is a temperature and frequency-dependent shift in the phonon frequency whereas the imaginary part, Γ is responsible for giving the phonon a finite lifetime. The real and imaginary parts of the self-energy are related by Kramers–Kronig transformations. Inspection of the above expression reveals that the argument of the delta function $\delta(\omega_1 + \omega_2 + \Omega)$ only vanishes when $\omega_1 = \omega_2 = \Omega = 0$ which obviously does not contribute to Γ at zero frequency and can therefore be neglected. The anharmonic coupling coefficients are also symmetrical in λ_1 and λ_2, leading to further simplification:

$$\Gamma_{\text{bubble}}(\Omega) = \frac{18}{\hbar^2} \sum_{\lambda_1,\lambda_2} |V_3(\lambda, \lambda_1, \lambda_2)|^2 \times \{[\bar{n}(\omega_2) - \bar{n}(\omega_1)] + [\delta(\omega_1 - \omega_2 - \Omega) + \delta(\omega_1 - \omega_2 + \Omega)] + [\bar{n}(\omega_1) + \bar{n}(\omega_2) + 1]\,\delta(\omega_1 + \omega_2 - \Omega)\}\,.$$

For a zone centre transverse optic (TO) phonon mode with $\lambda, \lambda' = \{\mathbf{q} = 0, j\}$, momentum conservation at the vertices dictates that the internal modes λ_1 and λ_2, whilst residing on different branches, have equal yet opposite wavevectors $\mathbf{q}$. The third-order dynamical tensor in this case is given by the derivative of the dynamical matrix

$$\begin{aligned} V_3(\lambda, \lambda_1, \lambda_2) &= V_3(\mathbf{0}j, \mathbf{q}j_1, -\mathbf{q}j_2) \\ &= \left(\frac{\hbar}{8N^3\omega_{\mathbf{0}j}\omega_{\mathbf{q}j_1}\omega_{-\mathbf{q}j_2}}\right)^{\frac{1}{2}} \sum_{\substack{\kappa_1\kappa_2\kappa_3 \\ \alpha_1\alpha_2\alpha_3}} \frac{\partial}{\partial u^{\kappa_3}_{\alpha_3}(\mathbf{0})} \Psi^{\kappa_1\kappa_2}_{\alpha_1\alpha_2}(\mathbf{q}, -\mathbf{q}) \\ &\times \frac{\varepsilon^{\kappa_3}_{\alpha_3}(\mathbf{0}j)}{\sqrt{M_{\kappa_3}}} \frac{\varepsilon^{\kappa_1}_{\alpha_1}(\mathbf{q}j_1)}{\sqrt{M_{\kappa_1}}} \frac{\varepsilon^{\kappa_2}_{\alpha_2}(-\mathbf{q}j_2)}{\sqrt{M_{\kappa_2}}}. \end{aligned} \tag{6.7.10}$$

6.7.3 *Higher Order Interactions*

It is worthwhile considering higher order interactions such as the one shown below in Fig. 6.6, with self-energy

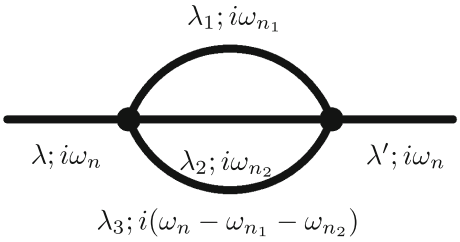

Fig. 6.6 Feynman diagram of higher order interaction

$$\Sigma_{\text{tri}} = -\frac{96}{\hbar^2}\sum_{n_1,n_2}\sum_{\lambda_1,\lambda_2,\lambda_3} V_4(\lambda,-\lambda_1,-\lambda_2,-\lambda_3)V_4(-\lambda',\lambda_1,\lambda_2,\lambda_3) \times G_0(\lambda_1;i\omega_{n_1})G_0(\lambda_2;i\omega_{n_2})G_0(\lambda_3;i\omega_n - i\omega_{n_1} - i\omega_{n_2}). \tag{6.7.11}$$

The above Green function product is

$$f(i\omega_{n_1}) = \frac{1}{(\beta\hbar)^3}\left\{\frac{1}{\omega_1 + i\omega_{n_1}} + \frac{1}{\omega_1 - i\omega_{n_1}}\right\}\left\{\frac{1}{\omega_2 + i\omega_{n_2}} + \frac{1}{\omega_2 - i\omega_{n_2}}\right\} \times \left\{\frac{1}{\omega_3 + i(\omega_n - \omega_{n_1} - \omega_{n_2})} + \frac{1}{\omega_3 - i(\omega_n - \omega_{n_1} - \omega_{n_2})}\right\}$$

Poles occur for $i\omega_{n_1} = \pm\omega_1, i\omega_{n_2} \pm \omega_2, i\omega_n = \pm\omega_3 - (i\omega_{n_1} + i\omega_{n_2})$. For the pole at $i\omega_{n_1} = +\omega_1$, the residue is

$$\frac{+i}{(\beta\hbar)^3}\left\{\frac{1}{\omega_2 + i\omega_{n_2}} + \frac{1}{\omega_2 - i\omega_{n_2}}\right\}\left\{\frac{1}{\omega_3 - \omega_1 + i(\omega_n - \omega_{n_2})} + \frac{1}{\omega_3 + \omega_1 - i(\omega_n - \omega_{n_2}}\right\}.$$

For the pole at $i\omega_{n_1} = -\omega_1$, the residue is

$$\frac{+i}{(\beta\hbar)^3}\left\{\frac{1}{\omega_2 + i\omega_{n_2}} + \frac{1}{\omega_2 - i\omega_{n_2}}\right\}\left\{\frac{1}{\omega_3 + \omega_1 + i(\omega_n - \omega_{n_2})} + \frac{1}{\omega_3 - \omega_1 - i(\omega_n - \omega_{n_2}}\right\}.$$

For the pole at $i\omega_{n_2} = +\omega_2$, the residue is

$$\frac{+i}{(\beta\hbar)^3}\left\{\frac{1}{\omega_1 + i\omega_{n_1}} + \frac{1}{\omega_1 - i\omega_{n_1}}\right\}\left\{\frac{1}{\omega_3 - \omega_2 + i(\omega_n - \omega_{n_1})} + \frac{1}{\omega_3 + \omega_2 - i(\omega_n - \omega_{n_1}}\right\}.$$

For the pole at $i\omega_{n_2} = -\omega_2$, the residue is

$$\frac{+i}{(\beta\hbar)^3}\left\{\frac{1}{\omega_1 + i\omega_{n_1}} + \frac{1}{\omega_1 - i\omega_{n_1}}\right\}\left\{\frac{1}{\omega_3 + \omega_2 + i(\omega_n - \omega_{n_1})} + \frac{1}{\omega_3 - \omega_2 - i(\omega_n - \omega_{n_1}}\right\}.$$

For the pole at $i\omega_n = +\omega_3 - (i\omega_{n_1} + i\omega_{n_2})$, the residue is

$$\frac{-i}{(\beta\hbar)^3}\left\{\frac{1}{\omega_1 + \omega_3 - (i\omega_n + i\omega_{n_2})} + \frac{1}{\omega_1 - \omega_3 + (i\omega_n + i\omega_{n_2})}\right\} \times \left\{\frac{1}{\omega_2 + \omega_3 - (i\omega_{n_1} + i\omega_n)} + \frac{1}{\omega_2 - \omega_3 + (i\omega_{n_1} + i\omega_n)}\right\}.$$

For the pole at $i\omega_n = -\omega_3 - (i\omega_{n_1} + i\omega_{n_2})$, the residue is

$$\frac{-i}{(\beta\hbar)^3}\left\{\frac{1}{\omega_1 - \omega_3 - (i\omega_n + i\omega_{n_2})} + \frac{1}{\omega_1 + \omega_3 + (i\omega_n + i\omega_{n_2})}\right\} \times \left\{\frac{1}{\omega_2 - \omega_3 - (i\omega_{n_1} + i\omega_n)} + \frac{1}{\omega_2 + \omega_3 + (i\omega_{n_1} + i\omega_n)}\right\}.$$

After some algebra we obtain the real part of the self energy:

$$\Delta(\omega) = \frac{96}{\hbar^2}\sum_{\lambda_1\lambda_2\lambda_3} |V_4(\lambda, \lambda_1, \lambda_2, \lambda_3)|^2 \times \wp\left\{[(\bar{n}_1+1)(\bar{n}_2+1)(\bar{n}_3+1) - \bar{n}_1\bar{n}_2\bar{n}_3]\left(\frac{1}{\omega - \omega_1 - \omega_2 - \omega_3} - \frac{1}{\omega + \omega_1 + \omega_2 + \omega_3}\right)\right.$$
$$\left. + 3\,[\bar{n}_1(\bar{n}_2+1)(\bar{n}_3+1) - (\bar{n}_1+1)\bar{n}_2\bar{n}_3]\left(\frac{1}{\omega + \omega_1 - \omega_2 - \omega_3} - \frac{1}{\omega - \omega_1 + \omega_2 + \omega_3}\right)\right\}$$

and the imaginary part:

$$\Gamma(\omega) = \frac{96}{\hbar^2}\sum_{\lambda_1\lambda_2\lambda_3} |V_4(\lambda, \lambda_1, \lambda_2, \lambda_3)|^2 \times \{[(\bar{n}_1+1)(\bar{n}_2+1)(\bar{n}_3+1) - \bar{n}_1\bar{n}_2\bar{n}_3]\,[\delta(\omega - \omega_1 - \omega_2 - \omega_3) - \delta(\omega + \omega_1 + \omega_2 + \omega_3)]$$
$$+ 3\,[\bar{n}_1(\bar{n}_2+1)(\bar{n}_3+1) - (\bar{n}_1+1)\bar{n}_2\bar{n}_3]\,[\delta(\omega + \omega_1 - \omega_2 - \omega_3) - \delta(\omega - \omega_1 + \omega_2 + \omega_3)]\},$$

where $\bar{n}(\omega_i)$ has been abbreviated by $\bar{n}_i$.

6.8 Dyson's Equation and Dressed Phonons

The diagram calculations so far have used the bare non-interacting phonon Green function propagator G_0. A more accurate representation takes the actual self-energy of the interacting phonon into account. The self-energy Σ is the sum of all irreducible connected Feynman diagrams, yet the Green function still consists of an infinite chain of self-energy diagrams as shown in Fig. 6.7. This can be represented as the series:

$$G = G_0 + G_0\,\Sigma\,G_0 + G_0\,\Sigma\,G_0\Sigma\,G_0 + G_0\,\Sigma\,G_0\,\Sigma\,G_0\,\Sigma\,G_0 + \cdots$$

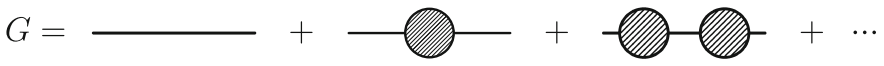

Fig. 6.7 Dyson's equation for the Green function. The *shaded circles* are the self-energy (summed reducible series of diagrams)

which can be factored to yield a much simplified and more elegant relation:

$$\begin{aligned} G &= G_0(1 + \Sigma\, G_0 + \Sigma\, G_0\, \Sigma\, G_0 + \Sigma\, G_0\, \Sigma\, G_0\, \Sigma\, G_0 + \cdots) \\ &= \frac{G_0}{1 - \Sigma\, G_0}. \end{aligned}$$

This is known as Dyson's equation and the resulting phonon propagator is described as *dressed* since it interacts with other phonons and acquires self-energy in doing so. If we take the Green function representing the free phonon propagator and assume $\lambda \equiv \{\mathbf{q}j\}$ for brevity, then

$$G_0(\lambda; i\omega_n) = \frac{1}{\beta\hbar}\left\{\frac{1}{\omega(\lambda) + i\omega_n} + \frac{1}{\omega(\lambda) - i\omega_n}\right\} = \frac{1}{\beta\hbar}\frac{2\omega(\lambda)}{\omega(\lambda)^2 + \omega_n^2}.$$

The dressed phonon propagator can be written using Dyson's equation

$$G(\lambda; i\omega_n) = \frac{G_0(\lambda; i\omega_n)}{1 - \Sigma(\lambda; i\omega_n)G_0(\lambda; i\omega_n)},$$

which upon substitution of the free phonon propagator $G_0(\lambda; i\omega_n)$ yields

$$G(\lambda; i\omega_n) = \frac{1}{\beta\hbar}\frac{2\omega(\lambda)}{\omega(\lambda)^2 + \omega_n^2 - 2\omega(\lambda)\Sigma(\lambda; i\omega_n)}.$$

The poles of $G(\lambda; i\omega_n)$ occur when

$$(i\omega_n)^2 = \omega(\lambda)^2 - 2\omega(\lambda)\Sigma(\lambda; i\omega_n),$$

which, if $\Sigma(\lambda; i\omega_n) \ll \omega(\lambda)$, can be approximated as

$$(i\omega_n) = \omega(\lambda) - \Sigma(\lambda; i\omega_n).$$

To see how this affects the previous diagram calculations we can replace the bare phonon propagator in the bubble diagram with a dressed phonon propagator as shown in Fig. 6.8. The calculations using Matsubara sums are similar, although the algebra

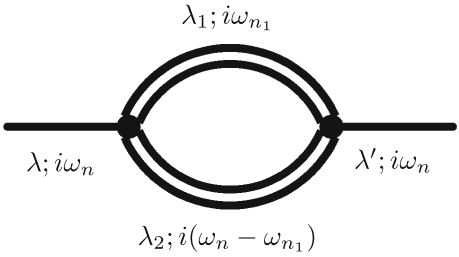

Fig. 6.8 Feynman diagram of 'bubble' interaction with dressed phonons

is slightly more tedious because the poles are complex. The imaginary part of the self energy, Γ is then

$$\Gamma_{\text{bubble}}(\Omega) = 18 \sum_{1,2} |V_3(0, TO; 1; 2)|^2 \times \frac{\bar{\Gamma}}{(\Omega - \omega_1 + \omega_2)^2 + \bar{\Gamma}^2} \left[n(\omega_1) - n(\omega_1 - \Omega) + n(\omega_2 + \Omega) - n(\omega_2) \right],$$

where the inverse lifetimes $\Gamma_1(\omega_1)$ and $\Gamma_2(\omega_2)$ of phonons λ_1 and λ_2 are assumed to be of similar order of magnitude and therefore replaced by an average value $\bar{\Gamma}$. Note that the delta functions become Lorentzians which provide a larger contribution when the inverse lifetime $\bar{\Gamma}$ is of similar magnitude to the frequency Ω. To include the effects of dressed phonon propagators in calculations of this kind therefore requires a self-consistent approach, where self-energies are calculated for all phonons on a grid spanning the Brillouin zone and the process repeated until convergence is achieved.

6.9 Summary and Conclusions

The lattice dynamics of anharmonic crystals were investigated, leading to a quantum field theory-based definition of the self-energy of phonons in the interaction representation. The graphical technique for evaluating Feynman diagrams of phonon–phonon interactions was reviewed and used to derive expressions for the lowest order contributions to the self-energy.

References

1. R.A. Cowley, Lattice dynamics of an anharmonic crystal. Adv. Phys. **12**, 421 (1963)
2. A.I. Alekseev, The application of the methods of quantum field theory in statistical physics. Sov. Phys. Uspekhi **4**, 23 (1961)
3. L.P. Kadanoff, G. Baym, *Quantum Statistical Mechanics: Green's Function Methods in Equilibrium and Nonequilibrium Problems* (Benjamin, New York, 1962)
4. M. Balkanski, R.F. Wallis, E. Haro, Anharmonic effects in light scattering due to optical phonons in silicon. Phys. Rev. B **28**, 1928 (1983)
5. R.F. Wallis, I.P. Ipatova, A.A. Maradudin, Temperature dependence of the width of the fundamental lattice vibration absorption peak in ionic crystals. Sov. Phys. Solid State **8**, 850 (1966)
6. M. Born, K. Huang, *Dynamical Theory of Crystal Lattices*, 1st edn. (Oxford University Press, Oxford, 1954)
7. D.J. Thouless, *Quantum Mechanics of Many-Body Systems* (Academic Press, New York, 1961)
8. W. Jones, N.H. March, *Theoretical Solid State Physics – Volume 1: Perfect Lattices in Equilibrium* (Wiley, New York, 1973)

9. A.A. Abrikosov, L.P. Gorkov, I.E. Dzyaloshinski, *Methods of Quantum Field Theory in Statistical Physics* (Prentice-Hall, Englewood Cliffs, 1963)
10. R.G. Della Valle, P. Procacci, Equation of motion for the Green's function in anharmonic solids. Phys. Rev. B **46**, 6141 (1992)
11. S. Weinberg, *The Quantum Theory of Fields*, vol. 2 (Cambridge University Press, Cambridge, 1996)

Chapter 7
Anharmonic Properties of MgO

7.1 Introduction

In this chapter, the anharmonic properties of Magnesium Oxide (MgO) will be investigated. The harmonic properties calculated using density functional perturbation theory (DFPT) in Chap. 5 and the quantum field theory (QFT) of anharmonic phonons developed in Chap. 6 will be combined to predict the temperature dependence of thermal expansion, dielectric loss and relative permittivity. MgO is studied here due to its simple crystal structure and phonon dispersion relations. Having only two atoms per unit cell makes calculations more manageable and computationally affordable whilst still retaining the generality of the theoretical framework and providing proof of principle.

7.2 Self-energy of Phonons

The self-energy for a phonon λ as a function of frequency Ω is

$$\Sigma_\lambda(\Omega) = \Delta_\lambda(\Omega) + i\Gamma_\lambda(\Omega), \tag{7.2.1}$$

where $\Delta_\lambda(\Omega)$ is a real-valued frequency shift and $\Gamma_\lambda(\Omega)$ is the linewidth. The lowest order anharmonic processes that contribute to the self-energy are shown in Fig. 7.1. The 'tadpole' diagram (a) is associated with thermal strain and is frequency independent. This means that it does not contribute to the imaginary part of the phonon self-energy Γ, only providing a shift in the real part $\Delta_\lambda^{\mathrm{T}}$. The 'loop' diagram (c) is also frequency independent like the 'tadpole' diagram and contributes a shift in the phonon frequency of $\Delta_\lambda^{\mathrm{L}}$. The 'bubble' diagram (b) is frequency dependent and therefore contributes to both the real and imaginary parts of the phonon self-energy,

J. Breeze, *Temperature and Frequency Dependence of Complex Permittivity in Metal Oxide Dielectrics: Theory, Modelling and Measurement*, Springer Theses, DOI 10.1007/978-3-319-44547-2_7

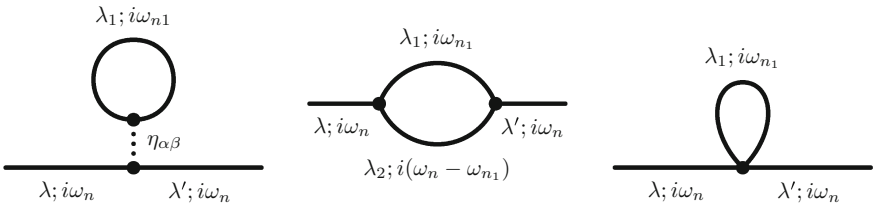

(a) Tadpole diagram. (b) Bubble diagram. (c) Loop diagram.

Fig. 7.1 Feynman diagrams for self-energy of transverse optical phonons

$\Sigma^{\mathrm{B}}_{\lambda}(\Omega) = \Delta^{\mathrm{B}}_{\lambda}(\Omega) + i\Gamma^{\mathrm{B}}_{\lambda}(\Omega)$. The diagrams in Fig. 7.1 can be summed to give an approximation for the self-energy;

$$\Sigma_{\lambda}(\Omega) \approx \Sigma^{\mathrm{T}}_{\lambda} + \Sigma^{\mathrm{B}}_{\lambda}(\Omega) + \Sigma^{\mathrm{L}}_{\lambda}. \tag{7.2.2}$$

Since the 'tadpole' and 'loop' diagrams only contribute to the real part of the self-energy, we can write

$$\begin{aligned} \Delta_{\lambda}(\Omega) &= \Delta^{\mathrm{T}}_{\lambda} + \Delta^{\mathrm{B}}_{\lambda}(\Omega) + \Delta^{\mathrm{L}}_{\lambda} \\ \Gamma_{\lambda}(\Omega) &= \Gamma^{\mathrm{B}}_{\lambda}(\Omega). \end{aligned} \tag{7.2.3}$$

The Hamiltonian of a crystal can be written in terms of phonon creation and annihilation operators, $a^{\dagger}(\lambda)$ and $a(\lambda)$, phonon eigenfrequencies ω_{λ} and phonon field operators $A(\lambda) = a(\lambda) + a^{\dagger}(\bar{\lambda})$,

$$H = \hbar \sum_{\lambda} \omega_{\lambda} \left[a^{\dagger}(\lambda)\, a(\lambda) + \frac{1}{2} \right] + H_A, \tag{7.2.4}$$

where the anharmonic Hamiltonian H_A is given by

$$\begin{aligned} H_A = &\sum_{\substack{\alpha\beta \\ \lambda\lambda'}} V_{\alpha\beta}(\lambda\lambda')\eta_{\alpha\beta}A(\lambda)A(\lambda') \\ &+ \sum_{\lambda_1\lambda_2\lambda_3} V(\lambda_1\lambda_2\lambda_3)A(\lambda_1)A(\lambda_2)A(\lambda_3) \\ &+ \sum_{\lambda_1\lambda_2\lambda_3\lambda_4} V(\lambda_1\lambda_2\lambda_3\lambda_4)A(\lambda_1)A(\lambda_2)A(\lambda_3)A(\lambda_4) + \ldots \end{aligned} \tag{7.2.5}$$

The first term in H_A is the *strain Hamiltonian* represented by the 'tadpole' diagram in Fig. 7.1a is associated with thermal strain $\eta_{\alpha\beta}$ of the unit cell. The real frequency shift Δ^{T} as a function of temperature is then representative of the change in phonon eigenfrequency due to thermal expansion. The contribution to Σ is

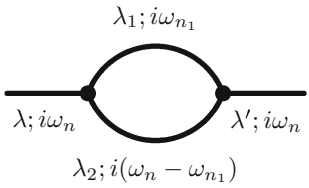

Fig. 7.2 Bubble diagram

$$\Delta^{\mathrm{T}} = \frac{2}{\hbar} \sum_{\alpha\beta} V_{\alpha\beta}(\lambda\lambda')\eta_{\alpha\beta}. \tag{7.2.6}$$

The 'bubble' diagram, Fig. 7.2, is the lowest order contribution to the frequency dependent imaginary part of the self-energy $\Gamma(\Omega)$, where a zone-centre transverse optical phonon $\lambda = \{\mathbf{0}, j_{TO}\}$ interacts with phonons $\lambda_1 = \{\mathbf{q}, j_1\}$ and $\lambda_2 = \{-\mathbf{q}, j_2\}$.

The expression for $\Gamma(\Omega)$ is

$$\Gamma(\Omega) = \frac{18}{\hbar^2} \sum_{\mathbf{q}j_1, -\mathbf{q}j_2} |V_3(\mathbf{0}j, \mathbf{q}j_1, -\mathbf{q}j_2)|^2 \times \tag{7.2.7}$$
$$\{(n_1 - n_2)\,\delta(\omega_2 - \omega_1 - \Omega) + (n_2 - n_1)\,\delta(\omega_1 - \omega_2 - \Omega) + (n_1 + n_2 + 1)\,\delta(\omega_1 + \omega_2 - \Omega)\}\,.$$

which involves a summation over a regular mesh of $\mathbf{q}$ points spanning the whole Brillouin zone. At each point the following quantities are required:

- Anharmonic coefficient $V_3(\mathbf{0}j, \mathbf{q}j_1, -\mathbf{q}j_2)$.
- Eigenfrequencies $\omega_i = \omega(\mathbf{q}j_i)$.
- The Bose–Einstein phonon occupation numbers n_i for phonons of frequency ω_i at temperature T.
- The delta functions $\delta(\omega_1 \pm \omega_2 \pm \Omega)$.

Previous attempts to calculate $\Gamma(\Omega)$ for silicon and germanium using Density Functional Perturbation Theory (DFPT) have been reported in the literature by Debernardi [1–4], Lang [5] and Deinzer [6] who found predictions to be in good agreement with Raman linewidth measurements although these calculations only took two-phonon summation processes into account. These are easier to calculate than difference processes since the decay channel only involves phonons at specific $\mathbf{q}$-points in the Brillouin zone where the energy conservation condition $\hbar\omega_{\mathrm{TO}} = \hbar\omega_1 + \hbar\omega_2$ is satisfied. This fact has allowed workers in the field to fit simplified equations such as

$$\Gamma_{\mathrm{TO}} = \Gamma_0(n_1 + n_2 + 1)$$

to the linewidth Γ_{TO} measured by Raman spectroscopy as a function of temperature.

7.3 The Effect of Isotopes on Self-energy

Both magnesium and oxygen are isotopic, occurring in nature with abundances shown in Table 7.1. The mean masses of Mg and O are 24.3051 and 15.9994 with variances of 0.437 and 0.009. It is well known that isotopic disorder within insulating crystals can cause phonon scattering [7]. In fact for crystals with high atomic mass variances such as TiO_2 and Ge which have mass variances of $\sigma^2_{Ti} = 0.659$ and $\sigma^2_{Ge} = 3.019$, the isotopic scattering is comparable with ordinary thermal scattering. At low temperatures, phonon scattering by isotopes can be the dominant scattering mechanism. This has been observed experimentally for thermal conductivity measurements as functions of temperature [8]. Recently, isotopically pure samples of Ge single crystals have become available allowing a comparison between the naturally occurring Ge and various isotopes. Measurements of the thermal conductivity, κ of isotopically pure Ge at 2 °K have shown that κ is up to 8 times higher than in naturally occurring Ge [9]. Similarly, measurements of the linewidths of optic phonons in various isotopic Ge samples using Raman spectroscopy have been reported [10, 11]. The self-energy due to isotopic disorder has been studied extensively, especially in recent years since the availability of isotopically pure elements. The bulk of the work has been on germanium since it has very dispersive acoustic phonons. Serrano et al. [12] found that the linewidth of the E_2 phonon in ZnO at 439 cm^{-1} varied by as much as a factor of 12 at 7° K by changing the isotopic composition. Tamura [13] applied perturbation theory to Green functions accompanied by mass fluctuations and more recently Widulle [14] calculated the phonon scattering rate in a mono-atomic crystal due to isotopic disorder using second-order perturbation theory and found the self-energy due to isotopic scattering to be

$$\Gamma_{\text{iso}} = \tau_{\text{iso}}^{-1} = g\frac{\pi}{6}\omega^2\rho^{(1)}(\omega), \tag{7.3.1}$$

where $\rho^{(1)}(\omega)$ is the one-phonon density of states and g is the mass variance parameter representing the level of isotopic disorder in the crystal given by

Table 7.1 Isotopes of Mg and O

Isotope	Abundance (%)	Atomic weight (amu)
^{12}Mg	78.990	23.985
^{13}Mg	10.000	24.986
^{14}Mg	11.010	25.983
^{8}O	99.756	15.9949
^{9}O	0.039	16.9991
^{10}O	0.205	17.9992

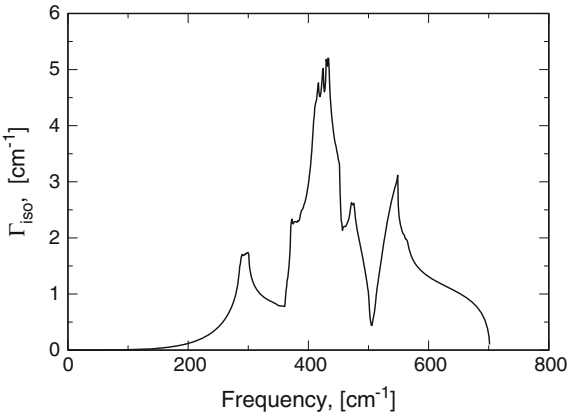

Fig. 7.3 Estimate of isotopic contribution to one-phonon self-energy in naturally occuring MgO

$$g = \sum_i f_i \left(\frac{\Delta M_i}{\bar{M}} \right)^2 . \tag{7.3.2}$$

The effect in a binary crystal such as MgO can be estimated as follows: for the case of the zone-centre transverse optic (TO) phonon at approximately 400 cm^{-1} for MgO, with $g_{\mathrm{Mg}} = 7.4 \times 10^{-4}$, $\rho^{(1)}(\omega) \approx 0.07$ states/cm^{-1}, $\Gamma_{\mathrm{iso}} \approx 3\ \mathrm{cm}^{-1}$ which is of the order of the measured linewidth of $6\,\mathrm{cm}^{-1}$. Since Γ_{iso} varies as ω^2, its value at microwave frequencies up to say 120 GHz ($\omega \approx 4\ \mathrm{cm}^{-1}$ and $\rho^{(1)}(\omega) \approx 10^{-7}$) is ten orders of magnitude smaller. This suggests that one-phonon processes do not contribute directly to the phonon self-energy at microwave frequencies. However, for two-phonon anharmonic processes between high-frequency phonons near the Brillouin zone boundary, the self-energy due to isotopic disorder may be significant. Figure 7.3 shows that the imaginary part of the phonon self-energy due to isotopic disorder in MgO has a similar shape to the one-phonon DOS as expected and is surprisingly significant above $300\,\mathrm{cm}^{-1}$. Unfortunately, without access to isotopically pure or purified MgO samples, it is impossible to draw any conclusions regarding the isotopic effect. Nevertheless, the possibility of such samples raises interesting questions which will be discussed further in the subsequent sections.

7.4 Linear Coefficient of Thermal Expansion

In the previous chapter, it was demonstrated that the harmonic properties of dielectrics, such as permittivity and phonon mode frequencies can be predicted accurately and efficiently from first principles using density functional perturbation theory (DFPT). However, real crystals are not harmonic and many important phenomena such as thermal conductivity, thermal expansion and sound absorption are due to the effect of anharmonic phonon interactions. The temperature dependence of the crystal

unit-cell volume is an example of a phenomenon due entirely to the anharmonicity of phonons and is therefore a good test of the ability to predict anharmonic effects from first principles using DFPT.

At absolute zero temperature ($T = 0$) and in the absence of external forces, the equilibrium atomic positions in a crystal occur at the minimum of the Helmholtz free energy:

$$F(T, V) = U(T, V) - TS(T, V),$$

where $U(T, V)$ is the potential energy and $S(T, V)$ is the entropy of the crystal. In the harmonic approximation the crystal can be considered as a collection of independent harmonic oscillators, so that the Helmholtz free energy can be expressed in vibrational terms:

$$F(V, T) = F^0(V) + F_{\mathrm{v}}(T, V),$$

where the $F^0(V)$ term corresponds to the free energy at $T = 0$, which can be written as

$$F^0(V) = \Phi^0(V) + F_{\mathrm{v}}^0(V),$$

where $\Phi^0(V)$ is the total energy and $F_v^0(V)$ is. $F_{\mathrm{v}}^0(V)$ is the zero-point vibrational energy:

$$F_{\mathrm{v}}^0(V) = \frac{1}{2} \sum_{\mathbf{q}j} \hbar\omega(\mathbf{q}j, V),$$

where $\omega(\mathbf{q}j)$ are the phonon eigenfrequencies at wave vector $\mathbf{q}$ on branch j at $T = 0$. The vibrational contribution to the Helmholtz free energy as a function of temperature is given by

$$F_{\mathrm{v}}(T) = \frac{1}{\beta} \sum_{\mathbf{q}j} \ln \left\{1 - \exp\left(-\beta\hbar\omega(\mathbf{q}j)\right)\right\}. \tag{7.4.1}$$

A consequence of neglecting phonon–phonon interactions in the harmonic approximation is that the equilibrium volume does not depend on temperature and the phonon eigenfrequencies do not depend on volume. Hence, in the harmonic approximation the linear coefficient of thermal expansion, defined by

$$\alpha(T) = \frac{1}{3V} \left.\frac{\partial V}{\partial T}\right|_P = -\frac{1}{3V} \left.\frac{\partial P}{\partial T}\right|_V \cdot \left.\frac{\partial V}{\partial P}\right|_T,$$

vanishes. Allowing the phonon eigenfrequencies $\omega(\mathbf{q}j)$ to be volume dependent leads to a modification of the vibrational part of the free energy

$$F_{\mathrm{v}}(T, V) = \frac{1}{\beta} \sum_{\mathbf{q}j} \ln \left\{1 - \exp\left[-\beta\hbar\omega_{\mathbf{q}j}(V)\right]\right\}. \tag{7.4.2}$$

This approximation is known as the *Quasi-Harmonic Approximation* (QHA). Expanding the free energy as a Taylor series about the equilibrium volume V_0 at $T = 0$:

$$F(T, V) = F(T, V_0) + (V - V_0)\left.\frac{\partial F(T, V)}{\partial V}\right|_{V_0} + \frac{1}{2}(V - V_0)^2\left.\frac{\partial^2 F(T, V)}{\partial V^2}\right|_{V_0} + \dots$$

yields the expansion coefficients:

$$\left.\frac{\partial F(T, V)}{\partial V}\right|_{V_0} = \left.\frac{\partial F^0(V)}{\partial V}\right|_{V_0} + \left.\frac{\partial F_{\text{vib}}(T, V)}{\partial V}\right|_{V_0}$$

and

$$\left.\frac{\partial^2 F(T, V)}{\partial V^2}\right|_{V_0} = \left.\frac{\partial^2 F^0(V)}{\partial V^2}\right|_{V_0} + \left.\frac{\partial^2 F_{\text{vib}}(T, V)}{\partial V^2}\right|_{V_0}.$$

At absolute zero temperature, the equilibrium volume V_0 is found by definition from

$$\left.\frac{\partial F^0(V)}{\partial V}\right|_{V_0} = 0,$$

and since the zero-point energy is only defined for V_0, the first-order coefficient is

$$\left.\frac{\partial F(T, V)}{\partial V}\right|_{T, V_0} = \left.\frac{\partial F_{\text{vib}}(T, V)}{\partial V}\right|_{T, V_0}.$$

In the QHA, only first-order derivatives of the eigenfrequencies with respect to volume are considered, hence the second-order coefficient can be written as

$$\left.\frac{\partial^2 F(T, V)}{\partial V^2}\right|_{T, V_0} \approx \left.\frac{\partial^2 F^0(V)}{\partial V^2}\right|_{V_0} \approx \frac{B_0}{V_0},$$

where B_0 is the bulk modulus of the crystal at equilibrium:

$$B_0 = -V_0\left.\frac{\partial P}{\partial V}\right|_{V_0}.$$

The equation of state

$$\left.\frac{\partial F(T, V)}{\partial V}\right|_{T} = 0$$

then leads directly to an expression for the crystal volume as a function of temperature

$$V(T) = V_0 - \frac{V_0}{B_0}\left.\frac{\partial F_{\text{vib}}(T, V)}{\partial V}\right|_{T, V_0}.$$

Introducing the mode Grüneisen parameter,

$$\gamma(\mathbf{q}j) = -\frac{V_0}{\omega(\mathbf{q}j, V_0)} \left.\frac{\partial\omega(\mathbf{q}j, V)}{\partial V}\right|_{V=V_0},$$

a measure of the fractional change in a phonon mode eigenfrequency with respect to changes to the volume, leads to a simplified form

$$\begin{aligned} V(T) &= V_0 + \frac{1}{B_0}\sum_{\mathbf{q}j} \frac{\hbar\omega(\mathbf{q}j, V_0)}{\exp\left(\beta\hbar\omega(\mathbf{q}j, V_0)\right) - 1}\gamma(\mathbf{q}j) \\ &= V_0 + \frac{1}{B_0}\sum_{\mathbf{q}j} \hbar\omega(\mathbf{q}j)n[\omega(\mathbf{q}j, T]\gamma(\mathbf{q}j), , \end{aligned}$$

where $n[\omega(\mathbf{q}j, T)]$ is the Bose–Einstein phonon population. The linear coefficient of thermal expansion can then be derived straightforwardly as

$$\begin{aligned} \alpha(T) &= \frac{1}{3V}\frac{\partial V}{\partial T} \\ &= -\frac{1}{3\beta V}\frac{V_0}{B_0}\frac{\partial^2}{\partial T\partial V}\sum_{\mathbf{q}j}\ln\left[1 - \exp\left(-\hbar\beta\omega(\mathbf{q}j, V)\right)\right] \\ &= -\frac{\hbar}{3V}\frac{V_0}{B_0}\frac{\partial}{\partial T}\sum_{\mathbf{q}j}\left[\exp\left(\hbar\beta\omega(\mathbf{q}j, V)\right) - 1\right]^{-1} \left.\frac{\partial\omega(\mathbf{q}j, V)}{\partial V}\right|_{V_0}. \end{aligned}$$

This expression can be further simplified by introducing the modal contribution to the specific heat at constant volume for a single phonon, $c_v(\mathbf{q}j, T)$:

$$c_v(\mathbf{q}j, T) = \frac{\hbar\omega(\mathbf{q}j, V_0)}{V_0}\frac{\partial}{\partial T}\left[\exp\left(\hbar\beta\omega(\mathbf{q}j, V_0)\right) - 1\right]^{-1}.$$

The resulting compact form for the linear coefficient of thermal expansion is then

$$\alpha(T) = \frac{1}{3B_0}\sum_{\mathbf{q}j}\gamma(\mathbf{q}j)c_v(\mathbf{q}j, T). \tag{7.4.3}$$

Figure 7.4 shows the excellent agreement between the calculated and experimentally determined linear coefficients of thermal expansion for single-crystal MgO.

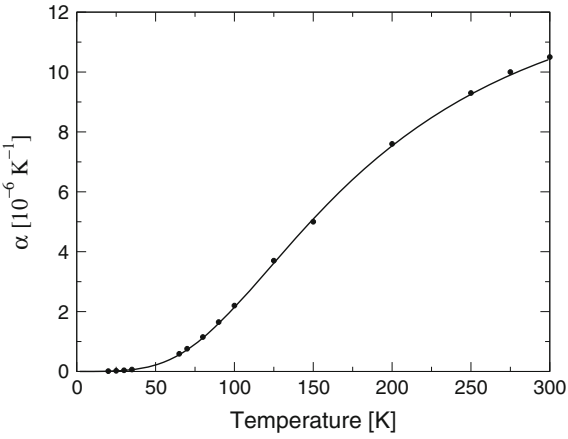

Fig. 7.4 Linear coefficient of thermal expansion α for MgO, calculated using the quasi-harmonic approximation (*solid line*). *Solid circles* are measured points by White and Anderson [15]

7.5 Thermal Strain Contribution to Phonon Self-energy

The real frequency shift of a phonon $\omega(\mathbf{q}j)$ with wave vector $\mathbf{q}$ on branch j due to thermal expansion, $\Delta^{\mathrm{T}}(\mathbf{q}j)$ can be calculated within the Quasi-Harmonic Approximation using the mode Grüneisen parameters and the expression for the volume as a function of temperature. Looking at the definition of the mode Grüneisen parameter,

$$\gamma(\mathbf{q}j) = -\frac{V_0}{\omega(\mathbf{q}j)}\frac{\partial\omega(\mathbf{q}j)}{\partial V}\bigg|_{V=V_0}$$

one can derive an expression for the change in the frequency $\Delta\omega(\mathbf{q}j)$ due to a change in volume ΔV:

$$\Delta\omega(\mathbf{q}j) = -\gamma(\mathbf{q}j)\omega(\mathbf{q}j)\frac{\Delta V}{V_0}.$$

and since

$$\Delta V = \hbar B_0^{-1}\sum_{\mathbf{q}j}\omega(\mathbf{q}j)n(\mathbf{q}j)\gamma(\mathbf{q}j),$$

an expression for the real frequency shift, $\Delta^T(\mathbf{q}j) = \Delta\omega(\mathbf{q}j)$, due to thermal strain can be found as

$$\Delta^T(\mathbf{q}j) = \Delta\omega(\mathbf{q}j) = -\frac{\gamma(\mathbf{q}j)\omega(\mathbf{q}j)\hbar}{V_0 B_0}\sum_{\mathbf{q}'j'}\omega(\mathbf{q}'j')n(\mathbf{q}'j')\gamma(\mathbf{q}'j'), \qquad (7.5.1)$$

where V_0 is the crystal unit-cell volume and B_0 is the Bulk modulus at absolute zero temperature. The mode Grüneisen parameters for the zone-centre TO and LO phonons in MgO were calculated to be $\gamma_T = 2.308$ and $\gamma_L = 1.148$. The real

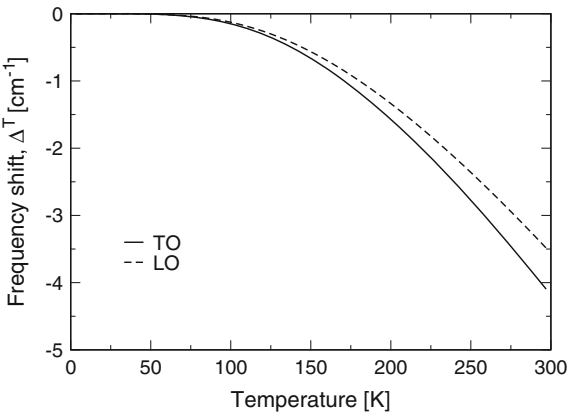

Fig. 7.5 Real frequency shift of zone-centre ($\mathbf{q} = 0$) transverse optical (TO) and longitudinal (LO) phonons due to thermal strain, calculated using the mode Grüneisen parameters, $\gamma_T = 2.308$ and $\gamma_L = 1.148$, within the quasi-harmonic approximation

frequency shifts for the TO and LO phonons of MgO were calculated using Eq. 7.5.1 and are shown in Fig. 7.5.

7.6 Temperature Coefficient of Permittivity

The static permittivity ε_r, expressed by the Lyddane–Sachs–Teller relation is dependent on the frequencies of the longitudinal and transverse optic phonon modes for an isotropic medium such as MgO,

$$\varepsilon_r = \varepsilon_\infty \frac{\omega_{\mathrm{L}}^2}{\omega_{\mathrm{T}}^2}. \tag{7.6.1}$$

The temperature coefficient of permittivity τ_ε, which is defined as

$$\tau_\varepsilon = \frac{1}{\varepsilon_r}\frac{\partial \varepsilon_r}{\partial T} \tag{7.6.2}$$

can be directly related to the mode Grüneisen parameters of the zone-centre ($\mathbf{q} = 0$) optic modes:

$$\begin{aligned}
\tau_\varepsilon &= \frac{1}{\varepsilon_r}\frac{\partial \varepsilon_r}{\partial T} \\
&= 2\frac{\partial V}{\partial T}\left(\frac{1}{\omega_{\mathrm{L}}}\frac{\partial \omega_{\mathrm{L}}}{\partial V} - \frac{1}{\omega_{\mathrm{T}}}\frac{\partial \omega_{\mathrm{T}}}{\partial V}\right) \\
&= \frac{2}{V_0}\frac{\partial V}{\partial T}\left(\gamma_{\mathrm{T}} - \gamma_{\mathrm{L}}\right) \\
&= \frac{6V\alpha}{V_0}\left(\gamma_{\mathrm{T}} - \gamma_{\mathrm{L}}\right).
\end{aligned}$$

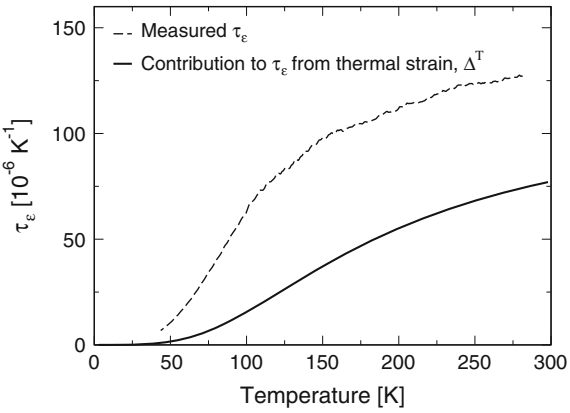

Fig. 7.6 Thermal strain contribution to temperature coefficient of permittivity τ_ε for MgO. Calculated contribution (*solid line*) and measured (*dashed line*). The measured data are from Chap. 3

If we take $V/V_0 \approx 1$ (since $V_{300}/V_0 = 1.004$), then

$$\tau_\varepsilon \approx 6\alpha\,(\gamma_\mathrm{T} - \gamma_\mathrm{L})\,.$$

Recalling that the mode Grüneisen parameters for the zone-centre optical phonons in MgO were calculated earlier to be $\gamma_T = 2.308$ and $\gamma_L = 1.148$, leads to an approximate relation for the thermal strain component of the τ_ε:

$$\tau_\varepsilon \approx 7\alpha,$$

where α is the linear coefficient of thermal expansion (Fig. 7.6).

7.7 Dielectric Loss

For a cubic system such as MgO, Gurevich's theory predicts that dielectric losses at low temperatures follow $\tan\delta \propto \omega^2 T^4$. These losses are mostly due to transitions between acoustic phonon branches due to their higher occupation at low temperatures compared with optical phonons. At higher temperatures where optical phonon branches become populated, losses are expected to follow $\tan\delta \propto \omega^2 T$. For MgO with two atoms per unit cell and possessing a single degenerate transverse optical (TO) mode, the complex relative permittivity as a function of field frequency, $\varepsilon(\omega)$ is

$$\varepsilon(\omega) = \varepsilon_\infty + \frac{\omega_\mathrm{TO}^2 \Delta\varepsilon}{\omega_\mathrm{TO}^2 - \omega^2 - 2i\omega_\mathrm{TO}\Gamma_\mathrm{TO}(\omega)},$$

where $\Delta\varepsilon = \varepsilon_0 - \varepsilon_\infty$, ε_0 is the static permittivity, ω_TO is the frequency and $\Gamma_\mathrm{TO}(\omega)$ is the relaxation frequency of the transverse optical mode. Since the microwave field frequency is very small compared to the transverse optical phonon frequency,

$\omega \ll \omega_{\mathrm{TO}}$, the real and imaginary parts of the complex permittivity, ε'' can be written as

$$\varepsilon'(\omega) \approx \varepsilon_0 \tag{7.7.1}$$

and

$$\varepsilon''(\omega) = \Delta\varepsilon \frac{2\Gamma_{\mathrm{TO}}(\omega)}{\omega_{\mathrm{TO}}}. \tag{7.7.2}$$

The loss tangent, $\tan\delta$, can then be simplified as

$$\tan\delta(\omega) = \frac{\Delta\varepsilon}{\varepsilon_0} \cdot \frac{2\Gamma_{\mathrm{TO}}(\omega)}{\omega_{\mathrm{TO}}}. \tag{7.7.3}$$

This expression shows that the loss tangent is inversely proportional to the frequency of the transverse optic mode. A rough estimate of the relaxation frequency at $\omega = 2\pi \times 8$ GHz and room temperature can be made for MgO, from knowledge of the $\tan\delta$. Since $\varepsilon'_{\alpha\beta}(0) \approx 9$, $\varepsilon_{\alpha\beta}(\infty) \approx 3$, $\tan\delta \approx 5 \times 10^{-6}$ and $\omega_j \approx 400$ cm^{-1} this yields $\Gamma(50\ \mathrm{GHz}) = 1.5 \times 10^{-3}$ cm^{-1}.

7.8 Phonon–Phonon Contribution to the Self-energy

The lowest order contribution to the frequency dependent and imaginary part $\Gamma(\Omega)$ of the TO phonon self-energy is the 'bubble' diagram Fig. 7.7, where a zone-centre transverse optical phonon $\lambda = \{\mathbf{0}, j_{TO}\}$ interacts with phonons $\lambda_1 = \{\mathbf{q}, j_1\}$ and $\lambda_2 = \{-\mathbf{q}, j_2\}$ on different branches.

The expression for $\Gamma(\Omega)$ is

$$\Gamma(\Omega) = \frac{18}{\hbar^2} \sum_{\mathbf{q}j_1,-\mathbf{q}j_2} |V_3(\mathbf{0}j, \mathbf{q}j_1, -\mathbf{q}j_2)|^2 \times \{2(n_1 - n_2)\,\delta(\omega_2 - \omega_1 - \Omega) + (n_1 + n_2 + 1)\,\delta(\omega_1 + \omega_2 - \Omega)\},$$

where $V_3(\mathbf{0}j, \mathbf{q}j_1, -\mathbf{q}j_2)$ are the anharmonic coupling coefficients, n_i are the Bose–Einstein phonon occupation numbers, $\omega_i = \omega(\mathbf{q}j_i)$ are the eigenfrequencies for phonons with wave vector $\mathbf{q}$ on branch i and Ω is the frequency of the microwave

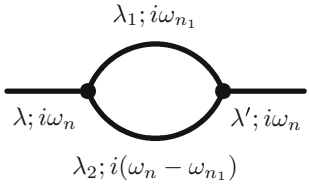

Fig. 7.7 Bubble diagram

field (now represented by a capitalised Greek letter to distinguish from phonon frequencies).

The Kronecker delta functions define points, lines and surfaces within the Brillouin zone, on which the energy conservation criteria are met. This provides valuable information and insight into the types of phonon–phonon interactions which contribute to the self-energy at particular frequencies and temperatures and the regions in reciprocal space in which they occur. The first delta function $\delta(\omega_2 - \omega_1 - \Omega)$ is represented by the Feynman diagrams shown in Fig. 7.8 and is known as a *difference process* since the difference in the energies of the two phonons $\omega_2 - \omega_1$ is an argument in the delta function. The second delta function $\delta(\omega_1 + \omega_2 - \Omega)$ is a *summation process* since a sum of the phonon energies, $\omega_1 + \omega_2$ is an argument. It is represented by the decay and coalescence Feynman diagrams in Fig. 7.9. The significance of the difference and summation processes will now be investigated further by paying attention to the *two-phonon density of states*.

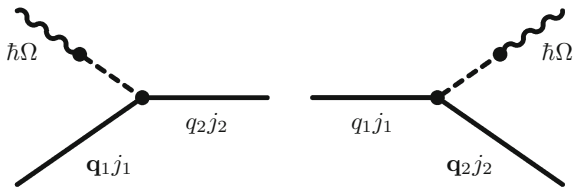

Fig. 7.8 **a** Diagram showing absorption of photon $\hbar\Omega$ by two-phonon difference process involving phonons $\boldsymbol{q}_1 j_1$, $\boldsymbol{q}_2 j_2$ and anharmonic optical phonon (*dashed line*). **b** Diagram showing emission of anharmonic phonon (*dashed line*) $\hbar\Omega$ by difference process between phonons $\boldsymbol{q}_1 j_1$ and $\boldsymbol{q}_2 j_2$, where $\boldsymbol{q}_1 = \boldsymbol{q}_2$

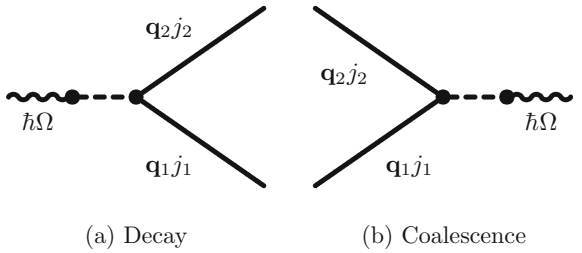

Fig. 7.9 **a** Diagram showing absorption of photon by two-phonon summation process where $\boldsymbol{q}_1 = -\boldsymbol{q}_2$ via anharmonic optical phonon decay. **b** Diagram showing emission of photon by two-phonon summation (combination) process where $\boldsymbol{q}_1 = -\boldsymbol{q}_2$

7.9 Two-Phonon Density of States

The two-phonon density of states (TPDOS), $\rho_2(\Omega)$ can be calculated in the same way as the phonon density of states, using Blöchl's improved tetrahedron method [16] for Brillouin zone integration of Kronecker delta functions of the form $\delta(\omega_{\mathbf{q}j'} \pm \omega_{-\mathbf{q}j} - \Omega)$, where $\mathbf{q}$ is the phonon wave vector and j labels the phonon branch. It can be split into two contributions by difference and summation processes over frequency bands in Ω for which the delta function arguments are satisfied:

$$\rho_2(\Omega) = \rho_2^-(\Omega) + \rho_2^+(\Omega) = \frac{1}{N}\sum_{\mathbf{q}jj'}\left[\delta(\omega_{\mathbf{q}j'} - \omega_{-\mathbf{q}j} - \Omega) + \delta(\omega_{\mathbf{q}j'} + \omega_{-\mathbf{q}j} - \Omega)\right],$$

where

$$\rho_2^-(\Omega) = \frac{1}{N}\sum_{\mathbf{q}jj'}\delta(\omega_{\mathbf{q}j'} - \omega_{-\mathbf{q}j} - \Omega) \tag{7.9.1}$$

and

$$\rho_2^+(\Omega) = \frac{1}{N}\sum_{\mathbf{q}jj'}\delta(\omega_{\mathbf{q}j'} + \omega_{-\mathbf{q}j} - \Omega). \tag{7.9.2}$$

The summations are taken over N $\mathbf{q}$-points for all phonon branches covering the Brillouin zone. Figure 7.10 shows the two-phonon density of states, $\rho_2(\Omega)$ calculated for MgO using Blöchl's improved tetrahedron method.

The difference-band is evident at low frequencies, increasing linearly very quickly up to about 0.5 THz and then decreasing steadily after 5.5 THz until it is negligible above 15 THz. The summation-band below these higher frequencies has a very low density of states (8 orders of magnitude less) due to the very small region

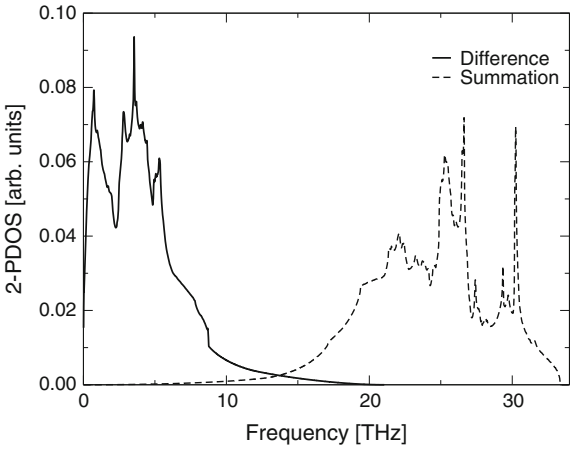

Fig. 7.10 Two-phonon difference-band and summation-band density of states for MgO. The difference-band plays the dominant role at low frequencies

within the Brillouin zone where energy is conserved, but comes into play at a much higher frequency band centred around 25 THz. Considering that the field frequencies of interest are in the sub-THz domain it follows that the summation processes can safely be neglected in the calculation of the TO mode self-energy $\Gamma_{\mathrm{TO}}(\Omega)$ for microwave and sub-millimetre wave field frequencies ($\Omega < 1$ THz) and that difference processes play the dominant role. Neglecting the summation-band processes leads to a simplified expression for the relaxation frequency:

$$\Gamma(\Omega) = \frac{36}{\hbar^2} \sum_{\mathbf{q}j_1,-\mathbf{q}j_2} |V_3(\mathbf{0}j, \mathbf{q}j_1, -\mathbf{q}j_2)|^2 \, (n_1 - n_2) \, \delta(\omega_2 - \omega_1 - \Omega). \qquad (7.9.3)$$

7.10 Energy Conservation Surfaces

The argument in the Kronecker delta function in (7.9.3) for the two-phonon difference-band contribution to the self-energy of the TO mode, $\Gamma_{\mathrm{TO}}(\Omega)$, is only satisfied at $\mathbf{q}$-points in the Brillouin zone where the following energy conservation criterion is satisfied:

$$\hbar\omega_2 - \hbar\omega_1 = \hbar\Omega,$$

where $\omega_2 > \omega_1$ are the frequencies of phonons on different branches and Ω is the microwave field frequency.

As the microwave frequency approaches zero, $\Omega \to 0$, energy conservation will occur around points, lines or surfaces in the Brillouin zone where the constant-frequency surfaces for different phonon eigenmode branches come into contact or intersect. The importance of the contact between constant-frequency surfaces of phonons was first noted by Herring [18, 19], who studied the effect of anharmonic interaction between acoustic phonons on sound absorption in crystals. It was found that constant-frequency surfaces intersected at points and along lines of high symmetry dependent on the group symmetry of the crystals. Balagurov et al. [20] then studied the effect of contact points on dielectric relaxation in cubic ferroelectrics and Gurevich [21–24] applied Herring's theory to study the role of acoustic phonons in microwave dielectric loss at low temperatures.

For transverse acoustic phonons in MgO, the intersection of the frequency isosurfaces is expected to occur along high-symmetry directions where the phonons are doubly degenerate as shown in Fig. 7.11. This would represent the limit of the field frequency going to zero, $\Omega \to 0$. For finite field frequencies, $\Omega > 0$, the lines would become cones whose radii would be a function of the modulus of the $\mathbf{q}$-vector. Figure 7.12 shows contours through a cross section of the Brillouin zone, where $\delta(\omega_1 - \omega_2 + \Omega)$ is satisfied for field frequencies Ω ranging from $1\,\mathrm{cm}^{-1}$ (30 GHz) to $28\,\mathrm{cm}^{-1}$ (840 GHz), where both ω_1 and ω_2 are transverse acoustic (TA) phonons. Along the Γ-K direction, the $\mathbf{q}$-points at which energy is conserved are a linear function of field frequency, $|\mathbf{q}|_\Omega \propto \Omega$, as one would expect for low-frequency linear dispersion phonons. For the $X - W$ direction along the edge of the Brillouin

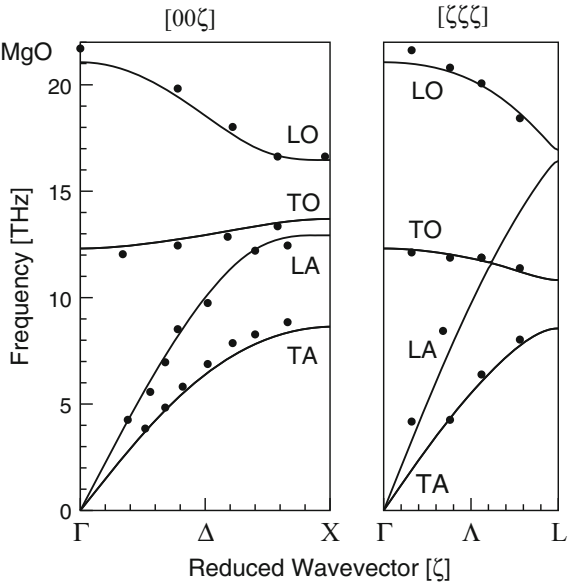

Fig. 7.11 Phonon dispersion curves for MgO along high-symmetry directions in the Brillouin zone. The transverse acoustic and optical phonon branches are doubly degenerate along these directions. Filled circles are neutron diffraction data [17]

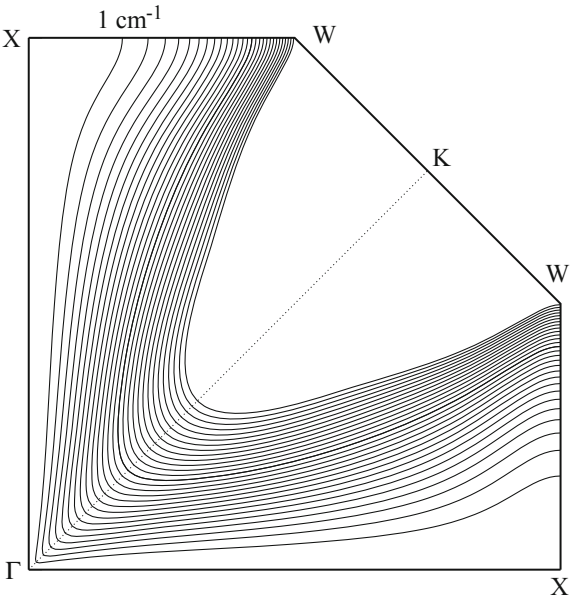

Fig. 7.12 Cross section through surfaces on which $\delta(\omega_1 - \omega_2 + \Omega)$ is satisfied for $\Omega = 1, 2, \ldots, 28\,\mathrm{cm}^{-1}$, where ω_1 and ω_2 are both transverse acoustic (TA) phonons. Along the direction Γ-K, the **q**-point on which isosurface contours intersect is a linear function of field frequency, $|\mathbf{q}|_\Omega \propto \Omega$, as one would expect for low-frequency linear dispersion phonons. The **q**-point intersections for the $X - W$ direction along the edge of the Brillouin zone boundary seems to follow a power law of roughly $|\mathbf{q}|_\Omega \propto \Omega^{\frac{1}{3}}$

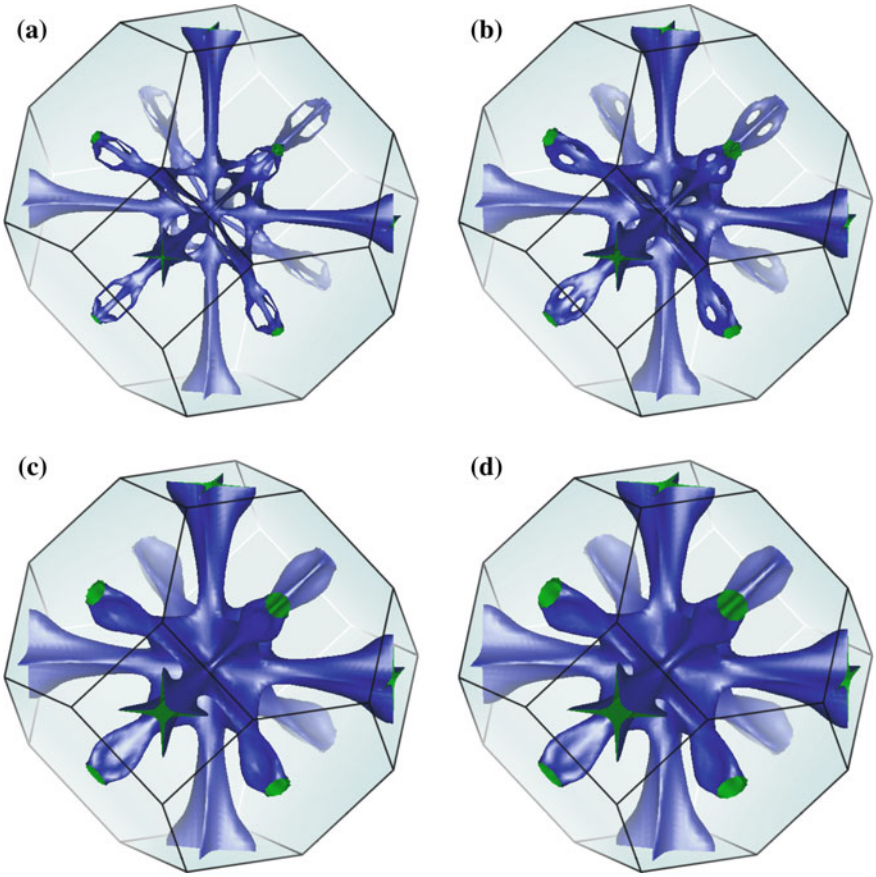

Fig. 7.13 Transverse acoustic phonons: Surfaces on which the energy conservation criterion, $\delta(\omega_{j_1} - \omega_{j_2} + \Omega)$ is satisfied, where $\omega_{j_2} > \omega_{j_1}$ and j_1 and j_2 are different transverse acoustic (TA) phonon branches. The microwave field frequency $\Omega = 9, 30, 60, 90$ GHz for (**a**), (**b**), (**c**) and (**d**), respectively. For $\Omega = 9$ GHz the energy conservation surface exists about the high-symmetry directions $\Gamma \rightarrow \Delta \rightarrow X$ and $\Gamma \rightarrow \Lambda \rightarrow L$, where for $\Omega \rightarrow 0$, the transverse acoustic phonons become doubly degenerate in frequency for $\Omega = 0$. The isosurface has fourfold and threefold symmetry about the Δ and Λ directions, respectively, and an interesting threefold connecting manifold between them for low microwave frequency Ω

zone boundary, they seem to follow a power law of roughly $|\mathbf{q}|_\Omega \propto \Omega^{\frac{1}{3}}$. To visualise the surfaces in three dimensions, a computer program was developed which applied the 'marching tetrahedra' algorithm [25] in conjunction with tricubic interpolation of the phonon frequencies to produce fine triangular meshes representing the surfaces on which the phonon transition energy conservation criteria $\delta(\omega_{j_1} - \omega_{j_2} + \Omega)$ are met throughout the Brillouin zone. Surfaces consisting of hundreds of thousands of triangles, were visually rendered using three-dimensional computer graphics[1]

[1] OpenGL.

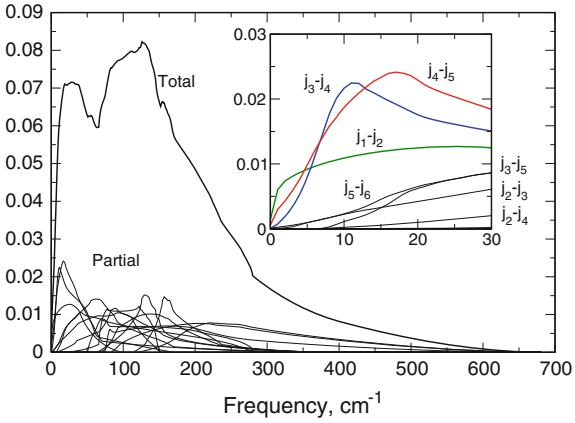

Fig. 7.14 The two-phonon difference-band density of states calculated by interpolated integration over a mesh generated by the marching tetrahedron method. Also shown are the partial contributions from phonon transitions $j_n \rightarrow j_m$, where $n = 1, \ldots, 5$ and $m = n + 1, \ldots, 6$. The inset shows which phonon transitions contribute most to the two-phonon difference-band density of states

and integrated analytically to calculate the partial two-phonon density of states in a similar way to Blöchl's tetrahedron method but with improved accuracy due to tricubic interpolation of the phonon frequencies (Fig. 7.14). Furthermore, the integration method serves as a basis for calculating the relaxation frequency $\Gamma_{\mathrm{TO}}(\Omega)$. For example, Fig. 7.13 shows manifolds on which energy conservation, defined by the Krönecker delta function $\delta(\omega_2 - \omega_1 + \Omega)$, is satisfied for transitions between the lowest acoustic phonon branches j_1 and j_2 for field frequencies of Ω of 9, 30, 60 and 90 GHz. The shape is evidently similar to the contours shown in Fig. 7.12, but also shows the fourfold and threefold symmetry about the Δ and Λ directions in the Brillouin zone.

7.11 Weighted Two-Phonon Density of States

If we compare the expressions for the two-phonon difference-band density of states, $\rho_2^-(\Omega)$ (7.9.1) with the expression for the self-energy due to the bubble diagram:

$$\Gamma_{\mathrm{TO}}^-(\Omega) = \frac{36}{\hbar^2} \sum_{\mathbf{q} j_1 j_2} |V_3(\mathbf{0} j_{\mathrm{TO}}, \mathbf{q} j_1, -\mathbf{q} j_2)|^2 \, (n_1 - n_2) \, \delta(\omega_2 - \omega_1 - \Omega)$$

it can be seen that the self-energy calculation is essentially a *weighted* two-phonon density-of-states calculation with weights defined by

$$w_{\mathbf{q} j j'}^- = \frac{36}{\hbar^2} |V_3(\mathbf{0} j_{\mathrm{TO}}, \mathbf{q} j_1, -\mathbf{q} j_2)|^2 \left[n(\omega_{\mathbf{q} j'}) - n(\omega_{\mathbf{q} j}) \right].$$

The weights encapsulate the third-order anharmonic coefficients $V_3(\mathbf{0} j_{\mathrm{TO}}, \mathbf{q} j_1, -\mathbf{q} j_2)$ and the difference in the Bose–Einstein phonon population numbers of the phonon branches j_1 and j_2. The Bose–Einstein phonon population is defined as

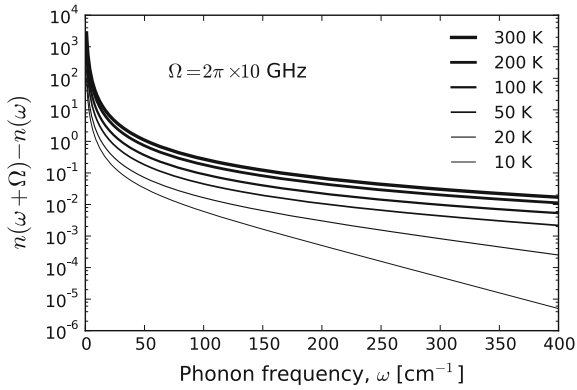

Fig. 7.15 Difference in Bose–Einstein phonon populations for transition between phonon branches with energy difference $\hbar\Omega$, where the microwave field frequency is $\Omega = 2\pi \times 10$ GHz

$$n(\omega_{\mathbf{q}j}) = \left[\exp\left(\frac{\hbar\omega_{\mathbf{q}j}}{kT}\right) - 1\right]^{-1},$$

so the population difference for two branches can be approximated for field frequencies Ω much lower than the phonon frequencies, $\Omega \ll \omega_j$, by

$$\begin{aligned} n_2 - n_1 = n(\omega_2) - n(\omega_1) &= n(\omega_1 + \Omega) - n(\omega_1) \\ &\approx \Omega \left.\frac{\partial n(\omega)}{\partial \omega}\right|_{\omega=\omega_1} \\ &= \frac{\hbar\Omega}{kT} n_1(n_1 + 1). \end{aligned} \tag{7.11.1}$$

This shows that the difference in phonon populations is far greater for acoustic low-frequency phonons which are much more heavily populated than optic phonons at low temperatures. The calculation of the relaxation frequency, $\Gamma(\Omega)$ therefore only requires a minor modification to the tetrahedron or marching tetrahedra integration methods used to calculate the two-phonon difference-band density of states.

Figure 7.15 shows the difference in phonon populations for a fixed field frequency of $\Omega = 2\pi \times 10$ GHz. For low-frequency acoustic phonons, the population difference is orders of magnitude greater than at higher optical frequencies.

7.12 Anharmonic Phonon Coupling Tensors

Third-order anharmonic coupling tensors were calculated using both the direct '$2n + 1$' method and the indirect 'frozen-phonon' finite-difference method. The '$2n + 1$' method directly calculates derivatives of the dynamical matrix using the third-order perturbation of the density with respect to phonon normal modes whereas the Frozen-Phonon method takes finite differences between dynamical matrices for

Table 7.2 Comparison of '$2n+1$' theorem and Frozen-phonon calculated derivatives of dynamical matrices with respect to the transverse optic (TO) phonon normal-mode coordinate, $\partial \widetilde{D}^{\kappa_1\kappa_2}_{\alpha_1\alpha_2}(\mathbf{q})/\partial Q(\mathbf{0}j_{\mathrm{TO}})$. Values shown here are for $\kappa_1 = 1$, $\kappa_2 = 2$, $\alpha_1 = 1$, $\alpha_2 = 1$

q-point	'$2n+1$' theorem	Frozen-phonon method
(0.00, 0.00, 0.00)	0.3441	0.3440
(−0.25, 0.25, −0.25)	0.3441	0.3440
(0.50, −0.50, 0.50)	0.4851	0.4347
(0.00, 0.50, 0.00)	0.0243	0.0315
(0.75, −0.25, 0.75)	0.332	0.3469
(0.50, 0.00, 0.50)	0.4854	0.4908
(0.00, −1.00, 0.00)	0.000	0.0001
(−0.50, −1.00, 0.00)	0.4865	0.4918

the equilibrium structure and structures with small normal-mode atomic displacement patterns 'frozen' into them. The '$2n+1$' and 'frozen-phonon' methods each produced derivatives of the dynamical matrix with respect to normal-mode coordinate of the TO phonon for eight special **q**-points corresponding to the Monkhorst-Pack set [26] for the irreducible wedge of a $4 \times 4 \times 4$ grid in reciprocal space. A comparison of the largest components obtained using these two techniques are shown in Table 7.2 where good agreement is evident.

The third-order anharmonic tensors can then be calculated via the Frozen-Phonon method by taking the dynamical-matrix derivatives with respect to TO phonon displacements:

$$V_3(\mathbf{0}j_{\mathrm{TO}}, \mathbf{q}j_1, -\mathbf{q}j_2) = \left(\frac{\hbar^3}{8N^3\omega_{\mathbf{q}j_1}\omega_{\mathbf{q}j_2}\omega_{\mathbf{0}j_{\mathrm{TO}}}}\right)^{\frac{1}{2}} \sum_{\substack{\alpha_1\alpha_2\\ \kappa_1\kappa_2}} \varepsilon^{\kappa_1}_{\alpha_1}(\mathbf{q}j_1)\varepsilon^{\kappa_2}_{\alpha_2}(\mathbf{q}j_2)\frac{\partial \widetilde{D}^{\kappa_1\kappa_2}_{\alpha_1\alpha_2}(\mathbf{q})}{\partial Q(\mathbf{0}j_{\mathrm{TO}})},$$

where $\varepsilon^{\kappa}_{\alpha}(\mathbf{q}j_i)$ is the α-component of the atomic displacement for atom κ associated with phonon mode on branch i with wave vector **q**. The dynamical-matrix derivatives were Fourier-interpolated onto a Monkhorst-Pack set of 3107 special points corresponding to a $50 \times 50 \times 50$ grid in reciprocal space. The anharmonic coupling tensors $V_3(\mathbf{0}j_{\mathrm{TO}}, \mathbf{q}j_1, -\mathbf{q}j_2)$ were finally calculated for the same $50 \times 50 \times 50$ set of points in reciprocal space upon which the phonon eigenfrequencies and difference-band isosurfaces were determined. Figure 7.16 shows anharmonic coupling tensor components for phonon branches along the high-symmetry directions of the MgO Brillouin zone.

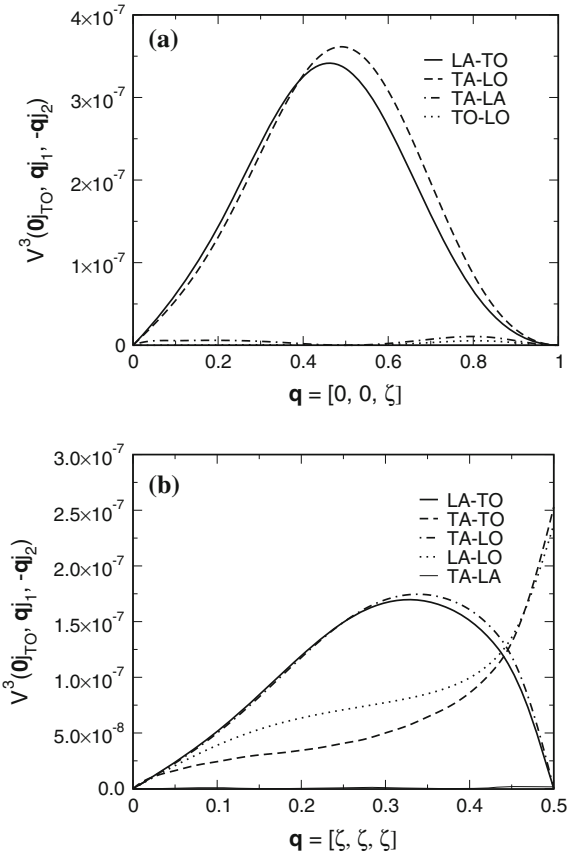

Fig. 7.16 **a** Anharmonic coupling tensor components between phonon branches along $\Gamma - \Delta - X$ direction. **b** Coupling along $\Gamma - \Lambda - L$ direction

7.13 The Relaxation Frequency, Γ

The relaxation frequency was calculated as a function of field frequency Ω and temperature T using the modified Blöchl tetrahedron method of integration over a $50 \times 50 \times 50$ mesh, essentially performing a two-phonon difference-band density-of-states calculation weighted with anharmonic phonon coupling constants and phonon occupation numbers according to the expression:

$$\Gamma^{-}_{\mathrm{TO}}(\Omega) = \frac{36}{\hbar^2} \sum_{\mathbf{q} j_1 j_2} |V_3(\mathbf{0} j_{\mathrm{TO}}, \mathbf{q} j_1, -\mathbf{q} j_2)|^2 \, (n_1 - n_2) \, \delta(\omega_2 - \omega_1 - \Omega).$$

The frequency dependence of $\Gamma(\Omega)$ will be investigated first before proceeding to probe its temperature dependence at microwave frequencies.

7.13.1 Frequency Dependence

Figure 7.17 shows the broadband frequency dependence of the TO mode relaxation frequency Γ (or inverse lifetime) at a temperature of 300 K where contributions from the dominant phonon transitions are highlighted. Note the interesting peak in Γ near $\Omega \approx 130\ \mathrm{cm}^{-1}$. It is also apparent that transitions between particular phonons are more likely within specific frequency ranges, implying that they are resonant. For example, for frequencies up to $50\,\mathrm{cm}^{-1}$ (1.5 THz) the $j_3 - j_4$ transition is dominant. This transition represents an acoustic to optic phonon transition, most probably LA to TO. Note that phonon branches are designated numerically by increasing frequency at a particular **q**-point and that they do not always coincide with the TA-LA-TO-LO sequence of modes near the Γ-point. In the 50–130 cm^{-1} range, the dominant transition is $j_1 - j_3$ which represents an acoustic–acoustic transition (TA to LA), with a smaller contribution from $j_2 - j_3$ (also TA to LA). Above $130\,\mathrm{cm}^{-1}$ various acoustic to optic transitions occur with a dominant contribution from $j_1 - j_6$ (TA-LO) above $250\,\mathrm{cm}^{-1}$.

Figure 7.18 shows the surfaces in the Brillouin zone where these processes occur. The TA-LA transitions (a) $j_1 - j_3$ and (b) $j_2 - j_3$ at $100\,\mathrm{cm}^{-1}$ take place upon manifolds which enclose the $\Gamma - \Delta - \mathrm{X}$ directions of fourfold symmetry with no apparent transitions in **q**-space extending toward the L-point at the edge of the Brillouin zone. The dominant transitions at $5\,\mathrm{cm}^{-1}$ have more complex manifolds which also have threefold symmetry and also include **q**-points at the L boundary. The relative permittivity as a function of field frequency Ω can be calculated using the dispersion relation and the calculated relaxation frequency, $\Gamma(\Omega)$,

$$\varepsilon(\Omega) = \varepsilon_\infty + \frac{\omega_{\mathrm{TO}}^2 \Delta\varepsilon}{\omega_{\mathrm{TO}}^2 - \Omega^2 - 2i\omega_{\mathrm{TO}}\Gamma(\Omega)}.$$

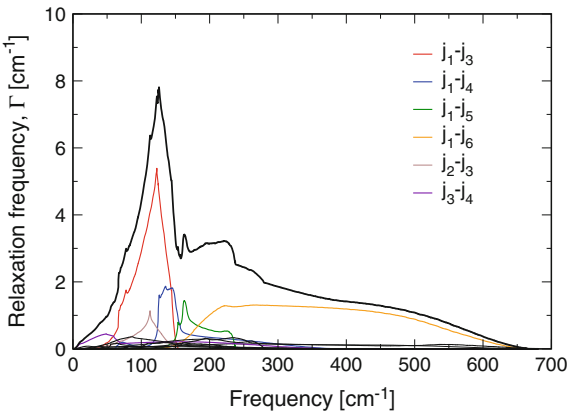

Fig. 7.17 Transverse optic relaxation frequency of MgO as a function of frequency, $\Gamma(\Omega)$ at a temperature of 300 K

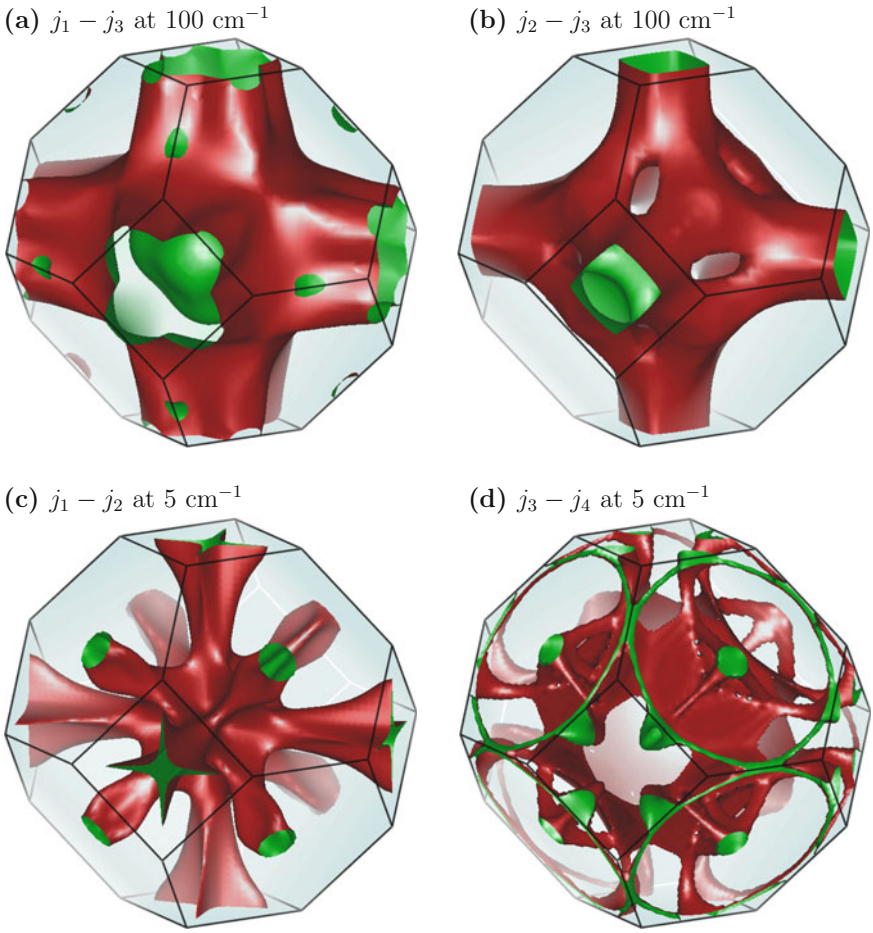

Fig. 7.18 Dominant phonon transitions at room temperature: Frequency surfaces for transitions between phonon branches j_a and j_b on which the energy conservation criteria $\delta(\omega_{j_b} - \omega_{j_a} + \Omega)$ are satisfied and which provide dominant contributions to the relaxation frequency at room temperature (300 K). Figures (**a**) and (**b**) show the $j_1 - j_3$ and $j_2 - j_3$ (TA-LA) contributions at 100 cm^{-1} (3 THz) which exhibit fourfold symmetry about the $\Gamma - \Delta - X$ directions. Figures (**c**) and (**d**) show the $j_1 - j_2$ (TA-TA) and $j_3 - j_4$ (LA-TO) contributions at 5 cm^{-1} (150 GHz), additional threefold symmetry about the $\Gamma - \Lambda - L$ directions

Taking the imaginary part yields the loss, ε'' and is shown in Fig. 7.19 with data measured using terahertz spectroscopy [27], and also the contribution due to isotopic disorder.

At microwave and millimetre wave frequencies, the real part of the relative permittivity is relatively constant and the loss tangent, $\tan\delta(\Omega)$, is given by $\varepsilon''/\varepsilon'$. Figure 7.20 shows the calculated loss tangent, $\tan\delta$ in the microwave frequency range at room temperature.

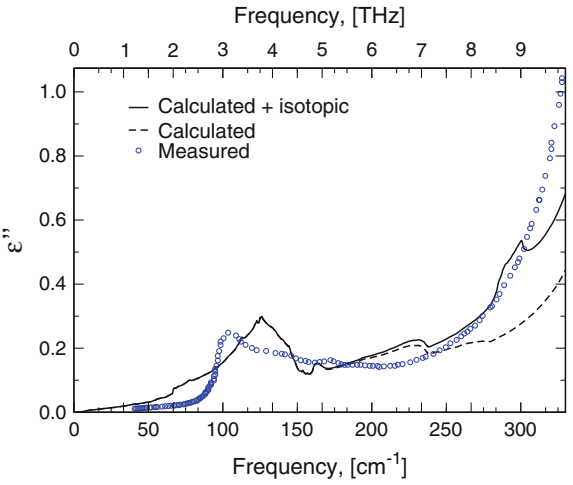

Fig. 7.19 Calculated and measured imaginary part of relative permittivity at room temperature in terahertz range: The measured data are for a MgO single crystal using terahertz spectroscopy [27]. The isotopic disorder contribution to $\Gamma(\Omega)$ has also been included out of interest

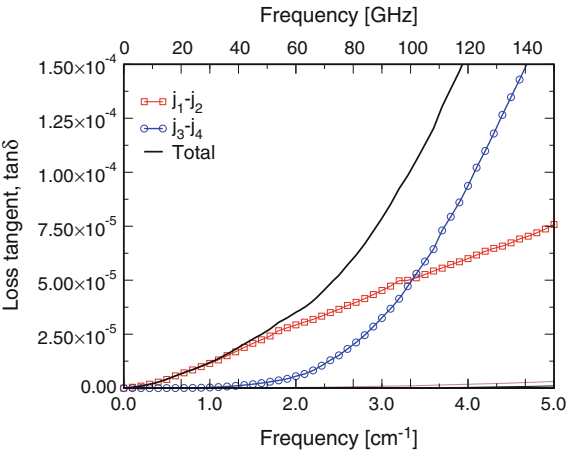

Fig. 7.20 Calculated microwave loss, $\tan\delta$ as a function of frequency at room temperature. The dominant phonon interactions are $j_1 - j_2$ (TA-TA) and $j_3 - j_4$ (LA-TO). The TA-TA mechanism has a linear field frequency dependence and is dominant below 100 GHz, whereas above 100 GHz the LA-TO transition comes into play with a Ω^2 frequency dependence

The calculated peak in loss around $130\,\mathrm{cm}^{-1}$ due to TA-LA phonon transitions is confirmed in the measured spectroscopic data and the magnitude of losses are in good agreement. At low field frequencies, $\Omega < 30$ GHz, the frequency dependence of the loss is linear ($\tan\delta \sim \Omega$), but then becomes quadratic ($\tan\delta \sim \Omega^2$) at higher frequencies as predicted by Gurevich's theory. There are two main contributions to the loss, each with different frequency dependencies and dominant over different frequency ranges. The $j_1 - j_2$ transitions between transverse acoustic phonons (TA-TA) are dominant below 100 GHz and have a linear frequency dependence. The $j_3 - j_4$ transitions between longitudinal acoustic and transverse optic phonons (LA-TO) are negligible below 40 GHz, but become dominant above 100 GHz with a Ω^2 frequency dependence. The calculated loss tangent at 10 GHz is 2.03×10^{-6} which compares very favourably with the room temperature measured value of $\tan\delta = 3.22 \times 10^{-6}$ at 10.3 GHz.

7.13.2 Temperature Dependence

At lower temperatures, high-frequency phonons such as optic and zone-boundary phonons are less populated and hence the population difference between phonon branches as shown in Fig. 7.15 is markedly higher for low-frequency phonons such as acoustic ones. It would be expected that as the temperature is decreased that LA-TO phonon interactions in the microwave loss spectrum would become less likely. Relaxation frequency spectra $\Gamma(\Omega)$ were calculated at temperatures in the range 10–340 K in steps of 10 K.

A subset for temperatures 100, 150, 200, 250 and 300 K is shown in Fig. 7.21. Note that the relaxation frequency decreases rapidly below 200 K and that the feature near 130 cm^{-1} remains prominent at 100 K due to absorption by low-frequency acoustic phonons. For microwave frequencies at a temperature of 100 K (see Fig. 7.22), the interaction between transverse acoustic phonons (TA-TA) becomes dominant over the entire frequency range up to 5 cm^{-1} (150 GHz) since the acoustic to optic (LA-TO) transition rate has decreased dramatically due to the decrease in high-frequency phonon population. The calculated loss tangent at 10 GHz is 1.55×10^{-7}, which is half the value of $\tan\delta = 3.98 \times 10^{-7}$ measured at 10.3 GHz. The larger measured losses are due to the onset of defect-induced dielectric losses below 100 K.

Figure 7.23 shows the calculated loss tangent at 10 GHz as a function of temperature compared with the measured values. The calculated values are lower by a small factor which is thought to be because the finite lifetimes of the phonons involved in transitions were not taken into account and that 4th order phonon interactions, which are expected to become more significant at high temperatures have been neglected. A log–log plot (Fig. 7.24) allows the temperature dependence of the measured and predicted losses to be compared. At low temperatures, the calculated loss tangent has a T^4 dependence as predicted by Gurevich's theory. As temperature increases the dependence becomes T^2, confirming Gurevich's prediction and agreeing with the measured losses. Unfortunately, the defect-induced losses in the

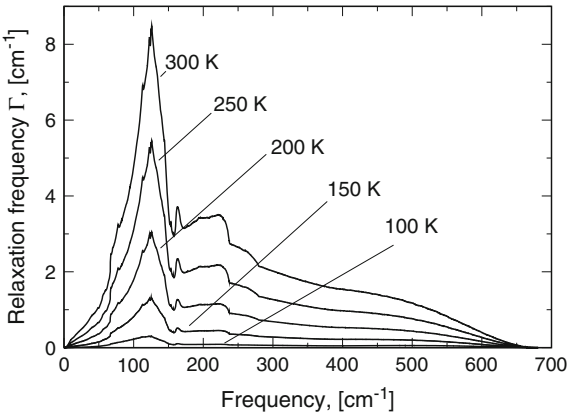

Fig. 7.21 Relaxation frequency, $\Gamma(\Omega)$ at temperatures of 100, 150, 200, 250 and 300 K

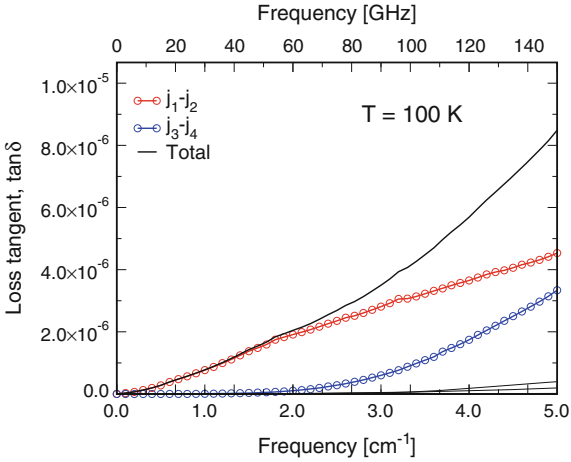

Fig. 7.22 Calculated microwave loss tangent, tan δ as a function of frequency at a temperature of 100 K: The dominant phonon interactions are still $j_1 - j_2$ (TA-TA) and $j_3 - j_4$ (LA-TO), but the longitudinal acoustic to transverse optical transition (LA-TO) has reduced relative to the (TA-TA) interaction

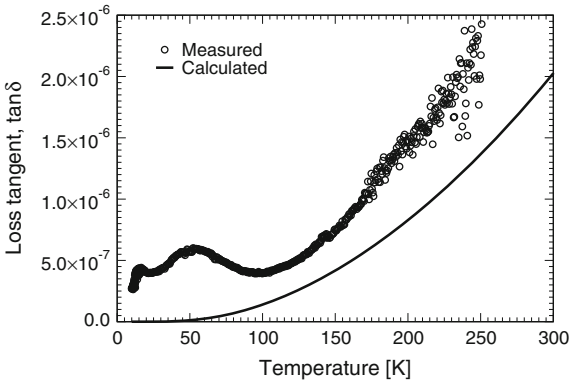

Fig. 7.23 Calculated and measured microwave dielectric loss tangent at 10 GHz as a function of temperature

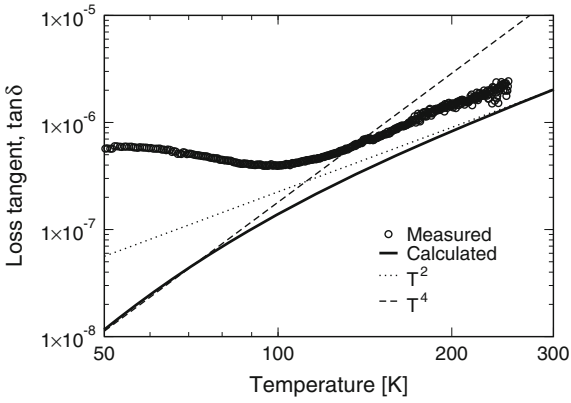

Fig. 7.24 Calculated and measured microwave dielectric loss tangent at 10 GHz as a function of temperature in log–log scale

measured MgO single crystal do not allow the low-temperature T^4 dependence to be confirmed. However, the agreement between calculated and measured losses is very encouraging. Finally, since $\Gamma(\Omega)$, the imaginary part of the TO phonon self-energy is calculated over a frequency range spanning the entire domain of phonons in MgO, a Kramers–Kronig transformation can be applied to produce the real part of the self-energy, $\Delta(\Omega)$. This will allow the temperature coefficient of permittivity prediction due to thermal strain, calculated earlier in the chapter, to be improved upon. The results of the Kramers–Kronig transformations appear in Fig. 7.25 for temperatures ranging from 10 to 300 K in steps of 10 K. The same was done for the LO phonon to produce the real frequency shifts for both TO and LO phonons as functions of temperature. The shifts at $\Omega = 0$ cm^{-1} were taken in order to calculate the static relative permittivity as a function of temperature (see Fig. 7.26). This result shows that the temperature coefficient of permittivity in microwave dielectric ceramics is a purely anharmonic phenomenon, partly due to thermal expansion, which for most ceramics is usually of similar magnitude, but more importantly also due in part to the same mechanism that is responsible for intrinsic dielectric losses.

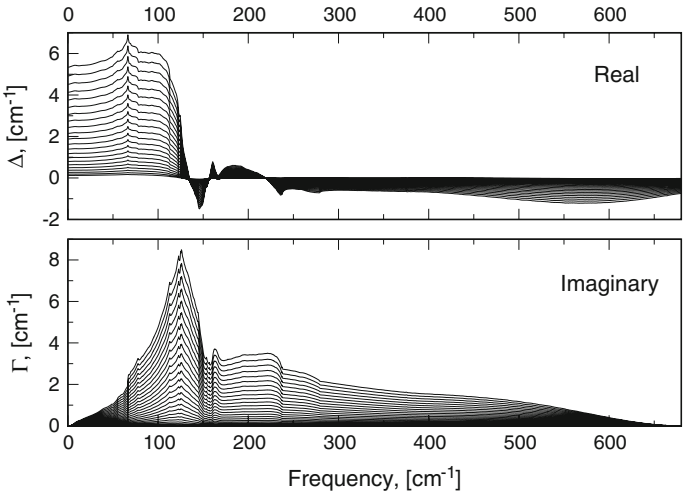

Fig. 7.25 Real and imaginary parts of TO phonon self-energy $\Sigma = \Delta + i\Gamma$ as functions of frequency for a range of temperatures from 10 to 300 K. The real parts of the self-energy Δ were calculated using a Kramers–Kronig transformation of the calculated imaginary part Γ

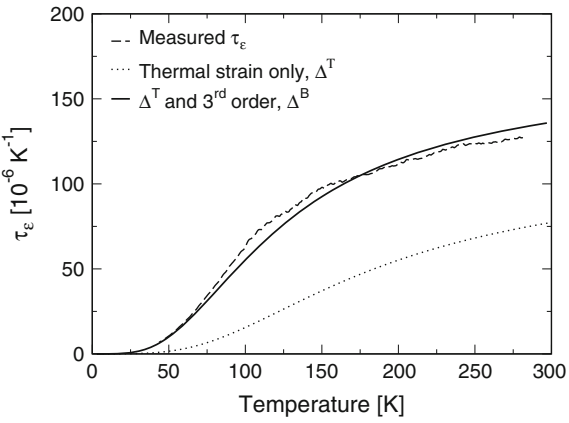

Fig. 7.26 Calculated temperature coefficient of permittivity τ_ε for MgO at microwave frequencies. The calculated value (*solid line*) includes contributions to the real shift in frequency of the TO and LO zone-centre optical phonons from both the thermal strain and the 3rd order bubble diagram. The calculated data agree well with the measured data (*dashed line*)

7.14 Summary and Conclusions

This chapter has investigated the anharmonic properties of MgO using the quasi-harmonic approximation, a simple quantum field theory of absorption and *ab initio* results from quantum mechanical calculations using density functional perturbation theory. No empirical data were used in the calculations which resulted in fairly accurate predictions of the linear coefficient of thermal expansion, electromagnetic absorption up to terahertz frequencies and the frequency and temperature dependence of the complex permittivity of MgO. Although the agreement was satisfactory, of more importance was the *information* the calculations and their subsequent analysis produced. For example, visualisation of the phonon–phonon energy conservation surfaces provides valuable insight into the structure of loss mechanisms. Furthermore, by calculating the contribution to the relaxation frequency of the interactions between specific pairs of phonon branches, a rich landscape of frequency and temperature dependence was revealed. This suggests that the techniques used here are powerful and valuable tools for the study of microwave dielectric materials and could be used in the terahertz regime where a new generation of devices and applications are emerging.

References

1. A. Debernardi, S. Baroni, E. Molarini, Anharmonic phonon lifetimes in semiconductors from density-functional perturbation theory. Phys. Rev. Lett. **75**, 1819 (1995)
2. A. Debernardi, M. Cardona, Isotopic effects on the lattice constant in compound semiconductors by perturbation theory: an ab initio calculation. Phys. Rev. B **54**, 11305 (1996)
3. A. Debernardi, Phonon linewidth in III–V semiconductors from density-functional perturbation theory. Phys. Rev. B **57**, 12847 (1998)

4. A. Debernardi, M. Cardona, First principles calculation of the real part of phonon self energy in compound semiconductors. Phys. B: Conden. Matter **263**, 687 (1999)
5. G. Lang et al., Anharmonic line shift and linewidth of the Raman mode in covalent semiconductors. Phys. Rev. B **59**, 6182 (1999)
6. G. Deinzer, G. Birner, D. Strauch, Ab initio calculation of the linewidth of various modes in germanium and silicon. Phys. Rev. B **67**, 144304 (2003)
7. J.M. Ziman, *Electrons and Phonons*, 1st edn. (Oxford University Press, Oxford, 1960)
8. R. Berman, E.L. Foster, J.M. Ziman, The thermal conductivity of dielectric crystals: the effect of isotopes. Proc. R. Soc. Lond. Ser. A **237**, 344 (1956)
9. V.I. Ozhogin et al., Isotope effect in the thermal conductivity of germanium single crystals. J. Exp. Theor. Phys. Lett. **63**, 490 (1996)
10. J.M. Zhang et al., Optical phonons in isotopic Ge studied by Raman scattering. Phys. Rev. B **57**, 1348 (1998)
11. A. Göbel et al., Effects of isotope disorder on energies and lifetimes of phonons in germanium. Phys. Rev. B **58**, 10510 (1998)
12. J. Serrano et al., Dispersive phonon linewidths: the E_2 phonons of ZnO. Phys. Rev. Lett. **90**, 055510 (2003)
13. S. Tamura, Isotope scattering of dispersive phonons in Ge. Phys. Rev. B **27**, 858 (1983)
14. F. Widulle, J. Serrano, M. Cardona, Disorder-induced phonon self-energy of semiconductors with binary isotopic composition. Phys. Rev. B **65**, 075206 (2002)
15. G.K. White, O.L. Anderson, Grüneisen parameter of magnesium oxide. J. Appl. Phys. **37**, 430 (1966)
16. P.E. Blöchl, O. Jepsen, O.K. Andersen, Improved tetrahedron method for Brillouin-zone integrations. Phys. Rev. B **49**, 16223 (1994)
17. M.J.L. Sangster, G. Peckham, D.H. Saunderson, Lattice dynamics of magnesium oxide. J. Phys. C **3**, 1026 (1970)
18. C. Herring, Accidental degeneracy in energy bands of crystals. Phys. Rev. **52**, 365 (1937)
19. C. Herring, Role of low-energy phonons in thermal conduction. Phys. Rev. **95**, 954 (1954)
20. Y. Balagurov, V.G. Vaks, B.I. Shklovskii, Attenuation of critical vibrations and dielectric losses in displacive-type ferroelectrics. Sov. Phys. Solid State **12**, 70 (1970)
21. V.L. Gurevich, Dielectric losses in crystals. Fizika Tverdogo Tela **21**, 3453 (1979)
22. V.L. Gurevich, A.K. Tagantsev, Intrinsic dielectric loss in crystals: low temperatures. Sov. Phys. JETP **64**, 142 (1986)
23. V.L. Gurevich, *Transport in Phonon Systems*, 1st edn. (North-Holland Physics Publishing, Amsterdam, 1986)
24. V.L. Gurevich, A.K. Tagantsev, Intrinsic dielectric loss in crystals. Adv. Phys. **40**, 719 (1991)
25. C.D. Hansen, C.R. Johnson, *Visualization Handbook* (Academic Press, New York, 2004), pp. 7–11
26. H.J. Monkhorst, J.D. Pack, Special points for Brillouin-zone integrations. Phys. Rev. B **13**, 5188 (1976)
27. G.A. Komandin et al., Multiphonon absorption in a MgO single crystal in the terahertz range. Phys. Solid State **51**, 1928 (2009)

Chapter 8
Discussion and Conclusions

Modelling and Measuring Dielectric Resonators

Various types of resonator for measuring the dielectric properties of microwave ceramics were reviewed. The shielded dielectric resonator was discussed in more detail and modelled analytically using Maxwell's equations. The radial mode matching method was successfully implemented and used to model an example dielectric resonator demonstrating efficiency and accuracy. Computer-controlled cryogenic apparatus was developed for measuring the resonant frequency and Q-factor of dielectric resonators containing samples of MgO, $LaAlO_3$, TiO_2 and Al_2O_3. Temperature measurements between 10 K and room temperature were taken and processed using the radial mode matching to produce accurate values of the relative permittivity and loss tangent. Anisotropy in the relative permittivity was tackled by measuring different resonant modes, close in frequency, with different polarizations.

Harmonic Properties of Metal Oxide Dielectrics from First Principles

The lattice dynamics of insulators and basic outline of density functional perturbation theory was reviewed followed by a discussion on how to calculate dynamical matrices, phonon frequencies, Born effective charges and dielectric tensors. The power and accuracy of DFPT within the LDA was then demonstrated by modelling the crystal structure, phonon frequencies and low-frequency relative permittivities of MgO, $LaAlO_3$, TiO_2 and Al_2O_3. The predicted values for the relative permittivity were in excellent agreement with the low-temperature experimental data as shown in the Table 8.1.

Theory of Anharmonic Phonons and Prediction of Properties for MgO

The lattice dynamics of anharmonic crystals were reviewed and a quantum field theory-based definition of the self-energy of phonons in the interaction representation was introduced. A graphical technique for evaluating Feynman diagrams of

J. Breeze, *Temperature and Frequency Dependence of Complex Permittivity in Metal Oxide Dielectrics: Theory, Modelling and Measurement*, Springer Theses, DOI 10.1007/978-3-319-44547-2_8

Table 8.1 Summary of predicted permittivities at 0 K compared with low-temperature experimental values

Material		Theory	Expt.
MgO	ε_r	9.674	9.651
$LaAlO_3$	ε_r	24.12	23.62
TiO_2	$\varepsilon_{r,\perp}$	110.9	112.6
	$\varepsilon_{r,\parallel}$	250.2	250.5
Al_2O_3	$\varepsilon_{r,\perp}$	9.363	9.260
	$\varepsilon_{r,\parallel}$	11.321	11.344

phonon–phonon interactions was used to derive expressions for the lowest-order contributions to the self-energy. Supporting this theoretical framework with numerical ab-initio calculations allowed the anharmonic properties of MgO to be investigated. The quasi-harmonic approximation yielded thermal expansion coefficients for MgO as functions of temperature which were in excellent agreement with experimental data. Two-phonon difference band density of states were analyzed and visualized, providing insight into the role of the different phonon branches at difference frequencies. The dielectric loss was then calculated to terahertz frequencies as a function of temperature and frequency. An interesting peak in the loss was found near 3 THz, confirmed by terahertz spectroscopy of a MgO single crystal and attributed to transverse acoustic to longitudinal acoustic phonon transitions. The microwave loss temperature dependence was in excellent agreement with the measured data, within a factor of two. Kramers–Kronig transformation of the self-energy inverse lifetime as a function of field frequency $\Gamma(\Omega)$ yielded the real part of the self-energy, a shift in phonon frequency. When this frequency shift was combined with the frequency shift due to thermal expansion and the 4^{th}-order anharmonic contribution, the relative permittivity, τ_ε was also in excellent agreement with the measured data.

In summary, it was shown that it is possible to produce fairly accurate predictions of the linear coefficient of thermal expansion, electromagnetic absorption up to terahertz frequencies and the frequency and temperature dependence of the complex permittivity of MgO from first principles using freely available ab-initio codes and a general theory of dielectric loss. Although the agreement was satisfactory, the *information* the calculations and their subsequent analysis produced was of much value. For example, visualization of the phonon–phonon energy conservation surfaces provide valuable insight into which phonons branches contributed to the loss within specific frequency ranges. Even a simple crystal like MgO generated a rich landscape showing the interplay of phonons over frequency and temperature ranges.

Scope for Future Work

The results of this thesis have for the first time predicted the dielectric properties of microwave dielectric materials as a function of temperature and frequency, demonstrating that the techniques used were powerful and valuable tools for the overall study of microwave dielectric materials. To improve the results, it would of course

be desirable to calculate higher order anharmonic terms and also to include the self-energy implicitly in the phonon propagators so that the lifetime of the phonons taking part in interactions could be taken into account. To accomplish this, it is envisaged that a self-consistent approach should be taken, where the self-energies of phonons are calculated on a grid spanning the Brillouin zone instead of only at the zone-centre Gamma point. Self-consistent iteration of the system would hopefully lead to convergence across all points and lead to more accurate predictions of losses. A calculation of this kind would be considerably more involved than the present one, but is entirely feasible within the context of currently available computational resources especially if parallel computation is considered. It would of course be interesting to continue this work further by calculating the losses for other microwave dielectric materials, such as $LaAlO_3$, TiO_2 and Al_2O_3, complex ordered perovskites such as Barium Magnesium Tantalate or high-resistivity Silicon. Although the thesis was primarily concerned with complex permittivity at microwave frequencies, it has also shown that the properties can be predicted into the terahertz range. This exciting frequency range has recently become accessible with new devices and applications emerging in fields as diverse as medicine, imaging, sensors and security.

Finally, being able to structure a material at the nanoscale enables the exciting possibility of being able to enhance or suppress the phonon density of states at specific frequencies or wave vectors and thus offers the promise of being able to engineer properties such as dielectric loss and thermal conductivity.